AD-E300 441

DNA 4531F-1

ADA064134

AERODYNAMIC ACCOUNTING TECHNIQUE FOR DETERMINING EFFECTS OF NUCLEAR DAMAGE TO AIRCRAFT

Volume I—Empirical Methods

General Dynamics Corporation
Fort Worth Division
P.O. Box 748, Grants Lane
Fort Worth, Texas 76101

28 February 1978

Final Report for Period 15 March 1977—30 January 1978

CONTRACT No. DNA 001-77-C-0075

D D C
RECEIVED
FEB 5 1979
B

Prepared for

Director

DEFENSE NUCLEAR AGENCY

Washington, D. C. 20305

79 01 10

Destroy this report when it is no longer
needed. Do not return to sender.

PLEASE NOTIFY THE DEFENSE NUCLEAR AGENCY,
ATTN: TISI, WASHINGTON, D.C. 20305, IF
YOUR ADDRESS IS INCORRECT, IF YOU WISH TO
BE DELETED FROM THE DISTRIBUTION LIST, OR
IF THE ADDRESSEE IS NO LONGER EMPLOYED BY
YOUR ORGANIZATION.

REPORT DOCUMENTATION PAGE	READ INSTRUCTIONS BEFORE COMPLETING FORM

1. REPORT NUMBER	2. GOVT ACCESSION NO.	3. RECIPIENT'S CATALOG NUMBER
DNA 4531F-1		

4. TITLE (and Subtitle)	5. TYPE OF REPORT & PERIOD COVERED
AERODYNAMIC ACCOUNTING TECHNIQUE FOR DETERMINING EFFECTS OF NUCLEAR DAMAGE TO AIRCRAFT. Volume I. Empirical Methods.	Final Report for Period 15 Mar 77—30 Jan 78
	6. PERFORMING ORG. REPORT NUMBER

7. AUTHOR(s)	8. CONTRACT OR GRANT NUMBER(s)
Roy Schemensky George Howell	DNA 001-77-C-0075

9. PERFORMING ORGANIZATION NAME AND ADDRESS	10. PROGRAM ELEMENT, PROJECT, TASK AREA & WORK UNIT NUMBERS
General Dynamics Corporation Fort Worth Division, P.O. Box 748, Grants Lane Fort Worth, Texas 76101	Subtask N99QAXAE506-02

11. CONTROLLING OFFICE NAME AND ADDRESS	12. REPORT DATE
Director Defense Nuclear Agency Washington, D.C. 20305	28 February 1978
	13. NUMBER OF PAGES
	228

14. MONITORING AGENCY NAME & ADDRESS(if different from Controlling Office)	15. SECURITY CLASS (of this report)
	UNCLASSIFIED
	15a. DECLASSIFICATION/DOWNGRADING SCHEDULE

16. DISTRIBUTION STATEMENT (of this Report)

Approved for public release; distribution unlimited.

17. DISTRIBUTION STATEMENT (of the abstract entered in Block 20, if different from Report)

18. SUPPLEMENTARY NOTES

This work sponsored by the Defense Nuclear Agency under RDT&E RMSS Code B342077464 N99QAXAE50602 H2590D.

19. KEY WORDS (Continue on reverse side if necessary and identify by block number)

Drag Prediction	Roughness	Computer Program
Lift Prediction	Blast	Nuclear Damage
Aircraft	Overpressure	
Damage	Thermal Effects	

20. ABSTRACT (Continue on reverse side if necessary and identify by block number)

This report (Volume I, Empirical Methods) presents the methods, equations and substantiating data for an empirically based computer program which calculates lift, moment, and drag characteristics of an undamaged baseline aircraft in addition to calculating the aerodynamics of an aircraft which has sustained nuclear damage. The input requires a simple definition of the basic undamaged configuration geometry along with parameters specifying the mode of damage, magnitude, and dimension of the damaged area. Up to fourteen different modes —>

DD FORM 1473 EDITION OF 1 NOV 65 IS OBSOLETE
1 JAN 73

20. ABSTRACT (Continued)

of damage can be specified which can model most types of damage. The computer code has the capability of assessing the aerodynamics effects of damage, such as rough, bent, and burnt skins, boundary-layer thickness effects, and loss of radomes, panels, doors and covers. Also, the computer code has the capability of analyzing changes in drag due to lift and trim caused by asymmetric loss of parts of the wing or trim surfaces. The accuracy of the program is verified through comparisons of the predicted results with experimental data for several configurations. Details of the input and output for this program along with a FORTRAN source deck listing and sample problem are contained in Volume II, Program User Guide.

ACCESSION for

NTIS	White Section	☑
DDC	Cuff Section	☐
UNANNOUNCED		☐
JUSTIFICATION		

BY
DISTRIBUTION/AVAILABILITY CODES

| Dist. | AVAIL and/or SPECIAL |

A

Table of Contents
Volume I

2

Section 6. (Continued)

Section 8. (Continued)

LIST OF FIGURES

6

LIST OF FIGURES, Continued

8

LIST OF FIGURES, (Continued)

LIST OF FIGURES, (Continued)

LIST OF FIGURES, (Continued)

LIST OF FIGURES, (Continued)

1. INTRODUCTION

The need exists for a fast, accurate, and easy-to-use method for performing preliminary design trade studies and aircraft roughness and damage assessment studies. The evaluation of the mission completion capability of an aircraft that survives an exposure to a nuclear weapon blast mainly requires an assessment of the increase in drag resulting from the damage caused by the nuclear blast. Mission completion studies also must determine the maximum levels of nuclear overpressure, gust, and thermal exposure that the aircraft can sustain and that causes drag buildup to reach a level where the assigned mission is just achievable. This report documents a computerized Aerodynamic Accounting Technique (AAT), which was devised to greatly simplify and systematize the task of predicting the aerodynamics of aircraft, including roughness and various modes of damage.

The AAT computer code is a modification of an existing Aircraft Aeroanalysis computer program (Reference 1), which was designed to predict baseline aerodynamic data for the undamaged aircraft. The existing Aeroanalysis code incorporates new subroutines to read the input for damage specifications, perform the calculations, and print out the results of the damage evaluation.

Input to the AAT computer code requires a definition of the basic undamaged configuration geometry along with parameters specifying the mode of damage and magnitude and dimension of the damaged area. Basic aircraft geometry is represented by a seris of component bodies and airfoil surfaces. Up to 14 different modes of surface components, 7 for body components and 7 for airfoil surface components, can be specified, providing the user with a great deal of flexibility in modeling any conceivable type of damage. The AAT code has the capability of assessing the aerodynamic effects of damage such as rough , bent, and burnt skins (and paint) and loss of radomes, panels, doors, and covers. Also, the AAT methods have the capability to analyze changes in drag due to lift and trim caused by asymmetric loss of parts of the wing or trim surface.

The methods, equations, and substantiating data for the AAT computer code are presented in this volume. Details of the input and output of this program along with a FORTRAN source deck listing and sample problems are contained in Volume II, Program User Code.

2. GEOMETRY

The Aerodynamic Accounting Technique computer code requires a minimum of input data since most of the geometric parameters used in the aerodynamic methods are calculated internally within the program. Some geometric parameters such as wetted areas and mean geometric chords can be either generated internally by the program or accepted as input data. The conventions and equations used by the AAT procedure to determine the geometric parameters used in aerodynamic calculations are described in this section.

2.1 COMPONENT GEOMETRY

Two types of components are used to represent the basic aircraft geometry. The fuselage, canopy, stores, and nacelles are represented by a series of bodies; the wing, tail surfaces, pylons, and ventrals are represented by a series of single-panel airfoil surfaces. For cranked or complex wing planforms the wing can also be represented with two interconnected surface panels. Provision is also incorporated into the program for computing the geometric parameters for variable-wing-sweep configurations.

2.1.1 Body Geometry

The minimum geometry input requirements for the body components are length, width, height, nose length, and boattail length; in addition, for open-nosed bodies, the inlet and exit area must be specified. If the maximum cross-sectional area of the component, A_{MAX}, is not input, the value is calculated by

$$A_{MAX} = \frac{\pi}{4} \text{ (width x height)} \tag{2-1}$$

Also, if wetted area for the component is not input, a value is then calculated. The wetted area for N close-nosed bodies is determined by

$$A_{wet} = \left[2.8 \, \ell_N + 2.5 \, \ell_{BT} \left(1 + \sqrt{\frac{A_{base}}{A_{max}}} \right) + 4(\ell - \ell_N - \ell_{BT}) \right] \sqrt{\frac{\pi}{4} A_{max}} \cdot N \tag{2-2}$$

14

For N open-nosed bodies, wetted area is determined by

$$A_{wet} = \left[2.5 \, \ell_N \left(1 + \sqrt{\frac{A_{inlet}}{A_{max}}} \right) + 2.5 \, \ell_{BT} \left(1 + \sqrt{\frac{A_{exit}}{A_{max}}} \right) + 4 \, (\ell - \ell_N - \ell_{BT}) \sqrt{\frac{\pi}{4} \, A_{max}} \right] \cdot N \qquad (2-3)$$

2.1.2 Airfoil Surface Geometry

The input required to define the planform for the airfoil surface components are the exposed root chord, tip chord, exposed semi-span, and the leading-edge sweep angle.

The taper ratio, exposed area, the aspect ratio of the wing panels and horizontal surface components are calculated by these equations:

$$\lambda_s = C_T / C_{R_X} \qquad (2-4)$$

$$S_{exp} = C_{R_X} \, (1 + \lambda_s) \, (b/2)_X \qquad (2-5)$$

$$AR_s = 4 \, (b/2)_X^2 / S_{exp} \qquad (2-6)$$

For vertical surface components the exposed area and aspect ratio are half the values given by equations (2-5) and (2-6). Left and right symmetry is assumed if the vertical surface has a Y displacement off the configuration centerline. The mean exposed geometric chord for each panel is calculated by the equation

$$\bar{c}_s = \frac{2}{3} \, C_{R_X} \left[1 + \frac{\lambda_s^2}{1 + \lambda_s} \right] \qquad (2-7)$$

If the component wetted area is not input, it is calculated internally in the computer code by the equation

$$S_{WET} = S_{exp} \left[2 + .1843(t/c)_s + 1.5268(t/c)_s^2 - .8395(t/c)_s^3 \right] \qquad (2-8)$$

15

The wetted area is essentially twice the exposed area with a small factor to account for thickness.

The leading edge sweep for each surface component is entered by the user; the quarter chord, mid-chord, trailing edge, and max thickness sweep angles are calculated using the following equations

$$\Lambda_{C/4} = \arctan\left[\tan\Lambda_{LE} - \frac{CO}{4}\right] \qquad (2\text{-}9)$$

$$\Lambda_{C/2} = \arctan\left[\tan\Lambda_{LE} - \frac{CO}{2}\right] \qquad (2\text{-}10)$$

$$\Lambda_{TE} = \arctan\left[\tan\Lambda_{LE} - CO\right] \qquad (2\text{-}11)$$

$$\Lambda_{MAX\ t/c} = \arctan\left[\tan\Lambda_{LE} - (X/C)_{MAX \atop t/c} \cdot CO\right] \qquad (2\text{-}12)$$

where

$$CO = \frac{4}{ARs}\ \frac{1 - \lambda_s}{1 + \lambda_s} \qquad (2\text{-}13)$$

For trim calculations the fuselage station location of the horizontal tail or canard quarter-chord point on the mean geometric chord is calculated from

$$X_{HT} = \frac{1}{3}\,(b/2)_x \left[\frac{1 + 2\lambda_s}{1 + \lambda_s}\right]\tan\Lambda_{LE} + \frac{\bar{c}_s}{4} + X_{LE} \qquad (2\text{-}14)$$

The moment arm of the trim surface at any angle of attack is computed from

$$\ell_{HT} = X_H \cos(\Omega - \alpha) \qquad (2\text{-}15)$$

where

$$X_H = \sqrt{(Z_{LE} - Z_{CG})^2 + (X_{HT} - X_{CG})^2}$$

and

$$\Omega = \arctan\left[\frac{(Z_{LE} - Z_{CG})}{(X_{HT} - X_{CG})}\right]$$

X_{CG} and Z_{CG} are the longitudinal and vertical locations of the moment reference point, and X_{LE} and Z_{LE} are the input values of the longitudinal and vertical location of the leading edge of the exposed root chord of the trim surface.

2.1.3 Wing Geometry

If the main wing is defined as one panel, total planform area, taper ratio, and aspect ratio are computed from input

16

with the following equations (see Figure 2-1a)

$$C_R = C_T + (C_{R_x} - C_T) \frac{Y + (b/2)_x}{(b/2)_x} \qquad (2\text{-}16)$$

$$\lambda = C_T/C_R \qquad (2\text{-}17)$$

$$S_{PLAN} = C_R (1 + \lambda) b/2 \qquad (2\text{-}18)$$

$$AR_p = b^2/S_{PLAN} \qquad (2\text{-}19)$$

The geometry for an arbitrary wing defined with two panels, shown in Figure 2-1b, is calculated from the following equations.

$$C_R = C_{Ti} + (C_{Rxi} - C_{Ti}) \frac{Y_i + (b/2)_{xi}}{(b/2) \, xi} \qquad (2\text{-}20)$$

$$S_{PLAN} = (C_{Rxo} + C_{To}) (b/2)_{xo} + (C_R + C_{Ti})$$

$$(Y_i + (b/2)_{xi}) \qquad (2\text{-}21)$$

$$\lambda = (b/2) C_{To}/(S_{PLAN} - (b/2) C_{To}) \qquad (2\text{-}22)$$

Average values of thickness and camber are computed by the root-mean-square equations

$$(t/c) = \sqrt{\frac{(t/c)_i^2 S_i + (t/c)_o^2 S_o}{S_i + S_o}} \qquad (2\text{-}23)$$

$$C_{Ld} = \sqrt{\frac{(C_{\ell d})_i^2 S_i + (C_{\ell d})_o^2 S_o}{S_i + S_o}} \qquad (2\text{-}24)$$

Certain aerodynamic calculations, such as wing wave drag and lift-curve slope, require the use of an "equivalent" trapezoidal wing that approximates the planform of the arbitrary wing. The sweep angle of the equivalent wing is obtained by area-weighting the sweep according to the equations

$$(\Lambda_{LE})_e = \arctan \left[\frac{\tan \Lambda_{LE_i} S_i + \tan \Lambda_{LE_o} S_o}{S_i + S_o} \right] \qquad (2\text{-}25)$$
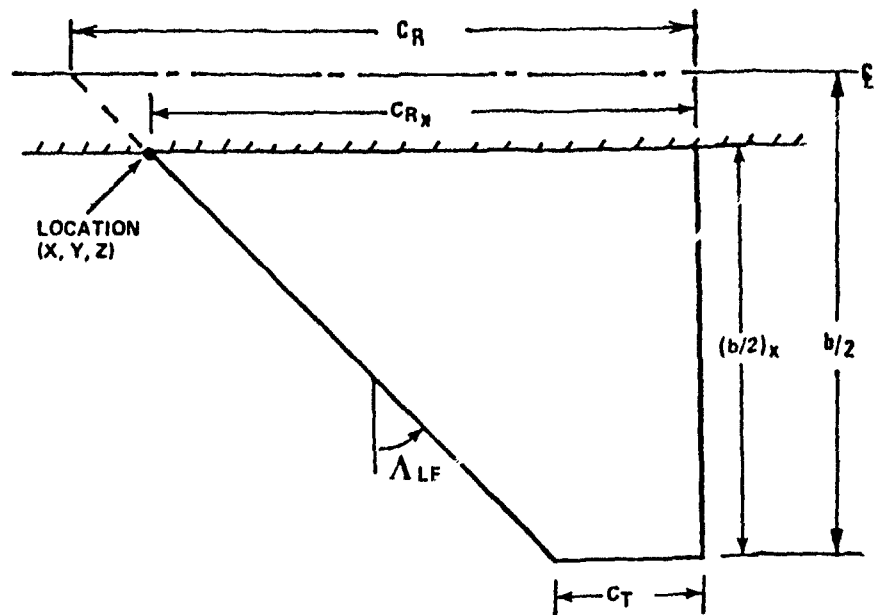
(a) Single-Panel Wing
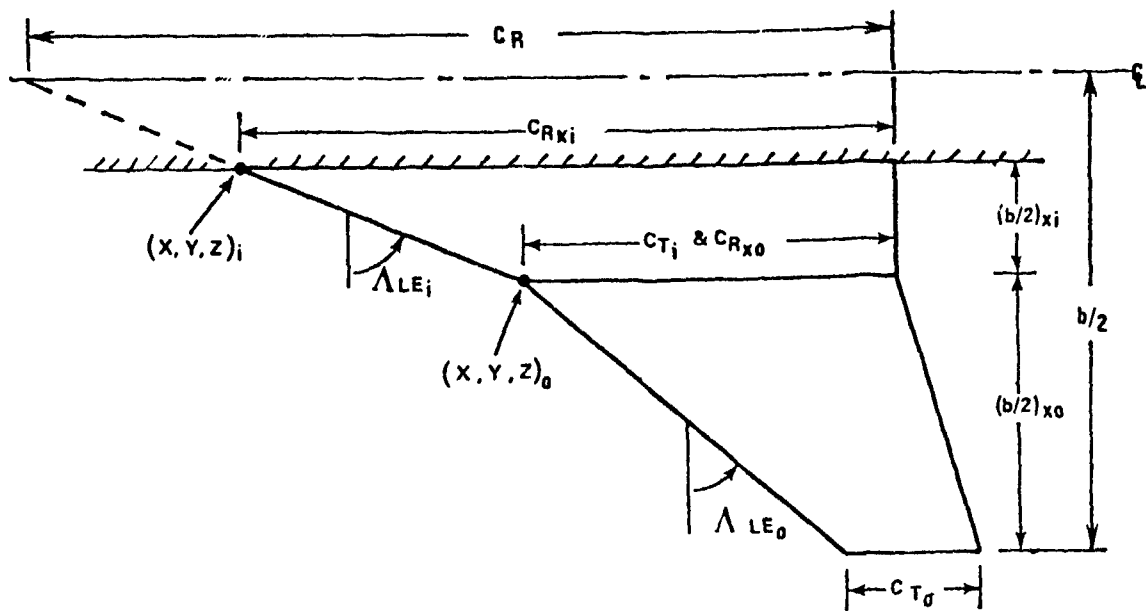
(b) Two-Panel Wing

Figure 2-1   Wing Geometric Parameters

18

$$\left(\Lambda_{C/4}\right)_e = \text{arcos} \left[\frac{\cos\Lambda_{C/4_i}\, S_i + \cos\Lambda_{C/4_o}\, S_o}{S_i + S_o}\right] \quad (2\text{-}26)$$

$$\left(\Lambda_{C/2}\right)_e = \text{arcos} \left[\frac{\cos\Lambda_{C/2_i}\, S_i + \cos\Lambda_{C/2_o}\, S_o}{S_i + S_o}\right] \quad (2\text{-}27)$$

$$\left(\Lambda_{TE}\right)_e = \text{arctan} \left[\frac{\tan\Lambda_{TE_i}\, S_i + \tan\Lambda_{TE_o}\, S_o}{S_i + S_o}\right] \quad (2\text{-}28)$$

For a double-panel wing the planform area can be input rather than calculated in Equation (2-21) by summing the panel exposed areas and adding the area obtained by extending the innermost panel to the centerline of the aircraft. In the case of a wing whose innermost panel represents a strake with a large leading-edge sweep angle, extending this panel to the centerline of the aircraft would result in an extremely large planform area. In this case the value of the theoretical planform area of the wing, ignoring the strake, should be input. The aspect ratio is defined as

$$AR = b^2/S_{PLAN} \quad (2\text{-}29)$$

Lift and drag parameters are calculated by use of the aspect ratio defined with the wing planform area, and the final results are then referenced to the reference area, S_{REF}, which is input. In most typical cases, S_{PLAN} equals S_{REF}.

2.2 VARIABLE-SWEEP CONFIGURATION

The planform for a variable-sweep configuration is defined by a trapezoidal movable panel and an optional glove panel, as shown in the sketch below.

19
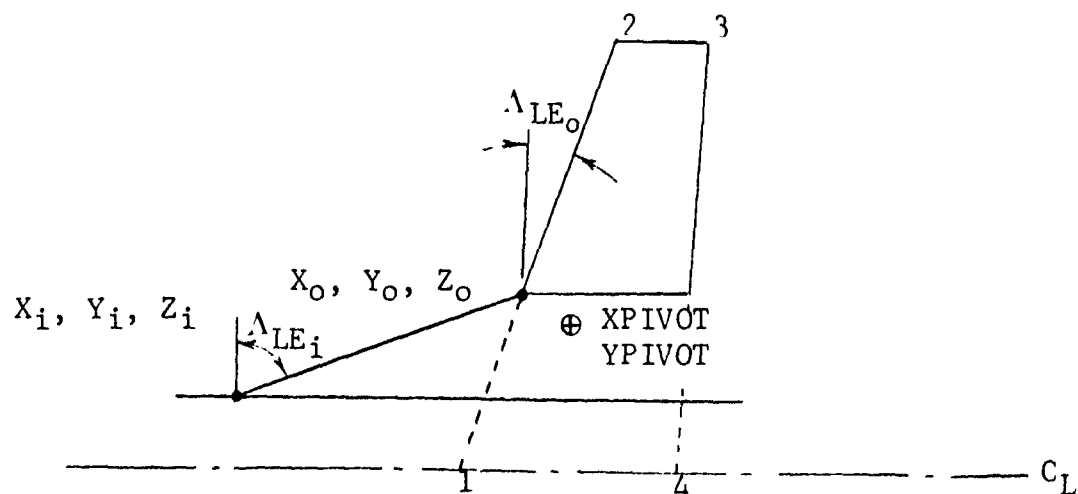
The procedure first defines the coordinates of Points 1, 2, 3, and 4 from the input. (The input planform area is equal to twice the area enclosed by these four points.) When the movable panel is rotated about the pivot point, the resulting geometry is as sketched below. The coordinates of Points 2, 3, 5, and 6 are
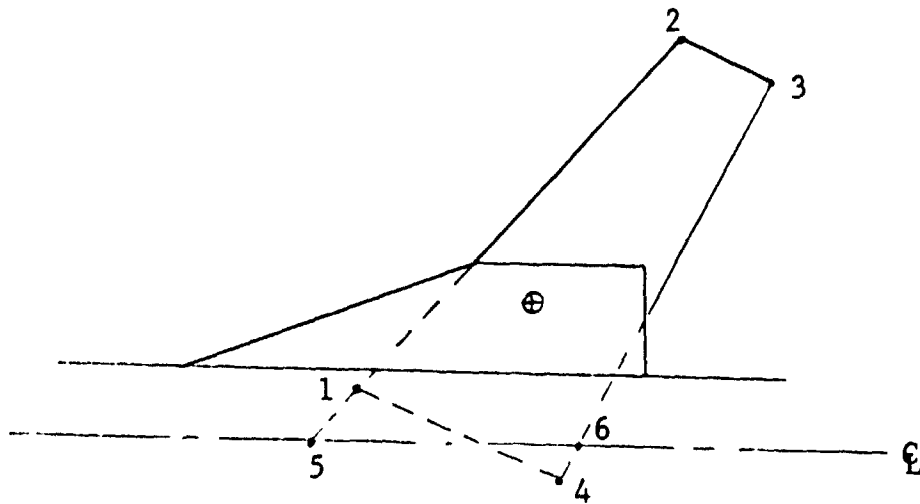
then determined. The planform area is calculated as twice the area enclosed by these four points. Since the tip chord is assumed streamwise at the forward reference sweep, the distance from Point 2 to the centerline is the semi-span, $b/2$. The aspect ratio is thus defined as

$$AR = b^2/S_{PLAN} \tag{2-30}$$

The taper ratio is calculated as

$$\lambda = C_T/C_R \tag{2-31}$$

where C_T and C_R are as defined in the following sketch.

20
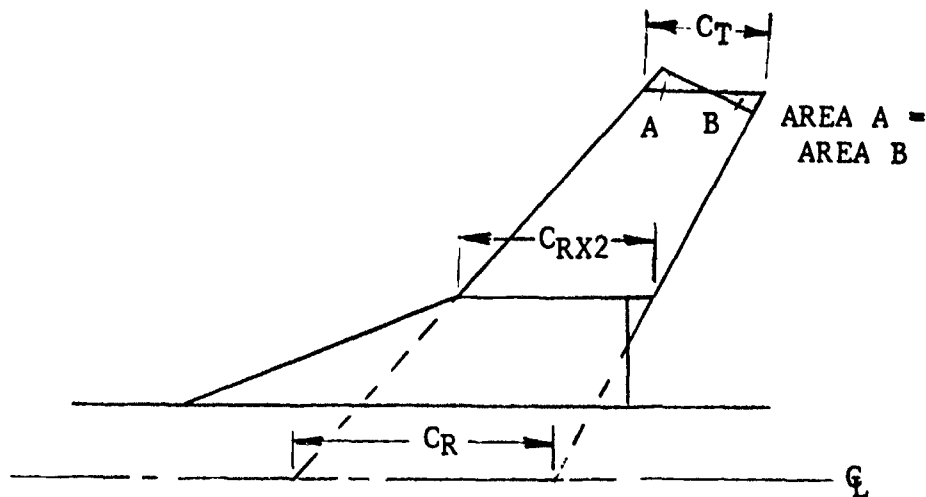
The mean aerodynamic chord (MAC) and wetted area of the outboard panel are calculated by use of the tip chord, C_T, and the chord, $C_{R_{X_O}}$. The (MAC)$_{calculated}$ is expressed for the outboard panel as

$$(MAC)_{calculated} = \frac{2}{3} \, C_{RX2} \left[1 + \frac{\lambda'^2}{1 + \lambda'} \right] \qquad (2-32)$$

where $\lambda' = C_T/C_{RX2}$. The wetted area (A$_{wet}$)$_{calculated}$ is computed using twice the exposed area of the panel and the thickness correction to wetted area expressed by Equation 2-8. These calculated values for MAC and A$_{wet}$ are compared with the optional input values at the forward-reference-sweep and the aft-reference-sweep conditions. If the calculated and input values differ, as might occur for non-trapezoidal planforms, the input values are used and the incremental differences between the two are used for interpolation purposes in the calculation of MAC and A$_{wet}$ at intermediate sweep angles. The equations are as follows:

$$MAC = MAC_{calc.} + \Delta MAC_1 + (\Delta MAC_2 - \Delta MAC_1) \, \frac{\Lambda - \Lambda_1}{\Lambda_2 - \Lambda_1} \qquad (2-33)$$

$$A_{wet} = A_{wet_{calc.}} + \Delta A_{wet_1} + (\Delta A_{wet_2} - \Delta A_{wet_1}) \, \frac{\Lambda - \Lambda_1}{\Lambda_2 - \Lambda_1} \qquad (2-34)$$

21

where

$$\Delta \text{MAC} = \text{MAC}_{calc.} - \text{MAC}_{input}$$

$$\Delta A_{wet} = A_{wet_{calc.}} - A_{wet_{input}}$$

and where the subscript 1 refers to the forward reference sweep position, and the subscript 2 refers to the aft reference sweep position.

The maximum-thickness sweep angle, $\Lambda(t/c)_{max}$, used in friction drag calculations, is calculated from the quarter-chord sweep of the panel and the input $\Lambda(t/c)_{max}$ at the forward and aft reference sweep positions. The equation is

$$\Lambda(t/c)_{max} = \Lambda_{c/4} + \Delta\Lambda_1 + (\Delta\Lambda_2 - \Delta\Lambda_1)\frac{\Lambda - \Lambda_1}{\Lambda_2 - \Lambda_1} \qquad (2\text{-}35)$$

where

$$\Delta\Lambda = (\Lambda_{c/4})_{calc.} - (\Lambda(t/c)_{max})_{input}$$

The streamwise camber and thickness of the outboard panel at a given sweep are calculated by

$$(C_{L_d})_{calc.} = (C_{L_d})_{ref} \cdot \frac{C'/C}{(C'/C)_{ref}} \qquad (2\text{-}36)$$

$$(t/c)_{calc.} = (t/c)_{ref} \cdot \frac{C'/C}{(C'/C)_{ref}} \qquad (2\text{-}37)$$

where

$$C'/C = 0.5\left[\frac{\cos\Lambda_{LE}}{\cos(\Lambda_{LE}-\Lambda_{c}/2)} + \frac{\cos\Lambda_{TE}}{\cos(\Lambda_{c}/2-\Lambda_{TE})}\right] \qquad (2\text{-}38)$$

Equation 2-38 is the relationship between the chord perpendicular to the mid-chord sweep, C', and the streamwise chord, C. For a variable-sweep wing, C' remains constant so that the camber and thickness perpendicular to the mid-panel sweep also remain constant. Finally, the outboard panel thickness is compared with the aft reference sweep input value and, if the calculated and input values differ, the input value is used for interpolation

purposes in the calculation of t/c at intermediate sweep angles. The equation is as follows:

$$(t/c) = (t/c)_{calc.} + (\Delta t/c) \cdot \frac{\Lambda - \Lambda_1}{\Lambda_2 - \Lambda_1} \qquad (2\text{-}39)$$

where $(\Delta t/c) = (t/c)_{input} - (t/c)_{calc.}$ at aft sweep.

The variation of wing twist with sweep can be calculated from

$$\tau = \arctan \left(\frac{\Delta Z}{C}\right)_{tip} \qquad (2\text{-}40)$$

where ΔZ is the vertical position of the leading edge (assuming the wing is twisted about the trailing edge) and C is the streamwise chord at the tip in the swept position. The tip displacement is calculated at the forward reference sweep position through the equation

$$(\Delta Z)_{tip} = (C_R \lambda) \tan \tau$$

The streamwise chord at the tip is calculated from

$$C_{tip} = C_R - (b/2)(\tan \Lambda_{LE} - \tan \Lambda_{TE})$$

The tip displacement is assumed to be independent of sweep.

The variation of wing incidence with sweep is calculated from

$$i = i_{ref} \left(1 - \tan \Delta \Lambda_{LE} \cdot \tan \Lambda_{TE_1}\right) \cos \Delta \Lambda_{LE} \qquad (2\text{-}41)$$

where $\Delta \Lambda_{LE} = \Lambda_{LE} - \Lambda_{LE_1}$. In calculating the variations of twist and incidence with wing sweep, it is assumed that the wing pivot is perpendicular to the wing chord plane.

2.3 AIRFOIL SECTION GEOMETRY

Several airfoil section parameters are used in the aerodynamic predictions. These parameters are generated internally in the program for the NACA 6-series and 4-digit airfoil sections and for biconvex airfoil sections. The procedure determines the leading-edge radius as a function

of thickness ratio, t/c, as shown in Figure 2-2. The distance of the position of maximum thickness from the leading edge, X_t/c_{max}, is listed in Table I. A leading-edge sharpness parameter, Δ_y, expressed as

$$\Delta_y = A(t/c) \tag{2-42}$$

is defined for uncambered airfoils, where A is a function of the airfoil leading-edge geometry (shown plotted in Figure 2.2.1-8 of Reference 2). The trailing-edge angle of the upper surface of the airfoil is computed from

$$\emptyset_{TE} = B(t/c) + C(C_{\ell_d}) \tag{2-43}$$

A, B, C values used in the AAT program are listed in Table I.

If the airfoil section cannot be approximated by one of the sections contained within the AAT program, the user can input geometry to define any arbitrary airfoil section.

Two examples of the designation for a six-series airfoil are given by:

64-210 and
64A210

The 6 for the first digit indicates a 6-series airfoil. The second digit (4) designates the chordwise location (in tenths) of the minimum pressure for the basic symmetric airfoil at zero lift. The third digit (2) designates the camber design lift coefficient (in tenths). The last two digits (10) designate the airfoil thickness (in percent). The letter A appearing in some 6-digit series designations indicates that a modified thickness and camber distribution is used.

An example of the designation for a 4-digit airfoil is given by

0012-34

where the 12 designates the thickness (in percent chord), the 4 designates the position of maximum thickness (in tenths), and the 3 designates the leading-edge radius (3 designates 1/4 normal, 6 designates normal, and 9 designates 9X normal leading-edge radius).
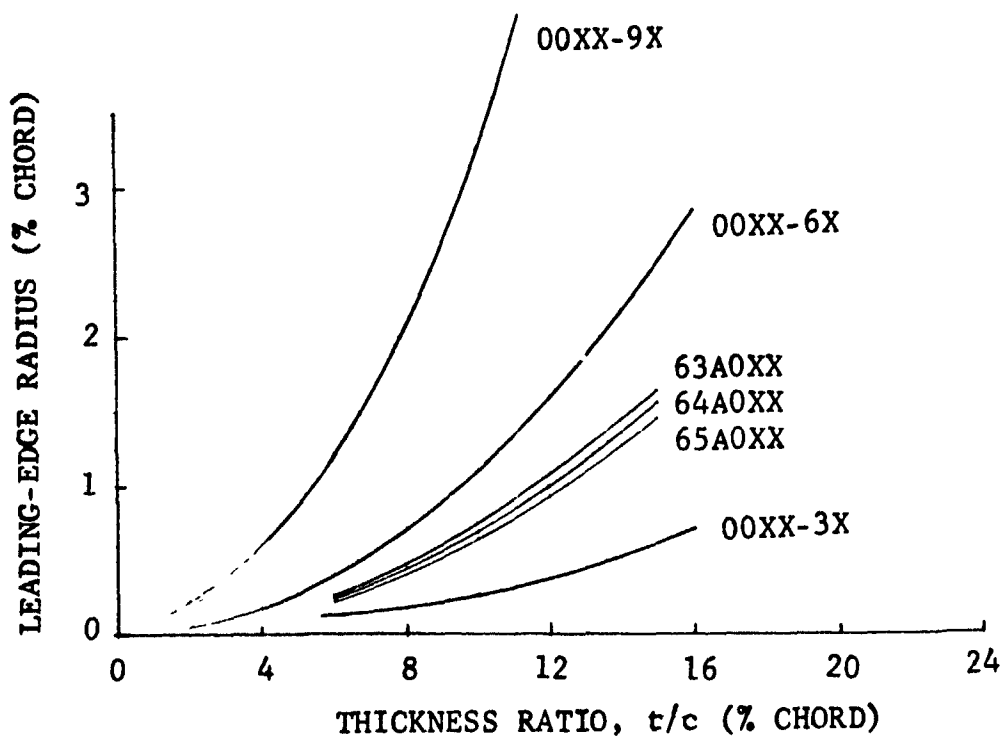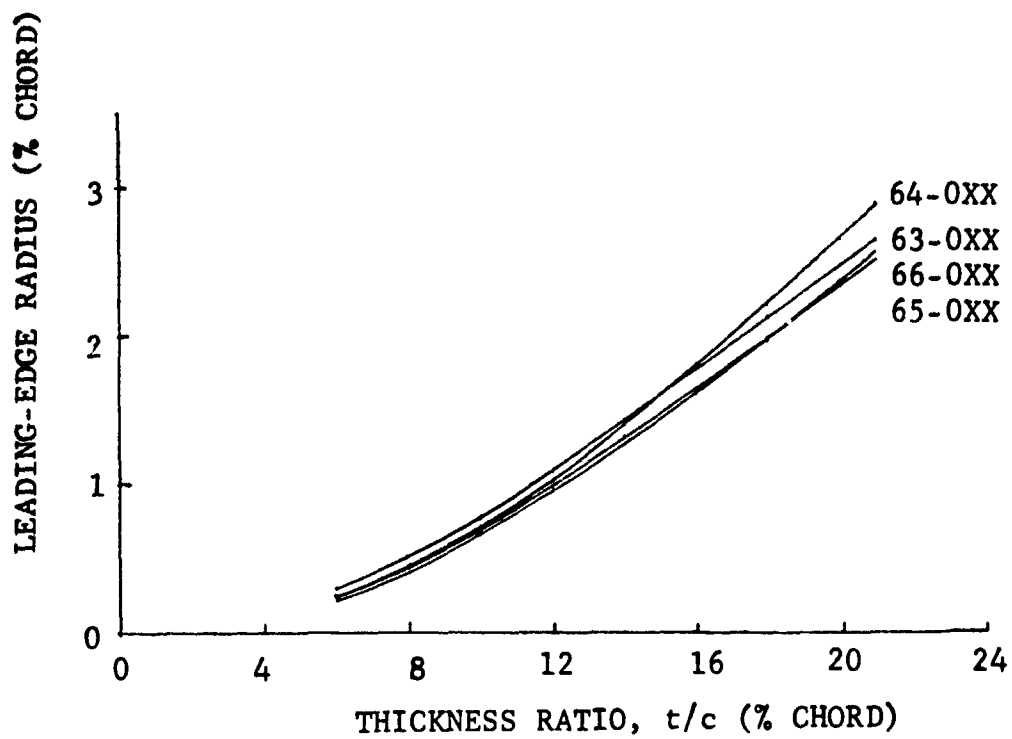
Figure 2-2   Variation of Leading-Edge Radius with
Thickness Ratio of Airfoils

Table 1

TABULATED AIRFOIL SECTION PARAMETERS

Airfoil Type	$X_{(t/c)_{max}}$	A	B	C
63-series	.35	22.0	34.6	14.8
64-series	.375	21.7	38.4	14.8
65-series	.41	19.2	46.4	14.8
66-series	.44	18.35	60.2	14.8
63A	.37	22.0	57.5	14.05
64A	.39	21.2	59.5	14.05
65A	.42	19.2	66.5	14.05
Biconvex	.50	11.75	95.0	0.0
00XX-62	.2	24.0	50.0	13.8
-63	.3	24.0	63.0	13.8
-64	.4	22.0	82.8	13.8
-65	.5	20.0	113.0	13.8
-66	.6	20.0	153.0	13.8
-33	.3	19.0	63.0	13.8
-34	.4	17.0	82.8	13.8
-35	.5	15.0	113.0	13.8
-93	.3	29.0	63.0	13.8
-94	.4	27.0	82.8	13.8
-95	.5	25.0	113.0	13.8

3. MINIMUM DRAG

The drag of an aircraft can be represented as the sum of minimum drag, plus drag due to lift, plus drag due to trim. The drag bookkeeping system used in the AAT code has minimum drag comprised of the drag items that are assumed to be independent of lift, such as friction, form, interference, wave, base, camber, roughness and proturberance. Drag due to lift is comprised of the drag items that vary with lift, such as induced drag, profile drag increment due to lift, and flow separation drag. Transonic drag rise, which varies with lift, is separated for bookkeeping purposes into an increment added to minimum drag and an increment added to drag due to lift. In transport aircraft where the fuselage has an upswept aft end, the increment in fuselage drag between an upswept fuselage and a symmetrical fuselage is tabulated in the program output as a function of lift. The drag buildup does not include incremental drag contributions due to propulsion installation such as spillage drag, bleed, nozzle effects, etc. This is consistent with thrust-drag accounting systems in which the propulsion-related drag increments are included in the propulsion force buildup since these drag increments vary with power setting. If a horizontal tail or canard is present on the configuration, the untrimmed lift and drag is computed for a zero tail deflection condition. The effect of horizontal tail deflection for trim is determined by computing the lift and drag increment relative to the zero tail setting.

The methods used to determine each of the minimum drag contributions and the fuselage aft-end upsweep drag are described in the following subsections. Drag rise, drag due to lift, and trim drag are discussed in Sections 5, 4, and 7, respectively.

3.1 FRICTION, FORM, AND INTERFERENCE DRAG

A large part of the subsonic minimum drag is comprised of the sum of friction, form, and interference drag of all the aircraft components. The drag of each component is computed as

$$C_D = (C_f \cdot \frac{A_{wet}}{S_{ref}}) \cdot FF \cdot IF \qquad (3-1)$$

where C_f is the compressible flat-plate skin-friction coefficient, A_{wet} is the component wetted area, and FF and IF are the component form and interference factors.

3.1.1 Friction Drag

The compressible, turbulent, skin-friction coefficient on a smooth flat plate is determined from the general equation given in Reference 3,

$$C_f = \frac{1}{F_1} C_{f_i} (R_{N_L} \cdot F_2) \tag{3-2}$$

where F_1 and F_2 are functions of the freestream Mach number and wall temperature. The incompressible skin-friction coefficient, C_{f_i}, is evaluated at the equivalent Reynolds number, $R_{N_L} F_2$. The Reynolds number, R_{N_L}, is computed as component length times Reynolds number/unit length obtained from atmospheric tables or input. White and Christoph (Reference 3) developed expressions for the transformation functions F_1 and F_2 along with a more accurate, explicit equation, based on Prandtl/Schlichting type relations, for computing the incompressible, turbulent, flat-plate friction coefficient (C_{f_i}) with the following results:

$$F_1 = t^{-1} f^{-1}$$

$$F_2 = t^{1+n} f$$

$$C_{f_i} = \frac{0.430}{\left(\log_{10} R_{N_L}\right)^{2.56}}$$

For an adiabatic wall condition, t and f are given by

$$t = T_\infty/T_{aw} = \left[1 + r \frac{\gamma-1}{2} M_\infty^2\right]^{-1} \tag{3-3}$$

$$f = 1 + 0.044 \, r \, M_\infty^2 \, t$$

Using a recovery factor $r = 0.89$ and a viscosity power-law exponent $n = 0.67$, recommended in Reference 3, results in the following expression for C_f:

$$C_f = t \, f^2 \, \frac{0.430}{\left(\log_{10}(R_{N_L} \cdot t^{1.67} \cdot f)\right)^{2.56}} \tag{3-4}$$

where

$$t = \left[1 + 0.178 \, M_\infty^2\right]^{-1}$$

$$f = 1 + 0.03916 \, M_\infty^2 \cdot t$$

28

The rough flat-plate skin-friction coefficient is determined from the formulas developed by Schlichting (Reference 4)

$$C_f = t \, (1.89 + 1.62 \, \log_{10} \, \ell/k)^{-2.5} \tag{3-5}$$

where t is a compressibility factor (Equation 3-3) applicable to rough plates (Reference 5), ℓ is the component length, and k is the equivalent sand grain roughness height.

The skin-friction coefficient used in the AAT computer code will vary according to Equation 3-4 with Reynolds number until it intersects the value of C_f determined by Equation 3-5 for a particular value of k. For higher values of R_{N_L}, the friction coefficient remains constant according to Equation 3-5. The AAT code computes C_f using both Equation 3-4 and 3-5, and uses the larger of the two values for friction drag calculations. Calculated values of C_f versus R_{N_L} and C_f versus ℓ/k are presented in Figures 3-1 and 3-2.

3.1.2 Form Factors

The component form factors, FF, account for the increased skin friction caused by the supervelocities of the flow over the body or surface and the boundary-layer separation at the trailing edge. The form factors for components represented as bodies are computed as

$$FF = 1 + 60/FR^3 + 0.0025 \cdot FR \tag{3-6}$$

where

$$FR = \frac{\text{Component Length}}{\sqrt{\text{Width} \times \text{Height}}}$$

For components represented as nacelles, the form factors are given by

$$FF = 1 + 0.35/FR \tag{3-7}$$

The airfoil form factors depend upon airfoil type and stream-wise thickness ratio. For 6-series airfoils, the form factor is given by

$$FF = 1 + 1.44(t/c) + 2(t/c)^2 \tag{3-8}$$

29
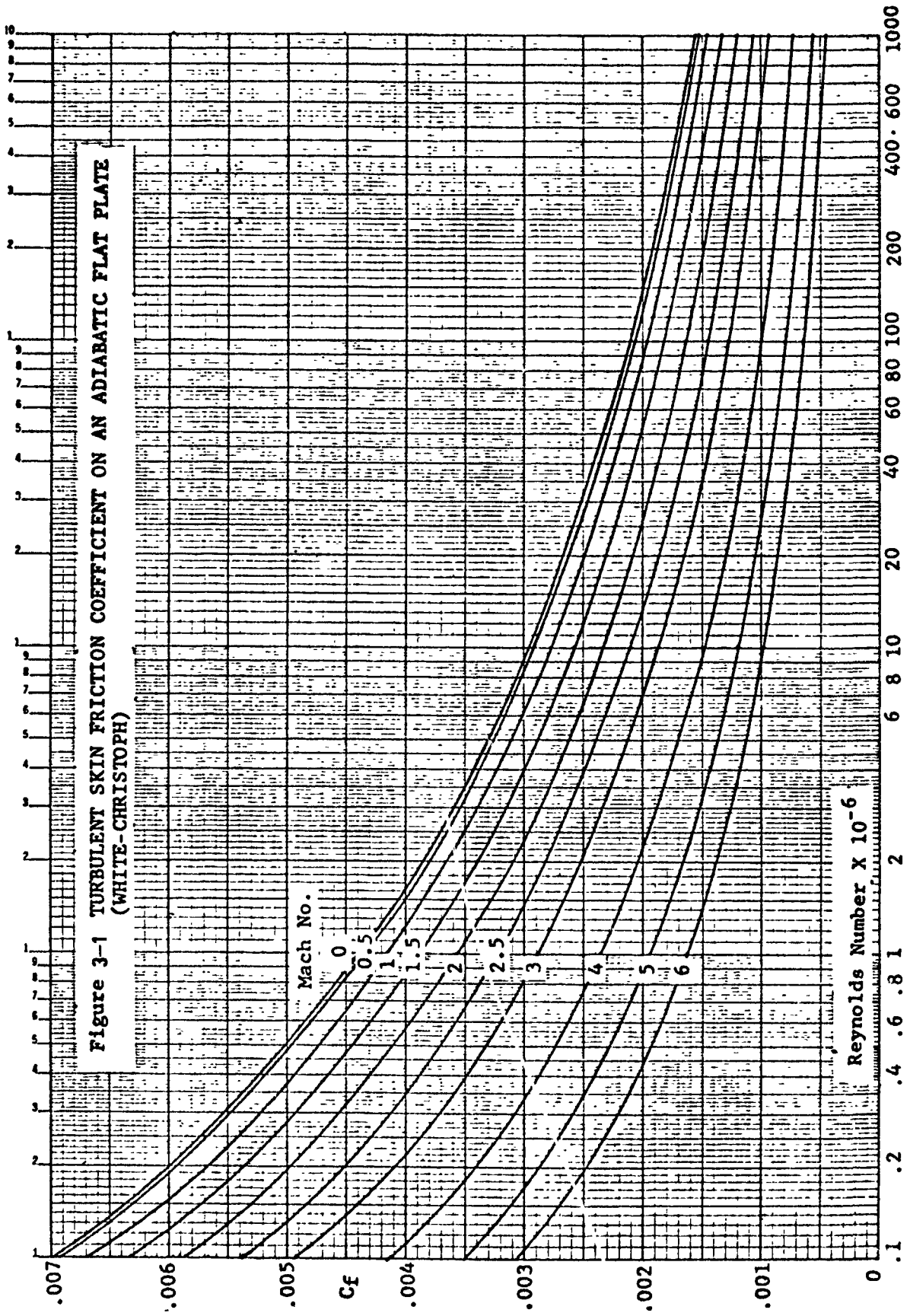
Figure 3-1 TURBULENT SKIN FRICTION COEFFICIENT ON AN ADIABATIC FLAT PLATE
(WHITE-CHRISTOPH)

30
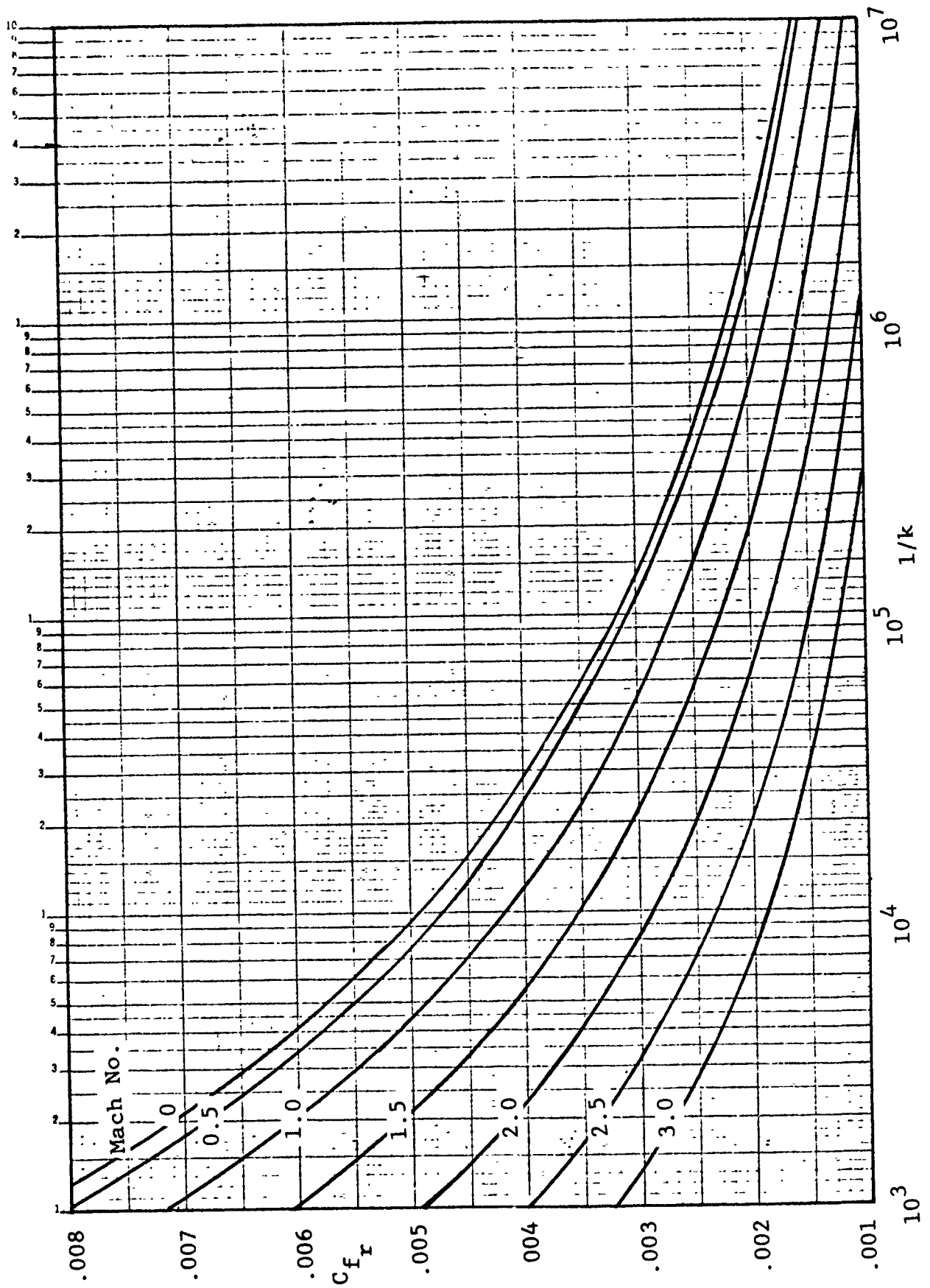
Figure 3-2 Roughness Skin-Friction Coefficient

31

For 4-digit airfoils, the form factor is given by

$$FF = 1 + 1.68(t/c) + 3(t/c)^2 \tag{3-9}$$

For biconvex airfoils, the form factor is given by

$$FF = 1 + 1.2(t/c) + 100(t/c)^4 \tag{3-10}$$

And for aribtrary input airfoils, the form factor is given by

$$FF = 1 + K_1 C_{1_d} + 1.44(t/c) + 2(t/c)^2 \tag{3-11}$$

The factor $K_1 C_{1_d}$ in Equation 3-11 is an empirical relationship which shifts the 6-series form-factor equation to account for the increased supervelocities caused by the section design camber C_{1_d}. The factor K_1 (derived from experimental data) is shown plotted in Figure 3-3 as a function of the Mach number relative to the wing Mach critical.

The form factors used in the AAT computer code were obtained from the General Dynamics Aerospace Handbook (Reference 6) and also appeared in the DATCOM (Reference 2).

3.1.3 Interference Factors

The component interference factors, IF, account for the mutual interference between components. For the fuselage, the interference factor is given by

$$IF = R_{W-B} \tag{3-12}$$

where R_{W-B} is shown plotted in Figure 3-4 as a function of fuselage Reynolds number and Mach number. For other bodies such as stores, canopies, landing gear fairings, and engine nacelles, the inter-ference factor would be an input factor based on experimental experiences with similar configurations. The General Dynamics Aerospace Handbook (Reference 6) recommends using

IF = 1.0 for nacelles and stores mounted out of the local velocity field of the wing

IF = 1.25 for stores mounted symmetrically on the wing tip

IF = 1.3 for nacelles and stores if mounted on moderate proximity of the wing

32
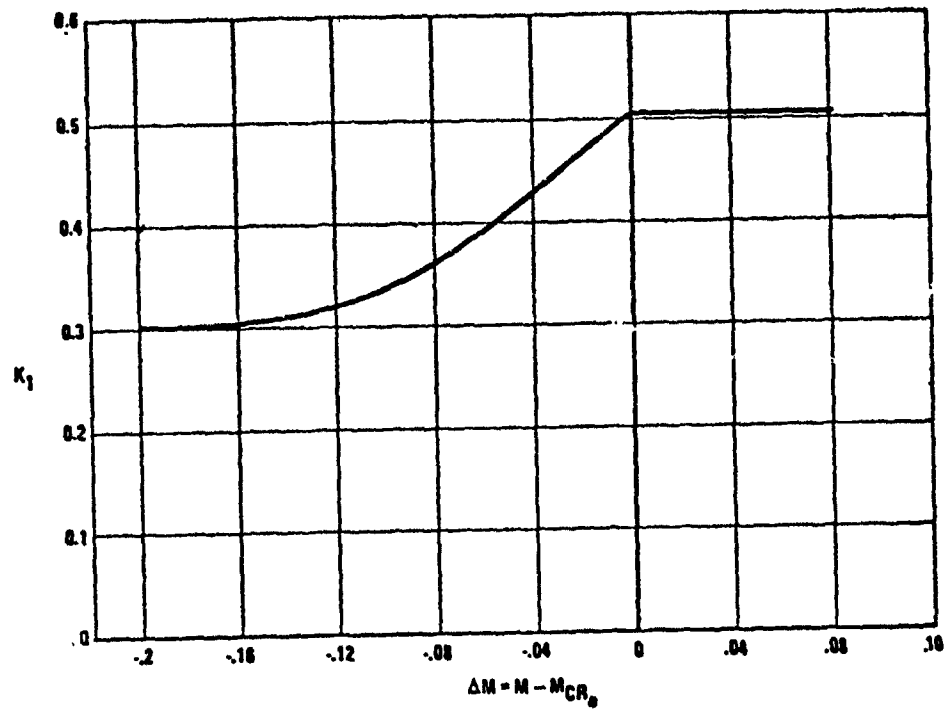
Figure 3-3   Supercritical Wing Compressibility Factor
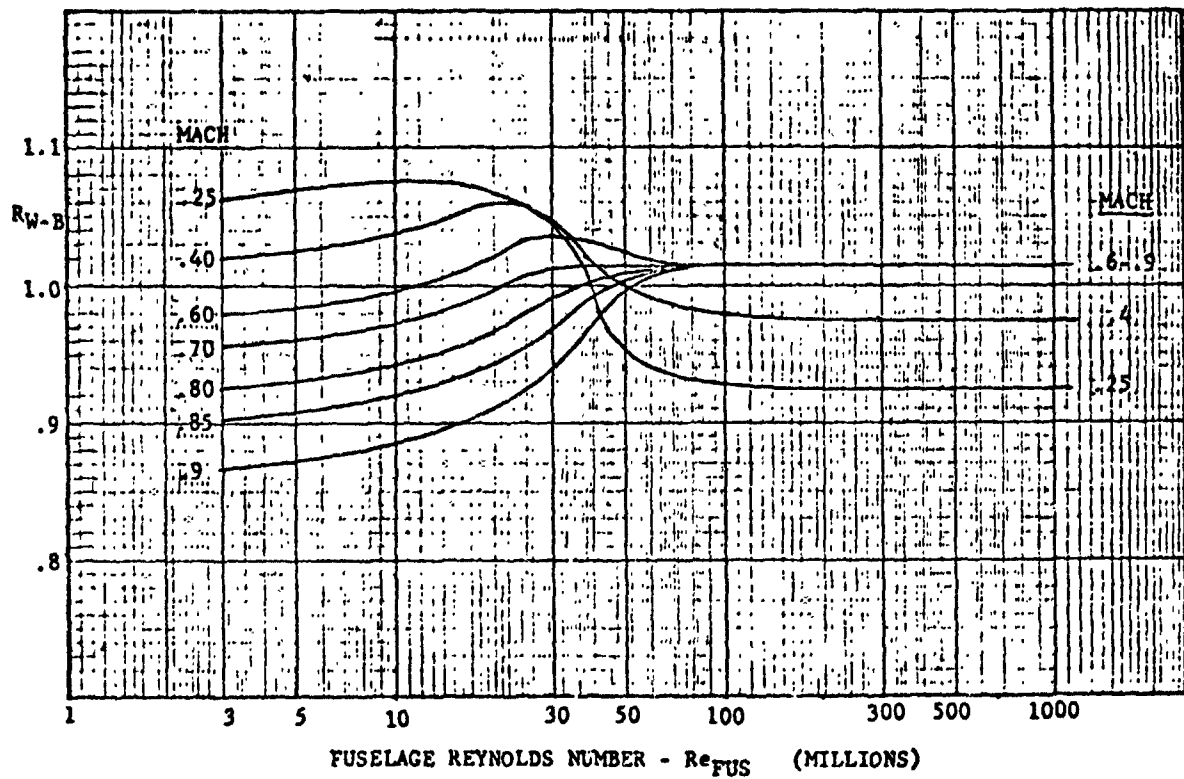
Figure 3-4   Wing-Body Correlation Factor for Subsonic Minimum Drag

IF = 1.5 for nacelles and stores mounted flush
to the wing or fuselage.

The interference factor for the main wing is computed as

$$IF = R_{LS} \cdot R_{W-B} \qquad (3-13)$$

where R_{W-B} is the wing-body interference factor presented in
Equation 3-12, and R_{LS} is the lifting surface interference factor
presented in Figure 3-5. Other airfoil surfaces such as horizontal
or vertical tails use an interference factor determined by

$$IF = R_{LS} \qquad (3-14)$$

The factors R_{W-B} and R_{LS} are plotted in Reference 6 and also
appear in the DATCOM.

3.2 CAMBER DRAG

The minimum drag contribution of the wing twist and camber
is related to the lift coefficient of the polar displacement,
ΔC_L, by the equation

$$C_{D_{CAMBER}} = \frac{e}{1-e} K \Delta C_L^2 \qquad (3-15)$$

This increment is called camber drag and represents a drag incre-
ment between minimum profile drag and $C_{D_{MIN}}$. The span efficiency
value, e, is related to the induced drag factor, K, by the equa-
tion

$$e = \frac{1}{\pi \cdot AR \cdot K}$$

If, for some reason, $e \geq 1$, an alternate equation, obtained from
Reference 6, is used,

$$C_{D_{CAMBER}} = 0.7 (\Delta C_L)^2 \frac{S_{EXPOSED}}{S_{REF}} \qquad (3-16)$$

3.3 BASE DRAG

Data presented in Reference 5 were used to establish equa-
tions from which the base drag of bodies could be determined.
The trends of these data show three different phases: (1) a
gradual rise of $C_{D_{Base}}$ at transonic speeds up to M = 1, (2) a
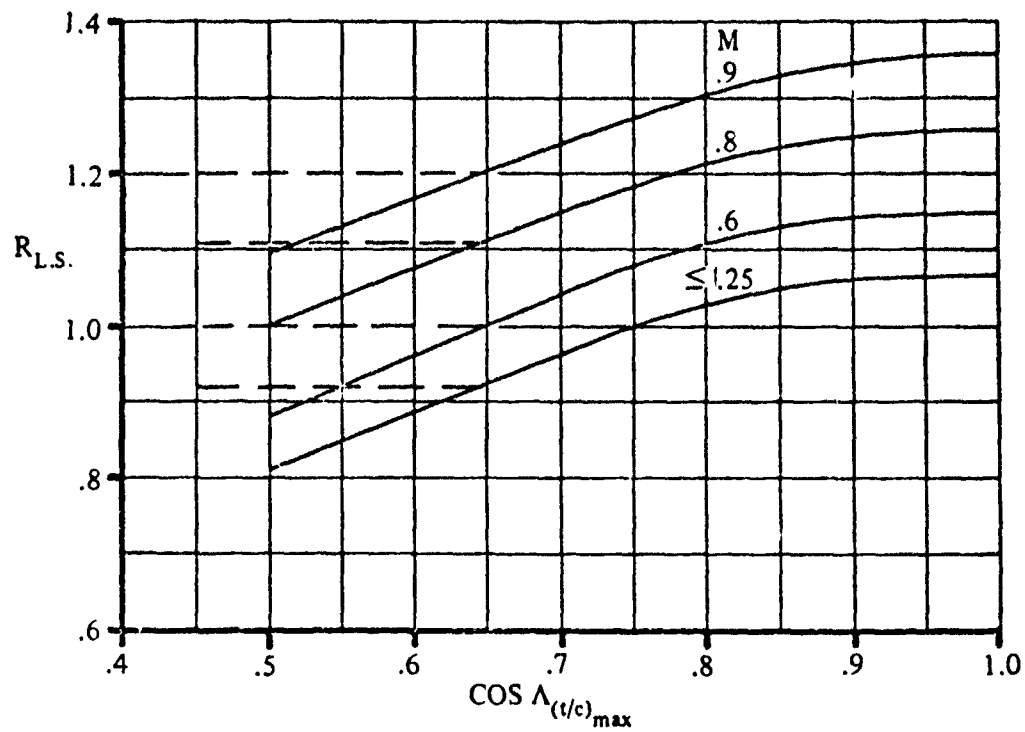
Figure 3-5   Lifting Surface Correlation Factor For
            Subsonic Minimum Drag

relatively constant drag level supersonically up to about M = 1.8, and (3) a steadily decreasing value of drag about M = 1.8. The resulting empirical equations are given as

$$C_{D_{Base}} = \begin{cases} (0.1 + 0.1222M^8) \dfrac{S_{Base}}{S_{Ref}}, & M \leq 1 \\[2ex] 0.2222 S_{Base}/S_{Ref}, & 1.0 < M \leq 1.8 \\[2ex] 1.42 S_{Base}/S_{Ref})/(3.15 + M^2), & M > 1.8 \end{cases} \qquad (3\text{-}17)$$

3.4 WAVE DRAG

Supersonic wave drag is determined on the basis of a component buildup for which simplified shapes are assumed. Three basic simplified shapes are used to represent the airplane: bodies, nacelles, and wings. The component buildup assumes that the total wave drag is the sum of the isolated wave drag of each component and does not allow for the mutual interference between components. However, the component-buildup method does give wave-drag results comparable to average configurations which have some favorable as well as some unfavorable interference.

3.4.1 Wing Wave Drag

The technique used to estimate wing wave drag evolved from a method that applies transonic similarity theory to straight wings. Data correlations at Mach 1 were performed on a large number of unswept wing configurations with blunt and sharp leading-edge airfoils. For the AAT computer code, these results were represented by an analytical function common to both types. The equations were then modified for M > 1 to produce a peak value at low supersonic speeds and then to decrease a high Mach numbers to values predicted by straight-wing linear theory for equivalent two-dimensional configurations. Finally, sweep effects were included. The resulting semi-empirical equations are presented below:

$$\tilde{C}_D = \cfrac{2K_t K_w K_c K_b}{\tilde{\beta} K_b K_w \cdot (F_\beta)^m + \left[\cfrac{1/\widetilde{AR}_e}{1+(1+\lambda)F_\beta \tilde{\beta}^{(1+K_w)}} + \cfrac{\widetilde{AR}_e^{\,3}}{1+\frac{1}{3}\widetilde{AR}_e^{\,3}\tilde{\beta}^4} \right]}$$

$$+ \cfrac{3.33\, K_t K_w K_c K_b}{\tilde{\beta} K_b K_w^{\,3.8} (F_\beta)^m + \left[\cfrac{2/\widetilde{AR}_e^{\,3}}{1+(\frac{2}{3}+\lambda)F_\beta \tilde{\beta}^{(1+K_w^{\,3.8})}} + \cfrac{1}{1+3\widetilde{AR}_e \tilde{\beta}^4} \right]}$$

36

where

$$\tilde{C}_D = C_D/(t/c)^{5/3}$$

K_t = airfoil thickness distribution factor

$$= 1 + 4\left[\frac{1}{2} - \frac{X_t}{c}(1 + \frac{1}{2}\sqrt{\frac{r_o}{t}})\right]^2 - \frac{1}{4}\sqrt{\frac{r_o}{t}}\ (1 - \frac{X_t}{c})^2$$

K_b, K_w, airfoil factors

K_b = 1.0, K_w = 1.2 for double-wedge sections

K_b = 1.069, K_w = 1.0 for curved-type sections

X_t = location of section maximum y ordinate

r_o = section leading-edge radius

K_c = airfoil camber factor

$$1 + \frac{5}{2}(h/t)^2$$

h = section camber (maximum y ordinate)

$$K_p = \frac{\cos\Lambda_{LE} + \frac{1/2}{(1+\lambda)^2}(\tan^2\Lambda_{LE} - \tan^2\Lambda_{TE})}{1 + \frac{1}{(1+\lambda^2)^2}(\tan\Lambda_{LE} + \tan\Lambda_{TE})^2}$$

$$F_\beta = 0.3 + 0.7 \, K_p^{(1+2\lambda^{1/3})}$$

$$\tilde{\beta} = \beta/(t/c)^{1/3} = \sqrt{M^2-1}/(t/c)^{1/3}$$

$$m = \frac{1+\lambda^2(2-\lambda)^3}{2} (\beta_{lim}/\beta)^Z \qquad \text{at} \quad \beta > \beta_{lim}$$

$$ = \frac{1+\lambda^2(2-\lambda)^3}{2} \qquad\qquad \text{at} \quad \beta \leqslant \beta_{lim}$$

$$Z = \cos\Lambda_{LE} + \cos\Lambda_{TE}$$

$$\beta_{lim} = \left| \tan\Lambda_{LE} \right|$$

and where $\tilde{AR}_e$ is the straight-wing $\tilde{AR}$ having the same value of $C_D/(t/c)^{5/3}$ at $M = 1.0$ as $\tilde{AR}$, where $\tilde{AR} = AR(t/c)^{1/3}$.

The value of $\tilde{AR}_e$ is determined by solving the following equation by use of an iterative method:

$$\frac{2}{\frac{1}{\tilde{AR}_e} + \tilde{AR}_e^3} + \frac{3.33}{\frac{2}{\tilde{AR}_e^3} + 1} = \left(\frac{2}{\frac{1}{\tilde{AR}} + \tilde{AR}^3} + \frac{3.33}{\frac{2}{\tilde{AR}^3} + 1} \right) K_p$$

The term β_{lim} represents the approximate value of β at which $C_D/(t/c)^{5/3}$ will maximize, provided the body is essentially cylindrical where the wing is attached. If the body is area-ruled, the estimate of the peak value if $C_D/(t/c)^{5/3}$ may be less accurate.

3.4.2 Body Wave Drag

The fuselage wave drag is computed by dividing the body into two parts, consisting of a simplified pointed nose and a simplified boattail. That is,

$$C_{D_{W_{BODY}}} = C_{D_{P_N}} \cdot \frac{A_{MAX}}{S_{REF}} + C_{D_{PBT}} \cdot \frac{A_{MAX}}{S_{REF}} \qquad (3\text{-}19)$$

Nose wave drag, $C_{D_{P_N}}$, is determined from Linnell's empirical equation

$$(f_N^2+1)C_{D_{P_N}} = \frac{1.2 + 1.15(\beta/\sqrt{f_N^2+1})}{1 + 1.9(\beta/\sqrt{f_N^2+1})} \qquad (3\text{-}20)$$

for the supersonic wave drag of parabolic noses (Reference 8). For Mach numbers between 1.2 and 1.0, the nose wave drag is determined from curves of Figure 3-6, which were derived from the transonic drag rise of ogive noses, as presented in Figure III.B.10-9 of Reference 6, and using Equation 3-20 as a supersonic limit. The nose fineness ratio, f_N, is calculated from the nose length, ℓ_N, and the maximum cross-sectional area, A_{MAX}, as

$$f_N = \ell_N \Big/ \sqrt{(\tfrac{4}{\pi})A_{MAX}}$$

Boattail wave drag, $C_{D_{PBT}}$, is determined as a function of boattail fineness ratio (f_B), base diameter to maximum diameter (d_B/d), and Mach number. This is done by computing $C_{D_{PBT}}$ at five values of (d_B/d) and interpolating to the desired value. The general form of these equations is given for two conditions of β/f_N.

For $\beta/f_N \le 1$ and $d_B/d = \dfrac{d_B(I)}{d}$,

$$C_{D_{PBT}}(I) = \frac{1}{f_B^2}\left[A_0(I) + A(I)\cdot\beta/f_B + A_2(I)\cdot(\beta/f_B)^2 + A_3(I)\cdot(\beta/f_B)^3\right]$$

$$(3\text{-}21)$$

For $\beta/f_N > 1$,

$$C_{D_{PBT}}(I) = \frac{1}{f_B^2}\ A_4(I)\cdot(f_N/\beta) \qquad (3\text{-}22)$$
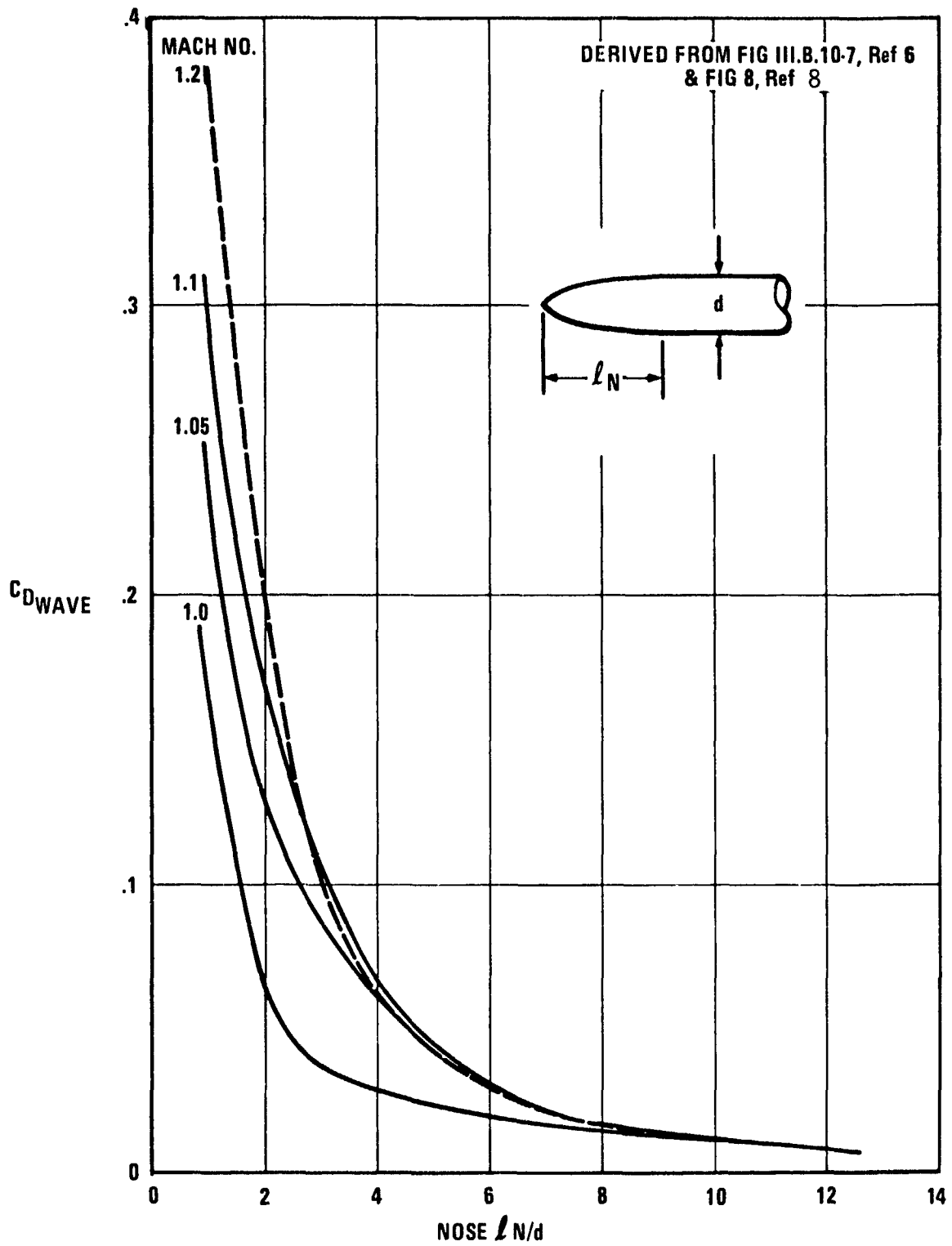
Figure 3-6 Transonic Wave Drag of Parabolic Noses

The polynominal coefficients of Equations 3-21 and 3-22, determined from a least-square fit of Fig. III.B.10-9 of Reference 6 for ogive boattails, are tabulated below:

I	d_B/d	A_0	A_1	A_2	A_3	A_4
1	0	1.165	-0.5112	-0.5372	0.3964	0.513
2	0.4	1.067	-1.709	1.6632	-0.686	0.3352
3	0.6	0.7346	-1.4618	1.5795	-0.6542	0.198
4	0.8	0.2555	-0.5008	0.5024	-0.2077	0.0494
5	1.0	0	0	0	0	0

3.4.3 Nacelle Wave Drag

The nacelle wave drag is calculated by a method similar to that used for the fuselage:

$$C_{D_{W_{Nac}}} = (C_{D_{ON}} + C_{D_{PBT}}) \frac{A_{MAX}}{S_{REF}} \tag{3-23}$$

The equation used to calculate $C_{D_{ON}}$ for open-nose bodies is

$$C_{D_{ON}} = \left[(1 - r_{IN}/R)/f_N \right]^{1.5} / \beta^{\frac{1}{2}} \tag{3-24}$$

where

$$r_{INLET} = \sqrt{A_{INLET}/\pi}$$

$$R = \sqrt{A_{MAX}/\pi}$$

This equation is a curve fit of Figure III.B.10-6 of Reference 6.

3.5 FUSELAGE AFT-END UPSWEEP DRAG

The main parameters affecting the fuselage aft-end upsweep drag are the upsweep angle and the crossflow drag coefficient of the rear fuselage sections in the local flow, including

modification by wing downwash. Data in Reference 9 indicate that the afterbody drag increases rapidly with upsweep angle β, but decreases with increasing fuselage angle of attack. The curves in Figure 3-7, obtained from the data presented in Reference 9, are used to predict aft-end drag as a function of angle of attack.

3.6 MISCELLANEOUS DRAG ITEMS

In the preliminary design stage of aircraft drag estimation the drag due to surface irregularities such as gaps and mismatches, fasteners, small protuberances, and leakage due to pressurization are estimated by adding a miscellaneous drag increment which is some percentage of the total friction, form, and interference drags. The miscellaneous drag varies between 10 and 20 percent of the total friction, form, and interference drags for typical aircraft. The AAT program computes miscellaneous drag by use of a percentage factor specified as input to the program.
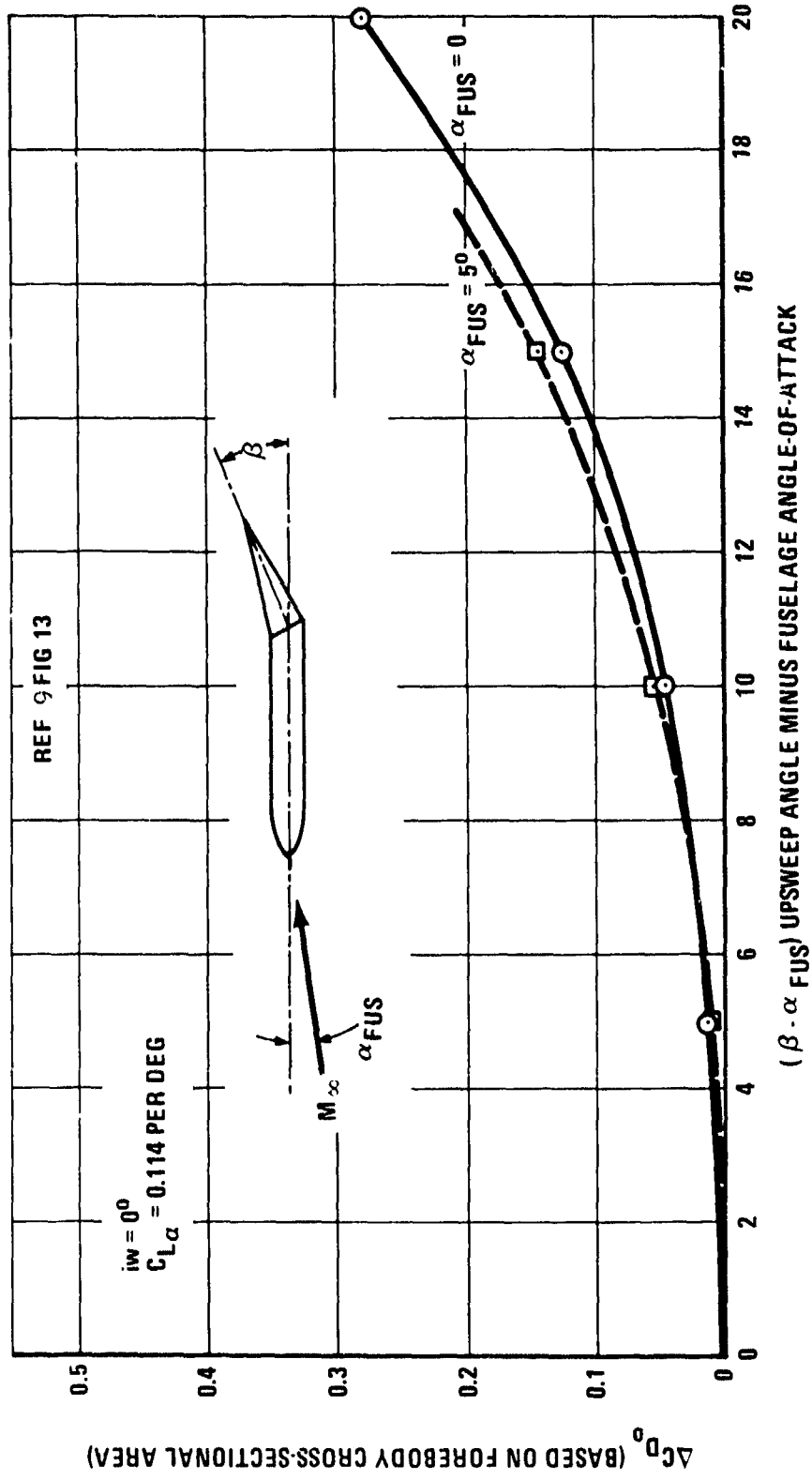
Figure 3-7 Effect of Fuselage Upsweep on Drag

4. DRAG DUE TO LIFT

The Aerodynamic Accounting Technique computer code predicts drag due to lift by one of several methods, depending on the aerodynamic conditions at which a solution is desired. The various regions are illustrated in Figure 4-1; they are discussed in the following subsections in the numerical order shown in the figure.
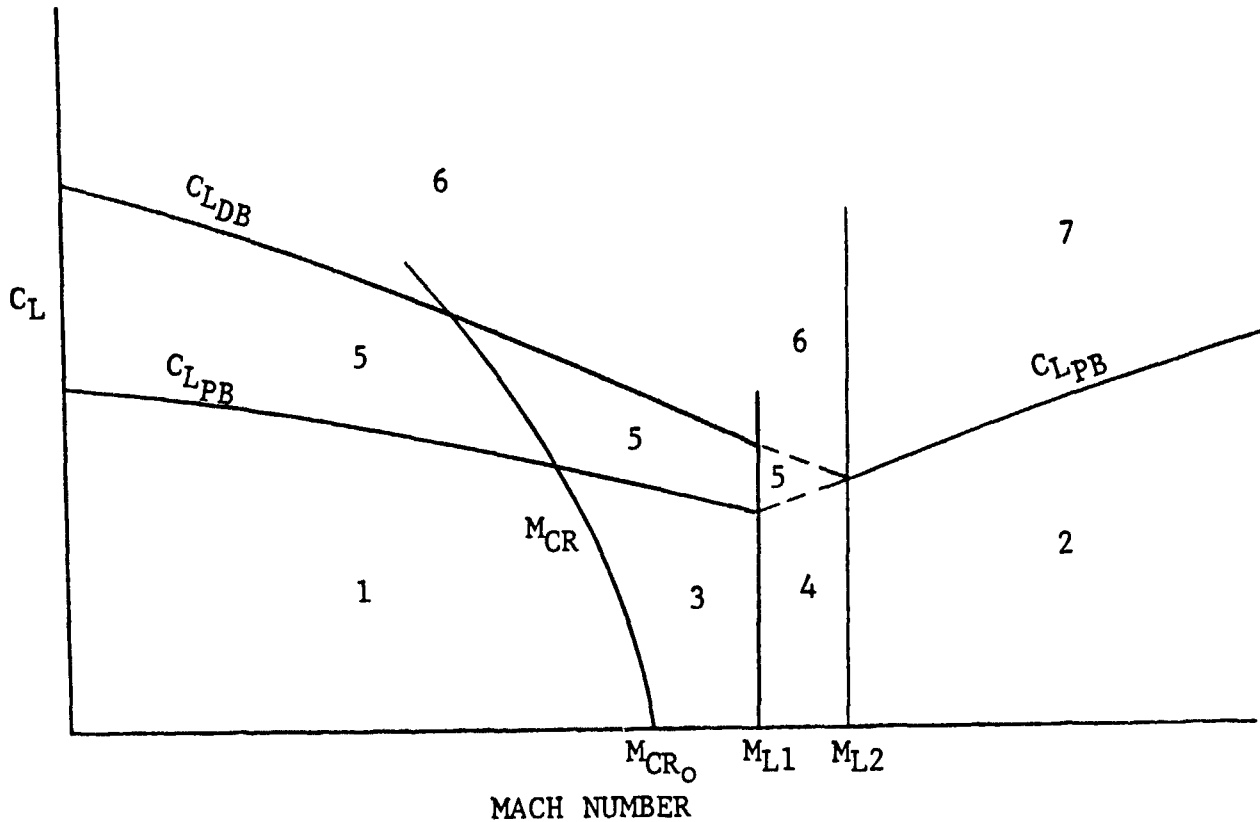
Figure 4-1 Lift and Speed Regions for Calculation of
Drag Due to Lift

4.1 SUBSONIC POLAR PREDICTION BELOW POLAR BREAK

Region 1 is bounded by the critical Mach number and by the C_L at which the polar break occurs, $(C_{L_{PB}})$. In this subsonic, low-lift region, the drag due to lift can be determined from

$$C_{D_L} = K(C_L - \Delta C_L)^2 \tag{4-1}$$

44

where the drag due to lift factor, K, is predicted by

$$K = \frac{1-R}{C_{L_\alpha}} + \frac{R}{\pi AR\ e_o} \tag{4-2}$$

In this equation, a leading-edge suction parameter R, is used to relate K to the lower bound of drag, $1/\pi AR$, for full leading-edge suction (R = 1.0) and to the upper bound of drag, $1/C_{L_\alpha}$, for zero leading-edge suction. Body effects are accounted for in Equation 4-2 by computing e_o, shown plotted in Figure 4-2 as a function of taper ratio and body-diameter-to-span ratio (d/b).

The correlation of leading-edge suction on induced drag was first developed by Frost (Reference 10) and was later extended for additional planform effects and higher subsonic Mach numbers (Reference 11). A study by NASA (Reference 12) showed that airfoil camber, conical camber, sharp leading edges, leading-edge flaps, Reynolds number, and sweep have significant effects on the suction parameter. H. John (Reference 13) improved the correlation of R for plane wings at low Reynolds number by including airfoil thickness along with leading-edge radius.

The procedure followed in the AAT computer code to determine R is as follows:

1. Using the leading-edge radius and the leading-edge sweep for each wing panel, compute Ω as follows:

$$\Omega = \begin{cases} R_{N_{LER}} \times 10^{-3}\ \cot \Lambda_{LE} \sqrt{1-M^2\cos^2 \Lambda_{LE}}\ ; & \Lambda_{LE} \geq 20^o \\[2em] R_{N_{LE}} \times 10^{-3}(5-6.511\ \Lambda_{LE}) \sqrt{1-M^2\cos^2 \Lambda_{LE}}\ ; & \Lambda_{LE} < 20^o \end{cases} \tag{4-3}$$

where Λ_{LE} is in radians. The switch from the cotangent term is made to prevent Ω from going to infinity as sweep approaches zero.

The value of Ω is then used to read R_T from Figure 4-3, which is a plot of leading-edge suction for thin, round-nose, uncambered airfoils developed in Reference 11.

2. Employing the leading-edge sweep of the wing panel, determine R_{MIN} from Figure 4-4. The plot of Figure 4-4 was
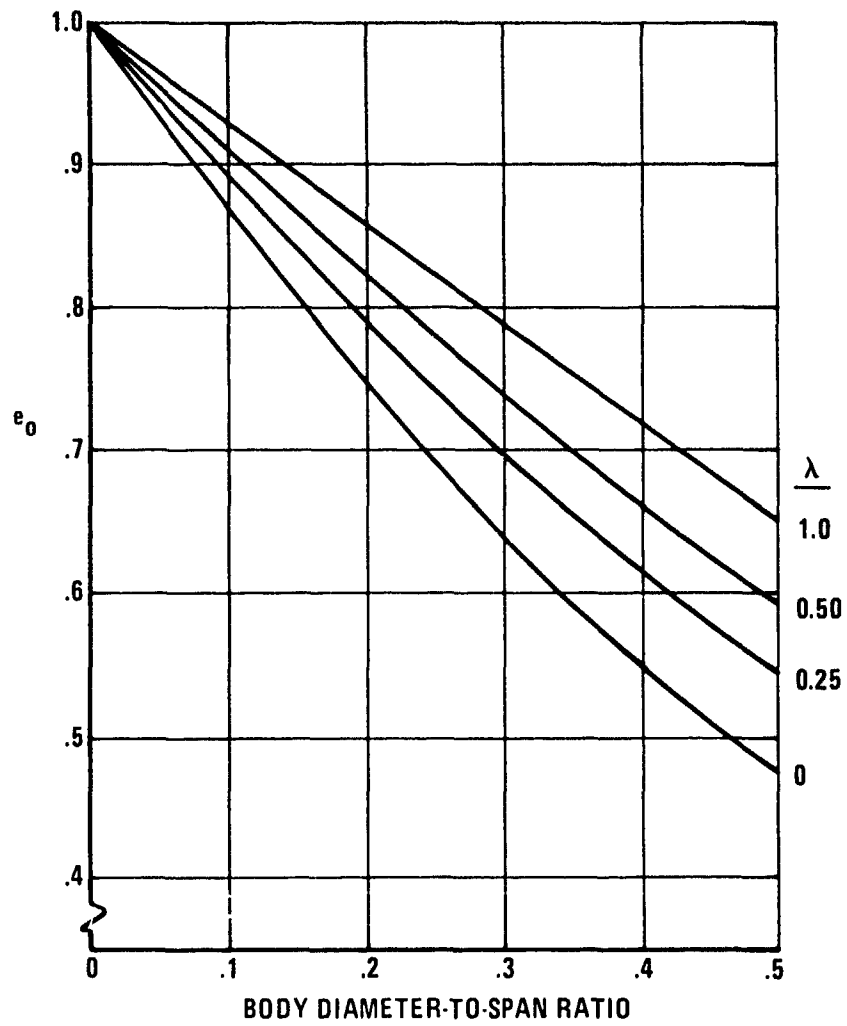
Figure 4-2   Body Effects on Wing Span Efficiency

46
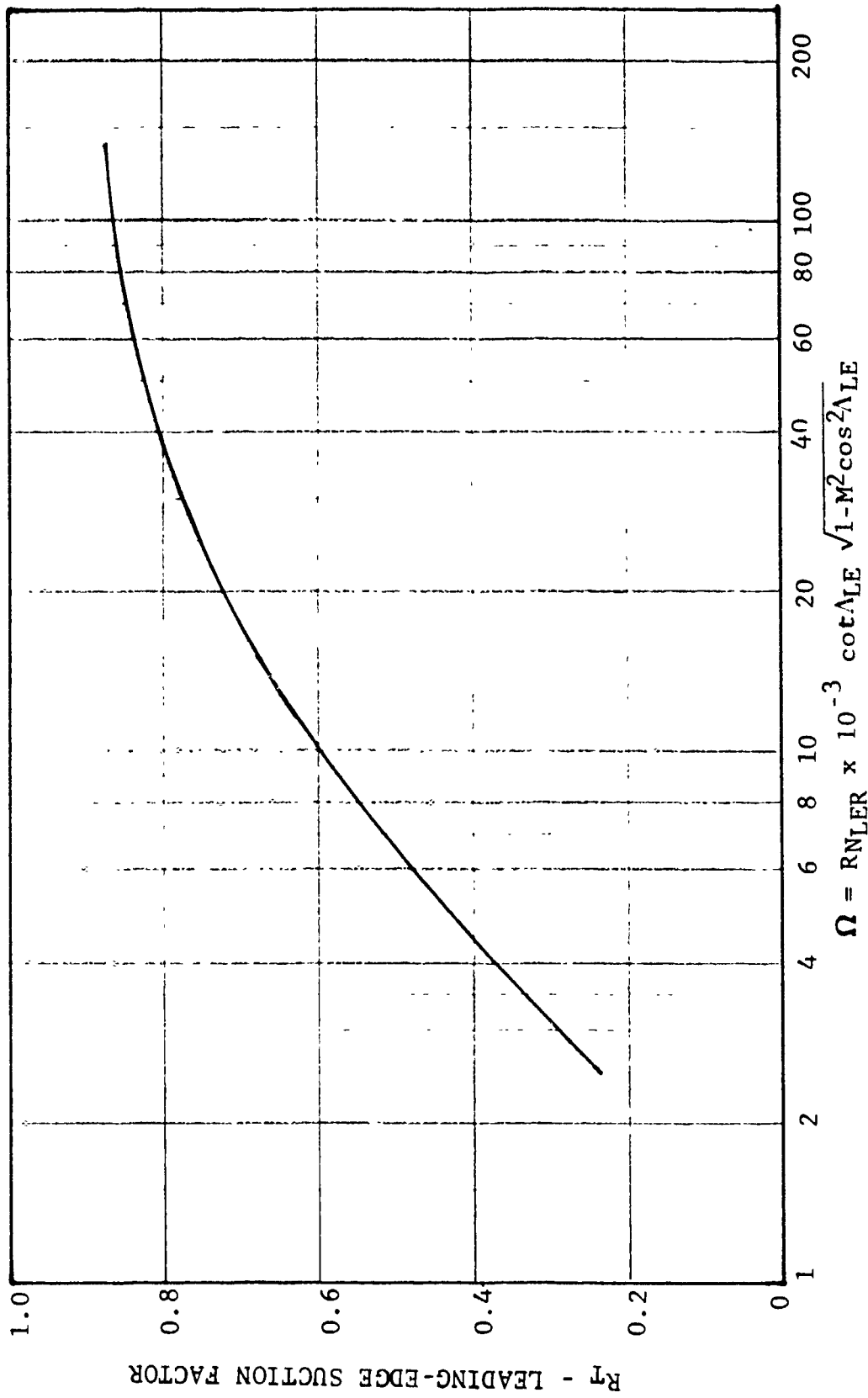
Figure 4-3 Effect of Reynolds Number on Leading-Edge
Suction for Blunt-Uncambered Airfoils
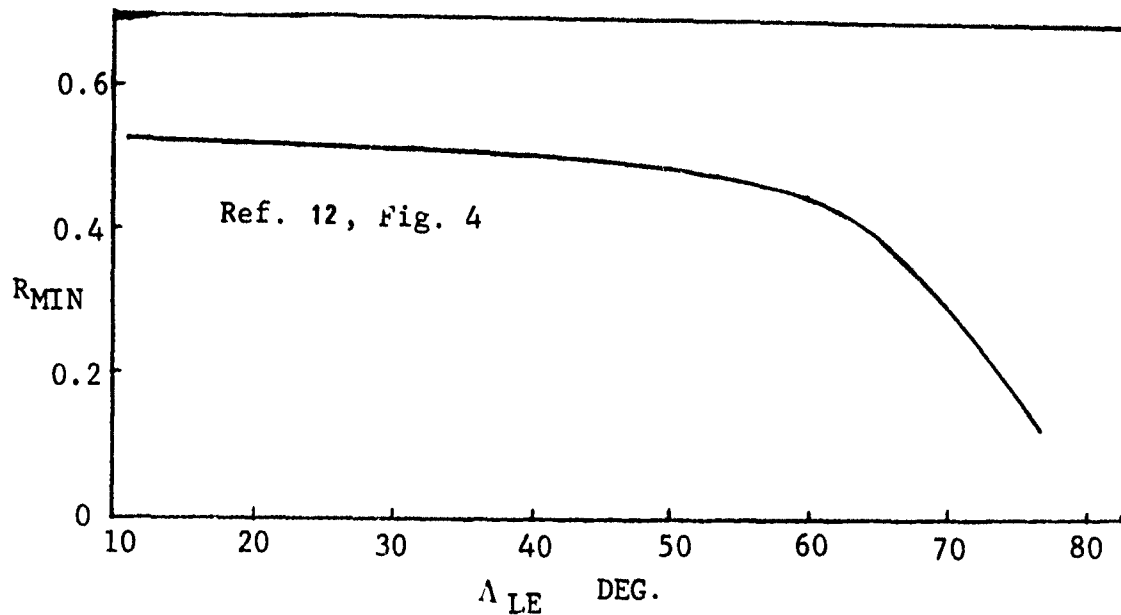
Figure 4-4 Leading-Edge Suction for Sharp Airfoils
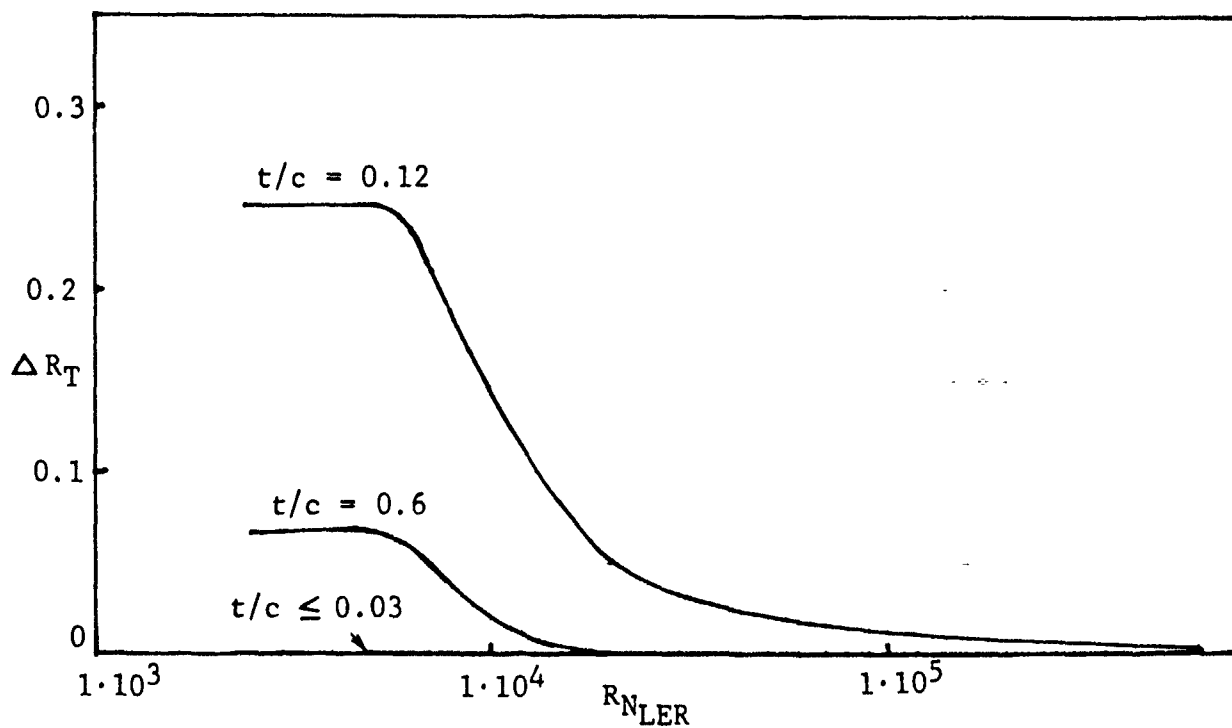
Figure 4-5 Effect of Reynolds Number and Thickness on
the Leading-Edge Suction Factor

48

obtained from the results reported in Reference 12 for sharp-leading-edge wings. The leading-edge-suction value for sharp-leading-edge wings is independent of Reynolds and Mach numbers.

3. If the value of R_T from step (1) is less than the value of R_{MIN} determined in step (2), set R_T equal to R_{MIN}.

4. Taking into account the wing panel thickness and leading-edge radius Reynolds number, determine a thickness correlation to leading-edge suction, ΔR_T, from Figure 4-5. This correction factor was developed from the data presented in Reference 13. The increment in suction parameter ΔR_T is then added to the value of R_T determined in step (3).

5. Calculate the effect of either section camber or conical wing camber on the R factor from

$$R = R_T + (0.824 - R_T) \cdot (C_{L_d} + C_{L_{con}})/0.6 \qquad (4\text{-}4)$$

If $R > 0.874$, $R = 0.874$.

Correlation of experimental data with the results of Reference 12 indicate that, for low Reynolds number, R does not decrease as much when the wing is cambered as when it is uncambered.

The accompanying sketch shows the relative effect of camber as predicted by Equation 4-4.
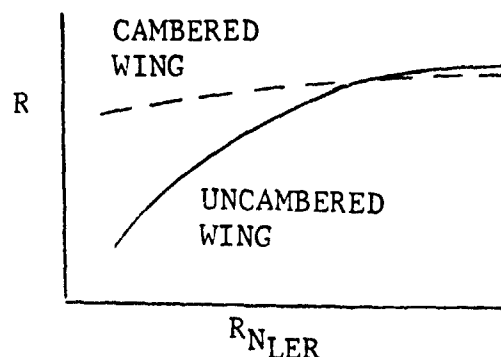
6. Obtain the effective R for the composite wing from a span-weighted average of the individual R for each panel as follows:

$$\overline{R} = \frac{R_i \, (b/2)_{xi} + R_o \, (b/2)_{xo}}{(b/2)_{xi} + (b/2)_{xo}}$$

where $(b/2)_{xi}$ and $(b/2)_{xo}$ are the widths of the inboard and outboard panels.

7. The effect of wing planform on R can be determined from Figure 4-6 as a function of the parameter $AR \cdot \lambda /\cos \Lambda_{LE}$. This increment due to planform, ΔR, is then added to $\bar{R}$ to obtain the final value of R for use in Equation 4-2.

The polar displacement, ΔC_L, is related to the lift coefficient for minimum profile drag, $C_{L_{OPT}}$, by the equation

$$\Delta C_L = (1 - \frac{1}{\pi \, AR \, K}) C_{L_{OPT}}$$

The lift coefficient for minimum profile drag is affected by the camber and twist of the configuration. Figures 4-7 and 4-8 present data from Reference 14 that show the effect of NACA camber and conical camber on $C_{L_{OPT}}$. For supercritical wings, the limited amount of data available for correlation indicate that

$$C_{L_{OPT}} = 0.5195 (C_{L_d})^{0.75} \qquad (4-5)$$

where C_{L_d} is the wing section design lift coefficient.

4.2 SUPERSONIC POLAR PREDICTION BELOW POLAR BREAK

The drag polar in the supersonic region beyond the second limit Mach number below polar break (Region 2) is predicted by Equation 4-1, where

$$K = \frac{1 - \tilde{R}}{C_{L_\alpha}} + \frac{\tilde{R}}{\pi \, AR \, e_o} \qquad (4-6)$$

This equation is similar to Equation 4-2 for the subsonic induced-drag factor except for the use of $\tilde{R}$, which is a transonic leading-edge suction factor. For Mach numbers greater than Mach critical, the suction factor is predicted by

$$\tilde{R} = R_o / (1 + n \Delta M + (n \Delta M)^2) \qquad (4-7)$$

where R_o = leading-edge suction factor at the critical
     Mach number at zero lift, M_{CR_o}

  $n = 12 (\cos \Lambda_{LE})^{1.6}$

  $\Delta M = M - M_{CR_o}$
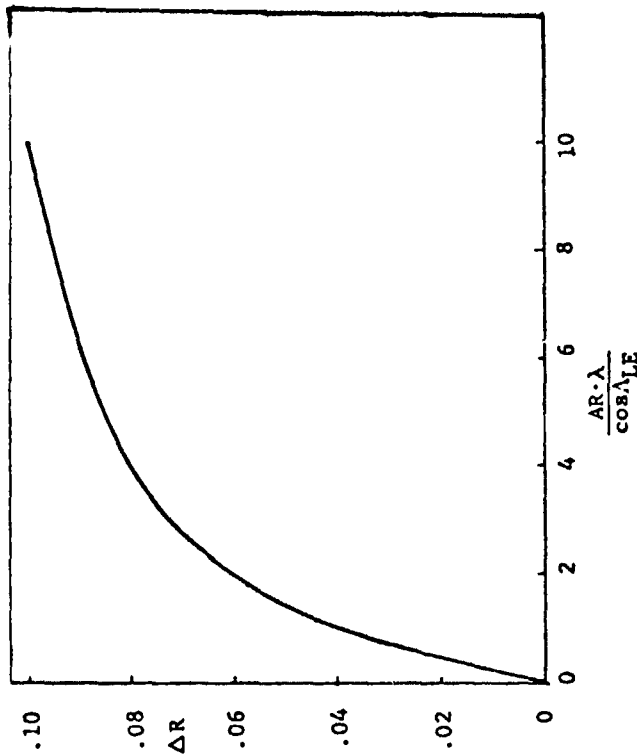
Figure 4-6 Effect of Wing Planform on Leading-Edge Suction

Figure 4-8 Lift Coefficient for Minimum Profile Drag - Conical Camber

Figure 4-7 Lift Coefficient for Minimum Profile Drag - NACA Camber

The variation of $\tilde{R}/R_O$ for Mach numbers greater than M_{CR_O} is shown in Figure 4-9. This method of predicting polar shape factor produces a continuous decrease in leading-edge suction so that at the limit, as the Mach number approaches the sonic leading-edge condition, the polar shape approaches $1/C_{L_\alpha}$.

The supersonic polar displacement for NACA camber is calculated from

$$\Delta C_L = \begin{cases} C_{L_d}(0.25-0.225\,\beta\cot\Lambda_{LE}); \beta\cot\Lambda_{LE} < 1.11 \\ \\ 0 \qquad\qquad\qquad\qquad\quad; \beta\cot\Lambda_{LE} \geqq 1.11 \end{cases} \qquad (4-8)$$

and the supersonic polar displacement for conical camber is calculated from

$$\Delta C_L = \begin{cases} C_{L_{con}}(0.111-0.1\,\beta\cot\Lambda_{LE}); \beta\cot\Lambda_{LE} < 1.11 \\ \\ 0 \qquad\qquad\qquad\qquad\quad; \beta\cot\Lambda_{LE} \geqq 1.11 \end{cases} \qquad (4-9)$$

These equations were obtained from a simple curve fit of the data presented in Figures 94 through 97 of Reference 14.

4.3   TRANSONIC POLAR PREDICTION

In the transonic region bounded by Mach critical (M_{CR}) and the first limit Mach number (M_{L1}) (Region 3), the induced drag is computed by adding drag rise to the basic polar:

$$C_{D_L} = K(C_L - \Delta C_L)^2 + C_{DR_{CL}} \qquad (4-10)$$

The basic polar shape is calculated up to M_{CR_O} in the same manner as described for Region 1. Beyond M_{CR_O}, the basic polar does not change. An incremental drag-rise term ($C_{DR_{CL}}$) is calculated as a function of lift and is added to the basic polar to determine the
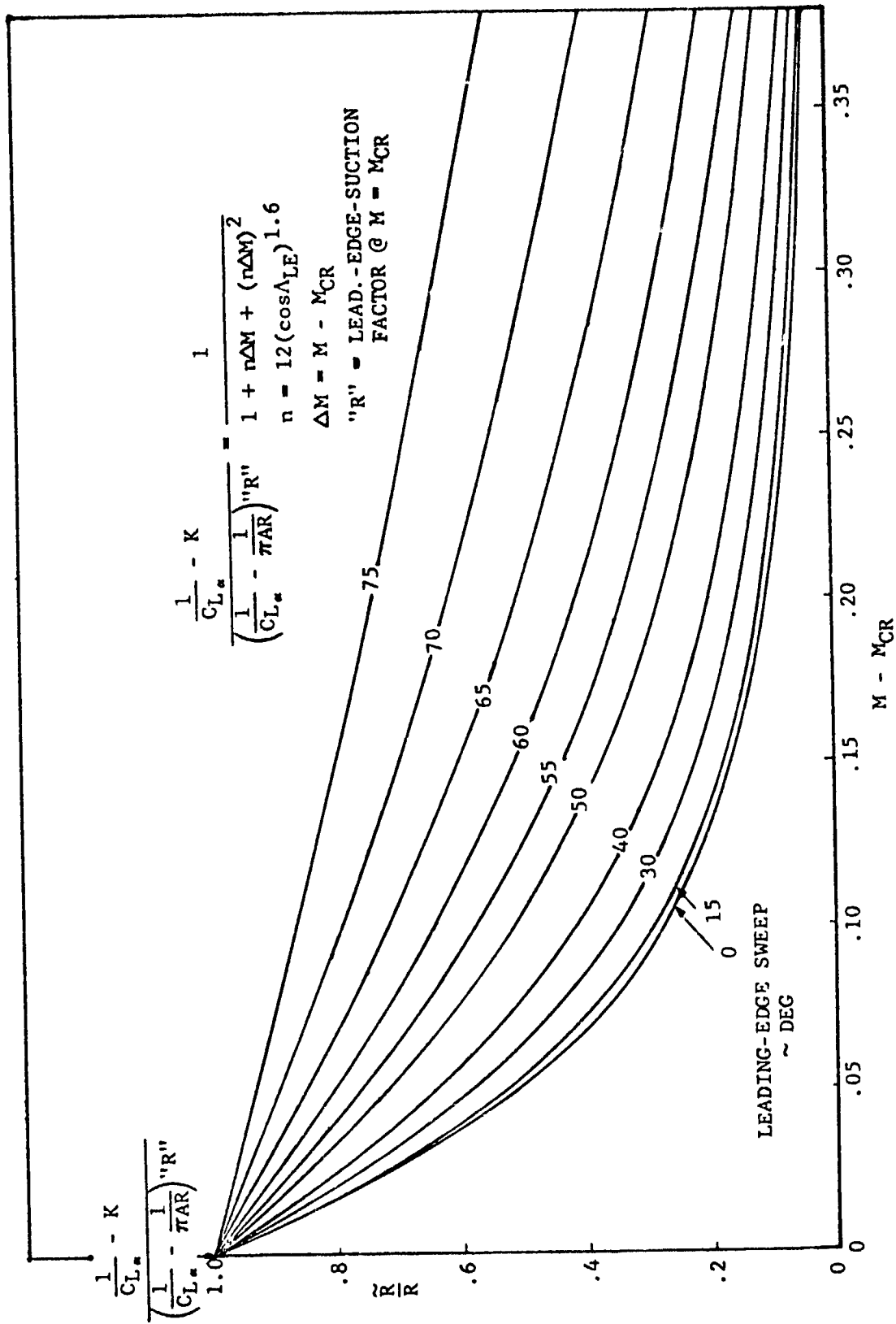
Figure 4-9   Transonic Suction Factor

53

total drag due to lift. A complete description of the techniques used to calculate the drag-rise increment is given in Subsection 5.3.

In the transonic region above the first limit Mach number, M_{L1} (Region 4), the drag-rise term in Equation 4-10 becomes less accurate. Therefore, the drag polar in Region 4 is calculated by interpolation between the polar shape factors computed for Regions 3 and 2. The equations for K and ΔC_L are given by

$$K = K_{L1} + (K_{L2} - K_{L1}) \frac{M-M_{L1}}{M_{L2}-M_{L1}} \qquad (4-11)$$

$$\Delta C_L = \Delta C_{L_{L1}} + (\Delta C_{L_{L2}} - \Delta C_{L_{L1}}) \frac{M-M_{L1}}{M_{L2}-M_{L1}} \qquad (4-12)$$

where $M_{L1} < M < M_{L2}$. The polar shape factors, K_{L1} and $\Delta C_{L_{L1}}$, are determined from a least-square curve fit of the polar shape computed at M_{L1} in Equation 4-10. The polar shape factors K_{L2} and $\Delta C_{L_{L2}}$ are computed from Equations 4-6 and 4-8 at M_{L2}. The limit Mach numbers are as follows:

$$M_{L1} = M_{CR_O} + 0.05$$

If $M_{L1} < 0.95$, then $M_{L1} = 0.95$

If $M_{L1} > 1.00$, then $M_{L1} = 1.0$

$$M_{L2} = M_{L1} + 0.15$$

4.4   SUBSONIC POLAR PREDICTION ABOVE POLAR BREAK

The polar region between the polar-break lift coefficient ($C_{L_{PB}}$) and the initial-stall lift coefficient ($C_{L_{DB}}$) is the region in which leading-edge separation and reattachment occurs, causing the polar to deviate from a parabolic shape (Region 5 in Figure 4-1). Whether or not this region exists (i.e., the flow reattaches after separation and allows the wing to reach a higher lift coefficient before final separation occurs at the trailing edge) is determined by the type of airfoil, the Reynolds number, and the leading-edge wing sweep. For thin wings, low Reynolds numbers, or highly swept wings, the values of $C_{L_{PB}}$ and $C_{L_{DB}}$ are equal.

Leading-edge sharpness ia a measure of the type of separation likely to occur. Blunt, thick airfoils generally exhibit trailing-edge separation, while very thin airfoils exhibit leading-edge separation. Airfoils of moderate thickness are likely to separate and reattach at the leading edge, followed by trailing-edge separation (stall) at higher lift coefficients. Associated with the leading-edge separation and reattachment is a loss in leading-edge suction, which produces an increase in drag due to lift. Above $C_{L_{DB}}$, the flow separates completely along the wing, and the drag increases more rapidly.

The prediction method in the AAT computer code utilizes the sharpness parameter of the airfoil, Δy, as defined in Equation 2-42. If Δy is less than or equal to 1.65, leading-edge flow separation is assumed to occur. Also, if the leading-edge sweep is greater than or equal to 50 degrees, it is assumed that leading-edge separation occurs. If Δy is greater than 2.05, a leading-edge separation and reattachment occurs, followed by a trailing-edge separation. For values of Δy between 1.65 and 2.05, a transition region exists in which the behavior varies between tge condition of full leading-edge separation at $\Delta y = 1.65$ and full leading-edge flow reattachment at $\Delta y = 2.05$.

Because the polar-break lift coefficient is a function of many variables, it has proved to be a difficult quantity to predict. Data correlations at subsonic and transonic speeds developed by the Reference 1 computer code indicate that the polar-break point can better be determined with angle of attack as the parameter rather than lift coefficient. These correlations resulted in a method that determines the angle of attack at polar break as a function of Mach number, Δy, sweep angle, and wing camber. Consequently, the polar break C_L, is calculated as

$$C_{L_{PB}} = C_{L_\alpha} \cdot (\alpha_{PBO} + \Delta\alpha_{PB}) \tag{4-13}$$

where $(\alpha_{PBO}/\cos \Lambda_{c/4})$ is shown plotted in Figure 4-10 as a function of Δy and $M \cos \Lambda_{c/4}$. The term $\Delta\alpha_{PB}$ accounts for section camber and is determined from

$$\alpha_{PB} = (12.05 - 4.1 \, M \cos \Lambda_{c/4})\left(\frac{c_{\ell_d}}{\cos \Lambda_{c/4}}\right)$$

55
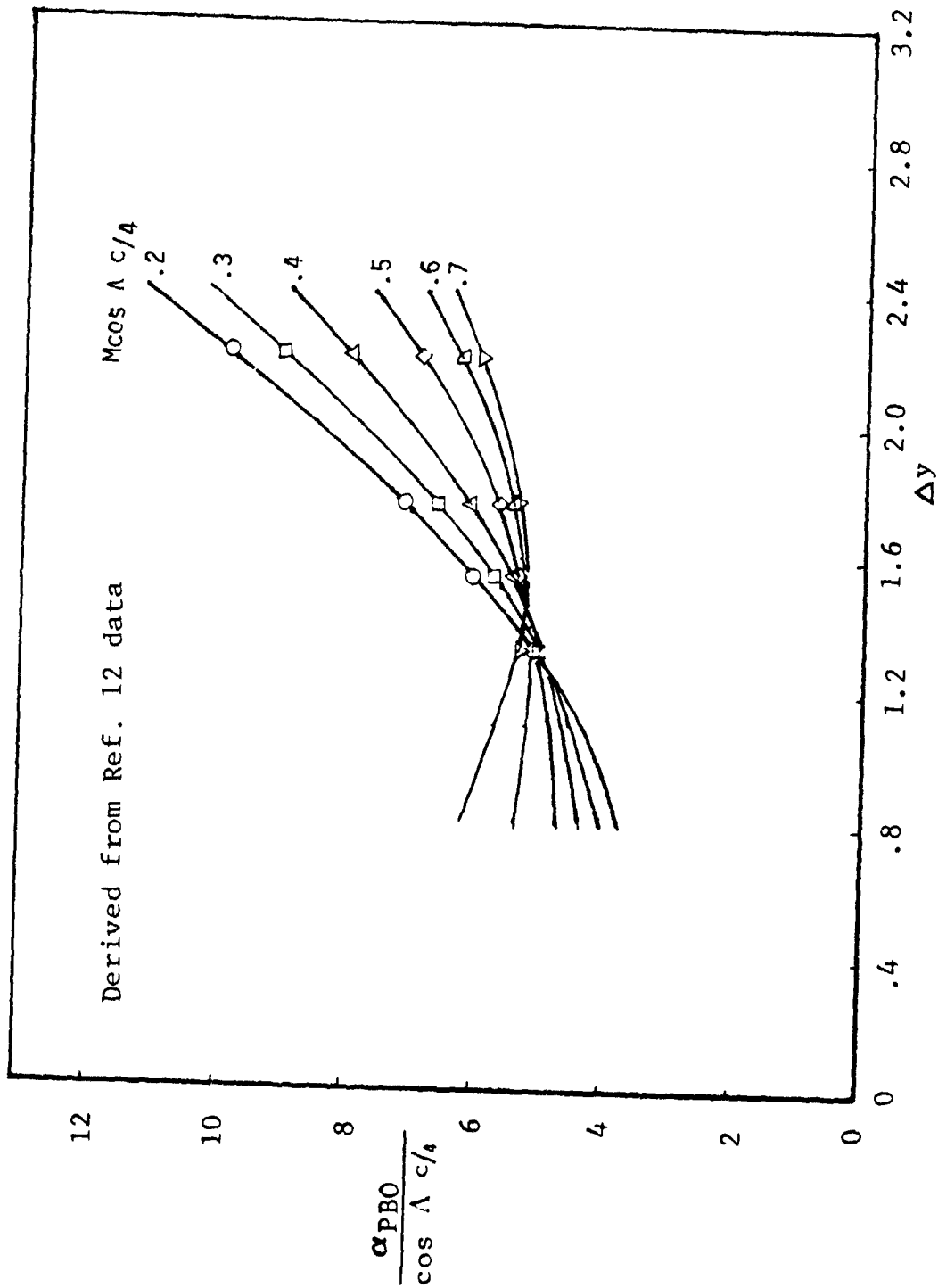
Figure 4-10 Airfoil Leading-Edge Shape Effect on α_{PB_O}

which was derived principally from correlating the experimental
data in Reference 15. For wings with conical camber, an incr-
ment in $C_{L_{PB}}$ is obtained from Figure 4-11.

The drag due to lift is expressed in Region 5 as

$$C_{D_L} = K(C_L - \Delta C_L)^2 + K'(C_L - C_{L_{PB}})^2 \qquad (4\text{-}14)$$

$$C_{L_{PB}} < C_L < C_{L_{DB}}$$

where $K' = 0.518/\sqrt{AR}$ (Reference 1).

The upper boundary of Region 5 represents the lift coeffi-
cient at which trailing-edge separation occurs. It is predicted
as

$$C_{L_{DB}} = C_{L_{PB}} + T\left[R_{N_{\overline{c}}} \cdot \left(\frac{\partial C_L}{\partial R_N}\right) - \delta C_L\right]$$

where

$$T = \begin{cases} 0 & ; \quad \Delta y \leqslant 1.65 \\ (\Delta y - 1.65)/0.4; & 1.65 < \Delta y < 2.05 \\ 1.0 & ; \quad \Delta y \geqslant 2.05 \end{cases}$$

and $(\partial C_L/\partial R_N)$ and δC_L are plotted in Figures 4-12 and 4-13.

The drag polar above $C_{L_{DB}}$ (Region 6 in Figure 4-1) increases
sharply from the subsonic attached-flow condition. The polar
prediction for lift coefficients above $C_{L_{DB}}$ is determined by a
modification of the empirical method presented in Reference 14
whereby

$$C_{D_L} = C_{D_{DB}} + K_D C_L^2 + \Delta C_{DB}; \ C_L > C_{L_{DB}} \qquad (4\text{-}15)$$

where $C_{D_{DB}}$ is the predicted lift-dependent portion of profile
drag at $C_{L_{DB}}$, $K_D C_L^2$ is the theoretical induced drag, and ΔC_{DB}
is a correlated separation-drag increment obtained as a function
of $C_{L_{DB}}$. The lift-dependent profile drag at $C_{L_{DB}}$ is given by

Derived from Fig. 71, Ref. 14
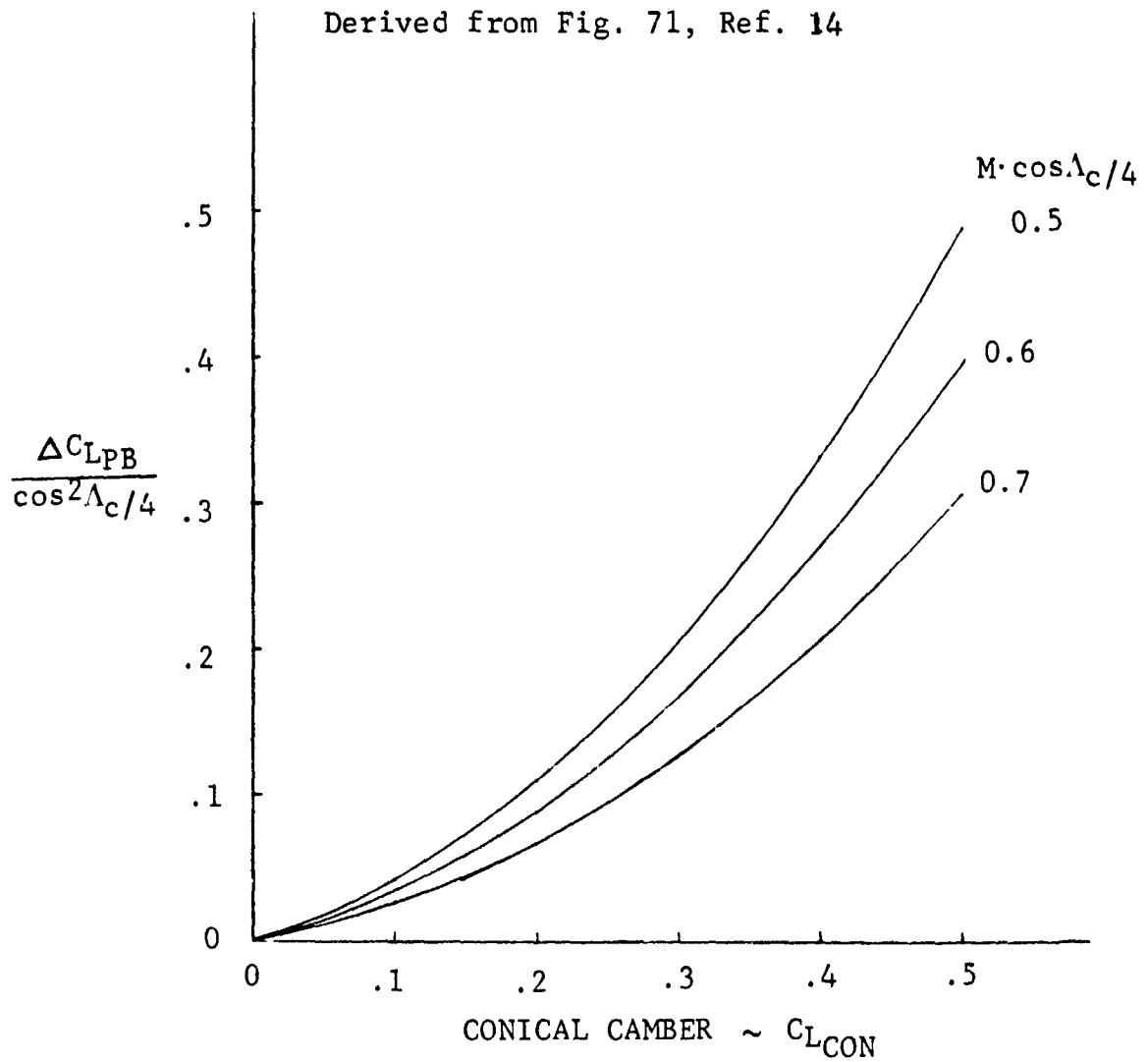
Figure 4-11 Conical Camber Effect on $C_{L_{PB}}$
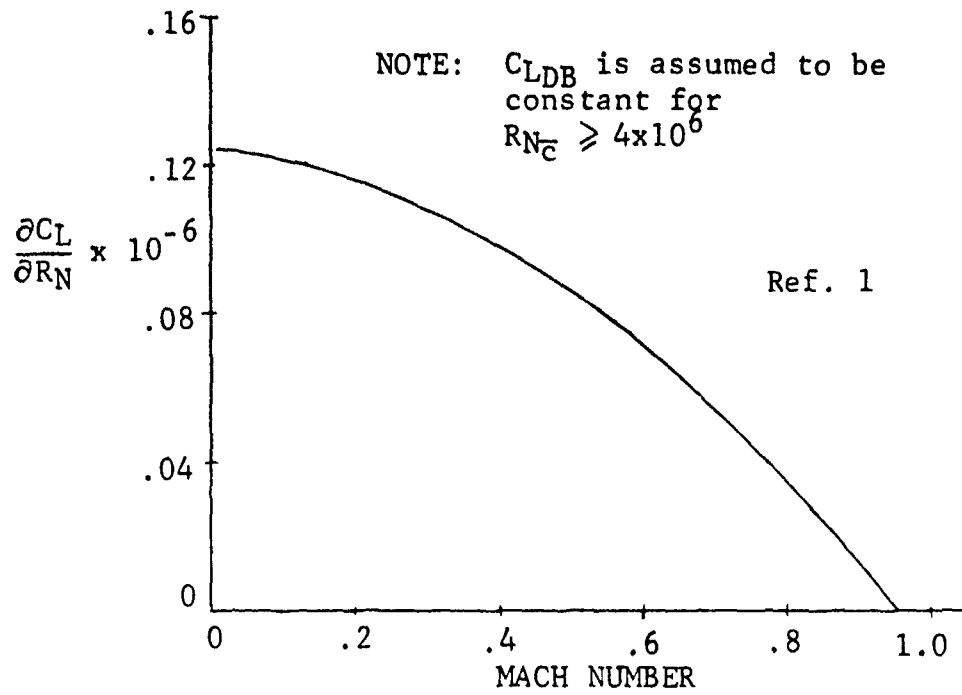
Figure 4-12 Reynolds Number Effect on $C_{L_{DB}}$
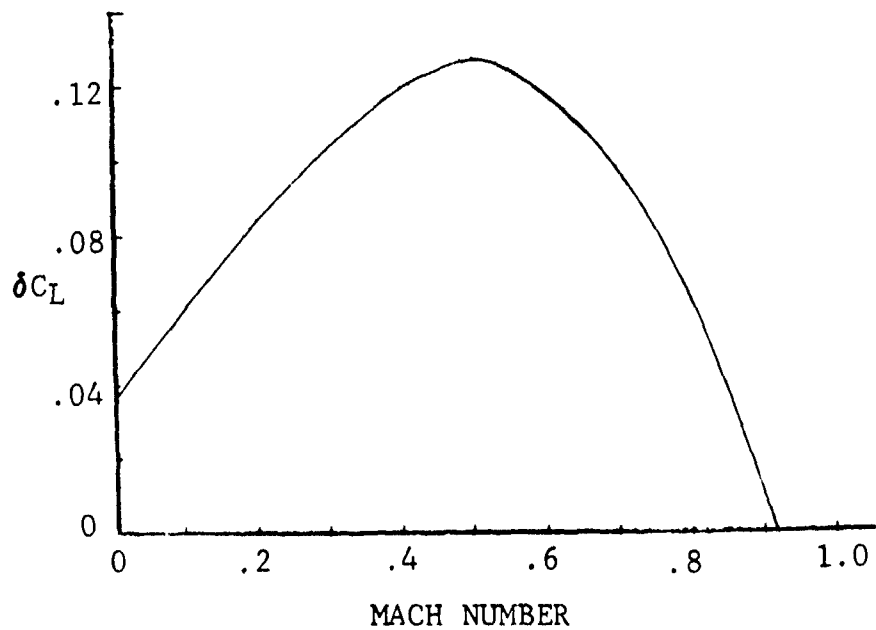
Figure 4-13 Correlation Lift Coefficient for $C_{L_{DB}}$

$$C_{D_{DB}} = K(C_{L_{DB}} - \Delta C_L)^2 + K'(C_{L_{DB}} - C_{L_{PB}})^2 - K_D C_{L_{DB}}^2 \qquad (4\text{-}16)$$

where the theoretical induced-drag factor, K_D, is predicted from

$$K_D = \frac{1}{\pi \, AR \, e'} \qquad (4\text{-}17)$$

where e', a modification of the classical theoretical drag-due-to-lift factor $1/\pi AR$, accounts for nonelliptical span loadings and body effects. The factor e' is calculated from

$$e' = e'_w \left[1 - (d/B)^2 \right] \qquad (4\text{-}18)$$

where the wing planform efficiency factor e'_w is as plotted in Figure 4-14 as a function of taper ratio, sweep, and aspect ratio. These data were obtained from a Weissinger lifting-line solution in Reference 14.

The drag above $C_{L_{DB}}$ represents the separation drag component when major separation effects are present. Simon et al. (Reference 14) measured this drag relative to the profile drag at the drag-break lift coefficient and show correlated curves of ΔC_{DB} versus C_L, $C_{L_{DB}}$, and Mach number. The $\Delta C_{D_{DB}}$ data were curve fitted and result in the equation

$$\Delta C_{DB} = K_B (C_L - C_{L_{DB}})^2 + .08 \sqrt{K_B (C_L - C_{L_{DB}})^2} \; ; \; C_L > C_{L_{DB}} \qquad (4\text{-}19)$$

The factor K_B is plotted in Figure 4-15. The program does not vary K_B with Mach number since the drag-rise term is included in the polar buildup above $C_{L_{DB}}$.

For conventional wings the polar predicted by Equation 4-15 is continued through $C_{L_{MAX}}$. For low-aspect-ratio or cranked wings (see Section 6) that develop vortex lift at the higher lift coefficients, the zero-suction drag polar predicted by

$$C_{D_L} = C_L \tan \alpha \qquad (4\text{-}20)$$

60
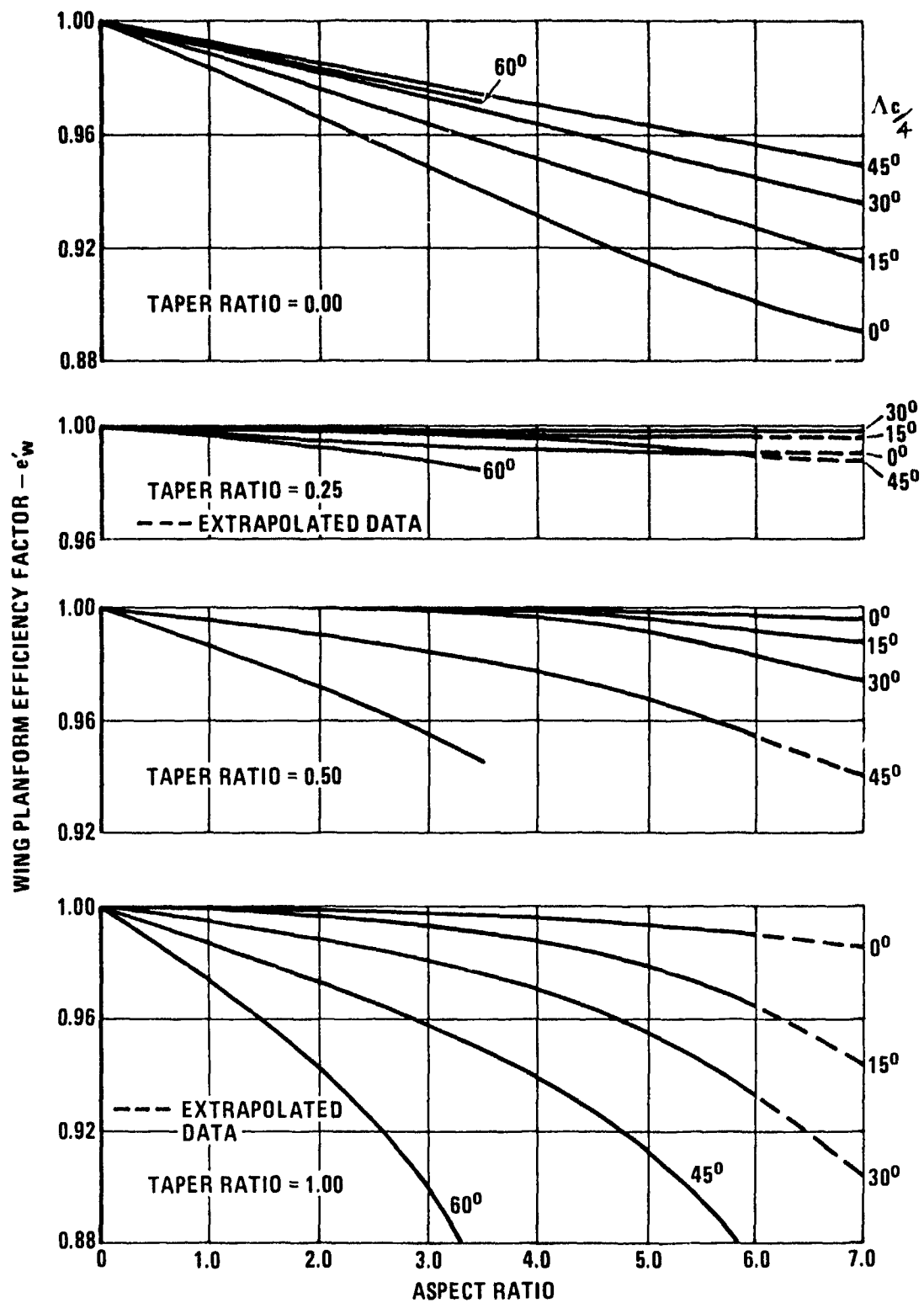
Figure 4-14   Weissenger Theoretical Wing Planform
Efficiency Factor

61
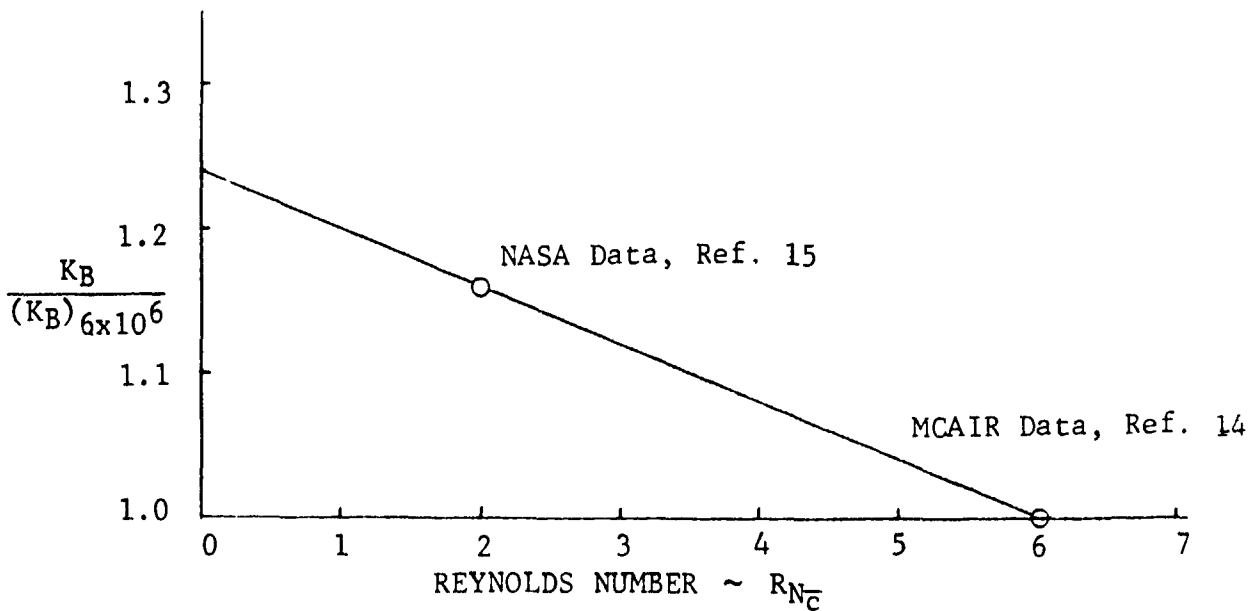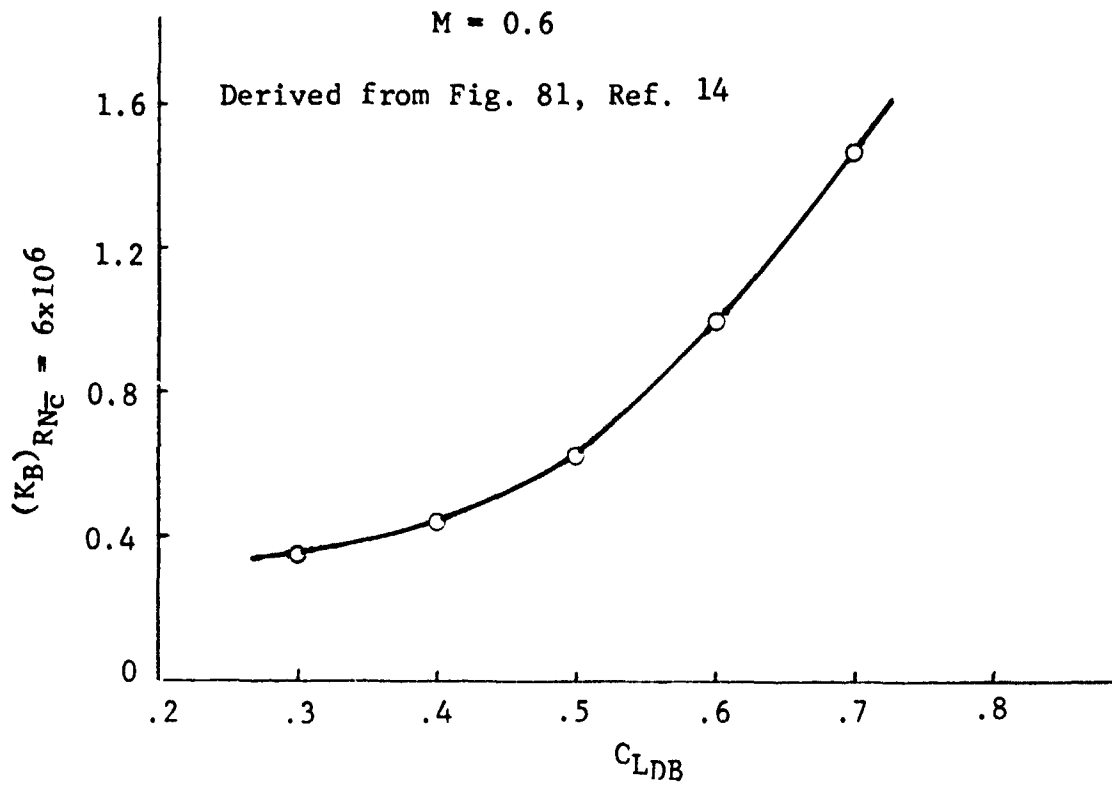
Figure 4-15   Separation Drag Factor

is compared against the drag polar predicted by Equation 4-15. The drag due to lift is then set equal to whichever is lowest, producing a drag polar as shown in the sketch below. The C_L-α variation for vortex lift is predicted by the methods given in Section 6.
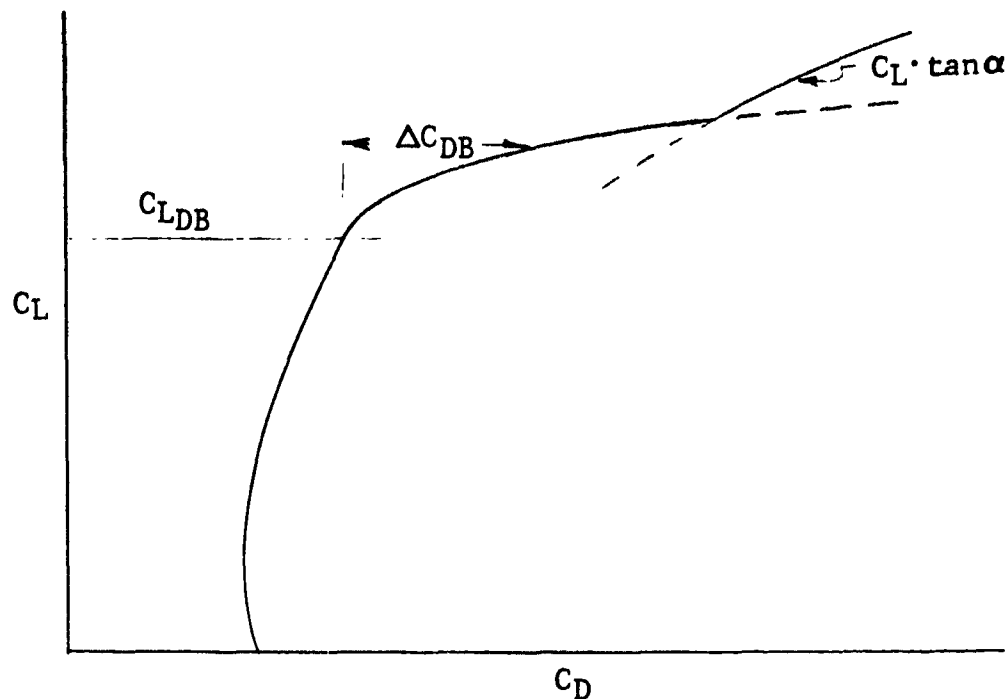
4.5   SUPERSONIC POLAR PREDICTION ABOVE POLAR BREAK

Supersonic Region 7 above polar break is predicted by the semi-empirical method developed in Reference 14. The equation for predicting supersonic drag due to lift, above polar break, is given by

$$C_{D_L} = (K-K')(C_{L_{PB}} - \Delta C_L)^2 + K'(C_L - \Delta C_L)^2; \quad C_L > C_{L_{PB}} \qquad (4\text{-}21)$$

where K and ΔC_L are the polar parameters in the low-lift region discussed in Subsection 4.2.

The polar-break lift coefficient, $C_{L_{PB}}$, is correlated as a function of sweep, aspect ratio, camber, etc. in Reference 14. A curve fit of the data in Reference 14 results in the following equation for $C_{L_{PB}}$:

$$C_{L_{PB}} = C_{LS_1} + 1.25(C_{LS_9} + \Delta C_{LS_9} - C_{LS_1})(\beta \cot \Lambda_{LE} - .1) + 0.5 C_{L_d} \quad (4\text{-}22)$$

where the factors C_{LS_1}, C_{LS_9}, and ΔC_{LS_9} are shown plotted in Figure 4-16 as a function of aspect ratio.

The polar shape factor, K', above $C_{L_{PB}}$ is computed in Reference 14 as

$$K' = \frac{H}{C_{L_\alpha}} \quad (4\text{-}23)$$

where

$$H = \begin{cases} 1.1 & ; \ AR \tan \Lambda_{LE} \leq 3.5 \\ \\ 1.1 + 0.1(AR \tan \Lambda_{LE}; \ AR \tan \Lambda_{LE} > 3.5 \end{cases} \quad (4\text{-}24)$$
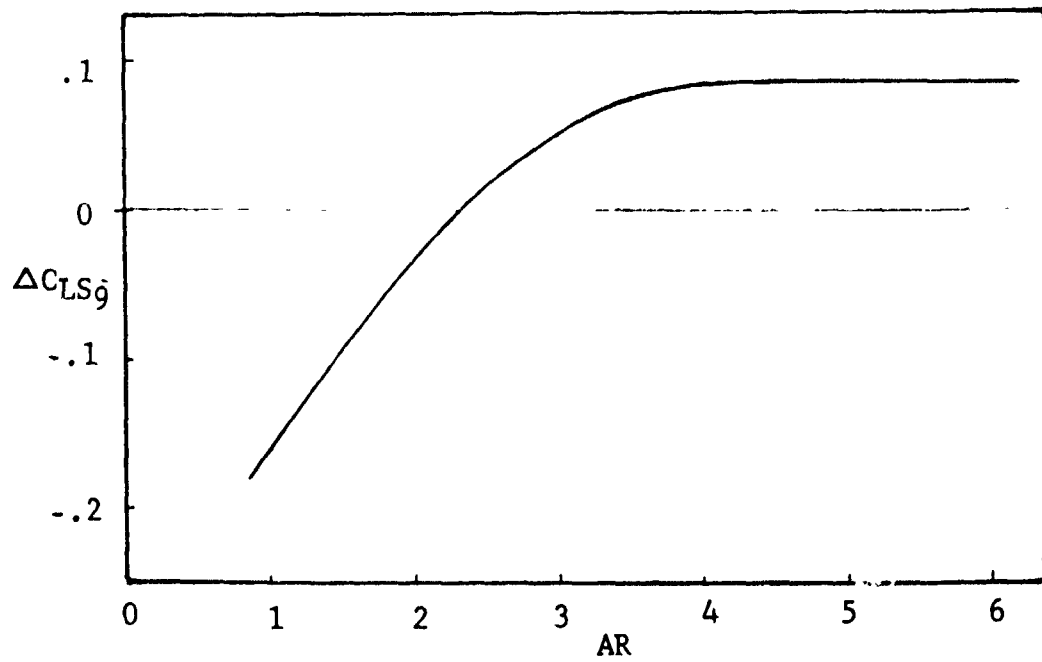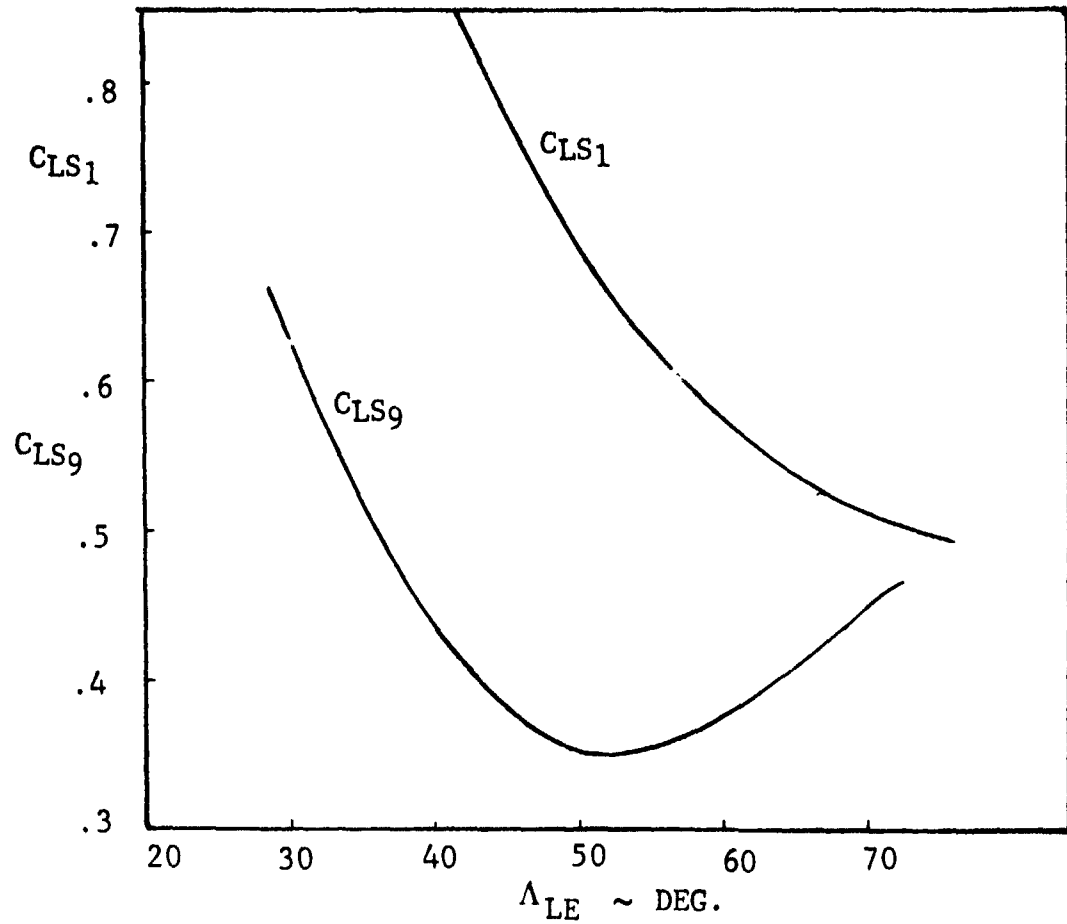
Figure 4-16   Supersonic Polar Break Lift Factors

5. CRITICAL MACH NUMBER AND DRAG RISE

The drag-divergence Mach number or Mach critical, is defined as the Mach number at which a rapid drag rise intercepts the subsonic trend in drag. The British method of predicting the critical Mach number for two-dimensional airfoils (Reference 16) appears to be the most accurate empirical method available. The British method uses the Sinnott "crest criteria", where the low-speed pressure at the airfoil crest is related to the drag-divergence Mach number.

The AAT computer code uses a method analogous to the British two-dimensional critical Mach number prediction procedure in order to predict Mach critical for a finite-aspect-ratio swept wing. The critical Mach number is defined as the value of freestream Mach number which produces a local supersonic flow measured normal to the sweep of the isobar at the crest. The local Mach number normal to the crest isobar has been determined to be 1.02 for conventional airfoils and 1.05 for supercritical airfoils at the freestream critical Mach number. The sonic condition at the crest can be predicted by means of a simple equation employing the incompressible pressure at the crest of the airfoil, and compressibility factors.

The value of 1.02 local Mach number, used in Sinnott's transonic airfoil theory (Reference 17), for the weak shock at crest condition for drag rise, was established empirically. Reference 16 shows that this method should predice M_{CR} to within ± 0.015 for the majority of conventional two-dimensional airfoils. However, as shown in Reference 16, with "peaky" airfoils (as in the supercritical airfoil) the onset of rapid drag rise may be delayed until the shock is substantially downstream of the crest. The predicted value of M_{CR} based on a local Mach of 1.02 at the crest may thus be conservative by more than 0.02, and a local Mach of 1.05 is necessary to achieve good correlation.

The following subsections discuss the methods used to predict the pressure distribution around an airfoil and to determine M_{CR} from the pressure at the crest along with the method used to estimate the drag rise above M_{CR}.

5.1 PRESSURE COEFFICIENT CALCULATIONS

The incompressible, inviscid pressure distribution around the airfoil is defined first, then the pressure at the crest is determined. Weber's method (Reference 18) was used for the pressure

distribution calculations. This method requires the airfoil surface coordinates to be determined at the chordwise locations defined by

$$X(\nu) = \frac{1}{2}(1 + \cos \frac{\nu\pi}{N}); \quad 0 \leq \nu \leq N \qquad (5\text{-}1)$$

N may be any integer, but, in this program, N is set equal to 32.

The Weber formula is essentially a second-order linear theory whereby the pressures are determined from multiplication of the matrix of thickness and camber ordinates of the airfoil by a matrix of constants given in Reference 18.

The formula for the incompressible pressure distribution on an infinite sheared wing was obtained from the incompressible form of Equation 93 in Reference 18, resulting in

$$1 - C_p = \left[\frac{1}{1 + \left(\dfrac{S^{(2)}(X) \pm S^{(5)}(X)}{\cos\Lambda}\right)^2} \right]$$

$$\times \left\{ \left[\cos\alpha \left(1 + S^{(1)}(X)\cos\Lambda \pm S^{(4)}(X)\cos\Lambda\right) \right.\right.$$

$$\left. \pm \sin\alpha \cos\Lambda \left(1 + \frac{S^{(3)}(X)}{\cos\Lambda}\right)\left(\frac{1-X}{X}\right)^{\frac{1}{2}} \right]^2$$

$$\pm \left[\cos\alpha \left(S^{(1)}(X)\sin\Lambda \pm S^{(4)}(X)\sin\Lambda\right) \right.$$

$$\left.\left. \pm \sin\alpha \sin\Lambda \left(1 + \frac{S^{(3)}(X)}{\cos\Lambda}\right)\left(\frac{1-X}{X}\right)^{\frac{1}{2}} \right]^2 \right\}$$

$$+ \sin^2\Lambda \, \cos^2\alpha \left[1 - \frac{1}{1 + \left(\dfrac{S^{(2)}(X) \pm S^{(5)}(X)}{\cos\Lambda}\right)^2} \right] \quad (5\text{-}2)$$

For C_p on the upper surface the + is used, and for the lower-surface C_p the - is used. Also,

$$S^{(1)}(X) = \sum_{\mu=1}^{N-1} S^{(1)}{}_{\mu\nu} \; Z_{t\mu}$$

$$S^{(2)}(X) = \sum_{\mu=1}^{N-1} S^{(2)}_{\mu\nu} \, Z_{t\mu}$$

$$S^{(3)}(X) = \sum_{\mu=1}^{N-1} S^{(3)}_{\mu\nu} \, Z_{t\mu} + S^{(3)}_{N\nu} \, \sqrt{\rho/2c}$$

$$S^{(4)}(X) = \sum_{\mu=1}^{N-1} S^{(4)}_{\mu\nu} \, Z_{s\mu}$$

$$S^{(5)}(X) = \sum_{\mu=1}^{N-1} S^{(5)}_{\mu\nu} \, Z_{s\mu}$$

Tables of the $S^{(\ )}_{\mu\nu}$ matrices of constants are given in Reference 18 . $Z_{t\mu}$ and $Z_{s\mu}$ are the thickness and camber distribution at the control point μ given by

$$Z_{t\mu} = \frac{1}{2} (y_u + y_\ell)$$

and

$$Z_{s\mu} = \frac{1}{2} (y_u - y_\ell)$$

where y_u and y_ℓ are the upper- and lower-surface ordinates defined at the control point μ given by

$$X(\mu) = \frac{1}{2} (1 + \cos \frac{\mu\pi}{N})$$

5.2 CRITICAL MACH NUMBER CALCULATION FROM CRESTLINE PRESSURE

The procedure followed to determine M_{CR} for swept wings is similar to the procedure outlined in Reference 16 to predict the M_{CR} for two-dimensional sections. Equation 5-2 is used to compute the pressure distribution around the airfoil at a sweep angle determined from

$$\Lambda = \begin{cases} \text{arc } \cos(\cos \Lambda_{c/2})^n & ; \quad \Lambda_{c/2} \leq 40^\circ \\[4mm] \text{arc } \cos \left[\dfrac{(\cos \Lambda_{c/2})^n + .76604^n}{2} \right] & ; \quad \Lambda_{c/2} > 40^\circ \end{cases} \qquad (5\text{-}3)$$

68

where $\Lambda_{c/2}$ is the wing mid-chord sweep at the semi-span of the wing and the factor n is determined from

$$n = \frac{AR}{1.4+AR}$$

The sweep angle Λ represents an effective isobar sweep at the mid-span region of the wing as affected by the root and tip regions of the wing. The procedure used to determine M_{CR} based on the crest pressures is as follows:

1. Determine a chordwise incompressible, inviscid pressure distribution for an angle of incidence (α). Integrate the pressure distribution to obtain the lift coefficient (C_{L_i}).

2. Determine the chordwise position of the crest for each α, the crest being defined as the point at which the airfoil surface is tangential to the undisturbed freestream direction ($\theta = \alpha$).

3. Determine the incompressible pressure coefficient at the crest ($C_{P_{crest}}$).

4. Use $C_{P_{crest}}$ to calculate M_{CR} in the relation

$$C_{P_{crest}} = \frac{(P/P_t)(1+0.2M_{CR}^2\cos^2\Lambda)^{3.5} - 1}{0.7M_{CR}^2 / \sqrt{1-M_{CR}^2\cos^2\Lambda}} \tag{5-4}$$

where (P/P_t) is the ratio of local static pressure to freestream atagnation pressure as computed in

$$P/P_t = \left[1 + 0.2M_\ell^2\right]^{3.5}$$

where M_ℓ is the local Mach number normal to the isobar sweep Λ at the crest of the airfoil. M_ℓ is set equal to 1.02 for conventional airfoils and 1.05 for "peaky" or supercritical airfoils. Equation 5-4 uses a Prandtl-Glauert compressibility factor to correct the incompressible pressure coefficient for Mach number rather than the Karman-Tsien factor used in Reference 16. References 19 and 20 recommend using the Prandtl-Glauert factor instead of the Karman-Tsien factor in the M_{CR} prediction method for highly cambered airfoils or general airfoils at high-lift coefficients. The relationship determined by Equation 5-4 is plotted in Figure 5-1.

5. Use the Prandtl-Glauert compressibility factor (β_D) evaluated at M_{CR} to obtain the lift coefficient C_{L_D} from
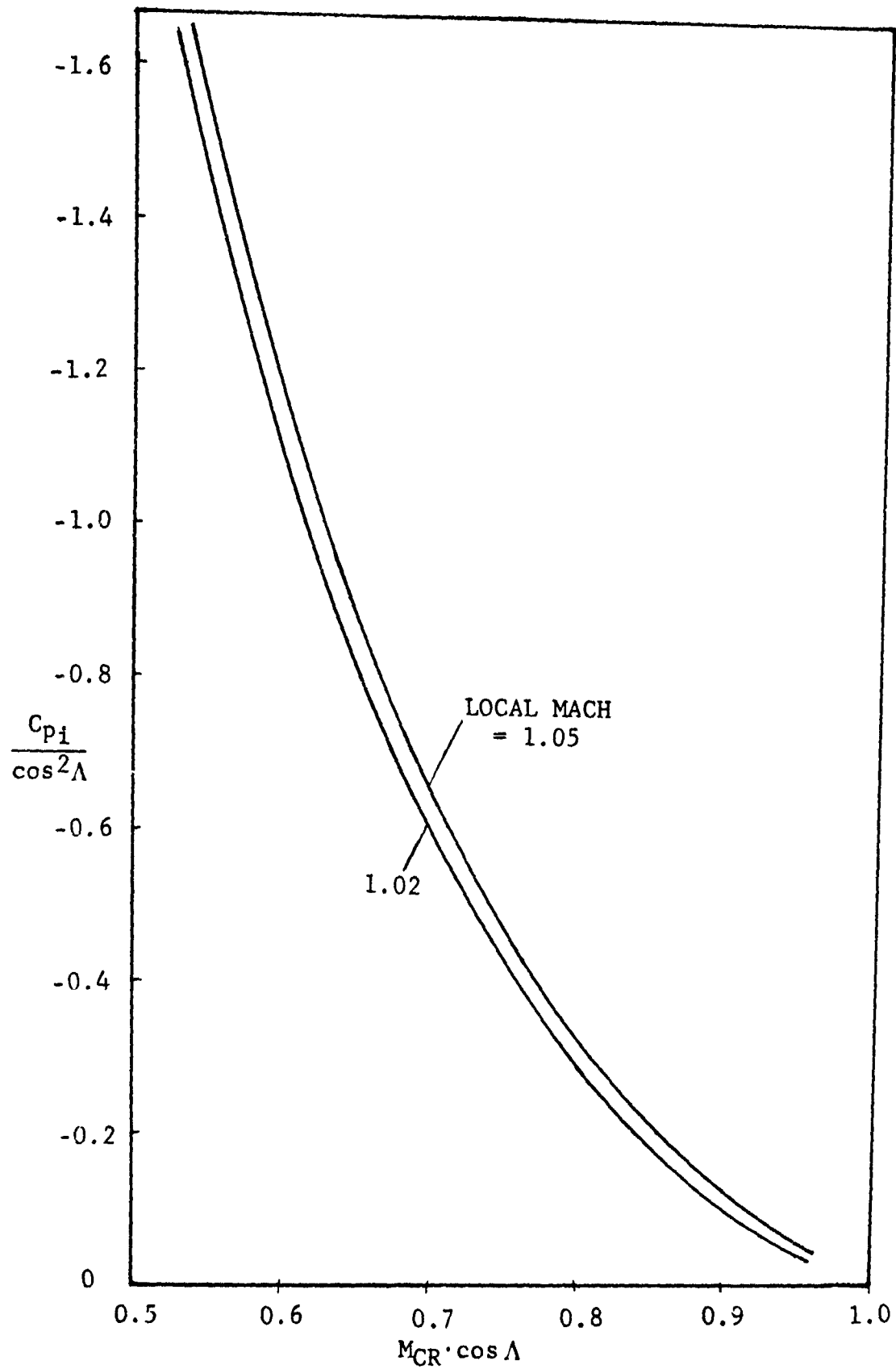
Figure 5-1   Mach Critical Prediction Chart

$$C_{L_D} = C_{L_i} / \beta_D$$

6. Repeat Steps 1 through 5 for a set of incidences in order to obtain a drag-rise boundary from the set of points (C_{L_D}, M_{CR}).

The critical Mach number predicted as a result of the above six steps, is prevented from exceeding the critical Mach number of the fuselage alone (shown plotted in Figure 5-2). For aircraft that are not area-ruled, where the isobars are allowed to unsweep at the wing-fuselage juncture, the method would tend to overpredict M_{CR} when the value approaches the fuselage M_{CR}. The prediction-versus-test M_{CR} correlation shown in Figure 5-3 is thus applied for conventional-wing predictions.

5.3 DRAG RISE

For Mach numbers less than M_{CR} the drag increases slowly with increasing Mach number. This drag component is known as compressible drag, or drag creep. Methodology for estimating this component of drag for conventional or supercritical wings is included in the subsonic drag buildup in Subsection 3.1. For Mach numbers greater than M_{CR}, drag rise begins and increases rapidly with Mach. Figure 5-4 illustrates the drag bookkeeping system followed in the AAT computer code whereby beyond Mach 1.0 the drag rise and the inter-ference plus form drag are replaced by wave drag. The drag rise is separated into two components: drag rise due to lifting surfaces and drag rise due to all other components on the aircraft. The drag rise due to lifting surfaces is represented by

$$C_{D_{RL}} = P_L \ (M-M_{CR})^2 \tag{5-5}$$

where

$$P_L = 5.4 \cdot (t/c + 2f/c)^{1/3} \cdot \cos \Lambda_{c/2}$$

The factor P_L is a function of the wing section thickness, t/c, maximum ordinate of the camber, f/c, and the midchord sweep, $\Lambda_{c/2}$. The drag rise due to the fuselage and non-lifting components is determined by

$$C_{D_{R_b}} = a_2 \ (M - M_{CR_b})^2 + a_3 \ (M - M_{CR_b})^3 \tag{5-6}$$

where a_2 and a_3 are solved for producing a continuous zero-lift drag curve between the fuselage Mach critical, M_{CR_b}, and Mach 1.0. The zero-lift body drag rise is curve-fitted to begin at M_{CR_b} with zero
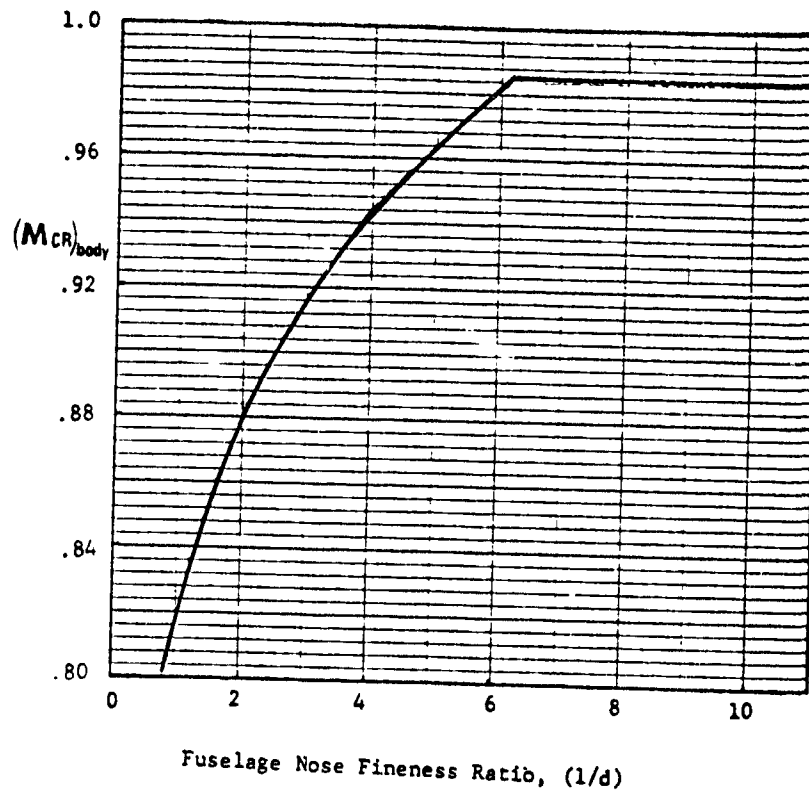
Figure 5-2   Prediction of Fuselage Critical Mach Number
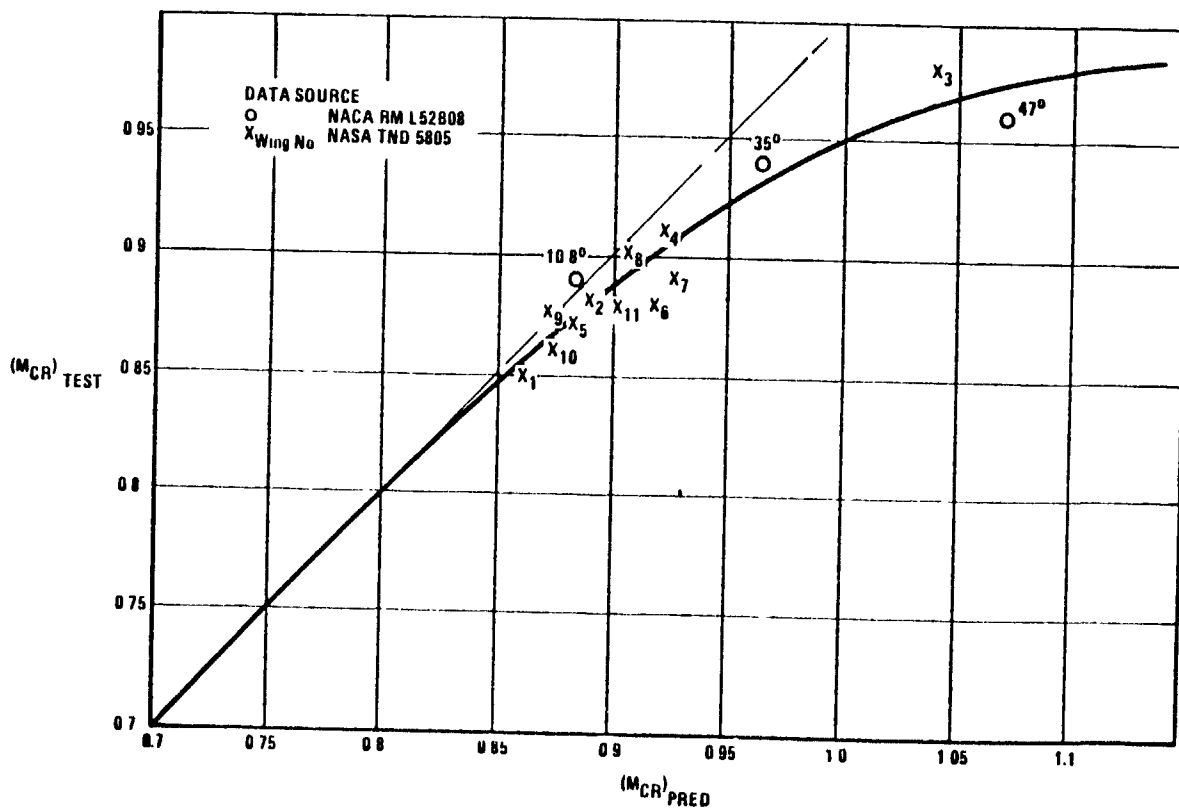
Figure 5-3   Correlation of Critical Mach Number for
Conventional Wings

72
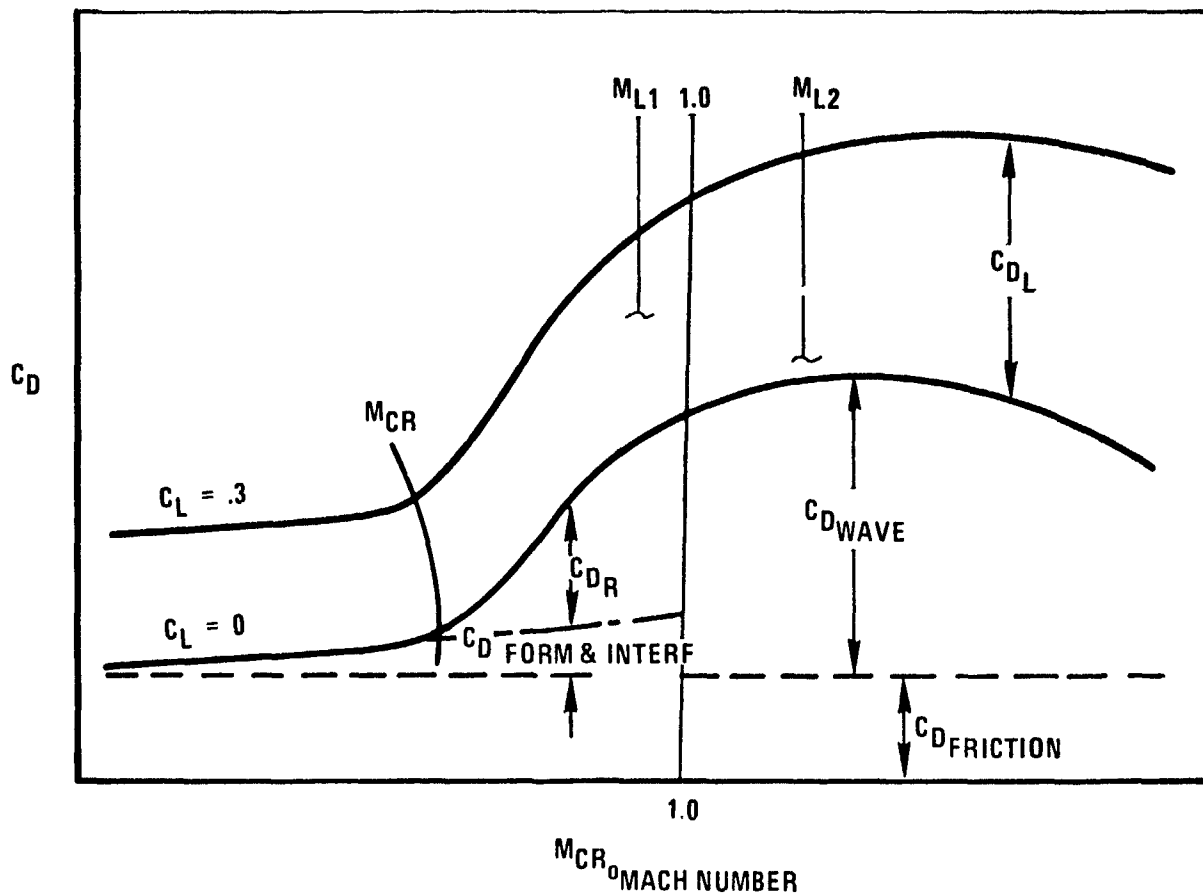
Figure 5-4   Transonic Drag Buildup

slope and end at Mach = 1.0 matching the value and slope of the wave-drag curve.

The change in M_{CR} with lift causes the subsonic drag polar to increase after M_{CR} (see Figure 5-4). For bookeeping, the drag rise is separated into a minimum drag contribution and a contribution to drag-due-to-lift. These increments are determined by subtracting the lifting-surface drag rise at zero lift from Equation (5-5) and adding that portion to Equation (5-6).

$$C_{D_{R_o}} = C_{D_{R_b}} + P_L (M - M_{CR_o})^2 \qquad (5\text{-}7)$$

$$C_{D_{R_{CL}}} = P_L (M - M_{CR})^2 - P_L (M - M_{CR_o})^2 \qquad (5\text{-}8)$$

6. LIFT

The untrimmed lift of an aircraft can be represented by the equation

$$C_L = C_{L_\alpha} (\alpha - \alpha_{Lo}) .$$

For moderate to high aspect ratios and moderate sweeps, the lift equation is linear with α so that the lift-curve slope, C_{L_α}, is constant. The total lift-curve slope of the aircraft is given by

$$C_{L_\alpha} = (C_{L_\alpha})_{W-B} + (C_{L_\alpha})_T + (C_{L_\alpha})_B \qquad (6-1)$$

which is the sum of the wing (including body carry-over effects), horizontal tail, and the forward portion of the fuselage.

The following subsections describe the methods by which C_{L_α} and α_{Lo} are calculated, and also the method of calculating the lift in the nonlinear range up to $C_{L_{MAX}}$.

6.1 WING LIFT-CURVE SLOPE

The value of $(C_{L_\alpha})_{W-B}$ is predicted by the use of several complex semi-empirical equations. These equations were developed to predict wing lift-curve slope as a continuous expression in the subsonic, transonic, and supersonic regions. The value of $(C_{L_\alpha})_{W-B}$ is expressed as

$$(C_{L_\alpha})_{W-B} = (C_{L_\alpha})_{Basic} \cdot K_t \cdot K_b \cdot \frac{S_{PLAN}}{S_{REF}} \qquad (6-2)$$

where $(C_{L_\alpha})_{Basic}$ is the wing-alone C_{L_α} with no thickness effects. The factors K_t and K_b account for the effect of airfoil-thickness plus camber and fuselage interference, respectively. The equation for $(C_{L_\alpha})_{Basic}$ was evolved from the Polhamus (Reference 21) equation for trapezoidal wings,

$$C_{L_\alpha} = \frac{\left(\frac{a_o}{2}\right) AR/57.3}{\left(\frac{a_o}{2\pi}\right) + \sqrt{\left(\frac{a_o}{2\pi}\right)^2 + \left[1 - (M\cos\Lambda_{c/2})^2\right]\left(\frac{AR}{2\cos\Lambda_{c/2}}\right)^2}} , \qquad (6-3)$$

75

for subsonic flow and the linear-theory level of

$$C_{L_\alpha} = \frac{4/57.3}{\sqrt{M^2-1}}$$

(6-4)

for supersonic flow at the leading edge $(M > 1/\cos\Lambda_{LE})$.

To extend the Polhamus equation for use with non-trapezoidal wing planforms, Spencer (Reference 22) replaces $\cos\Lambda_{c/2}$ with the effective cosine mid-chord sweep determined by Equation 2-27.

When Equation 6-3 results were compared with subsonic experimental data, it was deduced that better agreement would be achieved if the predicted peak C_{L_α} were to occur at $M < 1.0$ (for moderate and high AR) and if the rate of increase in C_{L_α} with increasing M were larger. Consequently, Equation 6-3 was altered to

$$(C_{L_\alpha})_{Basic} = \frac{\pi \cdot AR/57.3}{1+\sqrt{1+\left[1-(\cos\Lambda_{c/2})_e^{4/3}\left(\frac{M}{M*}\right)^{8/3}\right]\left[\frac{AR}{2(\cos\Lambda_{c/2})_e}\right]^2}}$$

(6-5)

where the sectional lift-curve slope a_0 equals 2π, and M* is the limiting M for the application of Equation 6-5. M* is a function of AR and $\Lambda_{c/2}$, and is defined by

$$M* = M_0* + (1-M_0*)\left[1-(\cos\Lambda_{c/2})_e\right]^2$$

(6-6)

where

$$M_0* = (10 + 0.91AR^3)/(10 + AR^3)$$

In effect, M* is the Mach number at which the rate of increase in C_{L_α} with M begins to decrease. Note that, at M=0, Equations 6-3 and 6-5 are identical. However, it was also found desirable (for improved correlation) to limit $(\cos\Lambda_{c/2})_e$ to the range $0.94 \geq \cos\Lambda_{c/2} \geq 0$. Thus, in applying Equation 6-5, sweep angles of less than 20 degrees are treated as having a value of $\cos\Lambda_{c/2} = 0.94$.

For thin wings, experimental levels of C_{L_α} characteristically reach a peak at speeds somewhat greater than M*. With low sweep and moderate to high AR, the peak occurs below M=1, while with high sweep and/or low AR, the peak may be at or above sonic speeds. At speeds well above sonic, C_{L_α} then decreases with increasing M and, when the leading-edge becomes supersonic ($M > \cos\Lambda_{LE}^{-1}$), the level approaches the two-dimensional-theory level of $C_{L_\alpha} = 4/(57.3\sqrt{M^2-1})$. To emulate these trends, Equation 6-5, was modified by a factor term and an adder term, each to be applied only at $M > M*$. These new terms are included in the modified equation

$$(C_{L_\alpha})_{Basic} = \frac{1/57.3}{(1/C_{L_{\alpha_O}})\left(\frac{M*}{M}\right)^Z + \beta'/4}; \quad M > M* \qquad (6-7)$$

where $C_{L_{\alpha_O}}$ is defined as $(C_{L_\alpha})_{Basic}$ at $M = M*$ in radians, and

$$\beta' = (M-M*)\left| 1 + (M*/M)^Y \right|^2$$

$$Y = \frac{1+\pi AR}{3+\pi AR}\left(2 + 2/3\sqrt{\lambda} - \lambda^2\right)$$

and

$$Z = M*C_{L_{\alpha_O}} + \frac{AR^2}{3\,\dfrac{\pi AR}{C_{L_{\alpha_O}}}\left(\dfrac{\pi AR}{C_{L_{\alpha_O}}}-1\right)(\cos\Lambda_c/2)_e^{2/3}}$$

Wings having thick airfoils undergo a degradation in C_{L_α} beginning at $M > M*$. The level of C_{L_α} versus M dips, usually reaching a minimum at $M < 1.0$, and then recovers to a second peak level at $M > 1.0$. To account for this phenomenon, the basic C_{L_α} equations have been modified by a factor, K_t, as defined by

$$K_t = \begin{cases} 1 - \left|4\sigma_1(1-\sigma_1)\right|^3 \cdot \gamma & ; \; M_1 \leq M \leq M_2 \\[2mm] 1 - \left|4\sigma_2(1-\sigma_2)\right|^3 \cdot \gamma & ; \; M_2 \leq M \leq M_3 \\[2mm] 1.0 & ; \; M_1 \geq M \geq M_3 \end{cases} \qquad (6-8)$$

where γ, σ_1, σ_2, M_1, M_2, M_3 are as defined by the equations below:

$$\gamma = \frac{9\Delta(t/c)/(\cos\Lambda_c/2)_e}{1+\frac{1}{2}AR\left[\Delta(t/c)/(\cos\Lambda_c/2)_e\right]}$$

where

$$\Delta(t/c) = t/c - (t/c)_{\mathcal{L}im}$$

$$(t/c)_{\mathcal{L}im} = \frac{1}{4.4AR(\cos\Lambda_c/2)_e^{3/2}} \qquad (6-9)$$

The equation for γ is applicable for

$$0 \leq \frac{\Delta(t/c)}{(\cos\Lambda_c/2)_e} \leq 0.07$$

$$0 \leq \frac{AR\Delta(t/c)}{(\cos\Lambda_c/2)_e} \leq 0.10$$

If $\Delta(t/c)/(\cos\Lambda_c/2)_e > 0.07$, use 0.07

If $AR\,\Delta(t/c)/(\cos\Lambda_c/2)_e > 0.10$, use 0.10

$$\sigma_1 = \frac{1}{2}\frac{M-M_1}{(M_2-M_1)}$$

$$\sigma_2 = \frac{1}{2}\left(1 + \frac{M-M_2}{M_3-M_2}\right)$$

$$M_1 = 1-2(t/c)(\cos\Lambda_c/2)_e^{3/2}\left[1+\frac{3}{2}(C_{L_d})^{3/2}\right]\frac{AR^3}{4+AR^3} \qquad (6-10)$$

$$M_2 = M_1 + t/c$$

Note: $0 \leq M_1 \leq M^*$

   If $M_1 > M^*$, use $M_1 = M^*$

$$M_3 = 1.0 + t/c$$

The derivation of Equation 6-8 is based on the data trends and analyses of Reference 23 and on other limited data (e.g., References 24 and 25). It should be noted that a C_{L_α} "bucket" is

predicted only if the wing streamwise airfoil t/c exceeds the limit thickness defined by Equation 6-9. The limit-thickness boundary was established from the statistical boundaries presented in Reference 26.

Another factor in the wing C_{L_α} prediction equation (Eq.6-1), is the fuselage interference factor, defined by

$$K_b = (1 + d/b)(1 - d/b)^f \qquad (6-11)$$

where

$$f = \frac{16 + 3AR^2}{8 + 5AR^2}$$

b = wing total span
d = body total width at wing junction

The factor K_b accounts for the change in wing lift due to the body segment which enshrouds the wing and to the wing-induced lift on that body segment. Based on semi-empirical derivations presented in Reference 27, K_b is independent of M (to the first order). It is noted that the total lift of a wing/body configuration is derived by adding the body-alone lift to that lift obtained for the wing-alone as modified by the factor K_b.

Application of Equations 6-2, 6-5, 6-7, 6-8, and 6-11, for the prediction of $(C_{L_\alpha})_{W-B}$ will yield trends as sketched in Figure 6-1. It is noted that this technique is strongly dependent on the value of (t/c) in the transonic speed regime if (t/c) exceeds the limiting value defined in Equation 6-9.

Substantiation of the C_{L_α} prediction technique, described above in the form of comparisons with a wide range of experimental data, is presented in Reference 28. The derivation of C_{L_α} for Mach numbers greater than M*, presented in Reference 28, relied heavily on transonic-bump test data, which characteristically produces a trend such as shown in Figure 6-1. The new derivation (Equation 6-7) relies on sting-mounted test data, which produces a less abrupt transition in (dC_{L_α}/dM) in the transonic region.
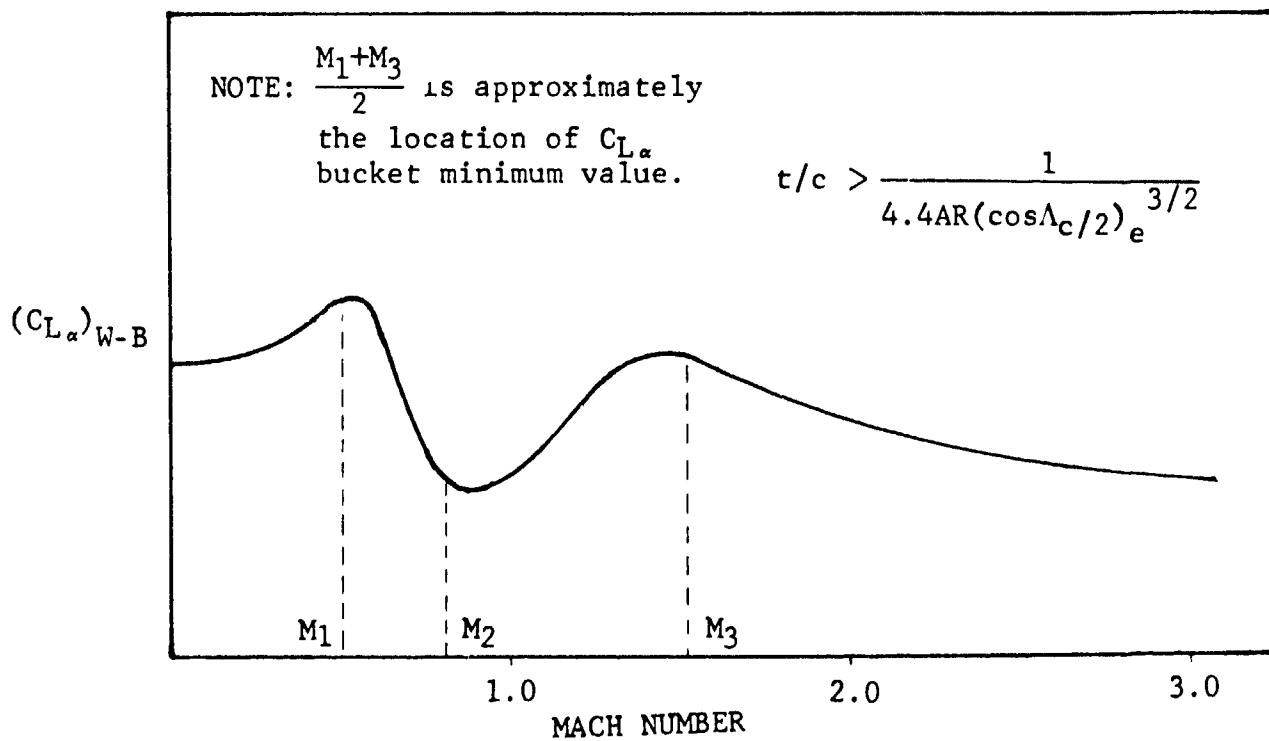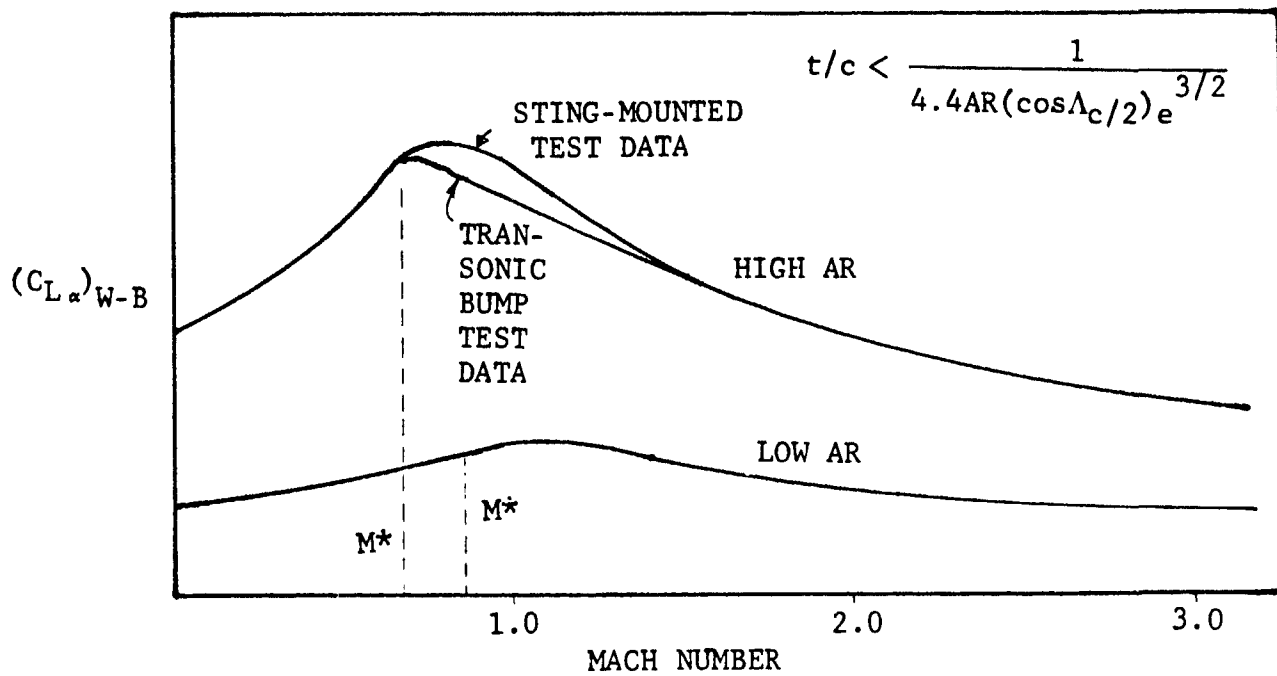
Figure 6-1 Typical Lift-Curve Slopes

For advanced technology airfoils, the onset of the lift divergence Mach Number, M_1, is delayed to a higher value than for conventional airfoils. For advanced technology wings, the factors M_1, M_2 and γ in Equation 6-8 are modified as follows:

$$(M_1)_{Adv} = (M_1)_{Conv} + 0.09$$

$$(M_2)_{Adv} = (M_2)_{Conv} + 0.045$$

$$(\gamma)_{Adv} = (\gamma)_{Conv} \cdot \frac{(M_3-M_1)_{Adv}}{(M_3-M_1)_{Conv}}$$

This modification delays the thickness correction factor to a higher Mach number and also decreases the extent by which K_t is reduced at M_2.

Supercritical airfoils have a higher sectional lift-curve slope compared with conventional airfoils. The program uses

$$\frac{a_o}{2\pi} = 1 + \frac{1.174 \, t/c}{\sqrt{1-M^2}} \tag{6-12}$$

for advanced technology wings in place of $a_o/2\pi = 1$, used for conventional wings.

6.2 TAIL LIFT-CURVE SLOPE

The lift-curve slope of the horizontal tail can be estimated from the equation

$$(C_{L\alpha})_T = (C_{L\alpha}')_T \left[K_{W(B)} + K_{B(W)} \right] \left(1 - \frac{\partial \epsilon}{\partial \alpha} \right) \frac{q_t}{q_\infty} \frac{S_T}{S_{REF}} \tag{6-13}$$

where $(C_{L\alpha}')_T$ is the exposed-area lift-curve estimate for the tail, $K_{W(B)}$ and $K_{B(W)}$ are the Pitts, Nelson, and Kaattari body-lift carry-over factors (Reference 29), $\partial\epsilon/\partial\alpha$ is the downwash gradient; q_t/q_∞ is the dynamic pressure ratio, and S_T is the

exposed tail area. The exposed-area lift-curve for the tail is estimated by use of the exposed planform of the tail and the method described in Section 6.1.

6.2.1 Downwash at the Tail

An empirical method of estimating the low-speed downwash gradient behind straight-tapered wings is given in the DATCOM by

$$\left(\frac{\partial \epsilon}{\partial \alpha}\right)_o = 4.44 \left[K_A K_\lambda K_H (\cos \Lambda_c / 4)^{\frac{1}{2}} \right]^{1.19} \tag{6-14}$$

The factors K_A, K_λ, and K_H are wing aspect ratio, wing taper ratio, and horizontal-tail-location factors, respectively. They are determined from

$$K_A = 1/AR - 1/(1+AR^{1.7})$$

$$K_\lambda = \frac{10-3\lambda}{7}$$

and

$$K_H = \frac{(1-h_t/b)}{(2\ell_t'/b)^{1/3}}$$

where AR and λ are the wing aspect and taper ratios, respectively, h_t is the height of the tail relative to the wing chord plane and ℓ_t' is the distance between the exposed MAC of the wing and the exposed MAC of the tail. At higher speeds the effect of compressibility on downwash is approximated by

$$\frac{\partial \epsilon}{\partial \alpha} = \left(\frac{\partial \epsilon}{\partial \alpha}\right)_o \frac{(C_{L_\alpha})_M}{(C_{L_\alpha})_o} \tag{6-15}$$

where $(C_{L_\alpha})_o$ and $(C_{L_\alpha})_M$ are the wing lift-curve slopes at low speed (M=0.1) and at the appropriate Mach number, respectively.

6.2.2 Dynamic Pressure at the Tail

The method for estimating the dynamic-pressure q_t/q_∞ at the tail is based on the DATCOM method which relates the dynamic-pressure ratio to the drag coefficient of the wing. The steps involved in determining the dynamic pressure at some distance aft of the wing root chord, outlined in Section 4.4.1 of the DATCOM report, are as follows

1. Compute the half-width of the wing wake by

$$\frac{Z_w}{c} = 0.68 \sqrt{C_{D_O} \left(\frac{x}{c} + 0.15\right)} \qquad (6\text{-}16)$$

   where x is the longitudinal distance measured from the wing-root-chord trailing edge, Z_w is the half-width of the wake at any position x, and C_{D_O} is the wing zero-lift drag coefficient.

2. Calculate the downwash in the plane of symmetry at the vortex sheet by

$$\epsilon = \frac{1.62}{\pi \text{AR}} (C_{L_\alpha} \cdot 2) \qquad (6\text{-}17)$$

3. Compute the vertical distance Z from the vortex sheet to the quarter-chord point of the MAC of the horizontal tail by

$$Z = x \tan (\gamma + \epsilon - 2) \qquad (6\text{-}18)$$

   where $\gamma = \tan^{-1} (h_t / \ell_t)$.

4. Determine the dynamic-pressure-loss ratio at the wake center by

$$\left(\frac{\Delta q}{q}\right)_o = \frac{2.42 (C_{D_O})^{1/2}}{\left(\frac{x}{c} + 0.3\right)} \qquad (6\text{-}19)$$

5. Determine the dynamic-pressure-loss ratio for points not on the wake centerline by

83

$$\frac{\Delta q}{q_\infty} = \left(\frac{\Delta q}{q}\right)_o \cos^2\left(\frac{\pi}{2} \frac{Z}{Z_W}\right) \tag{6-20}$$

6. Determine the dynamic pressure ratio at an arbitrary distance x aft of the wing-root-chord trailing edge by

$$\frac{q_t}{q_\infty} = 1 - \frac{\Delta q}{q_\infty} \tag{6-21}$$

6.3 CANARD LIFT-CURVE SLOPE

If the horizontal trim surface is located ahead of the wing the AAT computer code will treat the surface as a canard. The lift-curve slope of the canard is estimated from the equation

$$(C_{L_\alpha})_C = (C_{L_\alpha}')_C \left[K_{W(B)} + K_{B(W)}\right] \frac{S_C}{S_{ref}} \tag{6-22}$$

where all the terms are obtained in a similar manner as the corresponding terms in Equation (6-13). Note that the canard lift equation has no downwash or dynamic pressure loss terms. The upwash acting on the canard due to the wing is generally slight and can be ignored, while the canard produces a significant downwash field acting on the wing. The net effect of the canard-wing interaction, in the AAT code, is accounted for by reducing the wing lift by a factor proportional to the canard lift term. Thus, the equation for wing plus canard lift becomes

$$(C_{L_\alpha})_{W-B-C} = \left[(C_{L_\alpha})_{W-B} - \eta_L (C_{L_\alpha})_C\right] + (C_{L_\alpha})_C \tag{6-23}$$

The factor η_L is a canard interference term acting on the wing and is obtained from Figures 6-2 and 6-3 which are a function of h_c the height of the canard relative to the wing chord plane, Sc/Sw the ratio of canard exposed area to wing planform area, and Mach number. The canard lift interference factor, η_L, was derived from a systematic theoretical-experimental canard size and location study reported in Reference 30.
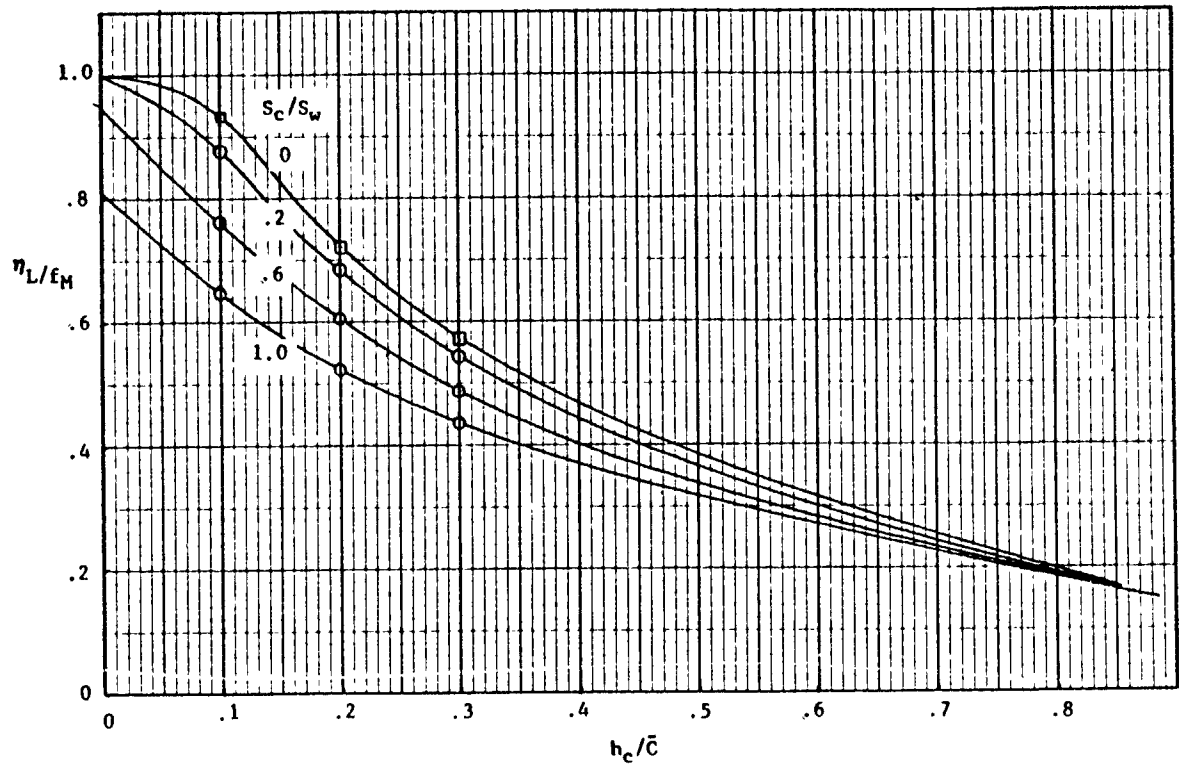
Figure 6-2   Canard Lift Interference Factor
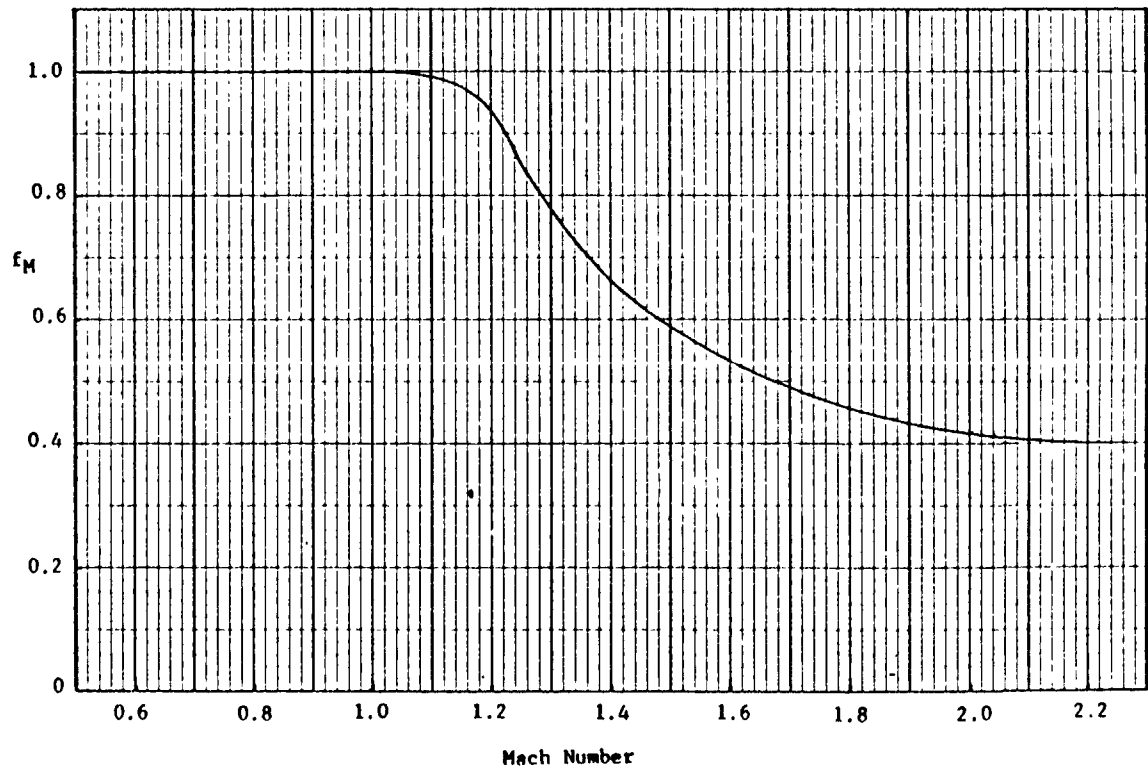
Figure 6-3   Canard Interference Factor - Mach Effect

85

6.4 BODY LIFT-CURVE SLOPE

As shown in Reference 31, the linearized lift-curve slope for a body can be expressed as

$$(C_{L_\alpha})_B = k_1 \frac{X_{LE}}{L_N}^{1/3} \frac{F}{S_{Ref}} \qquad (6\text{-}24)$$

where X_{LE} is the body length ahead of the wing, L_N is the fore-body length, F is the body cross-sectional area, and k_1 is a linear-potential lift-curve-slope parameter. The factor k_1 (a function of body width b, body height, h, and the perimeter of an elliptical body with equal area, p) is determined from the curve given in Figure 6-4, which is taken from Reference 31.
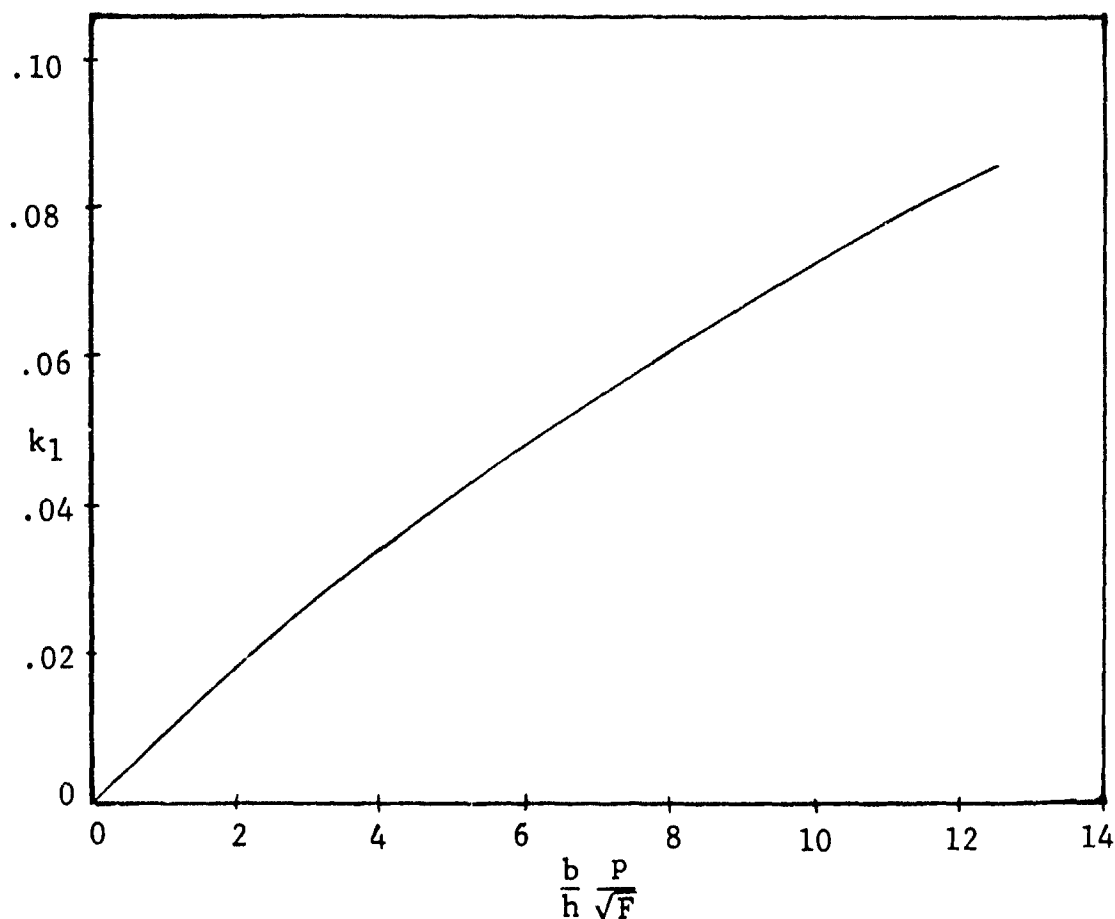
Figure 6-4 Factor Used in Determination of Body Lift-Curve Slope

6.5 ANGLE OF ATTACK AT ZERO LIFT

The angle of attack at zero lift, α_{Lo}, is determined from

$$\alpha_{Lo} = (\alpha_{Lo})_{CAMBER} + (\alpha_{Lo})_{TWIST} + (\alpha_{Lo})_{INCIDENCE} \qquad (6\text{-}25a)$$

The effect of camber, C_{L_d} on α_{Lo} is calculated from

$$(\alpha_{Lo})_{CAMBER} = \left(\frac{\partial \alpha_{Lo}}{\partial C_{\ell_d}}\right) C_{L_d} \qquad (6\text{-}25b)$$

where $(\partial \alpha_{Lo}/\partial C_{\ell_d})$ is shown plotted in Figure 6-5, which is obtained from two-dimensional data.

The increment in α_{Lo} due to wing twist, τ, is calculated from

$$(\alpha_{Lo})_{TWIST} = - \left(\frac{\partial \alpha_{Lo}}{\partial \tau}\right) \tau \qquad (6\text{-}25c)$$

Figure 6-5 Camber Factor for Zero-Lift
Angle of Attack

where

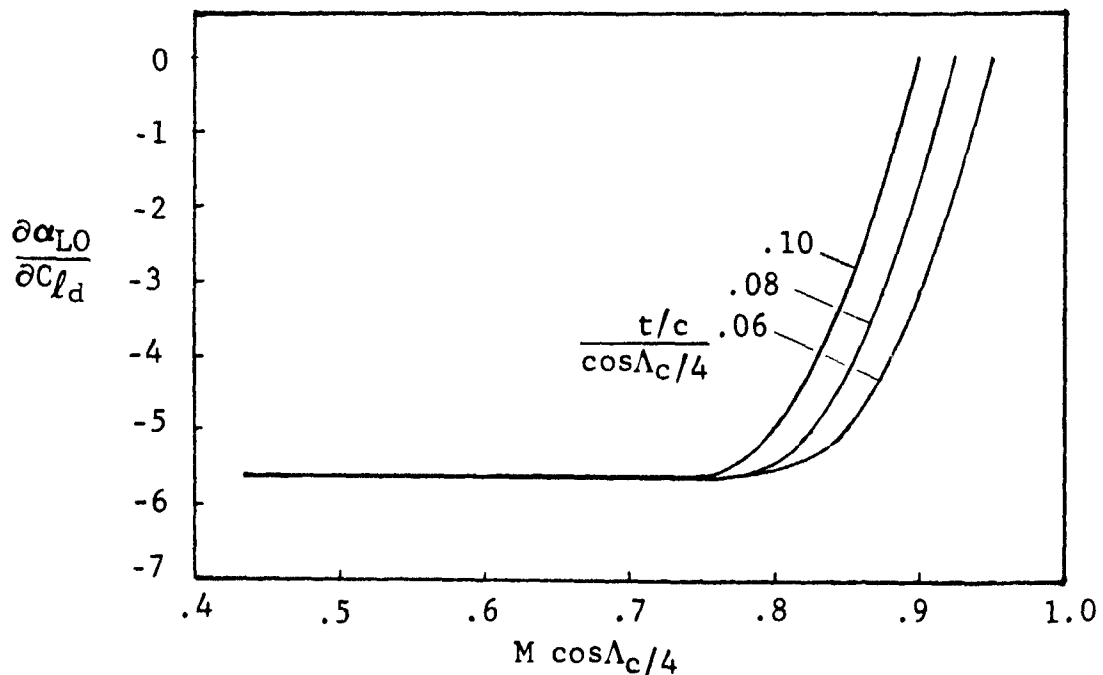$$\frac{\partial \alpha_{Lo}}{\partial \tau} = 0.093 - 0.000571 \Lambda_\beta + 0.5761 \lambda - 0.2645 \lambda^2$$

and

$$\Lambda_\beta = \tan^{-1} \frac{\tan \Lambda_{c/4}}{\beta} \qquad \text{(deg.)}$$

The equation for $(\partial \alpha_{Lo}/\partial \tau)$ was obtained from a curve fit of the parametric data reported by Gilman and Burdges (Reference 32) for wings with linear-element twist.

The angle of attack in the program is measured relative to the wing root-chord reference plane. For variable-sweep configurations the angle of attack for any sweep position is measured from the wing chord plane in the forward sweep position. The increment in α_{Lo} due to wing and horizontal tail incidence is calcualted from

$$(\alpha_{Lo})_{INCIDENCE} = \frac{(C_{L_\alpha})_{BODY} (i_w) + (C_{L_\alpha})_{TAIL} (i_w - i_t)}{C_{L_\alpha}}$$

$$+ (i_w - i_{w_{REF}}) \qquad (6\text{-}26)$$

where

$$(C_{L_\alpha})_{BODY} = (C_{L_\alpha})_{NOSE} + \left[\frac{K_{B(W)}}{K_{W(B)} + K_{B(W)}}\right] (C_{L_\alpha})_{W-B}$$

When $M > 1$, the contribution of camber and twist to α_{Lo} is set equal to zero and only the incidence effect is continued supersonically.

6.6 NONLINEAR LIFT OF HIGH-ASPECT-RATIO WINGS

The lift characteristics of a high-aspect-ratio wing is illustrated in the sketch. A high aspect ratio is defined as AR > AR$_{LOW}$, where AR$_{LOW}$ is defined in Section 6.9 (Equation 6-37). The lift varies linearly with angle of attack up to C$_{LS}$, after which the lift variation becomes non-linear.

88
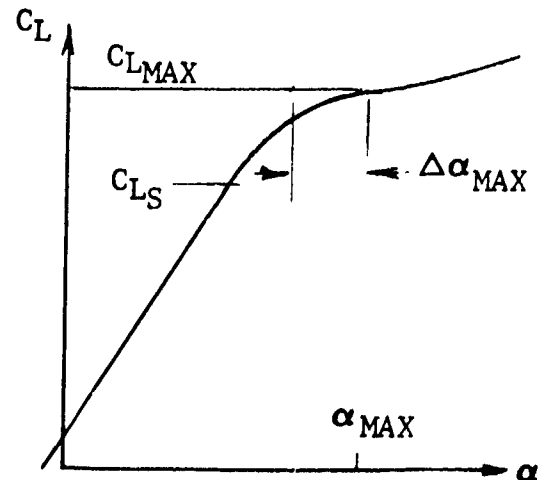
The angle of attack for a specified lift coefficient is calculated from

$$\alpha = \frac{C_L}{C_{L_\alpha}} + \alpha_{Lo} + \Delta\alpha \qquad (6-27)$$

where

$$\Delta\alpha = \begin{cases} 0; & C_L \le C_{LS} \text{ or } M > 1.0 \\[2ex] \left(\dfrac{C_L - C_{LS}}{C_{L_{max}} - C_{LS}}\right)^2 \cdot \Delta\alpha_{max}; & C_{LS} < C_L \le C_{L_{max}} \\[2ex] \left(\dfrac{C_L - C_{LS}}{C_{L_{max}} - C_{LS}}\right)^2 \cdot \Delta\alpha_{max} + 5^o; & C_L > C_{L_{max}} \end{cases} \qquad (6-28)$$

and $C_{LS} = C_L (\alpha - \alpha_{Lo} - 2\Delta\alpha_{max})$

The prediction of $C_{L_{max}}$ and $\Delta\alpha_{max}$ for high-aspect-ratio wings is discussed in Section 6.8.

6.7 NONLINEAR LIFT OF LOW-ASPECT-RATIO WINGS

The subsonic characteristic of a low-aspect-ratio wing is illustrated in the sketch. The total lift is equal to the potential lift plus the vortex-induced lift from the leading edge and tip of the wing. The equation
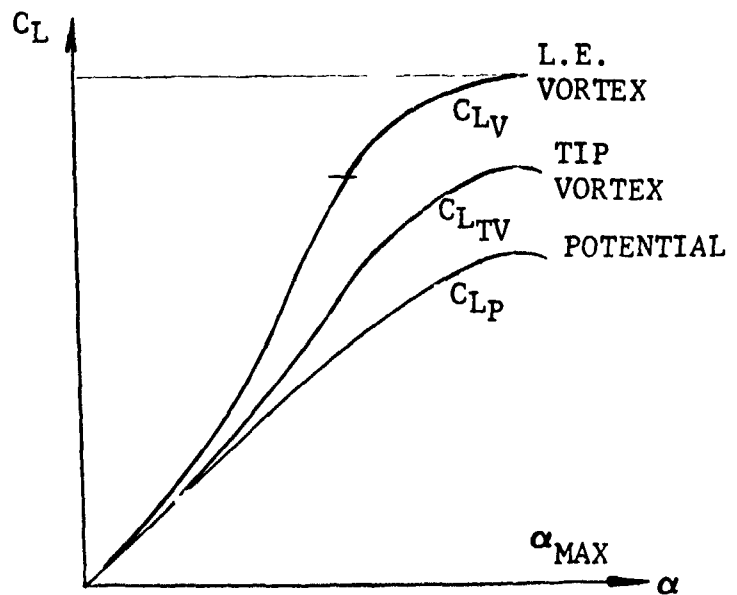
for lift can be expressed as

$$C_L = C_{L_P} + C_{L_V} + C_{L_{T_V}} \tag{6-29}$$

The method of predicting each of these terms is discussed in the following subsections.

6.7.1 Potential-Flow Lift

The potential-flow lift is determined from

$$C_{L_P} = K_p \sin\alpha\cos^2\alpha + C_{L_O} \tag{6-30}$$

where K_p is the lift-curve slope given by small-disturbance potential-flow lifting-surface theory, and the trigonometric terms account for the leading-edge separation effects (Reference 33). The value of K_p is the lift-curbe slope (C_{L_α}), converted to radians, obtained from Equation 6-1. The factor C_{L_O} is the lift at zero angle of attack predicted by

$$C_{L_O} = -C_{L_\alpha} \alpha L_O$$

6.7.2 Leading-Edge Vortex Lift

The leading-edge vortex lift is determined from

$$C_{L_V} = (1-R) \cdot F_{VB} \cdot K_V \sin^2\alpha \cos\alpha \tag{6-31}$$

In this equation, developed in Reference 34, the sharp-leading-edge suction analogy of Polhamus is modified to account for round-leading-edge and vortex-breakdown effects.

In Figure 6-6 (taken from Reference 35) the theoretical variation of the vortex lift factor K_V with aspect ratio and cutout factor is shown. The factor F_{VB} (shown in Figure 6-7 is a vortex-breakdown factor, which was obtained from the ratio of experimental data to theoretical for sharp-leading-edge delta wings. The factor R in Equation 6-31 is a leading-edge suction parameter (Reference 36). For a sharp leading edge, the suction parameter is near zero; for a rounded leading edge, the suction parameter is near unity at low alphas. The variation of R versus α is shown in Figure 6-8 as a function of thickness ratio.

$$f_M = \sqrt{\frac{1+\tan^2\Lambda_{LE}}{\beta^2+\tan^2\Lambda_{LE}}}$$
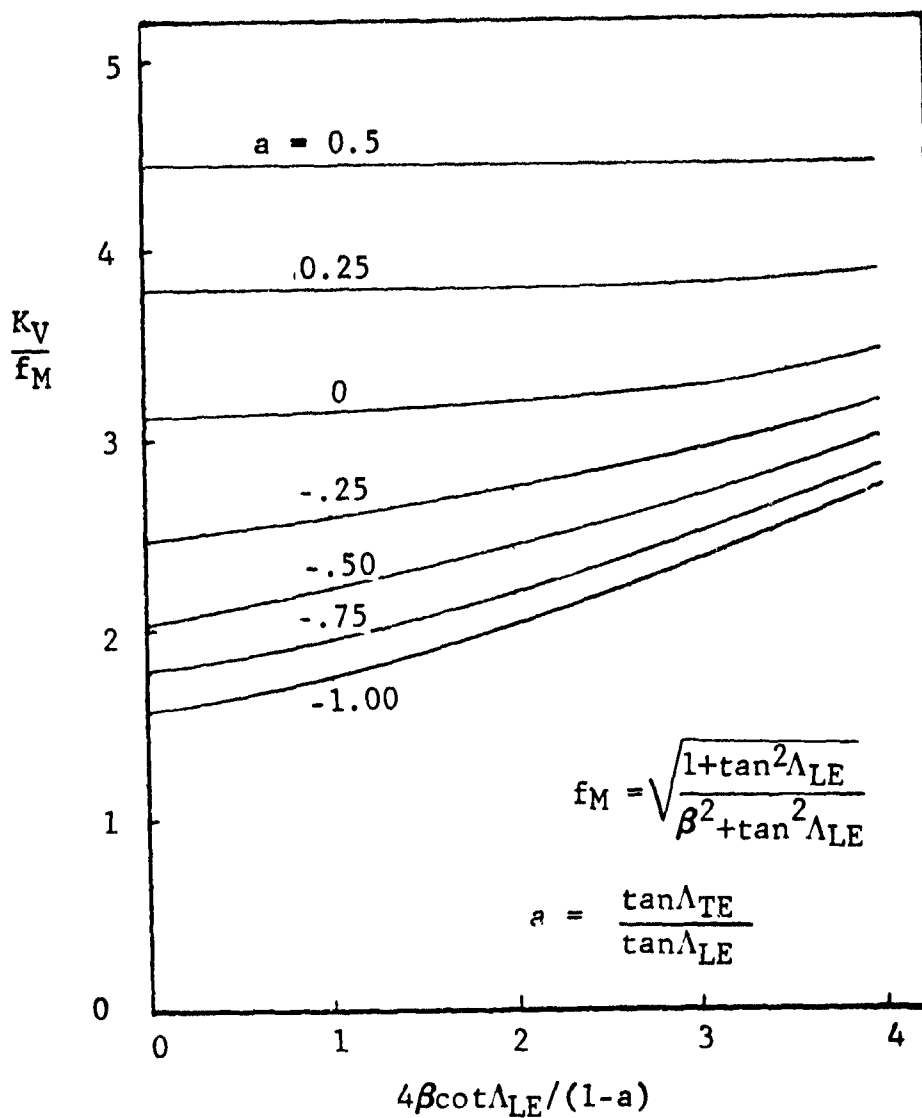
$$a = \frac{\tan\Lambda_{TE}}{\tan\Lambda_{LE}}$$

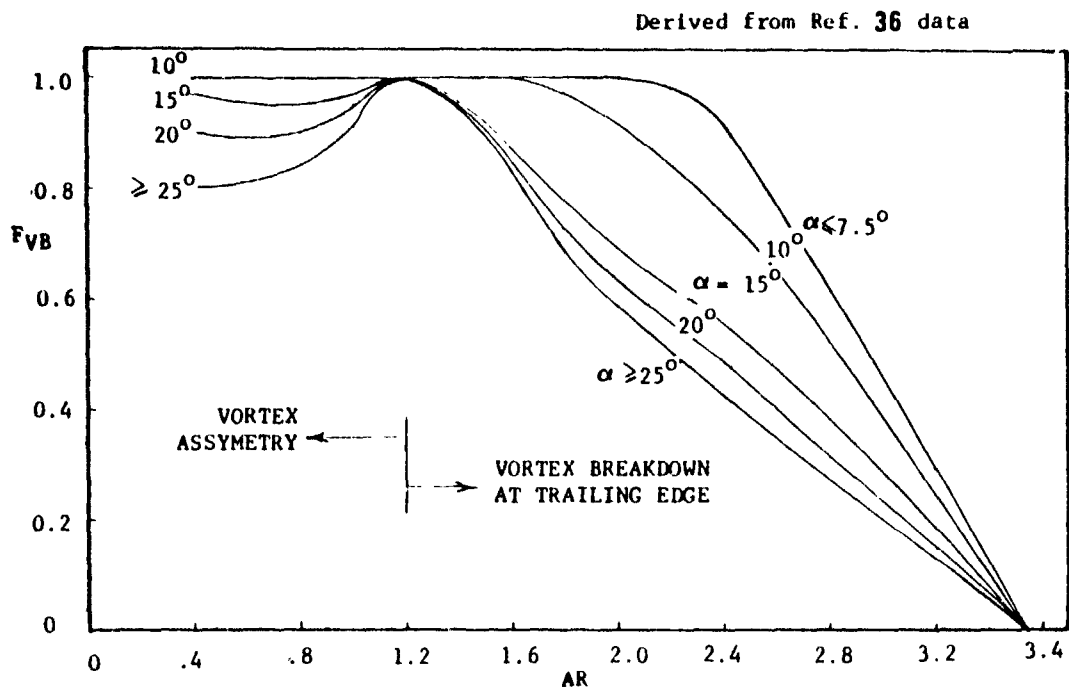Figure 6-6   Variation of Vortex-Lift Constant with Planform Parameters

Figure 6-7 Variation of Vortex Breakdown Factor with Aspect Ratio and
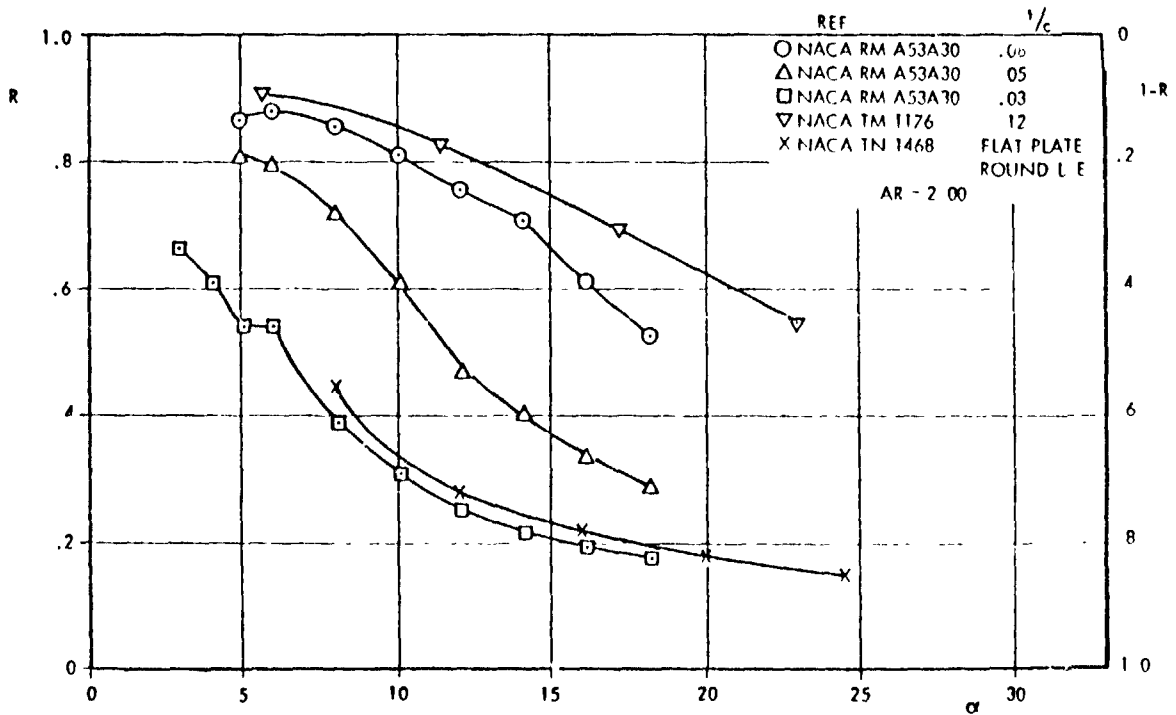Angle of Attack

Figure 6-8 Experimental Variation of Leading-Edg
Suction Parameter R with Angle of Att
For Round-Leading-Edge Delta Wings

6.7.3 Tip-Vortex Lift

For wings having a tip chord greater than zero, a tip vortex forms that induces an additional lift contribution on the wing. At low angles of attack the flow around the wing leading edge and tip is attached, and a vortex sheet is formed at the trailing edge (Figure 6-9a). At slightly higher angles of attack (Figure 6-9b), the flow possibly will make the turn around the leading edge of the wing without separating, but the flow around the tip separates. In this stage, the flow forms a vortex sheet consisting of a horizontal part originating from the trailing edge and two vertical sheets attached to it originating from the two sides of the wing. Kuchemann (Reference 37) noted that a spanwise cross-section through the vortex sheet has the same shape as that obtained behind a wing with end plates. The height of the "end-plate vortex" or tip vortex is approximated by

$$h/b = \frac{\alpha}{2} \frac{C_T}{\bar{c}} \frac{1}{AR} \tag{6-32}$$

where C_T is the tip chord. With the height of the tip vortex known, the incremental tip-vortex lift can be expressed as

$$C_{L_{T_V}} = \left[\frac{Z+\sqrt{1+Z^2}}{xZ+\sqrt{1+(xZ)^2}} - 1 \right] K_p \sin\alpha \tag{6-33}$$

where

$$Z = 2 \cos\Lambda_c/2 /AR$$

$$x = 1.0014-1.969(h/b)+3.0021(h/b)^2-2.0072(h/b)^3 \tag{6-34}$$

Equation 6-33 was derived (Reference 37) by modifying the Helmbold lift equation, where the effect of the end-plates are expressed as a factor 1/x to the aspect ratio. Equation 6-34 is a curve fit of the end-plate effect shown in Figure III.A.4-1 of Reference 6 .

It can be seen from Equation 6-32 that the end-plate effect becomes smaller with increasing aspect ratio. This explains why the end-plate effect of the tip vortex has rarely been noticed for wings of moderate and large aspect ratios, although it always existed. The tip-vortex method in Reference 37 gives good agreement with experimental data for unswept rectangular wings ranging in aspect ratio from 0.5 to 2.0. It is stated in Reference 37 that the end-plate analogy can be used for straight or swept wings.
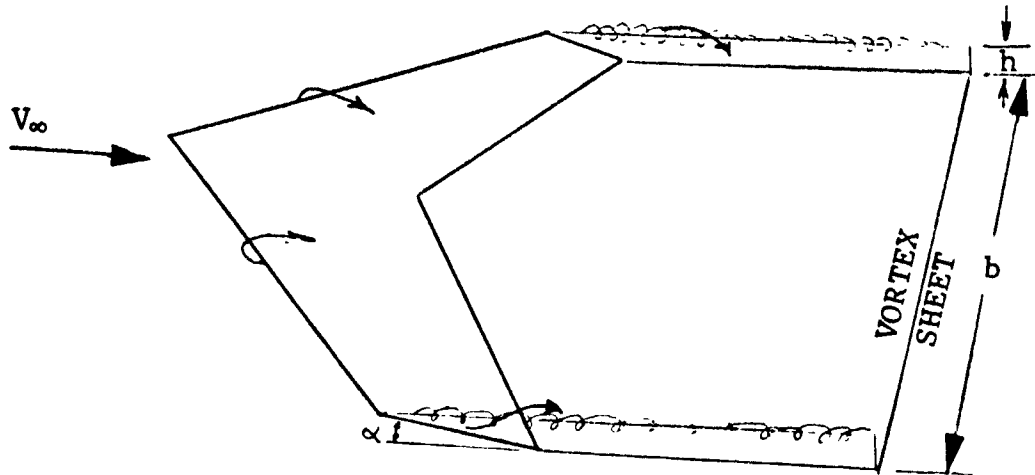
6-9(b)   moderate angle of attack
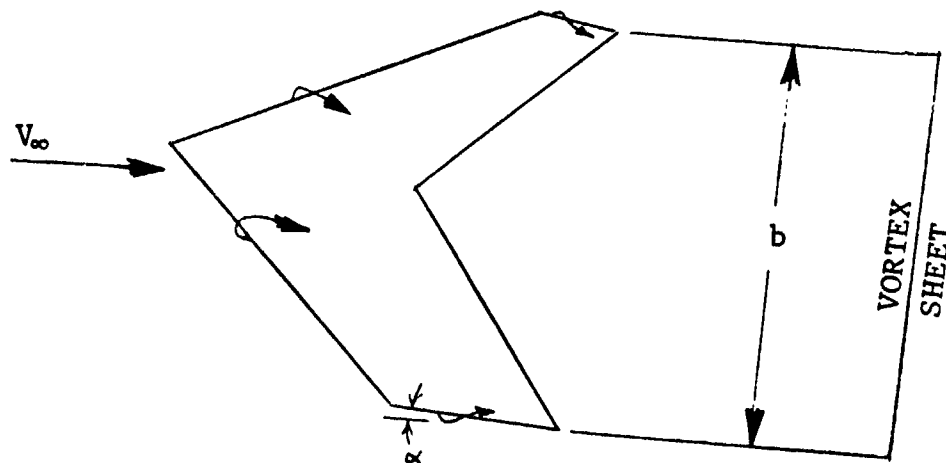
6-9(a)   low angle of attack

Figure 6-9 Sketch of Possible Flow Patterns

94

The nonlinear lift calculated by Equation 6-29 is limited by the maximum lift coefficient, $C_{L_{max}}$, of the wing. The value of $C_{L_{max}}$ and the angle at which maximum lift occurs, α_{max}, are predicted by the low-aspect-ratio method given in Section 6.9. The leading-edge vortex is then limited by the condition

$$C_{L_V} \leq C_{L_{MAX}} - (C_{L_P})_{MAX} - (C_{L_{TV}})_{MAX} \tag{6-35}$$

where $(C_{LP})_{MAX}$ and $(C_{LTV})_{MAX}$ are the values calculated for the potential lift and the tip-vortex lift at the maximum-lift angle of attack. If $(C_{LP})_{MAX} > (C_L)_{MAX}$, it is assumed that the leading-edge and tip vortices are too weak to add much lift to the wing, and the high-aspect-ratio method discussed in Section 6.6 is then used to predict the lift up to stall.

Results of applying the nonlinear lift prediction procedure are shown in Figures 6-10 through 6-13. The data were taken from Reference 38, which reports on a test of a series of clipped delta wings. The program results are shown as the solid lines for the complete lift and as dashed lines for the initial value of the lift-curve slope, C_{L_α}. In general, the test results and program results compare well and indicate a substantial amount of the lift is due to the vortices.

6.8   NONLINEAR LIFT OF CRANKED WINGS

The method available in the ATT procedure for predicting the subsonic lift variation of cranked wings is based on the technique presented in Reference 11. This method assumes that as the outboard panel of a cranked wing experiences stall, the inboard panel still continues to lift. This behavior is believed to be caused by the influence of the leading-edge vortex of the inboard panel. Consequently, the flow field is similar to that of a low-aspect-ratio delta wing with leading-edge separation.

This method employs the results of a data correlation that provides a technique for determining the nonlinear lift of double-delta wings. It is hypothesized that the nonlinear lift of a cranked wing should be similar to that of a double-delta wing. The nonlinear-lift curve construction technique for cranked wings is shown in Figure 6-12.

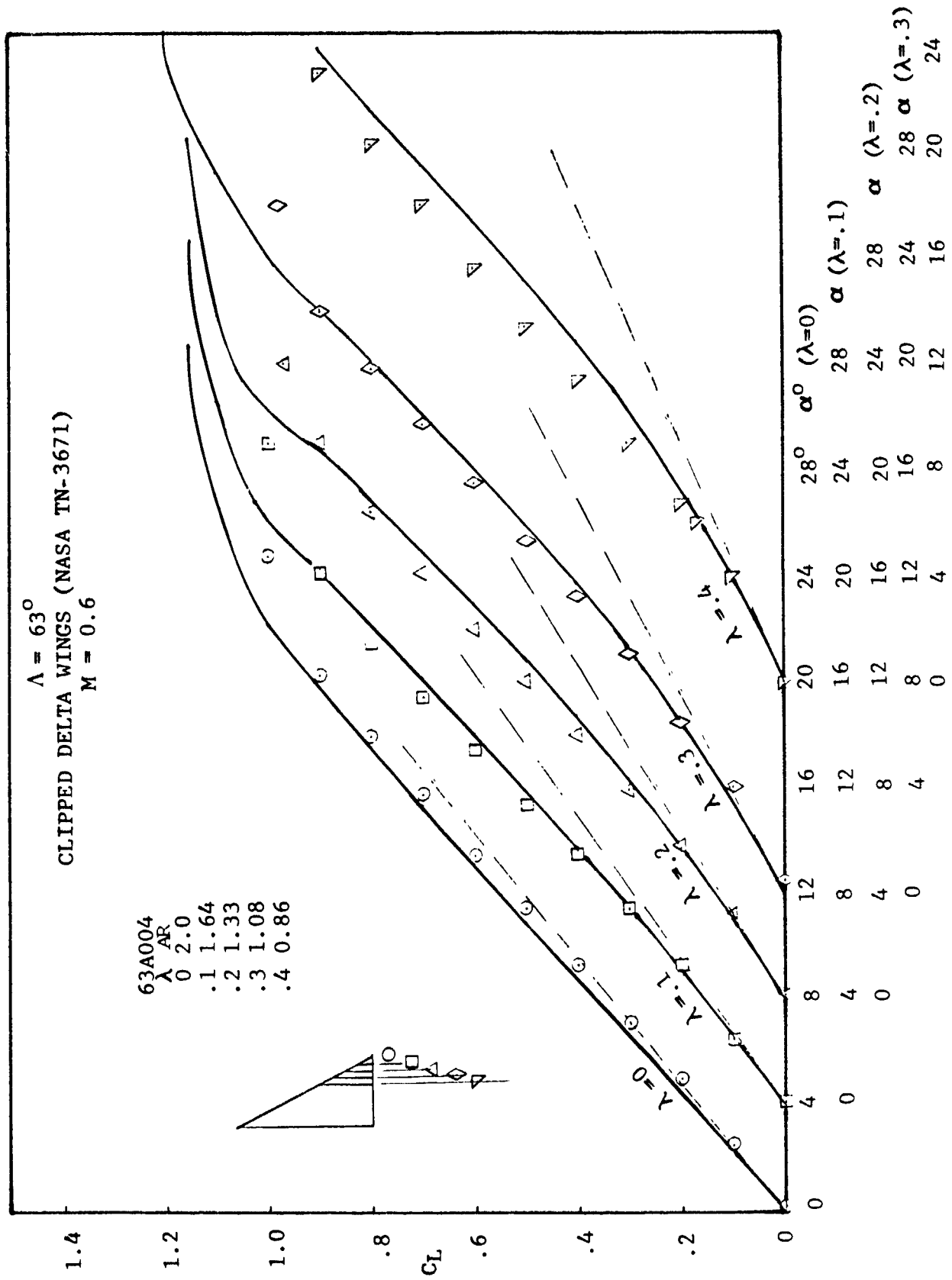Figure 6-10   Comparison of Program Results with Experi-
mental Data, $\Lambda = 63°$

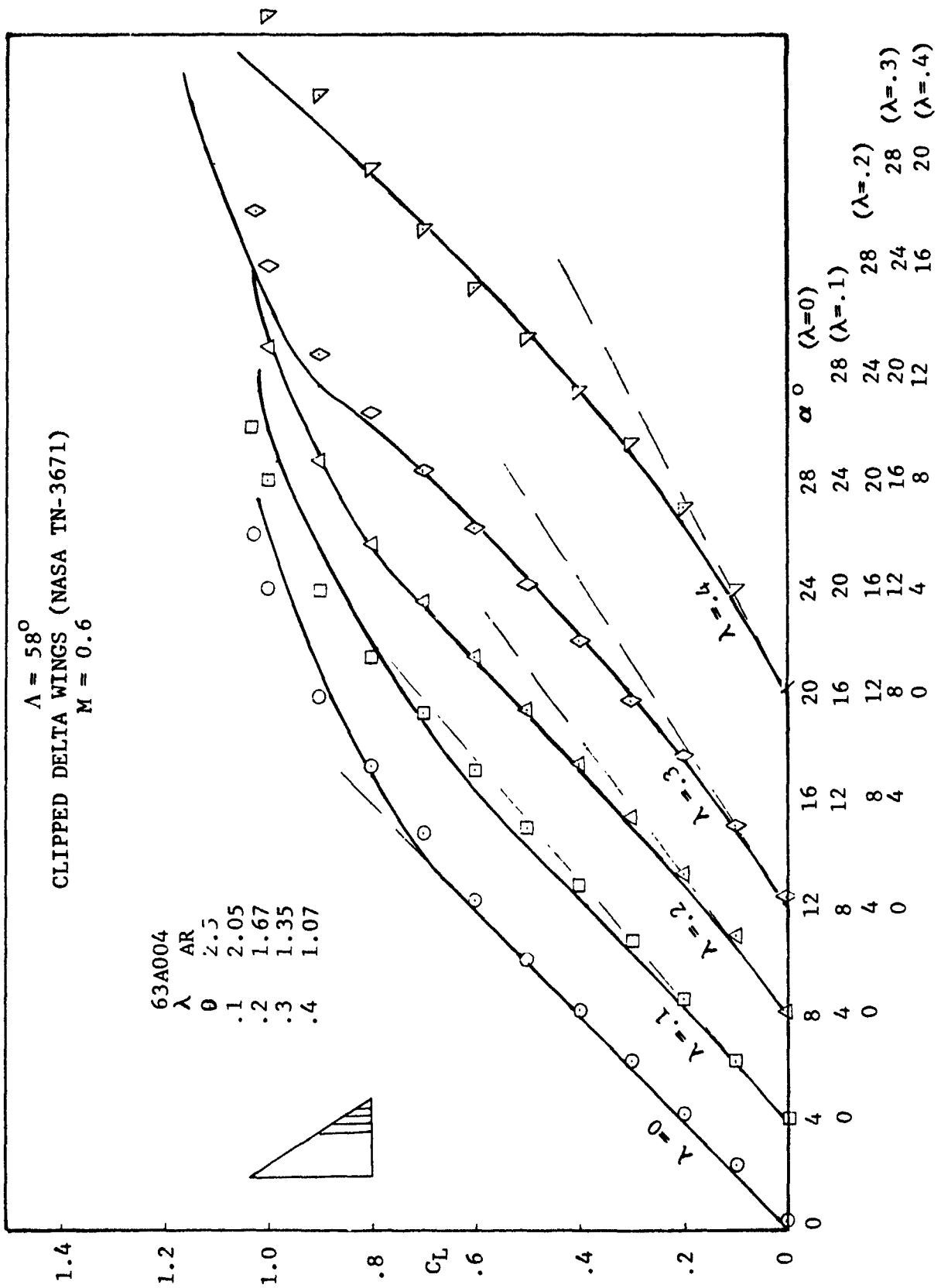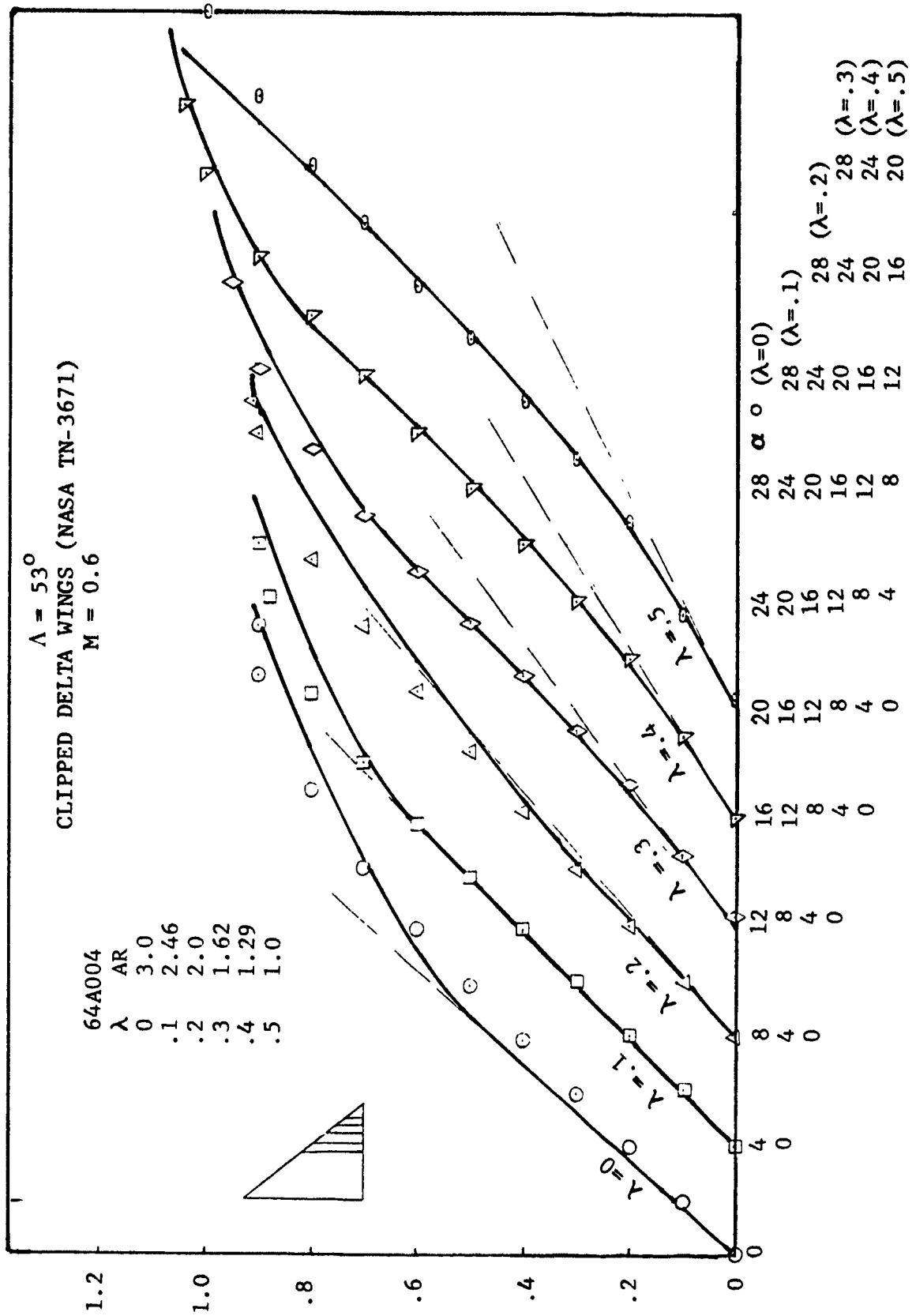Figure 6-11 Comparison of Program Results with Experimental Data, Λ = 58°

Figure 6-12 Comparison of Program Results with Experimental Data, $\Lambda = 53^\circ$

98
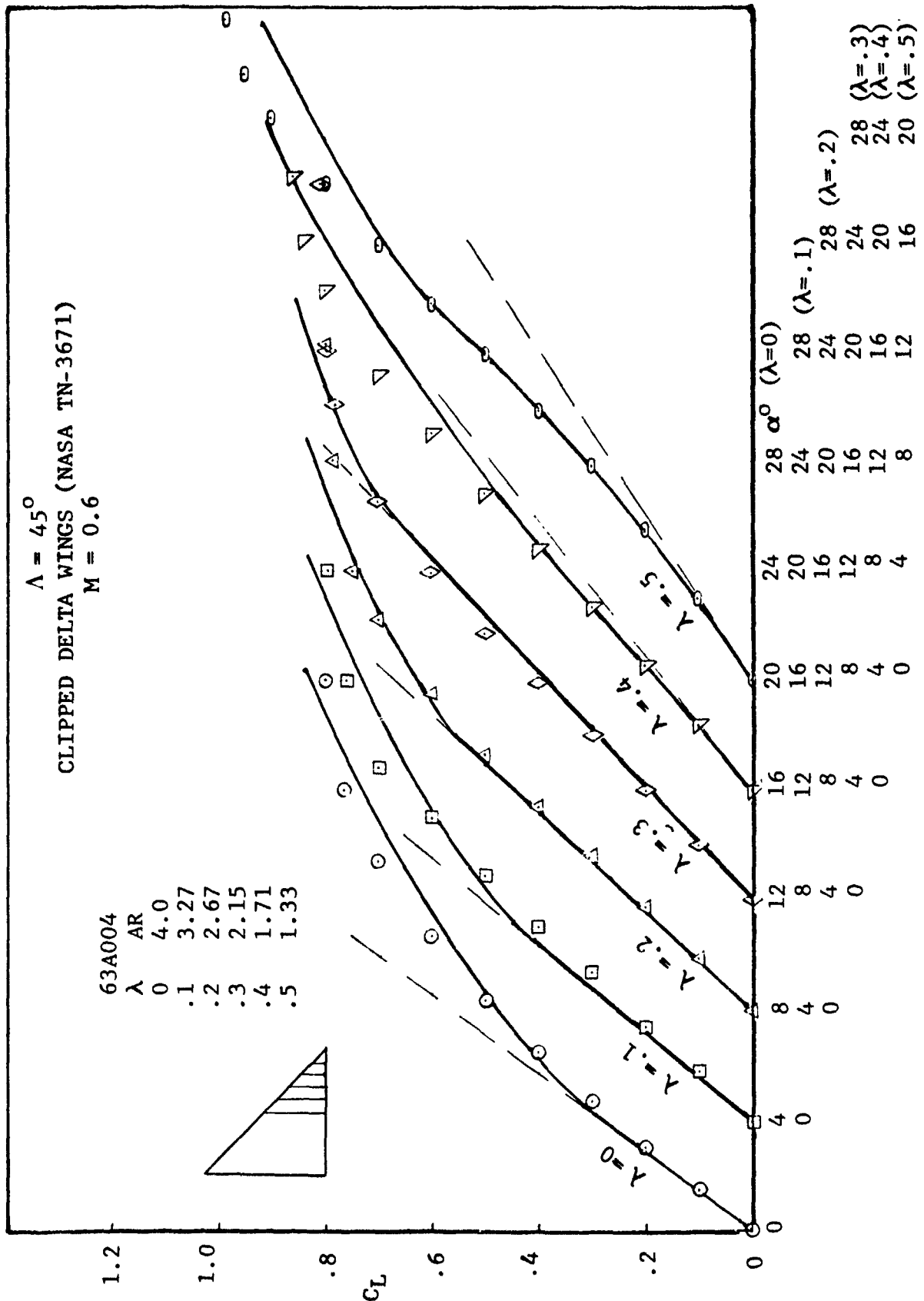
Figure 6-13 Comparison of Program Results with Experimental Data, $\Lambda = 45°$
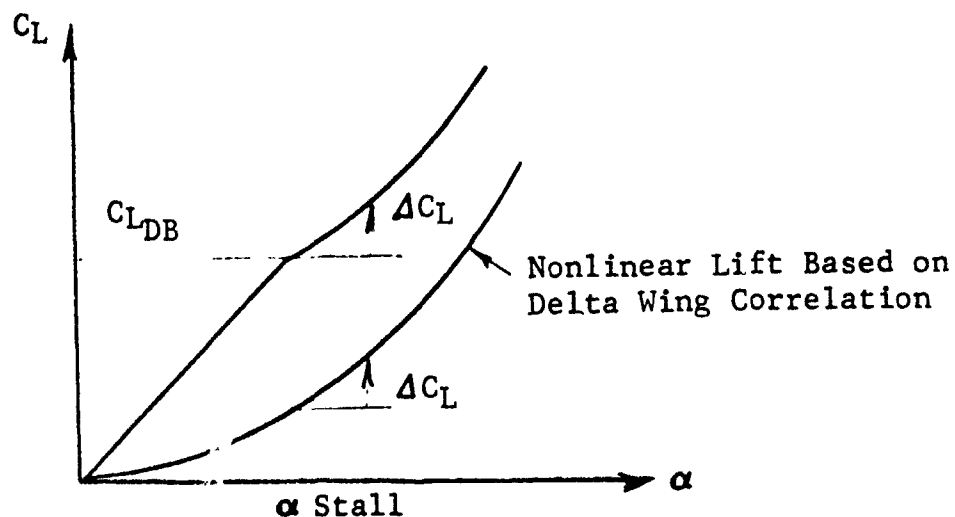
Figure 6-14   Construction of Nonlinear Lift Curve for
Cranked Wings

Except for some slight refairing of the data correlation curves to account for aspect ratios of less than 1.0, the method employed in the program is essentially the same as that presented in Reference 11. The nonlinear angle of attack for a given C_L is calculated from

$$\alpha = \left[\frac{1}{a} \frac{C_L}{C_{L_\alpha}} \frac{A_i}{\eta B} \right]^{1/n} \qquad (6\text{-}36)$$

where

C_{L_α} is the linear lift-curve slope (including outboard panel).

A_i is the aspect ratio of the inboard panel, as determined in Figure 6-15.

Figure 6-15 Definition of Cranked-Wing Planform
for Calculation of Angle of Attack
in Nonlinear Lift Range

Figure 6-16 Parameters Used in Calculation of Angle of
Attack in Nonlinear Lift Range

η_B is the nondimensional spanwise ordinate for the break point in the cranked wing.

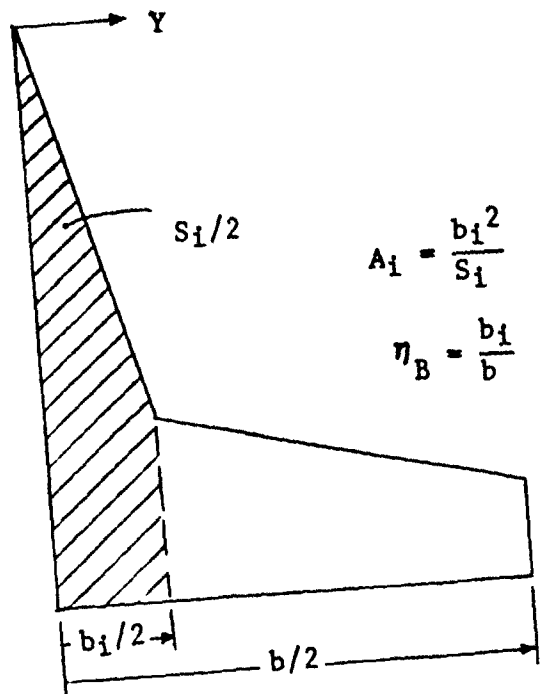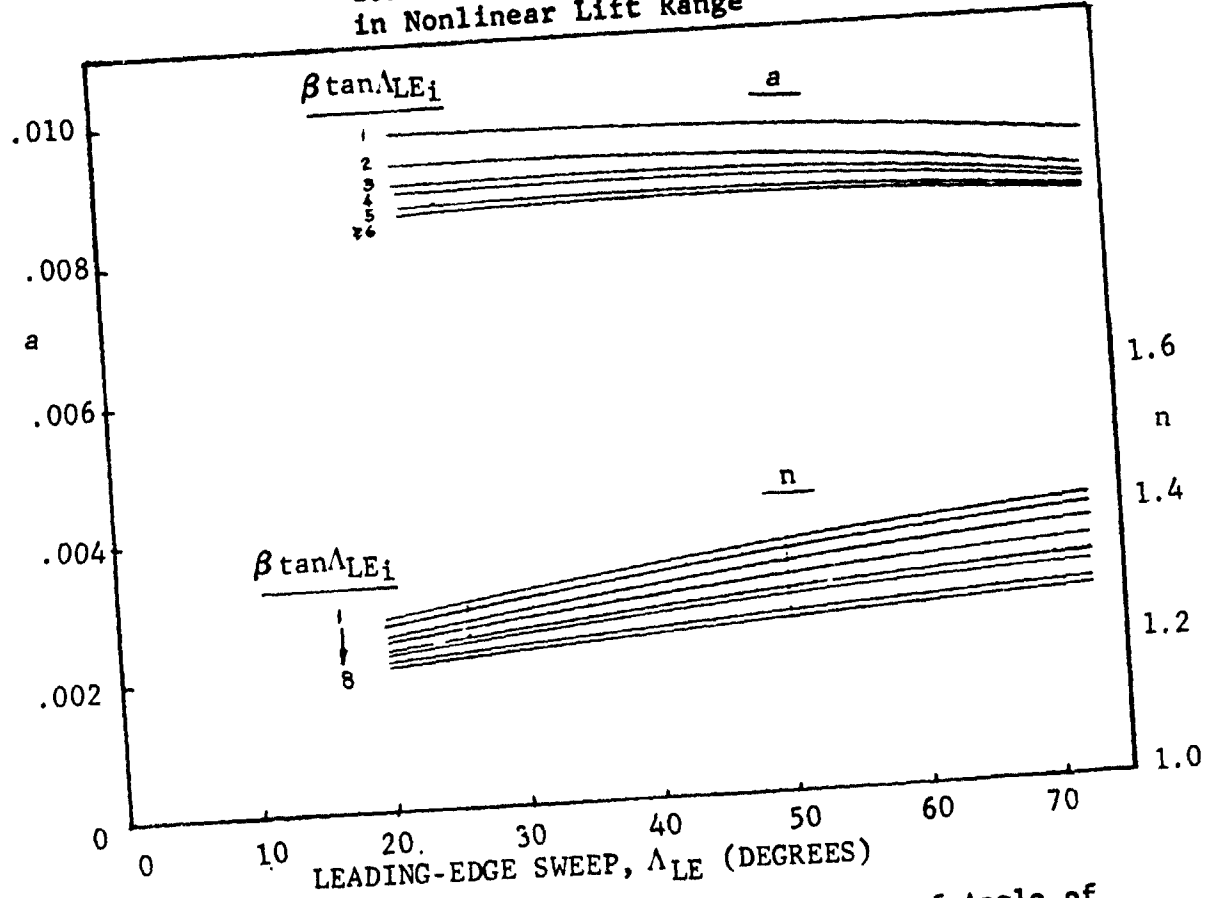a,n are correlation constants (shown in Figure 6-16), derived by modifying the Reference 11 method.

In the program it is assumed that α_{stall} is the angle of attack corresponding to $C_{L_{DB}}$, as shown in Figure 4-1 of Section 4. The accuracy of the nonlinear angle-of-attack prediction technique is, of course, strongly dependent on knowing α_{stall}.

6.9 MAXIMUM-LIFT COEFFICIENT

The method used in the AAT program to estimate the maximum lift and angle of attack for maximum lift is based on the DATCOM method for both the low- and high-aspect-ratio wings (Reference 2). The maximum lift of high-aspect-ratio wings at subsonic speeds is directly related to the maximum lift of the wing airfoil sections. The wing planform shape is a secondary influence on the maximum lift obtainable. However, for low-aspect-ratio wings, the wing planform is the primary effect on maximum lift, while sectional characteristics are secondary. The program uses the criteria established in the DATCOM method by the equation

$$AR_{LOW} = \frac{3}{(C_1+1)\cos\Lambda_{LE}} \qquad (6-37)$$

where C_1 is a function of taper ratio, as given in Figure 6-22. If $AR > AR_{LOW}$, the high-aspect-ratio method is used, and if $AR \leq AR_{LOW}$, the low-aspect-ratio method is used. These two methods are described in the following subsections.

6.9.1 High-Aspect-Ratio Method

The DATCOM method is an empirically derived method based on experimental correlations of high-aspect-ratio, untwisted, and constant-section wings. The equations for maximum lift and the angle of maximum lift are as follows:

$$C_{L_{MAX}} = \left(\frac{C_{L_{MAX}}}{C_{\ell_{MAX}}}\right) C_{\ell_{MAX}} + \Delta C_{L_{MAX}} \qquad (6-38)$$

102

$$\alpha_{MAX} = \left(\frac{C_{LMAX}}{C_{L_\alpha}}\right) + \alpha_{L_0} + \Delta\alpha_{MAX} \tag{6-39}$$

The first term in Equation 6-38 is the maximum lift coefficient at M=0.2; the second term is the lift increment to be added for Mach numbers greater than 0.2.

The factor $(C_{LMAX}/C_{\ell MAX})$ is computed by a curve fit of the curves in Figure 4.1.3.4-14a in the DATCOM given by

$$\frac{C_{LMAX}}{C_{\ell MAX}} = A - B \, \Delta y' \tag{6-40}$$

where

$$\Delta y' = \begin{cases} 0; & \Delta y < 1.4 \\ \Delta y - 1.4; & 1.4 \leq \Delta y \leq 2.5 \\ 1.1; & \Delta y > 2.5 \end{cases}$$

and the terms A and B are plotted in Figure 6-17 as a function of sweep. (Δy is defined by Equation 2-42.)

The increment to C_{LMAX} due to Mach number is computed from a curve fit of the curves of Figure 4.1.3.4-15 in the DATCOM, given by

$$C_{LMAX} = C + (D-C)\left(\frac{\Lambda_{LE}}{60}\right) \tag{6-41}$$

where the terms C and D are plotted in Figure 6-18 as a function of Δy and Mach number.

The section maximum lift coefficient at M=0.2, $C_{\ell MAX}$, is computed from

$$C_{\ell MAX} = (C_{\ell MAX})_{Base} + \Delta C_{\ell MAX} \tag{6-42}$$

where $(C_{\ell MAX})_{Base}$ and $\Delta C_{\ell MAX}$ are shown plotted in Figures 6-19 and 6-20 as a function of the sharpness factor, maximum-thickness location, and camber.
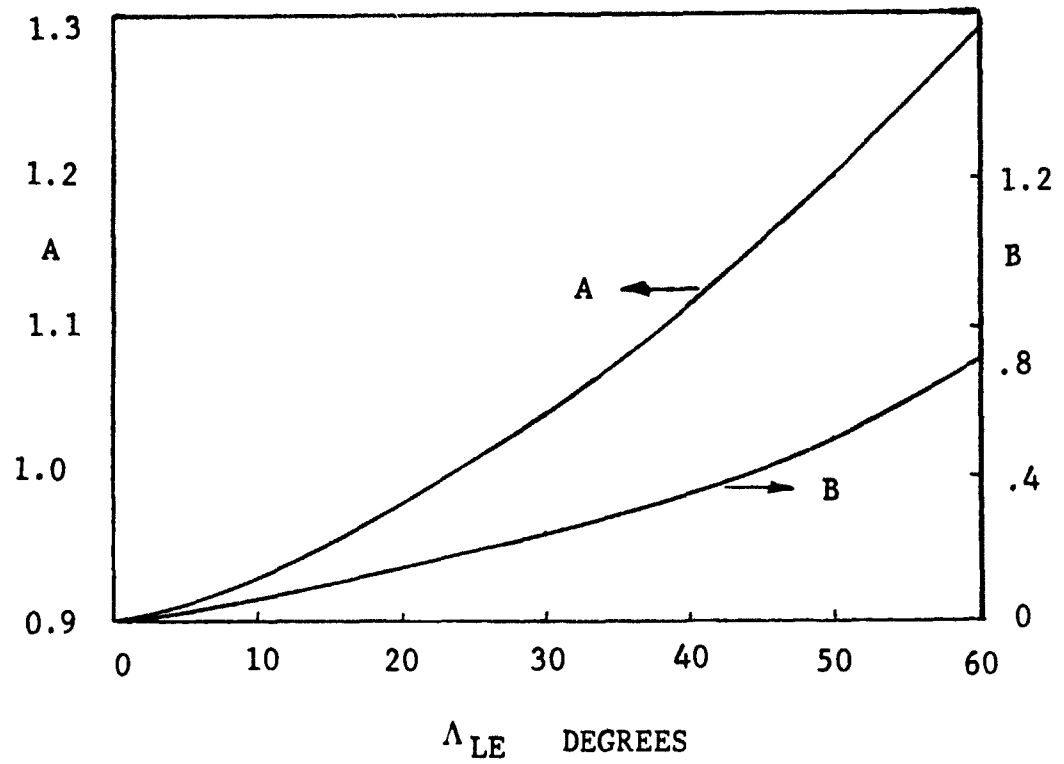
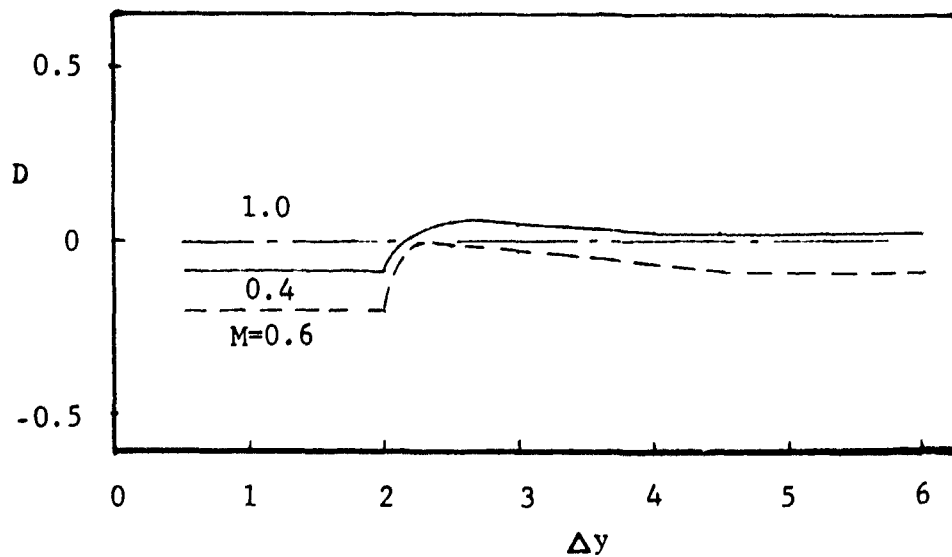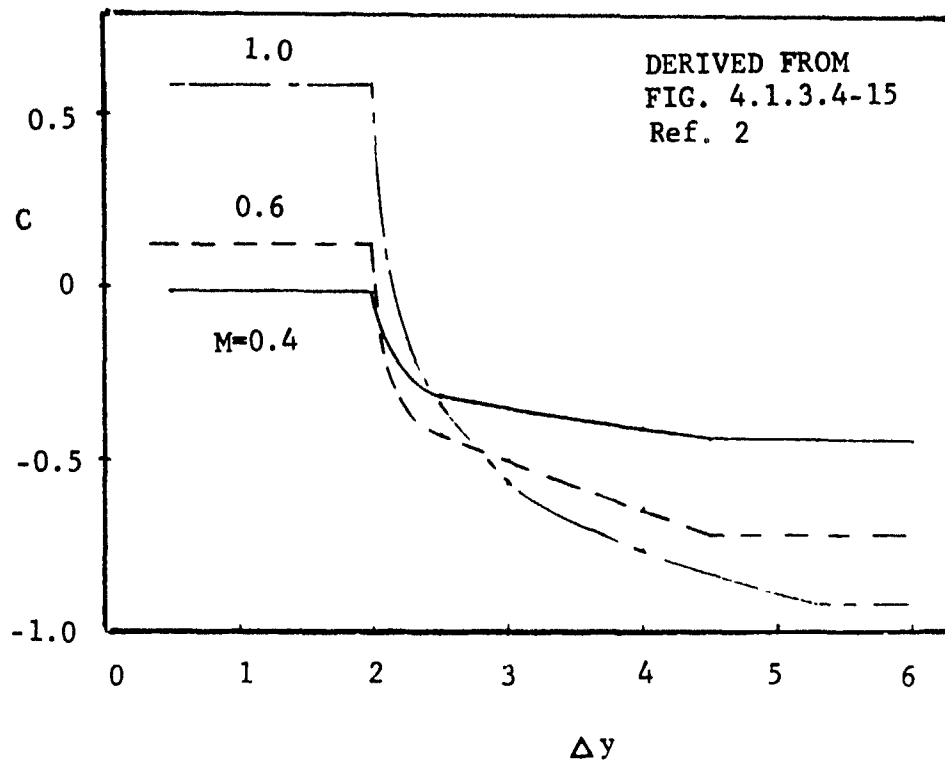Figure 6-17   Factors for Determining Subsonic Maximum Lift

Figure 6-18 Factors for Determining Mach Number Correction for Maximum Lift
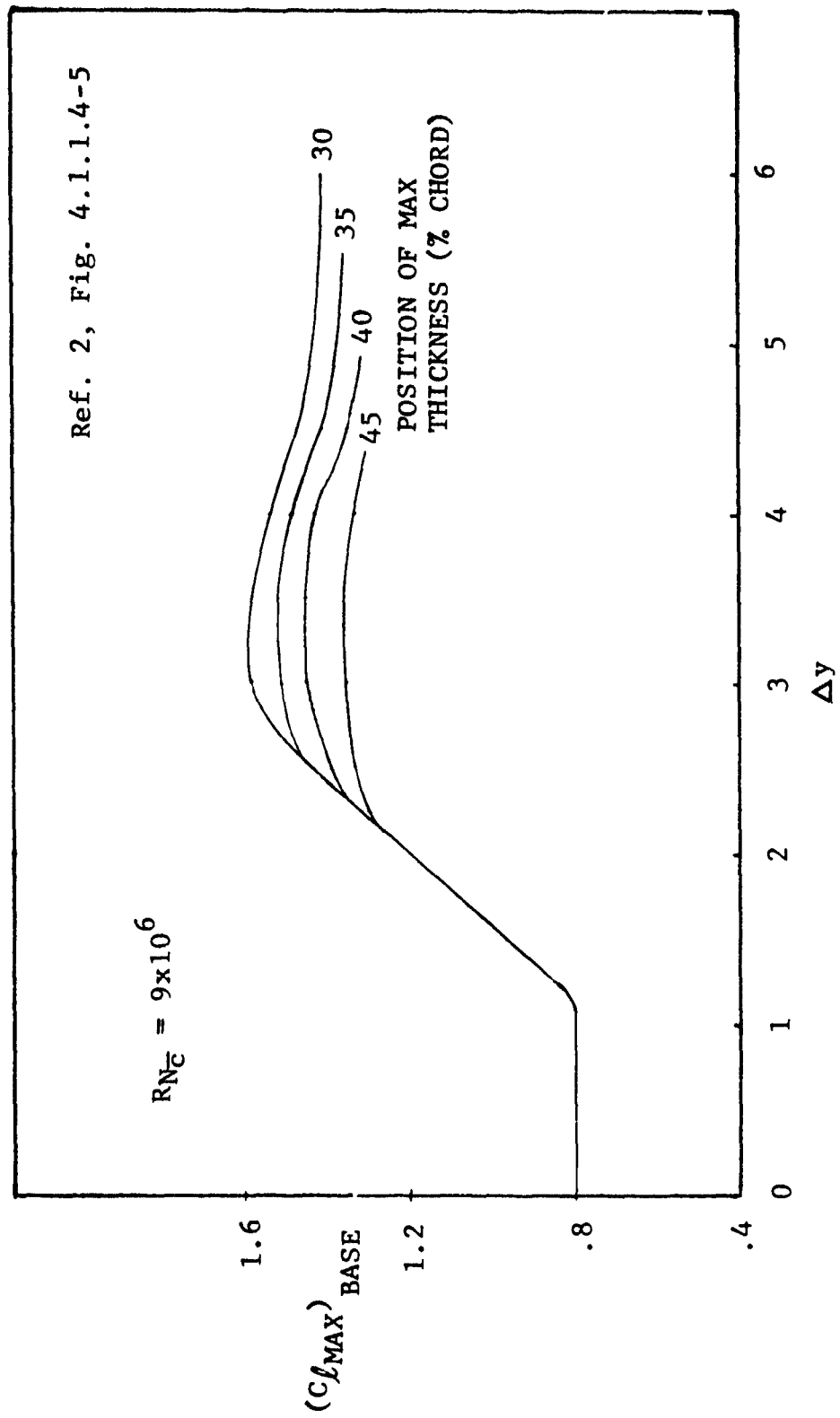
Figure 6-19   Section Maximum Lift for Uncambered Air-
foils

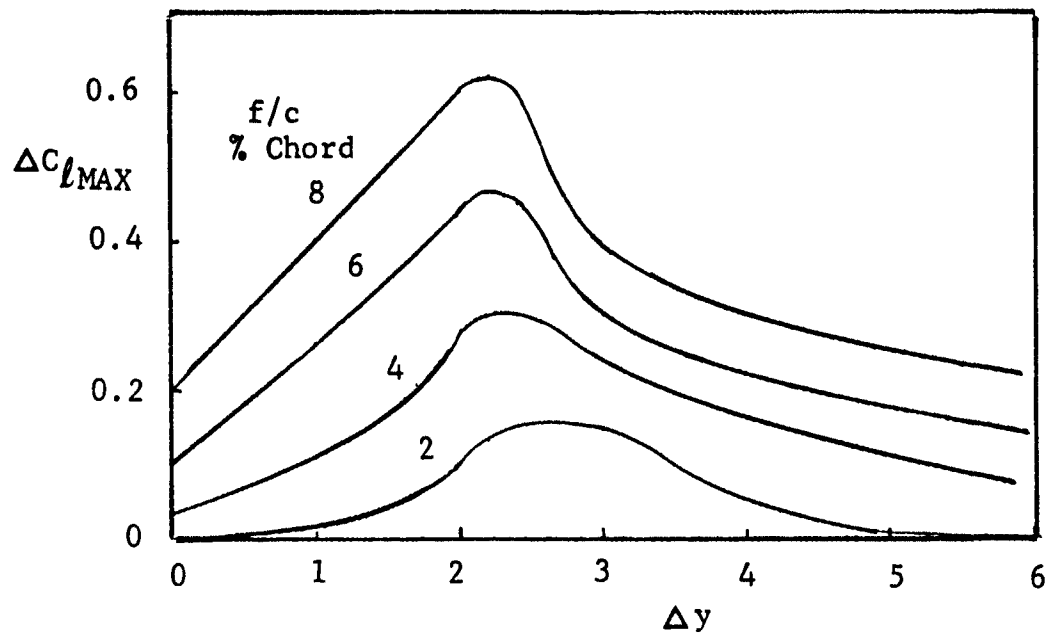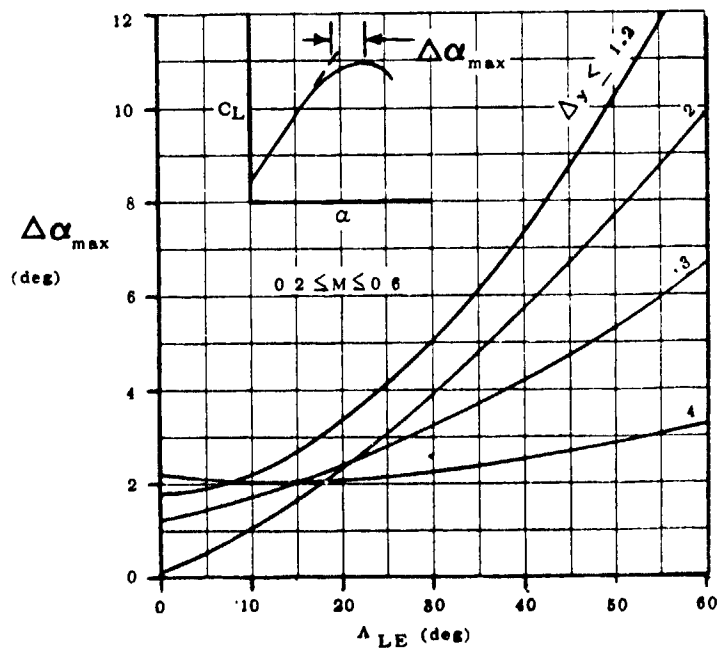Figure 6-20   Effect of Airfoil Camber on Maximum Lift

Figure 6-21   Angle-of-Attack Increment for Subsonic Maximum
Lift of High-Aspect-Ratio Wings

107

The angle-of-attack increment for maximum lift, α_{MAX}, is obtained from Figure 6-21, which is taken from Section 4.1.3.4 in the DATCOM.

6.9.2 Low-Aspect-Ratio Method

The empirical equations in DATCOM for estimating subsonic maximum lift and angle of attack for untwisted low-aspect-ratio wings are

$$C_{L_{MAX}} = (C_{L_{MAX}})_{Base} + \Delta C_{L_{MAX}} \qquad (6\text{-}43)$$

$$\alpha_{MAX} = (\alpha_{MAX})_{Base} + \Delta \alpha_{MAX} \qquad (6\text{-}44)$$

The base value of $C_{L_{MAX}}$ is obtained from Figure 6-22 if the position of maximum airfoil thickness, X_T, is forward of the 35-percent chord point, and from Figure 6-23 if X_T is aft of the 35-percent chord. The values of $\Delta C_{L_{MAX}}$, C_1, and C_2 are obtained from Figure 6-24, the base α_{MAX} from Figure 6-25, and the value of α_{MAX} from Figure 6-26. (Figures 6-20 through 6-26 are taken from Section 4.1.3.4 of the DATCOM.)

6.9.3 Tail-Lift Contribution to $C_{L_{MAX}}$

Because the horizontal tail usually has a smaller aspect ratio compared to the wing and is in a downwash field that counteracts the effect of angle of attack to some extent, it is assumed that the tail does not stall before the wing. The lift generated by the tail at the angle of attack of wing stall is added to the wing maximum lift coefficient to obtain the configuration maximum lift coefficient. The configuration maximum lift is given by

$$C_{L_{MAX}} = (C_{L_{MAX}})_{Wing} + (\Delta C_{L_{MAX}})_{Tail} \qquad (6\text{-}45)$$

where

$$(\Delta C_{L_{MAX}})_{Tail} = (C_{L_\alpha})_T \cdot 57.3 \sin \alpha_{max} (\cos \alpha_{max})^2$$

The term $(C_{L_\alpha})_T$ is the lift-curve slope of the horizontal tail as determined in Section 6.2.
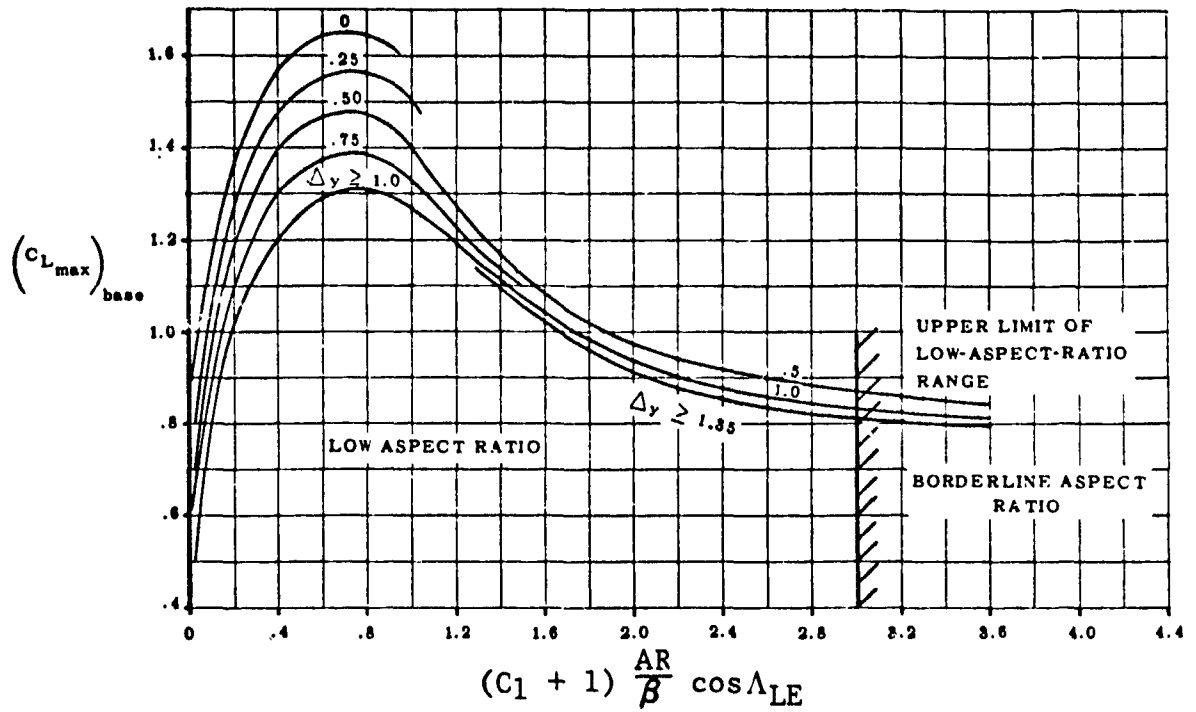
Figure 6-22 Subsonic Maximum Lift of Low-Aspect-Ratio Wings (X_T < 35%)
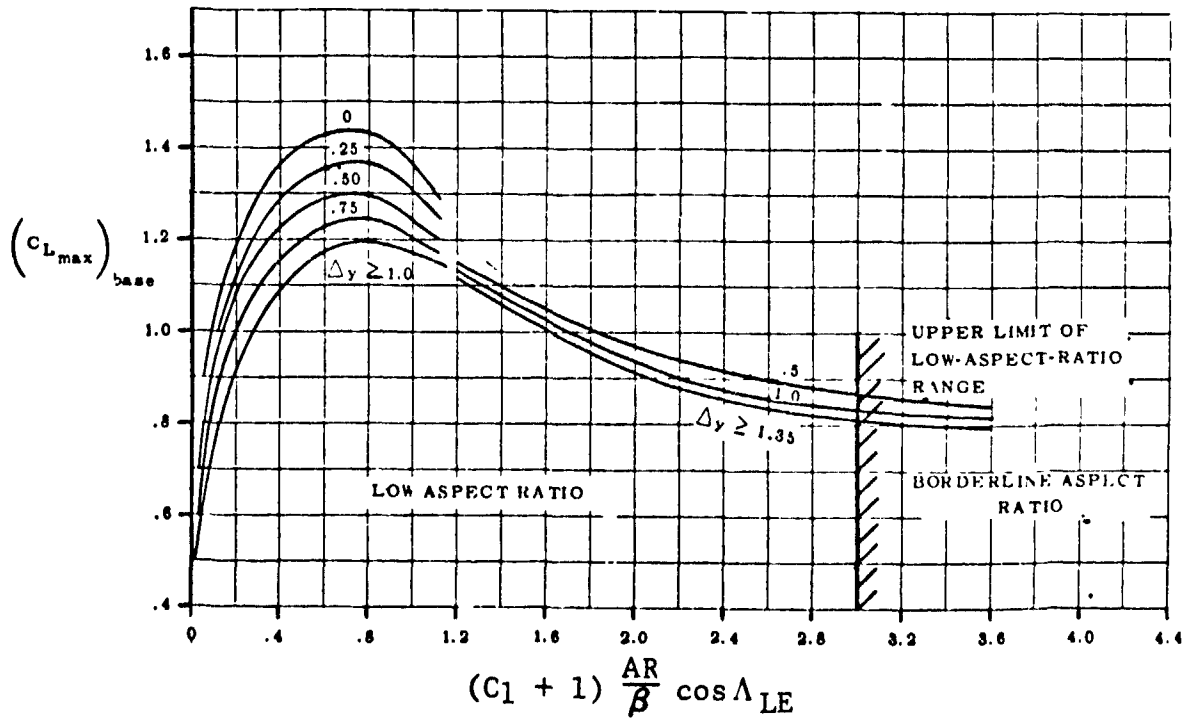

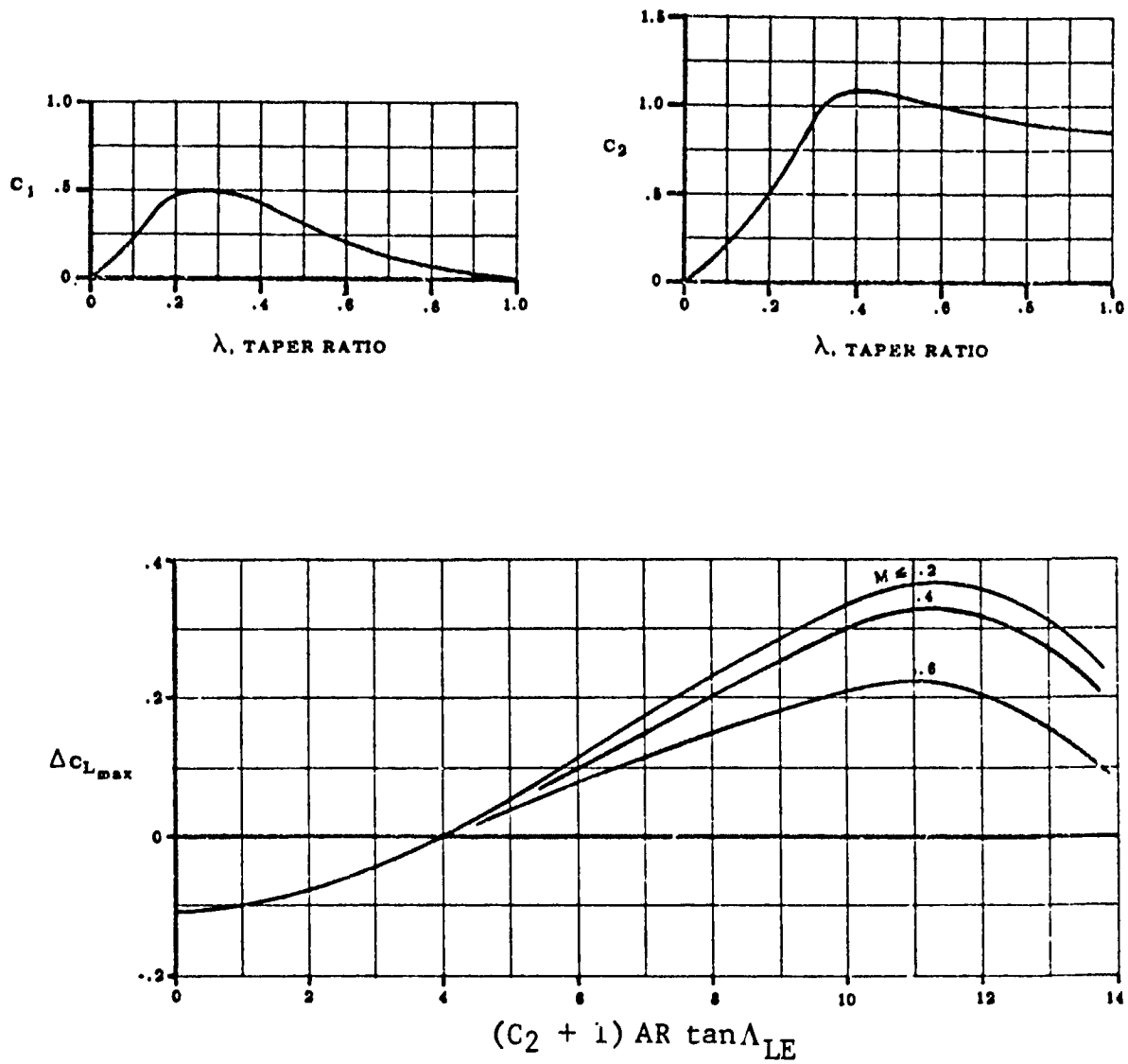Figure 6-23 Subsonic Maximum Lift of Low-Aspect-Ratio Wings (X_T ≥ 35%)

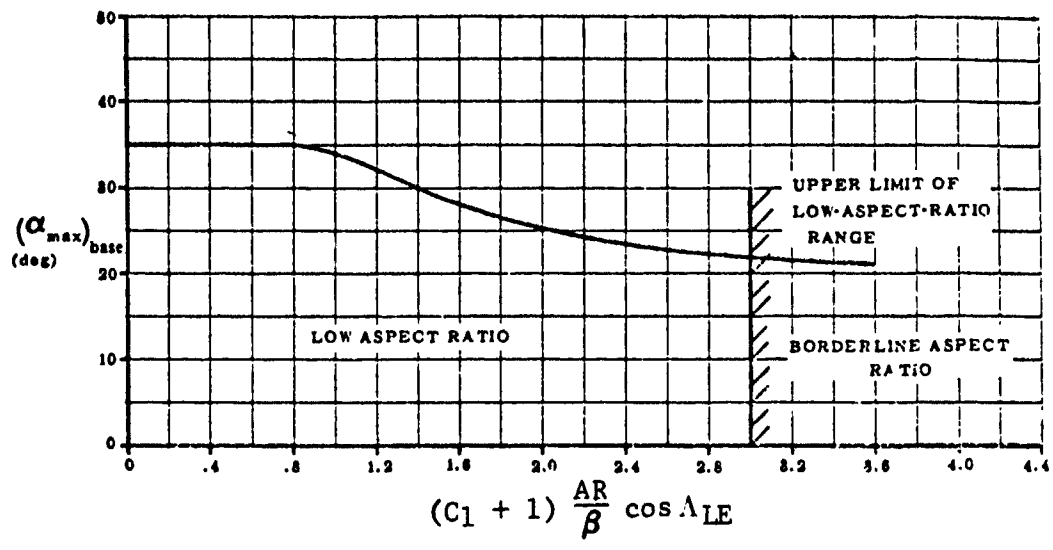Figure 6-24   Mach Number Correction for Low-Aspect-Ratio Maximum Lift

Figure 6-25 Angle of Attack for Subsonic Maximum Lift of Low-Aspect-Ratio Wing Maximum Lift
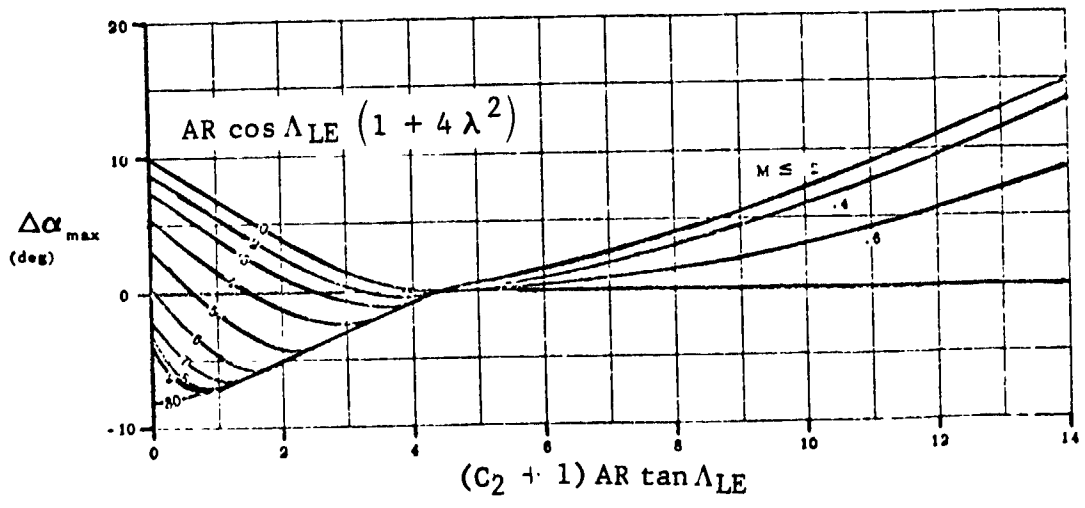

Figure 6-26 Mach Number Correction for Angle of Attack

111

7. MOMENT

The moment of a wing-body-tail configuration can be represented by the equation

$$C_m = C_{m_0} + \left(n - \frac{X_{ac}}{C_{R_e}}\right) \frac{C_{R_e}}{\bar{c}} C_{L_{WB}} - C_{L_{TAIL}} \cdot \ell_{HT}/\bar{c} \qquad (7\text{-}1)$$

where n is the chordwise distance to the moment reference point measured in exposed wing root chord (C_{R_e}), X_{ac}/C_{R_e} is the aerodynamic center location relative to C_{R_e}, and the last term represents the moment contribution of the tail lift times the moment arm ℓ_{HT}, determined from Equation (2-15).

The following subsections discuss the method used to predict the elements in Equation 7-1 along with a method of determining trimmed lift curves and polars.

7.1 ZERO-LIFT MOMENT

The method of predicting the zero-lift pitching moment for a wing-body configuration considers only the effect of the wing on C_{m_0} and does not include the effect of an asymmetrical fuselage or the effects of stores and nacelles located near the wing. However, the C_{m_0} prediction method in the AAT computer code can be adjusted by input so as to match the test data C_{m_0} on a similar configuration.

The subsonic zero-lift pitching moment for wings with linear twist, up to the critical Mach number, is given in the DATCOM as

$$C_{m_0} = \left[(C_{m_0})_{\tau=0} + \left(\frac{\Delta C_{m_0}}{\tau}\right)\tau \right] \frac{1 + 5.9(t/c)M^5}{\sqrt{1 - M^2 \cos^2 \Lambda_{c/4}}} \qquad (7\text{-}2)$$

where $(C_{m_0})_{\tau=0}$ is the C_{m_0} of an untwisted wing, and $(\Delta C_{m_0}/\tau)$ is the change in wing zero-lift pitching moment due to a unit change in wing twist, τ. The parameter $(\Delta C_{m_0}/\tau)$ was obtained from lifting-line theory and is shown in Figure 7-1.
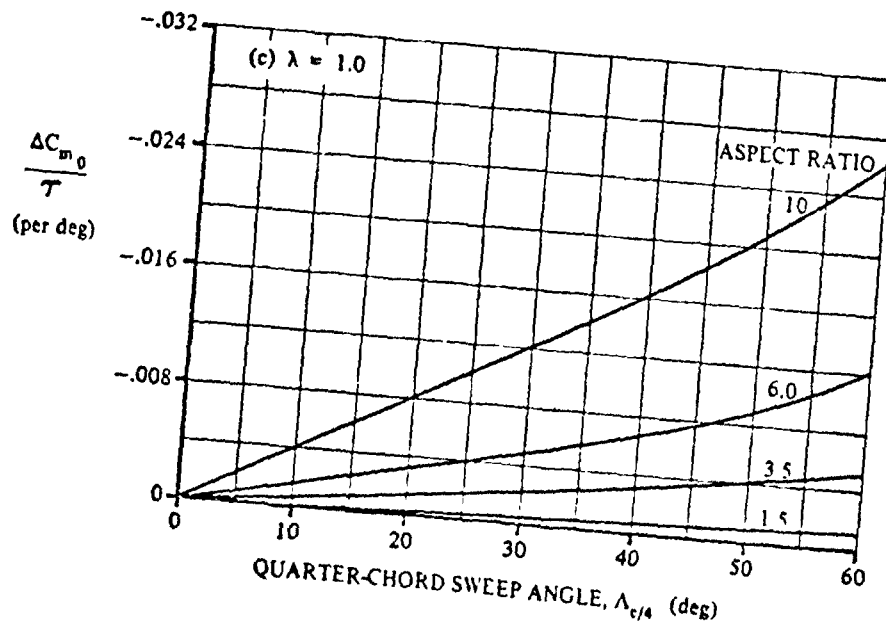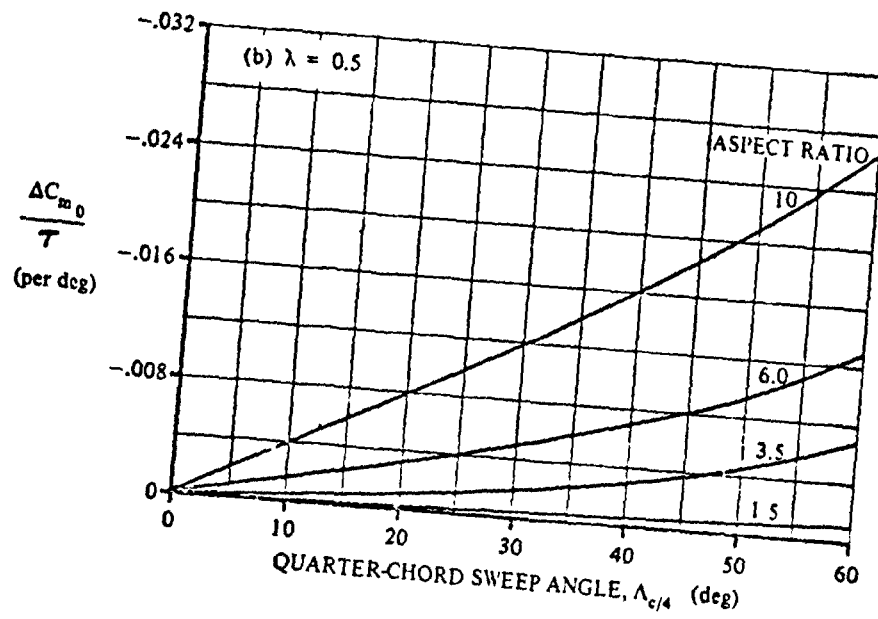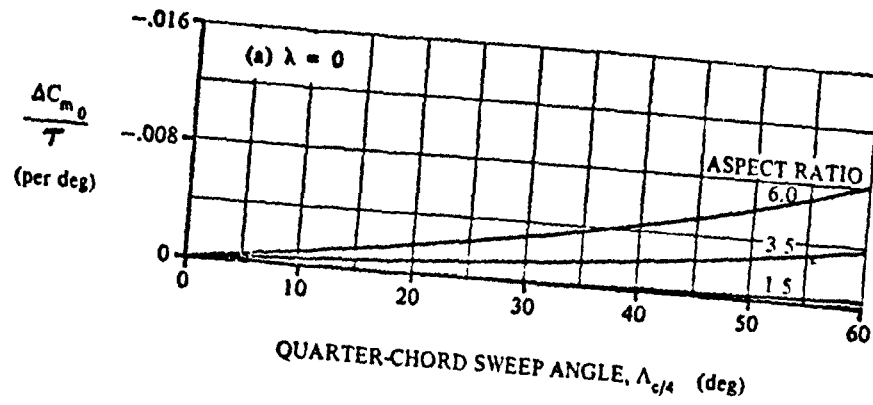
Figure 7-1   Effect of Linear Twist on the Wing Zero-Lift
Pitching Moment

113

The C_{m_0} of an untwisted wing is obtained from

$$(C_{m_0})_{\tau=0} = \frac{AR\cos^2 \Lambda_{c/4}}{AR+2\cos \Lambda_{c/4}} \; (\overline{C}_{m_0})_{SECT} \qquad (7-3)$$

where $(\overline{C}_{m_0})_{SECT}$ is the average section pitching moment coefficient determined by averaging the section C_{m_0} for each wing panel, using

$$(\overline{C}_{m_0})_{SECT} = \frac{\displaystyle\sum_{i=1}^{N} \left(\frac{C_m}{C_{\ell d}}\right) (C_{\ell d})_i \; S_i}{\displaystyle\sum_{i=1}^{N} S_i}$$

where $(C_m/C_{\ell d})$ is the theoretical pitching moment divided by the section design lift of the airfoil camber line obtained from Table 4.1.1-D in the DATCOM.

7.2   AERODYNAMIC CENTER

The aerodynamic center location of a wing-body configuration is given in the DATCOM as

$$\frac{X_{ac}}{C_{R_e}} = \frac{\left(\dfrac{X_{ac}}{C_{R_e}}\right)_N (C_{L_\alpha})_N + \left(\dfrac{X_{ac}}{C_{R_e}}\right)_{W(B)} (C_{L_\alpha})_{W(B)} + \left(\dfrac{X_{ac}}{C_{R_e}}\right)_{B(W)} (C_{L_\alpha})_{B(W)}}{(C_{L_\alpha})_N + (C_{L_\alpha})_{W(B)} + (C_{L_\alpha})_{B(W)}}$$

$$(7-4)$$

where the X_{ac}/C_{R_e} terms are the chordwise distances measured in exposed wing-root chords from the apex of the exposed wing to the aerodynamic center, positive aft. The subscripts N, W(B), and B(W) refer to the lift and aerodynamic center contribution of the forebody, exposed wing, and the wing-lift carryover on the body, respectively.

7.2.1   Aerodynamic Center of Forebody

The subsonic location of the aerodynamic center for forebodies with ogive nose cones is approximated in the DATCOM as

$$\left(\frac{X_{ac}}{C_{R_e}}\right)_N = (-0.54)\frac{L_N + 1.6(X_{LE} - L_N)}{C_{R_e}}$$

Figure 7-2 defines the geometric parameters, L_N, X_{LE}, and C_{R_e}. The supersonic forebody aerodynamic center is obtained from

$$\left(\frac{X_{ac}}{C_{R_e}}\right)_N = \frac{X_{LE}}{C_{R_e}}\left(\frac{X_{CP}}{\ell_B} - 1\right) \qquad (7\text{-}6)$$

where the term X_{CP}/ℓ_B is obtained from Figure 7-3 (Figure 4.2.2.1-23a in DATCOM).

7.2.2 Aerodynamic Center of Wing (Trapezoidal, Single Panel)

The aerodynamic center of the exposed wing is determined from the DATCOM charts presented in Figures 7-4a through 7-4f. These charts are valid for subsonic Mach numbers less than Mach critical and supersonic Mach numbers greater than 1.2. For transonic conditions, the data presented in the DATCOM in terms of transonic similarity parameters (Figures 7-5a through 7-5d) are used to determine the aerodynamic center position.

The procedure for obtaining aerodynamic center can be summarized as:

$$\text{For } M \leq M_{CR}, \quad \frac{X_{ac}}{C_{R_e}} = \left(\frac{X_{ac}}{C_{R_e}}\right)' \qquad (7\text{-}7)$$

For $M_{CR} + .05 \geq M > M_{CR}$,

$$\frac{X_{ac}}{C_{R_e}} = \left(\frac{X_{ac}}{C_{R_e}}\right)' + \left[\left(\frac{X_{ac}}{C_{R_e}}\right)'' - \left(\frac{X_{ac}}{C_{R_e}}\right)'\right]\frac{M - M_{CR}}{.05} \qquad (7\text{-}8)$$

Figure 7-2   Wing-Body Geometry

SUPERSONIC SPEEDS

Figure 7-3   Supersonic Center of Pressure of Ogive
with Cylindrical Afterbody

SUBSONIC AND SUPERSONIC SPEEDS
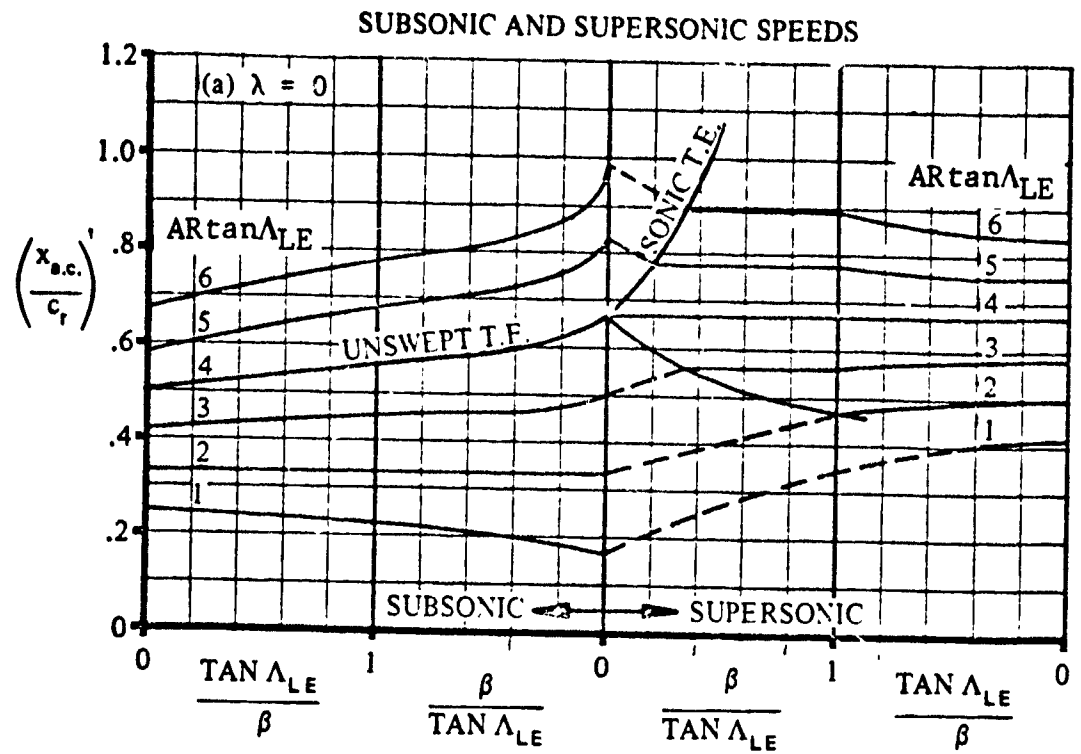
Figure 7-4   Wing Aerodynamic-Center Position

Figure 7-4 (Cont'd)

119

Figure 7-4 (Cont'd)

120
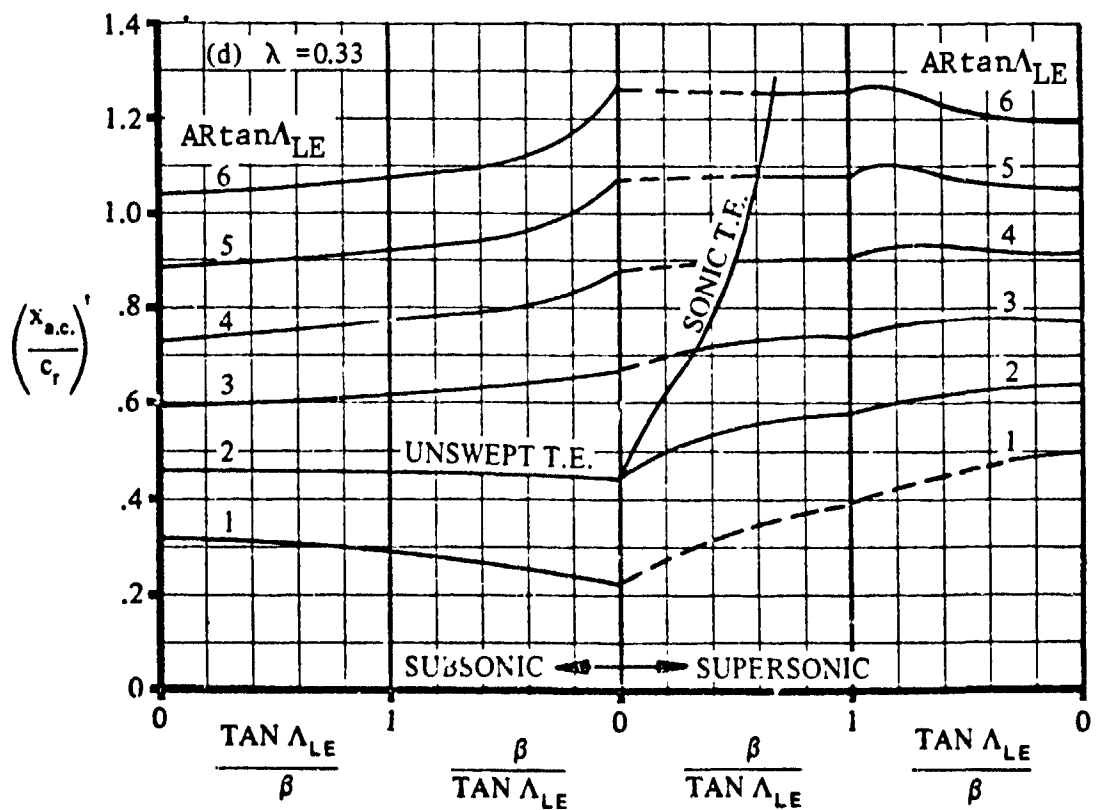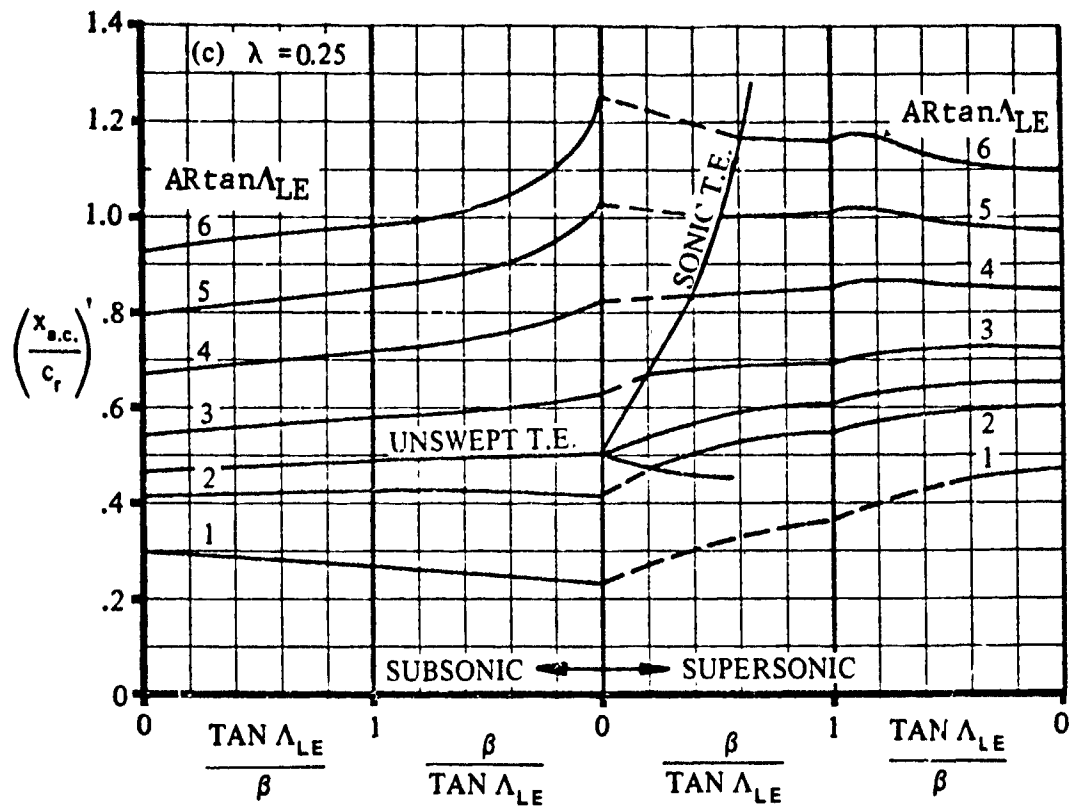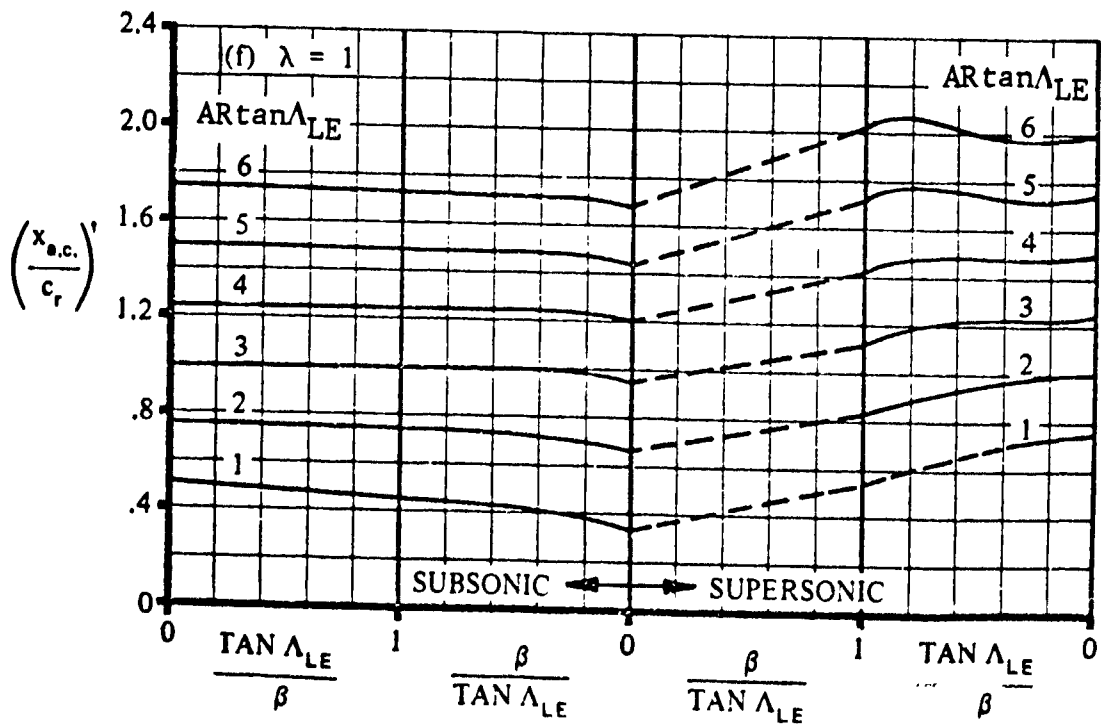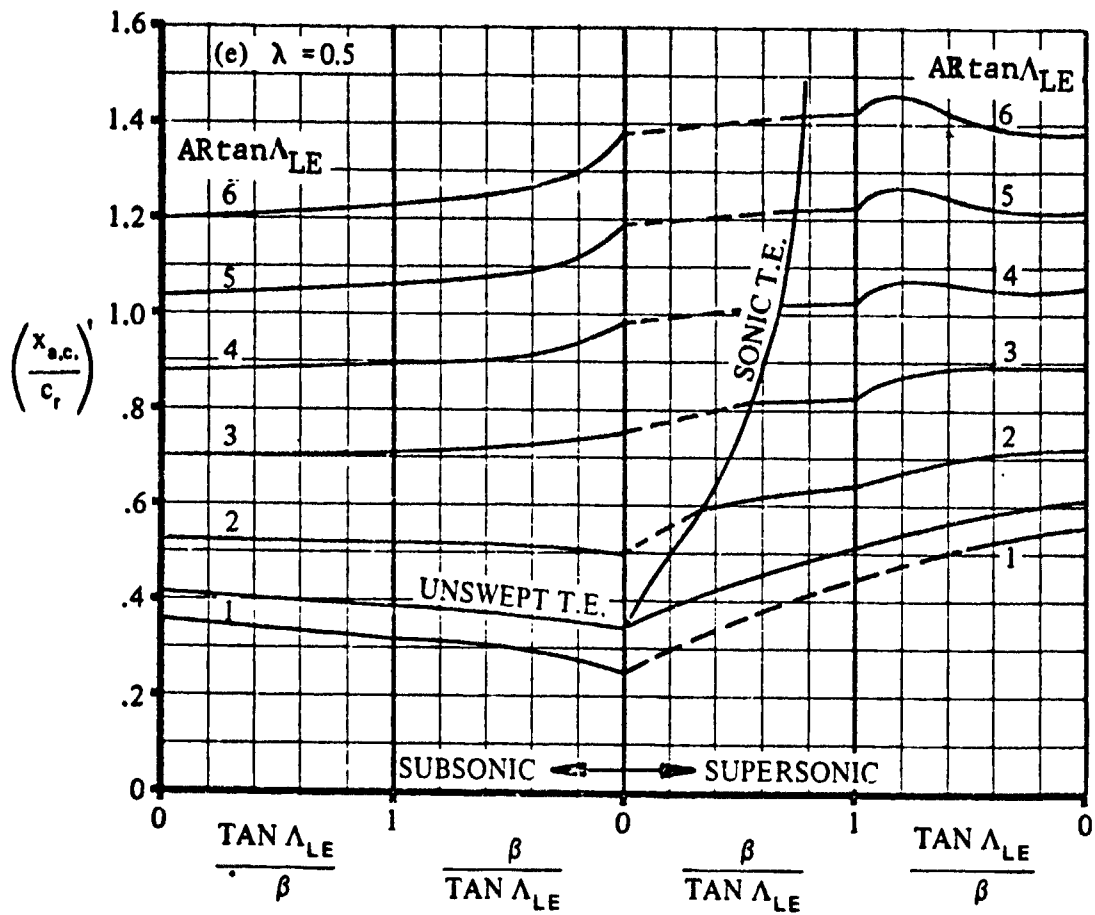
For $\sqrt{1+(t/c)^{2/3}} > M > M_{CR} + .05$,

$$\frac{X_{ac}}{C_{R_e}} = \left(\frac{X_{ac}}{C_{R_e}}\right)'' \tag{7-9}$$

For $1.2 > M \geq \sqrt{1+(t/c)^{2/3}}$,

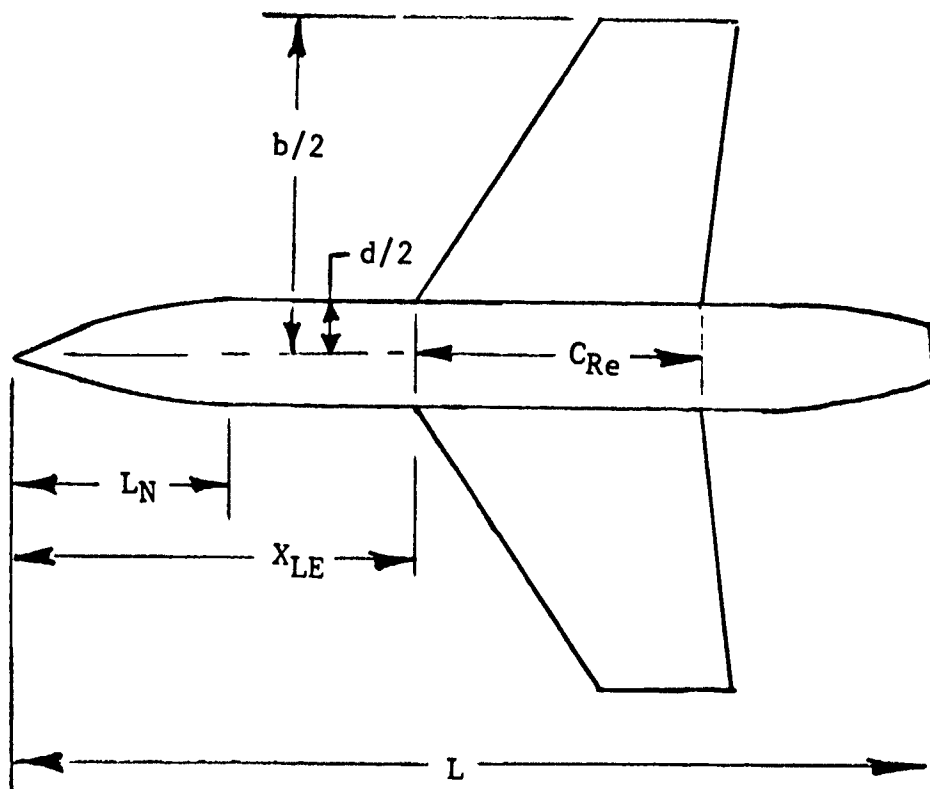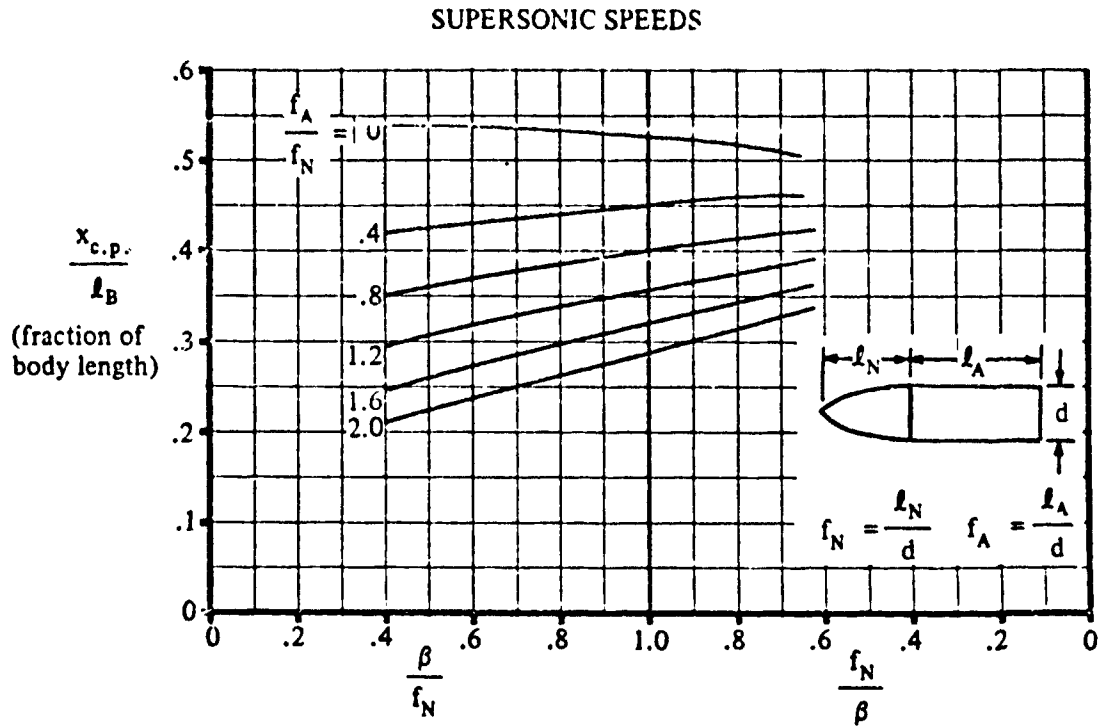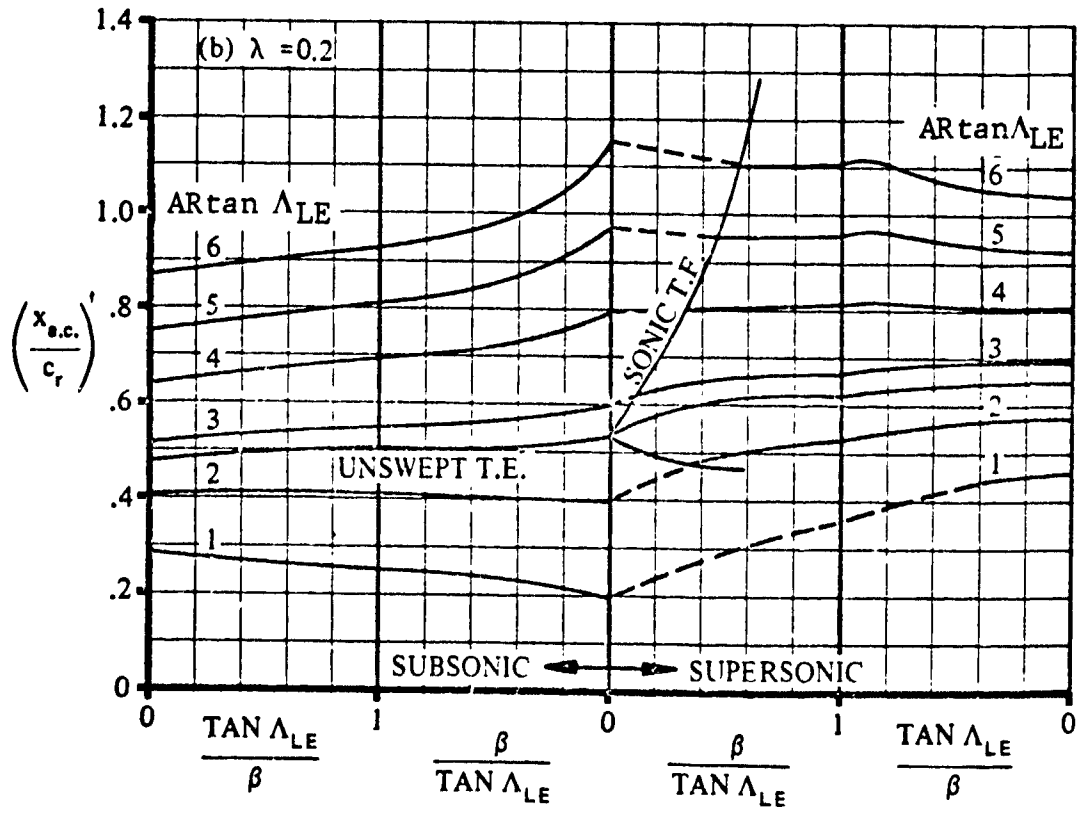$$\frac{X_{ac}}{C_{R_e}} = \left(\frac{X_{ac}}{C_{R_e}}\right)'' + \left[\left(\frac{X_{ac}}{C_{R_e}}\right)'' - \left(\frac{X_{ac}}{C_{R_e}}\right)'\right]\frac{M - \sqrt{1+(t/c)^{2/3}}}{1.2 - \sqrt{1+(t/c)^{2/3}}} \tag{7-10}$$

For $M \geq 1.2$,

$$\frac{X_{ac}}{C_{R_e}} = \left(\frac{X_{ac}}{C_{R_e}}\right)' \tag{7-11}$$

where $(X_{ac}/C_{R_e})'$ is read from Figure 7-4 and $(X_{ac}/C_{R_e})''$ is read from Figure 7-5.

7.2.3 Aerodynamic Center of Wing (Cranked or Double Delta)

The prediction of the a.c. location of cranked or double-delta wings is taken from the method developed at General Dynamics as reported in Reference 11. The non-straight-tapered wing is divided into two panels, with each panel having conventional, straight-tapered geometry. The individual lift-curve slope and a.c. are estimated for each panel, using the technique described above for the trapezoidal wing and treating each constructed panel as an isolated wing. The individual lift and a.c. location for each constructed panel are then combined, using an inboard-outboard weighted-area relationship

$$\frac{\overline{X}_{ac}}{C_{R_e}} = \frac{\left(\frac{X_{ac}}{C_{R_e}}\right)_i (C_{L_\alpha})_i S_i + \left(\frac{X_{ac}}{C_{R_e}}\right)_o (C_{L_\alpha})_o S_o}{(C_{L_\alpha})_i S_i + (C_{L_\alpha})_o S_o} \tag{7-12}$$
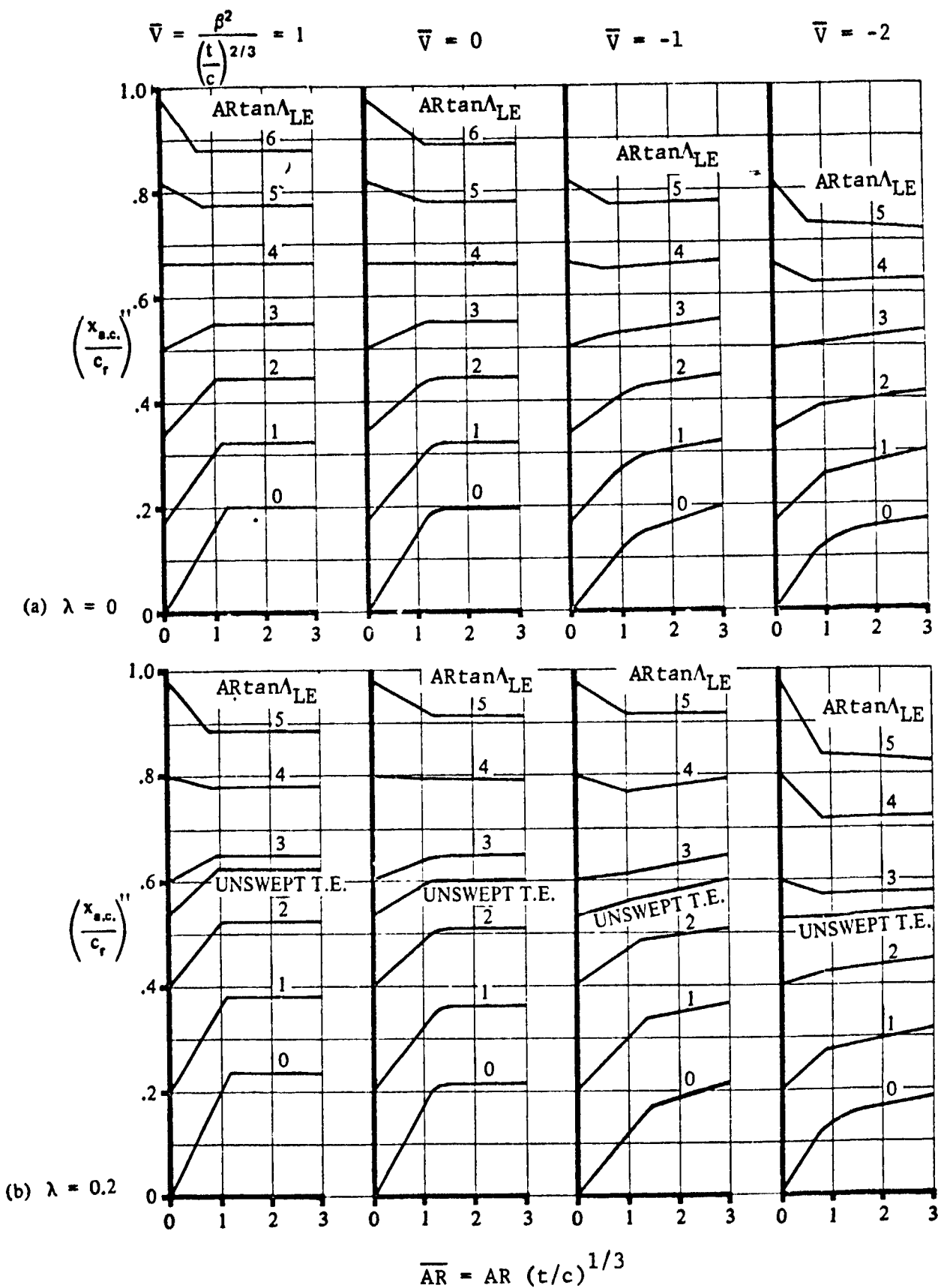
Figure 7-5   Transonic Wing Aerodynamic-Center Location
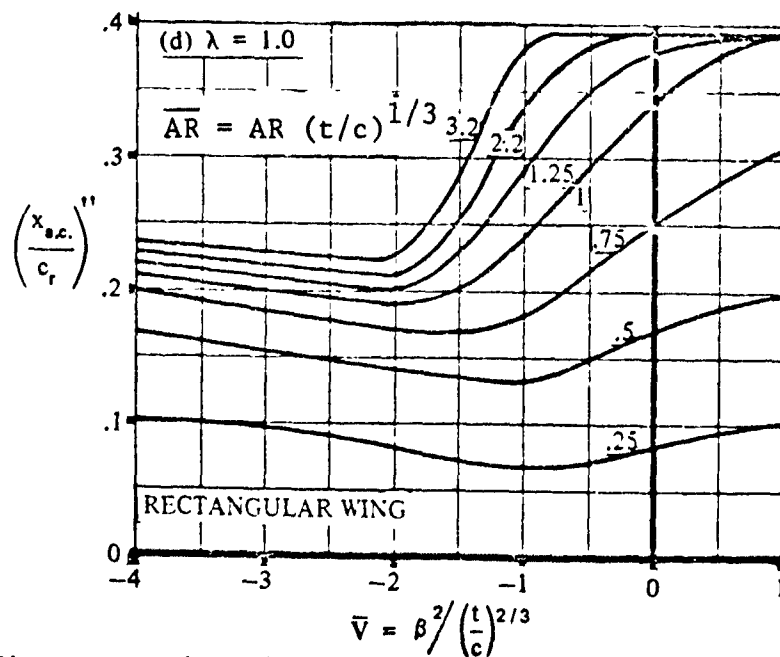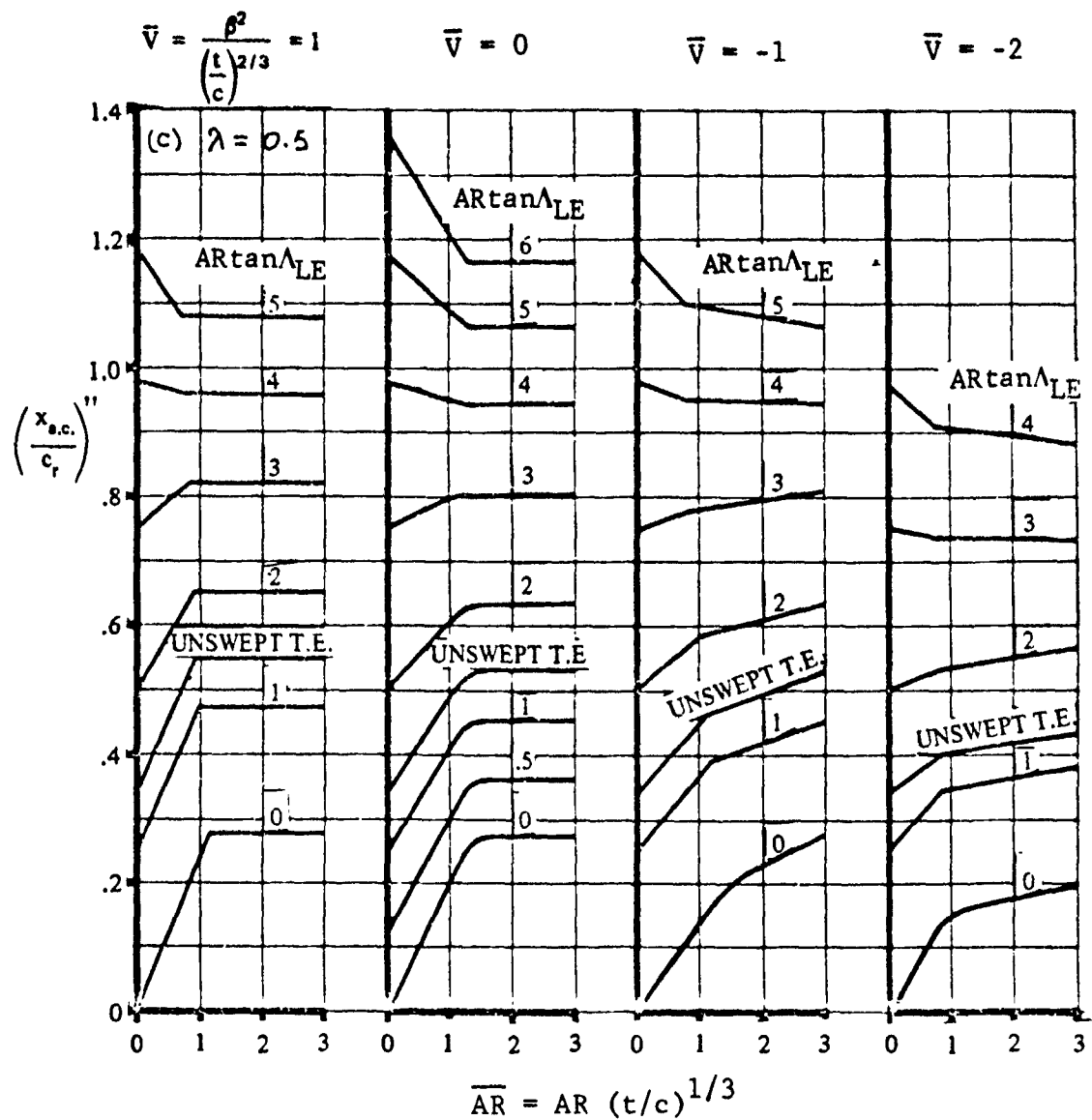
Figure 7-5 (Cont'd) 123

where the outboard wing a.c. is referenced to the inboard root chord length given by

$$\left(\frac{X_{ac}}{C_{R_e}}\right)_o = \left(\frac{X_{ac}}{C_{R_o}}\right)_o \frac{C_{R_o}}{C_{R_e}} - \frac{\Delta y}{C_{R_e}} (\tan \Lambda_{LE})_o + \frac{(b/2)_i}{C_{R_e}}(\tan \Lambda_{LE})_i$$

The geometry for the inboard-outboard panel arrangement is illustrated in Figure 7-6.

7.2.4 Aerodynamic Center of Wing-Lift Carryover on Body

The location of the a.c. due to the wing-lift carryover on the body is determined by use of the DATCOM method. For $\beta AR_e \geq 4$ the subsonic a.c. location is obtained from

$$\left(\frac{X_{ac}}{C_{R_e}}\right)_{B(W)} = \frac{1}{4} + \frac{b-d}{2C_{R_e}} \tan \Lambda_{c/4} \cdot f(d/b) \qquad (7\text{-}13)$$

where AR_e is the exposed-wing aspect ratio and the factor $f(d/b)$ is shown plotted in Figure 7-7. For $\beta AR_e < 4$ the a.c. location is determined from

$$\left(\frac{X_{ac}}{C_{R_e}}\right)_{B(W)} = \left[\left(\frac{X_{ac}}{C_{R_e}}\right)'' - \left(\frac{X_{ac}}{C_{R_e}}\right)'\right]\left(\frac{\beta AR_e - 4}{4}\right)^2 + \left(\frac{X_{ac}}{C_{R_e}}\right)' \qquad (7\text{-}14)$$

where $(X_{ac}/C_{R_e})'$ is the a.c. location determined from Equation 7-13 and $(X_{ac}/C_{R_e})''$ is the theoretical location for $\beta AR_e = 0$ determined from the equation

$$\left(\frac{X_{ac}}{C_{R_e}}\right)'' = \frac{1}{8} AR_e (1 + \lambda_e) \tan \Lambda_{LE} \qquad (7\text{-}15)$$

where λ_e is the exposed-wing taper ratio. Equation 7-15 is limited to values less than or equal to 0.5. For supersonic conditions the a.c. location is estimated from Figure 7-8. For transonic conditions the a.c. location is determined by linear interpolation of the a.c. values determined at the critical Mach number and Mach 1.1.

124
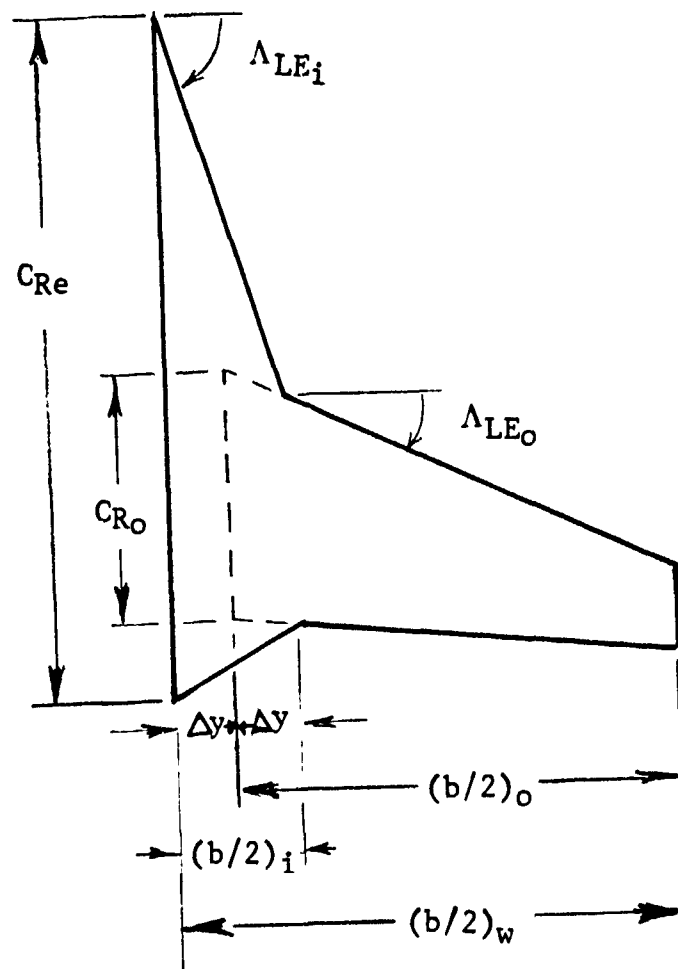
Figure 7-6   Geometry for Cranked Wing Aerodynamic-Center
              Prediction
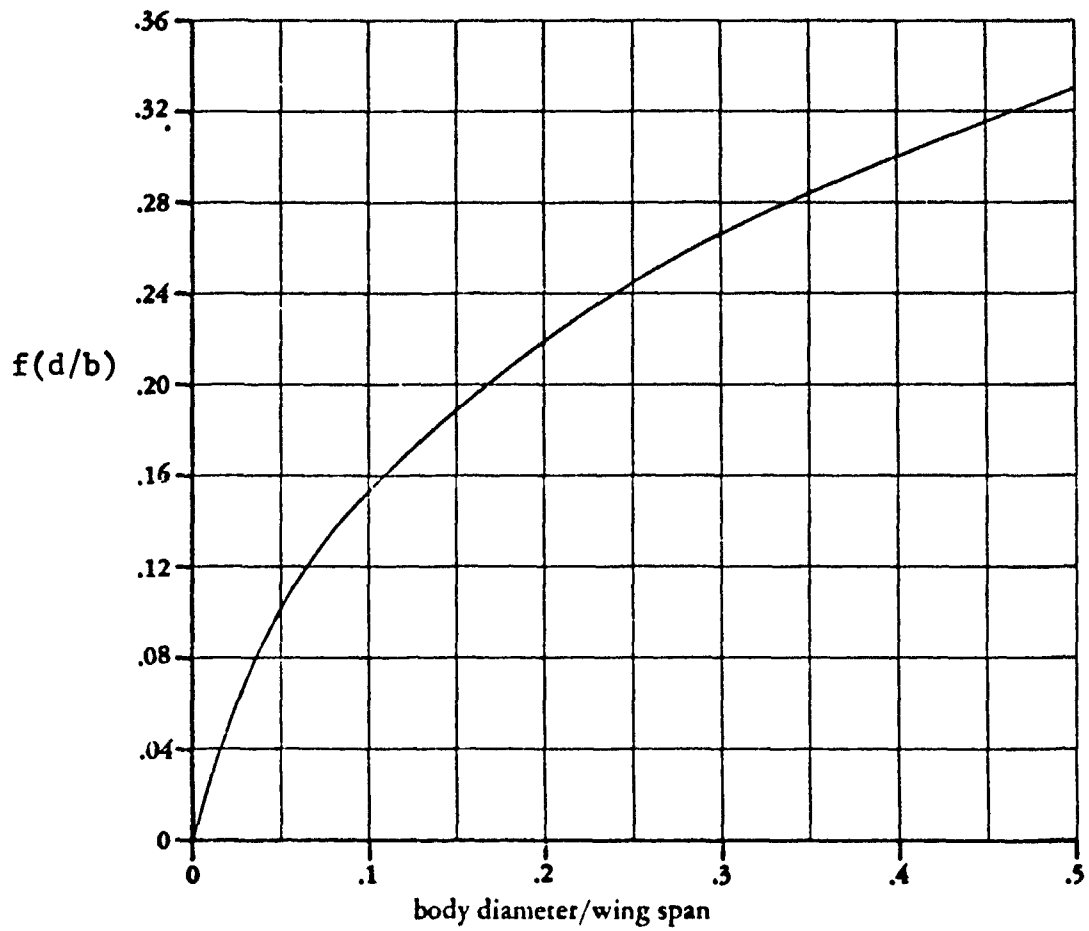
Figure 7-7   Parameter Used in Accounting for Wing-Lift
Carryover on the Body

(a) WITH AFTERBODY
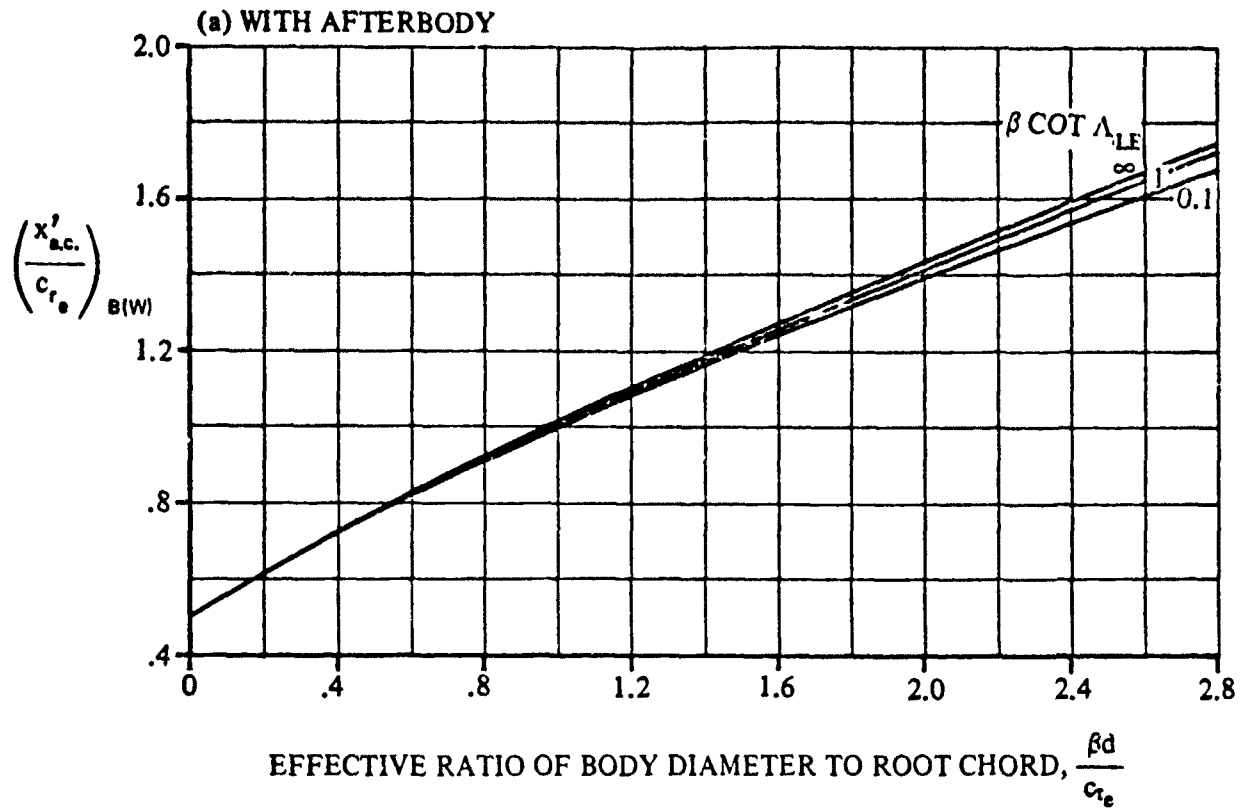
Figure 7-8   Aerodynamic-Center Locations for Lift Carry-
over onto Body at Supersonic Speeds

For complex wing planforms the equivalent wing-sweep values are used in the subsonic and supersonic a.c. location methods.

7.3 EFFECT OF TRIM DEFLECTION

The effect of trim deflection can be estimated by predicting the incremental change in lift, drag, and moment due to tail deflection along constant angles of attack. The total wing-body-tail lift, drag, and moment can be represented by

$$C_L = C_{L_{WB}} + C_{L_{\alpha_t}}(\alpha - \alpha_{o_t}) + C_{L_\delta} \cdot \delta_{HT} \qquad (7\text{-}16)$$

$$C_D = C_{D_{MIN}\atop TOTAL} + (C_{D_L})_{WB} + (C_{D_L})_{HT} \qquad (7\text{-}17)$$

$$C_m = C_{m_o} + (\frac{dC_m}{dC_L})_{W\text{-}B} - \left\{ C_{L_{\alpha\,t}}(\alpha - \alpha_{o_t}) + C_{L_\delta} \cdot \delta_{HT} \right\} \ell_{HT}/\bar{c} \qquad (7\text{-}18)$$

where the induced drag of the tail is predicted by use of a tail-induced drag factor K_t times the square of the lift generated by the tail, i.e.

$$(C_{D_L})_{HT} = K_t \left[C_{L_{\alpha\,t}}(\alpha - \alpha_{o_t}) + C_{L_\delta} \delta_{HT} \right]^2 \qquad (7\text{-}19)$$

From Equations 7-16 and 7-17, the incremental change in lift and drag at constant α due to a trim deflection can be determined by

$$\Delta C_L = C_{L_\delta} \cdot \delta_{HT} \qquad (7\text{-}20)$$

$$\Delta C_D = K_t \left[C_{L_{\alpha\,t}}(\alpha - \alpha_{o_t}) + C_{L_\delta} \cdot \delta_{HT} \right]^2 - K_t \left[C_{L_{\alpha\,t}}(\alpha - \alpha_{o_t}) \right]^2 \qquad (7\text{-}21)$$

Equation 7-21 can be reduced to

$$\Delta C_D = a\delta_{HT}^2 + b\delta_{HT}(\alpha - \alpha_{o_t}) \qquad (7\text{-}22)$$

where $a = K_t C_{L_\delta}^{\,2}$

$\quad\quad b = 2K_t C_{L_{\alpha_t}} \cdot C_{L_\delta}$

The factor C_{L_δ} for an all-movable horizontal tail is predicted from

$$C_{L_\delta} = (C_{L_{\alpha'}})_t K_{W(B)} \cdot q_t/q_\infty \quad\quad\quad (7\text{-}23)$$

where $(C_{L_{\alpha'}})_t$ is the exposed-area lift-curve estimate for the tail, and $K_{W(B)}$ is the surface lift in the presence of the body factor. The induced drag factor for the tail is determined by the leading-edge suction method described in Section 4, where

$$K_t = \frac{1-R_t}{57.3 K_{W(B)}(C_{L_{\alpha'}})_t} + \frac{R_t}{\pi AR_{HT}} \frac{S_{REF}}{(S_{EX})_{HT}} \quad\quad (7\text{-}24)$$

The AAT computer code can predict the lift, moment, and drag for a fixed tail setting, or the program can solve for δ_{HT} to trim out the moment. The tail deflection required for trim is obtained by setting Equation 7-18 equal to zero and solving for δ_{HT}.

129

7.4 ELEVON TRIM METHOD

Aircraft that are designed without a horizontal tail or canard can be trimmed by use of a trailing-edge flap (elevon) on the wing. The use of trailing-edge control device on the wing for longitudinal trim alters the basic wing load distribution, thus affecting lift and drag as well as the moment. The method used in the AAT procedure for predicting lift, drag, and moment required for trimming a tailless (or canardless) aircraft using elevons, was adapted from the method used in References 1 and 2 for predicting the effects of trailing-edge flaps deflections of high-lift systems at low speeds. The AAT elevon trim method assumes that the elevon is a plain flap, operating in the linear attached flow range, with no significant gap losses. The method of Reference 1 was extended to include compressibility effects.

7.4.1 Effect of Elevon Trim Deflection

The effect of trim deflection is computed by predicting the incremental change in lift, drag, and moment due to trailing-edge deflection, along constant angles of attack. The total wing-body lift, drag, and moment can be represented by

$$C_L = C_{L_{WB}} + C_{L_\delta} \delta_e \tag{7-25}$$

$$C_D = \left[C_{D_{min}} + C_{D_L} \right]_{WB} + K_D \; \delta_e^2 \tag{7-26}$$

$$C_M = \left[C_{M_o} + \frac{dC_M}{dC_L} \cdot C_L \right]_{WB} + \left(CG - \frac{X_{cp}}{\bar{c}} \right) C_{L_\delta} \cdot \delta_e \tag{7-27}$$

The elevon deflection required for trim (C_M=0) is then determined which is used to compute the incremental change in lift and drag at constant α due to the trim elevon deflection.

$$\Delta C_L = C_{L_\delta} \cdot \delta_e \tag{7-28}$$

$$\Delta C_D = K_D \; \delta_e^2 \tag{7-29}$$

The determination of the factors C_{L_δ}, K_D, and $\dfrac{X_{cp}}{\bar{c}}$ in equations 7-25, 7-26, and 7-27 are discussed in the following subsections.

7.4.2 Flap Lift Effectiveness

The subsonic lift increment developed by deflection of a trailing-edge flap control surface is given in Reference 1 by

130

$$C_{L_\delta} = \eta_P \, C_{l_\delta} \left(\frac{C_{L_\alpha}}{C_{l_\alpha}} \right) K_c \, K_b \qquad\qquad (7\text{-}30)$$

$$C_{l_\delta} = 2 \left[\phi_f + \sin \phi_f \right], \quad \phi_f = \text{arc cos} \left[1 - 2(e_f/C) \right]$$

$$\eta_P = 0.77 \text{ for } \delta_e + \phi_{TE} \leq 12.5^\circ$$

$$\frac{C_{L_\alpha}}{C_{l_\alpha}} = \frac{AR}{2 + \sqrt{4 + (1 - M^2 \cos^2 \Lambda_{c/2}) \left(\dfrac{AR}{\cos \Lambda c/2} \right)^2}}$$

K_C and K_b are shown plotted in Figures 7-9 and 7-10.

7.4.3 Control Surface Drag

The deflection of an elevon causes two increments of drag. First, the profile drag of the wing-flap combination is changed. Second, the deflection of the elevon changes the span load distribution and may, therefore, change the induced drag of the wing. The subsonic increment in profile drag can be estimated by the method in Reference 1 with a simple Pranddtl-Glauert compressibility correction

$$C_{D_{Profile}} = (1/\beta) \, \Delta C_{d_f} \cos \Lambda_{HL} \cdot K_d$$

$$\beta = \sqrt{1 - M^2} \, , \quad M \leq M_{CR} \qquad\qquad (7\text{-}31)$$

The term ΔC_{d_f} is the sectional drag increment due to flap deflection, shown plotted in Figure 7-11 for plain flaps. For moderate deflection, C_{d_f} can be approximated by

$$\Delta C_{d_f} = 0.00168 \, \left(\frac{C_f}{c} \right)^{2.322} \cdot \delta_e^2$$

The factor K_d, shown plotted in Figure 7-12, is a partial span correction.

The change in induced drag due to flap deflection, at zero angle of attack, is given by (Reference 1)

$$C_{D_I} = K_a \, K_f \, \frac{(C_{L_\delta} \cdot \delta_e)^2}{\pi \, AR} \qquad\qquad (7\text{-}32)$$

where K_a and K_f, shown plotted in Figure 7-13 are factors which account for the non-elliptical span loading of partial span flaps. It was assumed that the change in induced drag at all angles of attack for a constant δ_e deflection will parallel the basic wing polar.

131
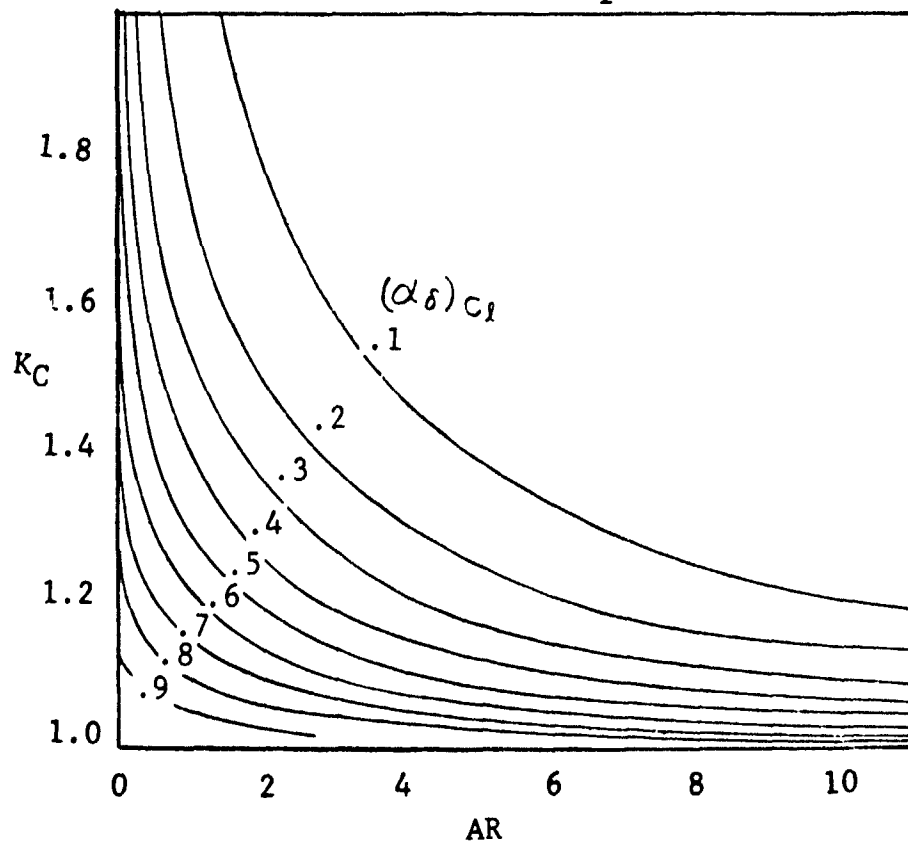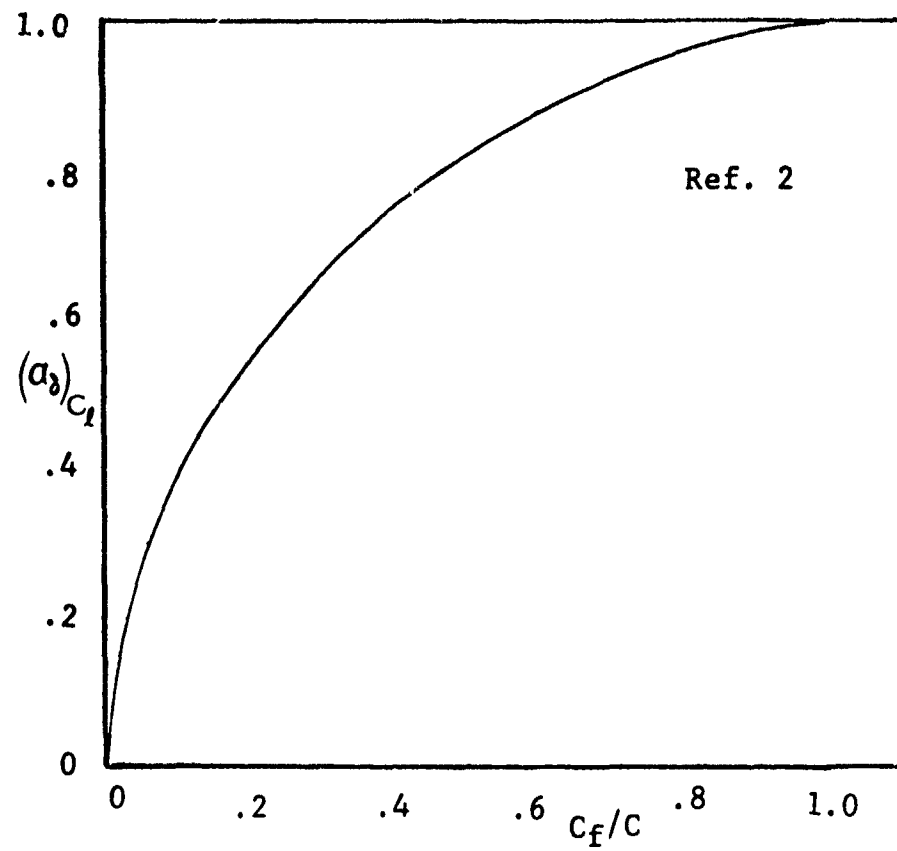
Figure 7-9   Flap Chord Factor
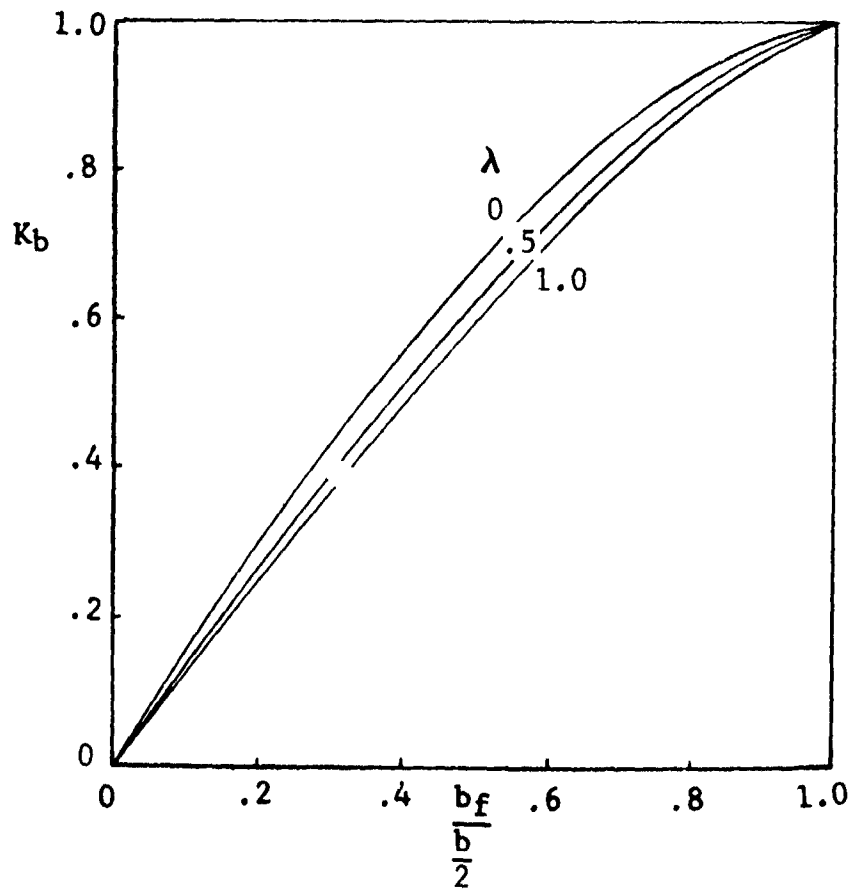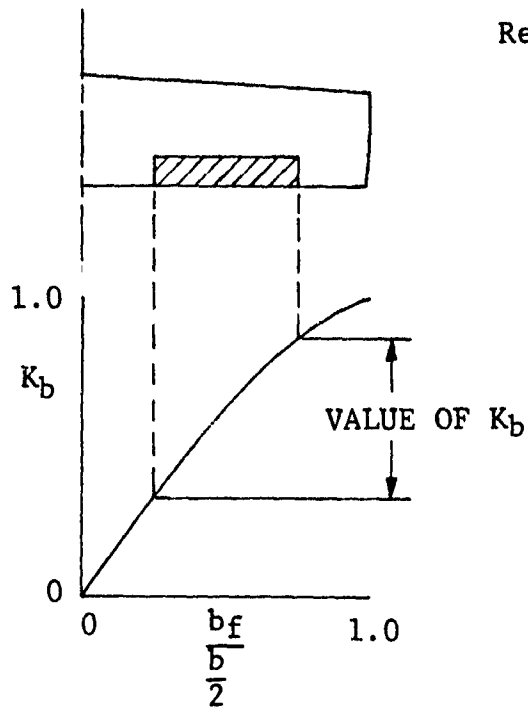
Figure 7-10 Flap Span Lift Factor
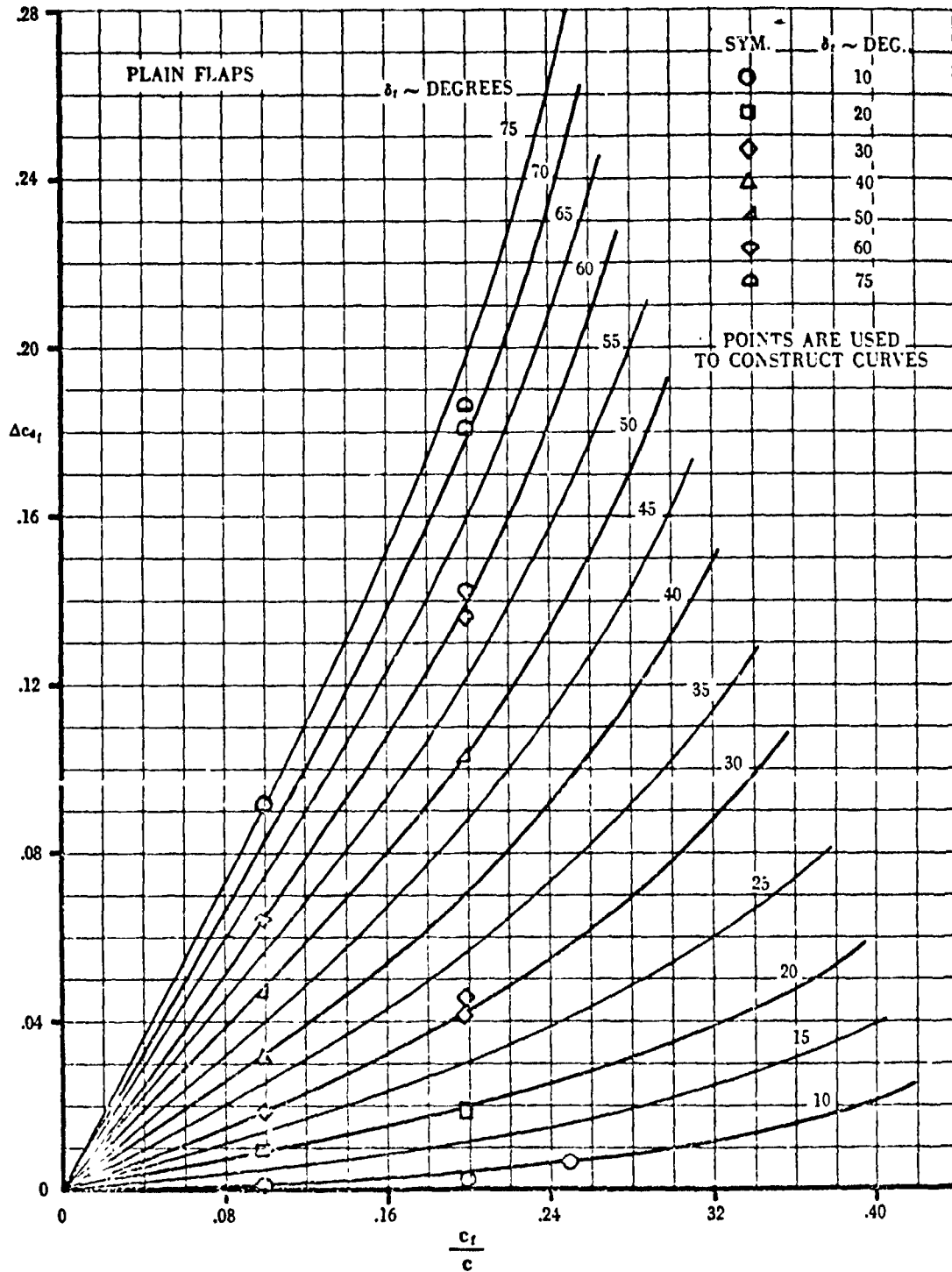
Figure 7-11 Two-Dimensional Drag Increment Due to Plain Flaps

134

EFFECTS OF FLAP SPAN ON DRAG
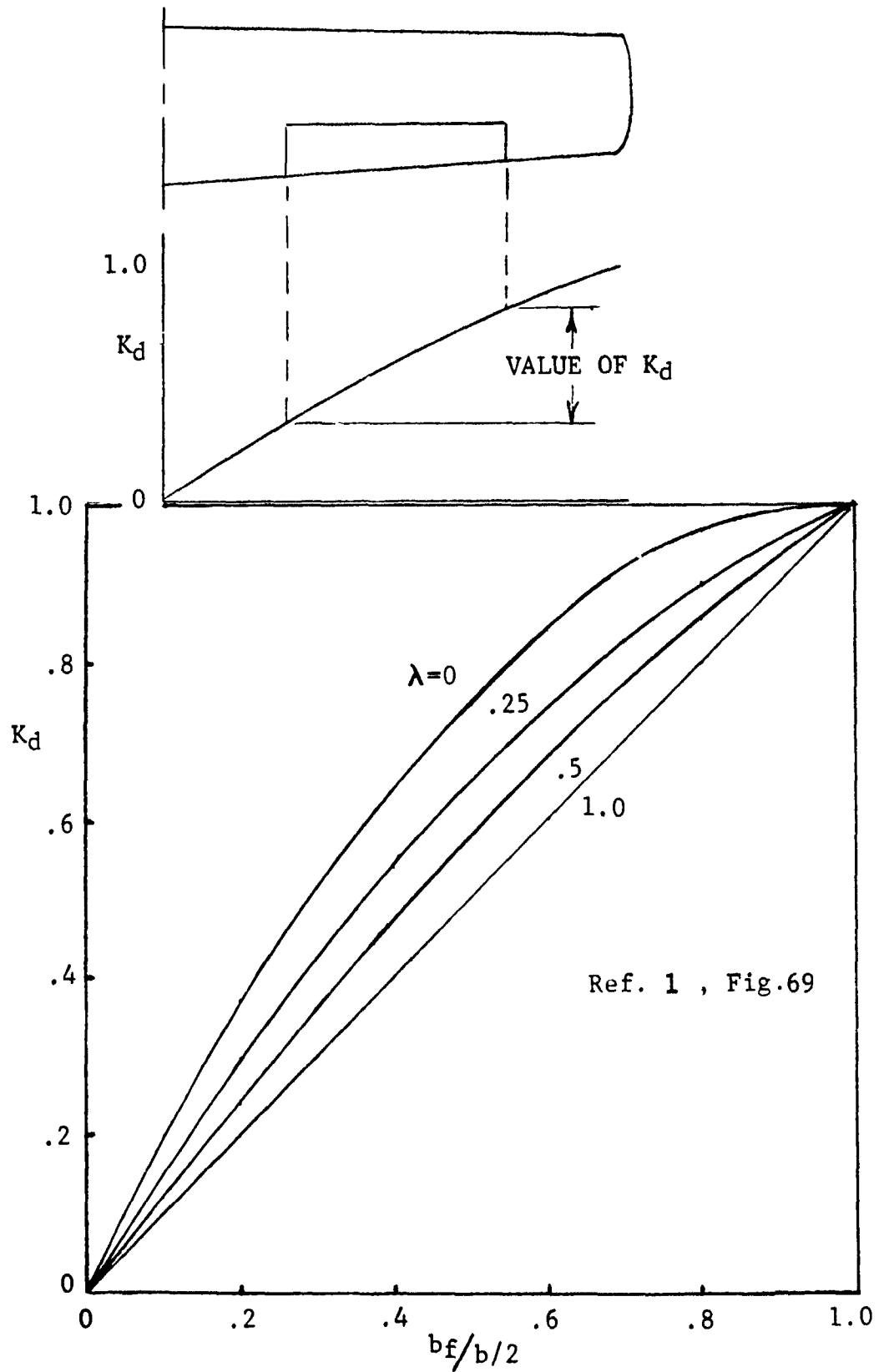
Figure 7-12 Flap Span Drag Factor

$$C_{D_I} = K_f \cdot K_A \cdot \frac{\Delta C_{L_o}^2}{\pi \cdot AR}$$
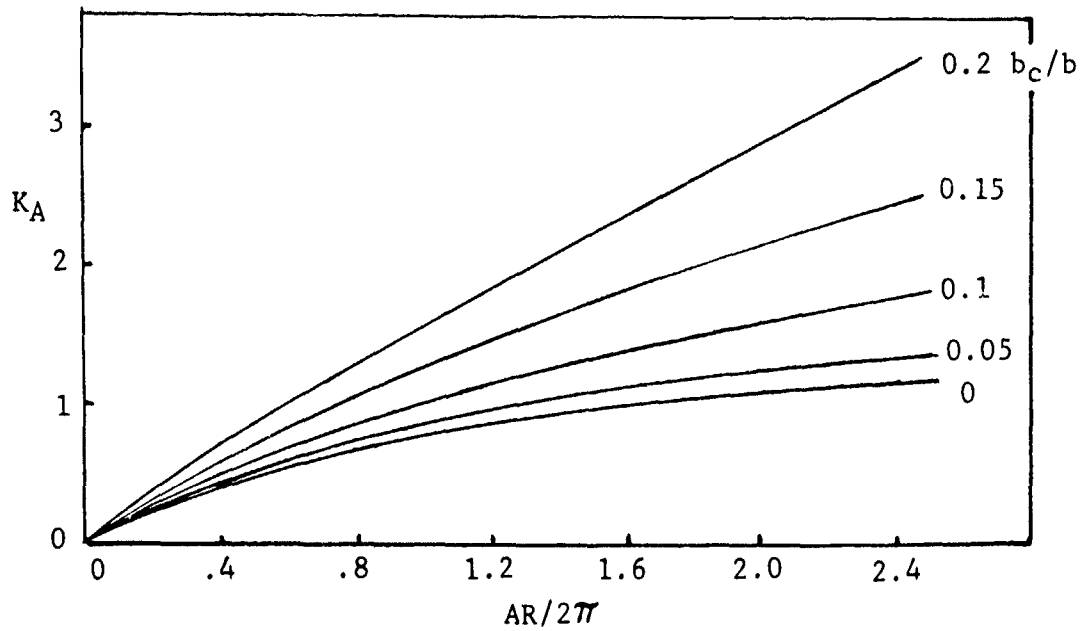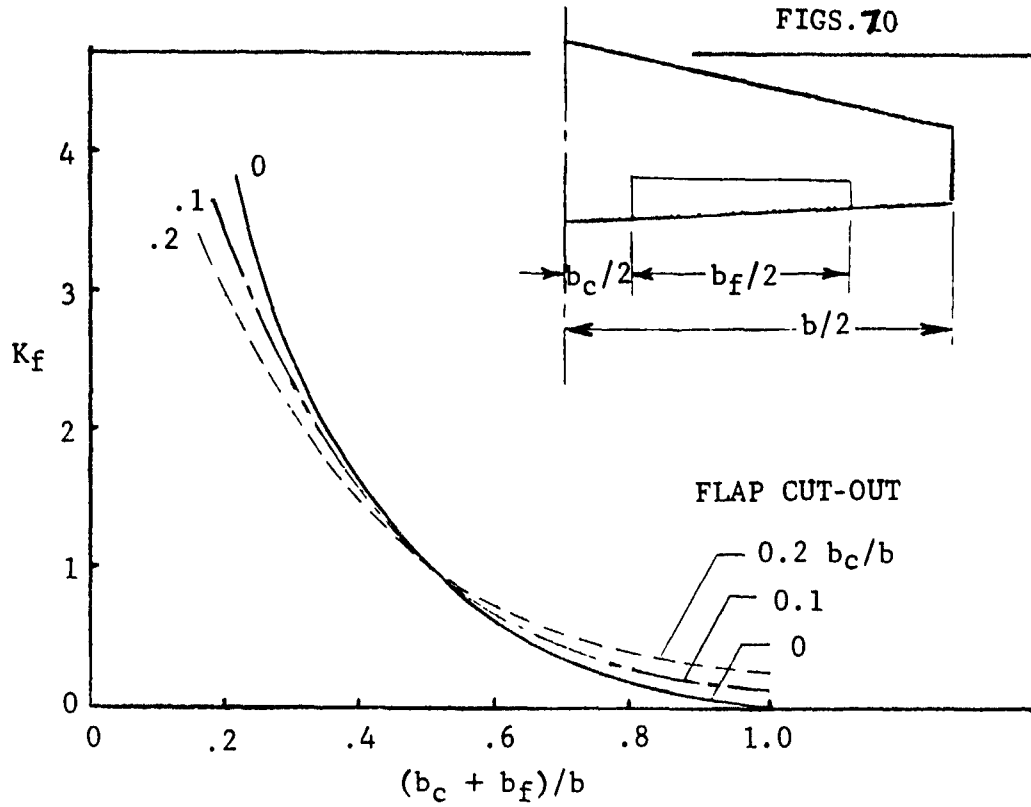
Figure 7-13 Flap-Induced Drag Factors

Equations 7-31 and 7-32 both vary with the square of the elevon deflection so they may be combined to yield the K_D factor of Equation 7-29.

7.4.4 Elevon Moment

Deflection of a plain flap alters the load distribution of the wing as shown in Figure 7-14. The incremental load due to the flap exhibits a peak over the airfoil leading edge and a peak over the hingeline. The higher loading at the hinge predominates, giving a nose-down moment (aft shift in section center of pressure). For attached flow, the center-of-pressure location due to the additional lift does not shift position with flap deflection.
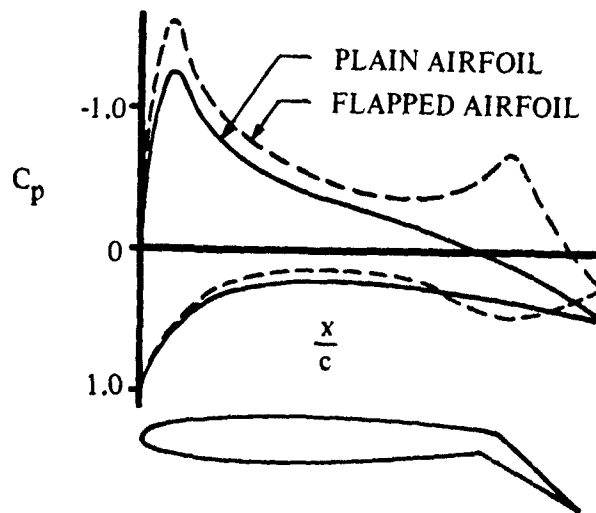
Figure 7-14 Flap Load Distribution

The change in pitching-moment increment due to flap deflection based on total wing area and chord and taken about the wing quarter-chord MAC given by DATCOM Equation 6.1.5.1.

$$\Delta C_M = \left\{ \left(\frac{\Delta C_M'}{\Delta C_L} \right) K_M + K_{S_W} \left(\frac{\cancel{R}}{1.5} \right) \tan \Lambda c/4 \right\} \Delta C_L' \qquad (7-33)$$

K_M is a flap span factor as a function of taper ratio and flap location obtained from Figure 7-15.

137
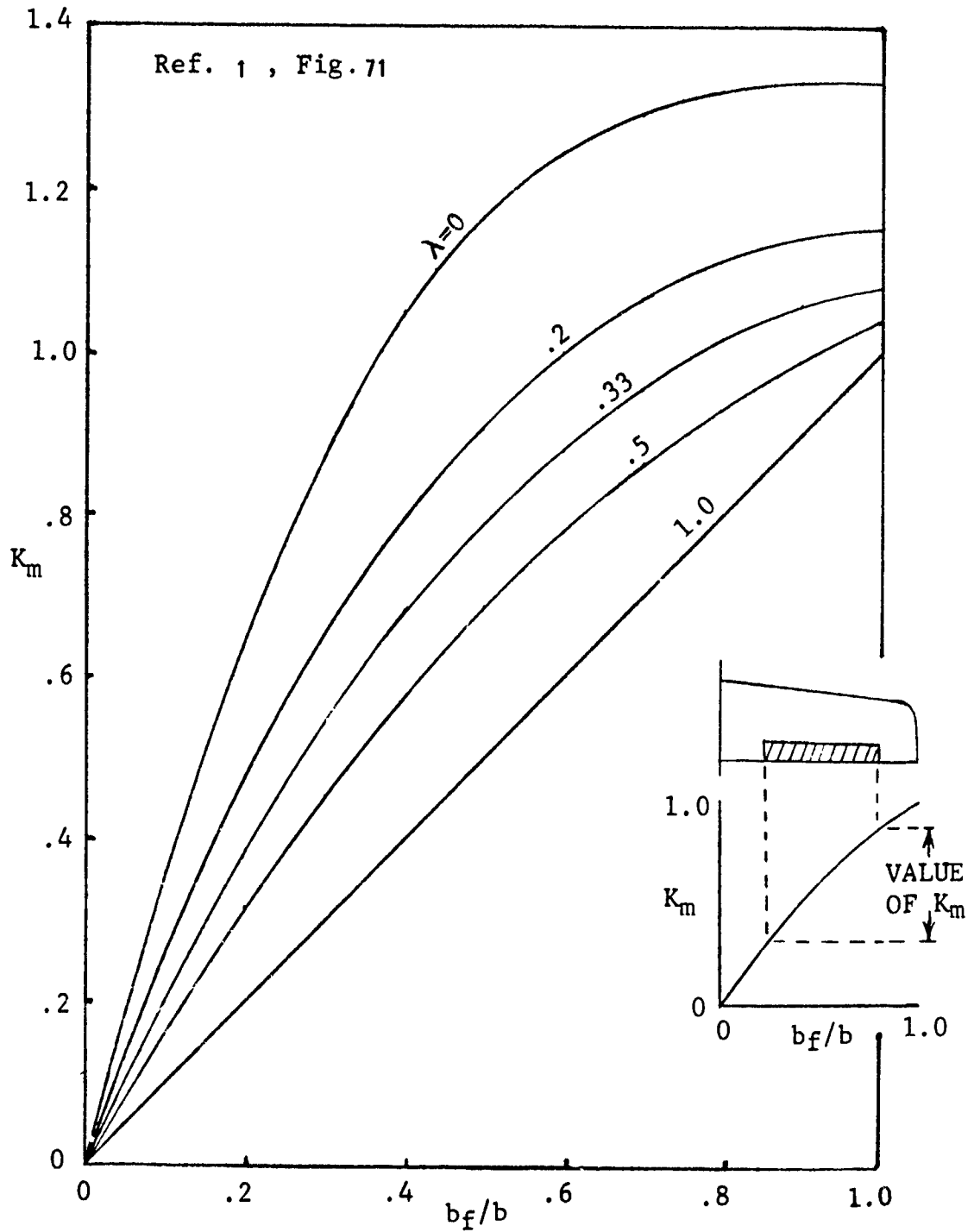
Figure 7-15   Span Effect on Moments

138

$(\Delta C_M{}' / \Delta C_L)$ is the ratio of the pitching-moment increment to lift for a full span flap obtained from Figure 7-16. K_{SW} is a conversion factor for a partial span flap on a swept-back wing obtained from Figure 7-17. $\Delta C_L{}'$ is the lift increment due to flap deflection for a full-span flap, on an aspect ratio six, zero midchord sweep wing. Using Equation 7-30 the incompressible lift increment, $\Delta C_L{}' = C_{L_\delta} \delta$, can be solved to obtain

$$\Delta C_L{}' = 0.7208 \; \eta_P \cdot C_{\ell_\delta} \cdot K_C \cdot \delta_e \tag{7-34}$$

or in terms of the partial span, arbitrary aspect ratio, sweep wing case

$$\Delta C_L{}' = \frac{0.7208}{\left(\dfrac{C_{L\alpha}}{C_{\ell\alpha}}\right) K_b} \cdot C_{L_\delta} \cdot \delta_e \tag{7-35}$$

The change in moment due to elevon deflection about the wing quarter-chord MAC is to be expressed in terms of $X_{cp}/\bar{c}$ as

$$\Delta C_M = (.25 - \frac{X_{cp}}{\bar{c}}) \; C_{L_\delta} \cdot \delta_e \tag{7-36}$$

Equations 7-36 and 7-33 combined with 7-35 can be used to determine the subsonic flap center of pressure

$$\frac{X_{CP}}{\bar{c}} = .25 - \left\{ \frac{\Delta C_M{}'}{\Delta C_L} K_M + K_{SW}\left(\frac{R}{1.5}\right) \tan \Lambda_{c/4} \right\}$$

$$\cdot \frac{0.7208}{(C_{L_\alpha}/C_{\ell_\alpha})} \; \frac{1}{K_b} \tag{7-37}$$

139

Figure 7-16 RATIO OF PITCHING-MOMENT-COEFFICIENT INCREMENT TO LIFT-
COEFFICIENT INCREMENT DUE TO FLAPS FOR UNSWEPT WINGS

Figure 7-17 Span Effect on Moments of Sweptback Wings

141

8. DAMAGE EVALUATION METHODS

The Aerodynamic Accounting Technique computer code includes methods for evaluating the aerodynamic effects of aircraft damage. Surface roughness, forward-facing and aft-facing steps, caved-in and missing panels, surface waviness, protuberances, body bluntness, and missing parts of wing and tail surfaces comprise the types of damage that can be evaluated. The program user should be able to model most actual aircraft damage into one or more of these categories.

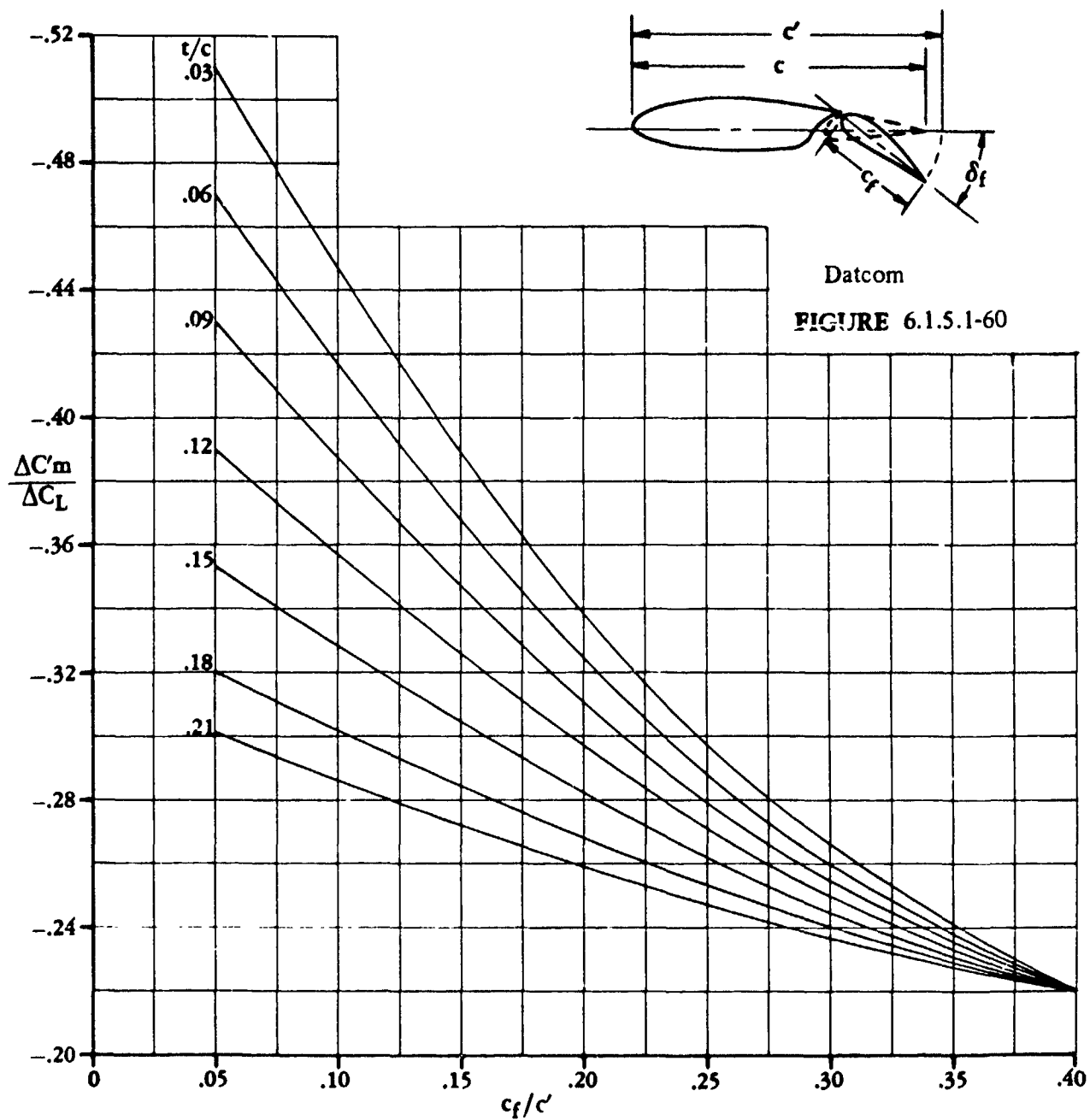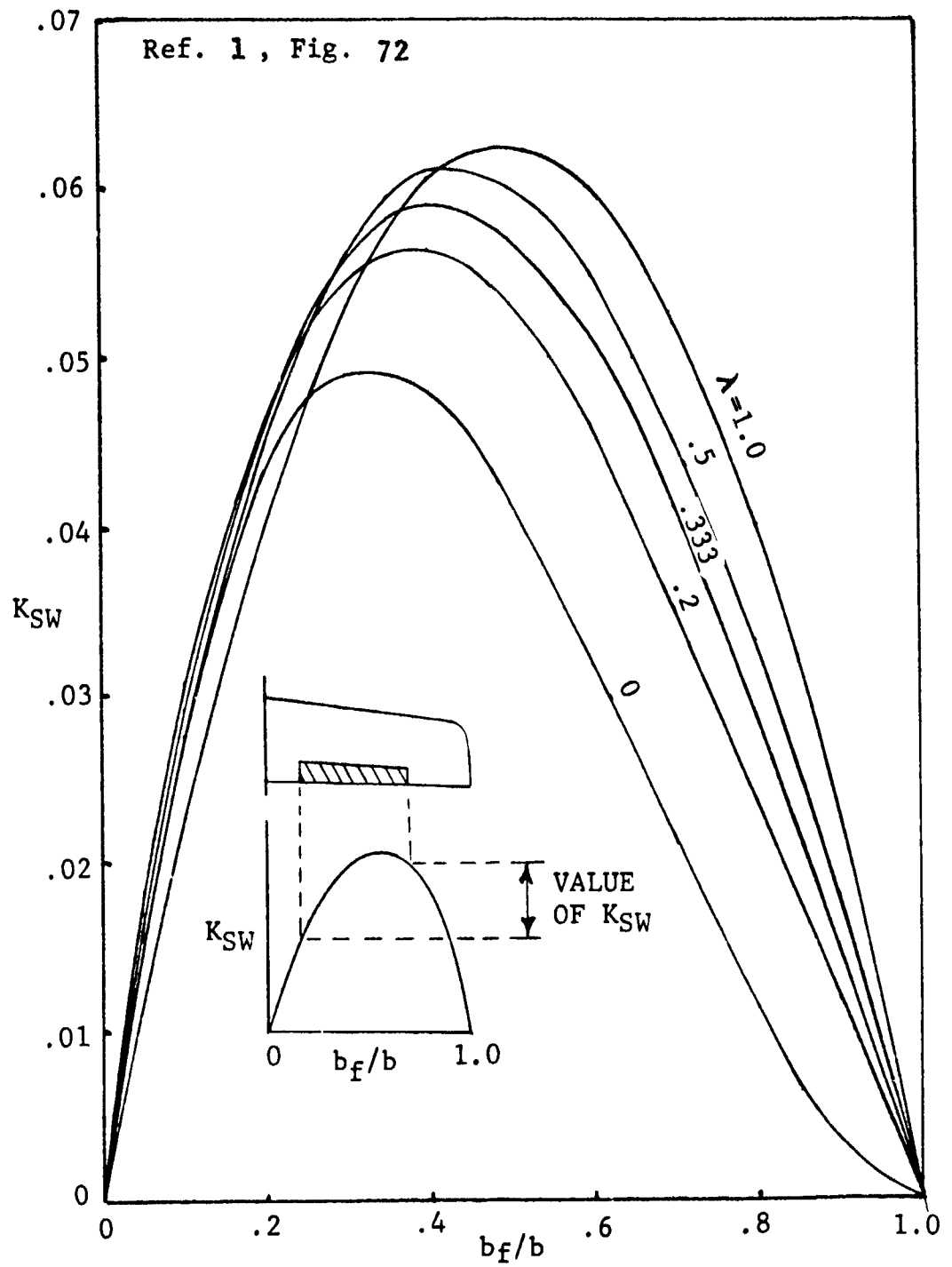Methods presented in Sections 3 through 7 of this report are used to evaluate the aerodynamics of the undamaged aircraft. Damage effects are computed on an incremental basis and are added to the estimates for the undamaged aircraft. Most empirical methods used to evaluate damage were selected from literature although some were developed in the course of this study to fulfill a need. These damage evaluation methods, combined with the basic aircraft aerodynamic prediction procedures in a computerized procedure, can provide the user with a convenient and systematic method to evaluate the aerodynamic effects of a broad range of aircraft damage.

8.1 MINIMUM DRAG

8.1.1 Roughness

Surface roughness is commonly grouped into two broad categories: distributed and discrete elements. Distributed roughness drag is characterized as a drag increment caused by sand particles of constant height, k, which are closely spaced in such a way that each lies completely in the wake of the others. Discrete roughness drag is characterized by roughness elements that are separated enough that the disturbances from an element will have died out before the next roughness element is reached.

The level of skin friction, when affected by roughness, follows the same turbulent drag law as a smooth surface as long as the protuberances on the rough surface are deeply submerged within the laminar sublayer of the boundary layer. Above a critical level of Reynolds number the drag is essentially constant.

The value of k is determined by relating the drag of a roughened plate to the appropriate sandgrain roughness height that produces the same drag. For instance, A.D. Young (Reference 39) found that the equivalent sandgrain roughness for camouglage paints is approximately 1.6 times the size of the mean geometrical protusions.

Typical values of k associated with various aircraft components
and surface conditions are presented in References 40 and 41.
A summary of these values is given in Table 8-1. Results pre-
sented in Reference 41 show that there is a fairly rapid increase
in roughness drag as the paint becomes blistered when exposed to
thermal radiation. Roughness rapidly reaches a plateau and stays
fairly constant with increasing heat absorption. When heat causes
the skin to debond, melt, or suffer other damage, the profile drag
becomes the dominant effect, and skin friction or roughness is no
longer meaningful.

TABLE 8-1 TYPICAL ROUGHNESS VALUES

Surface or Conditions of Surface	Roughness k ~ Inch
Average aircraft wing or tail surface	.0006
Average fuselage, nacelle surface	.0012
Aluminum skin with blistered paint	.0012
Fiberglass/Enamel with blistered paint	.0025
Fiberglass/Thick coatings and graphite with blistered paint	.0030
Broken Skin	.01
Exposed Honeycomb	.1

The total aircraft drag increase due to localized areas of
distributed roughness is equal to the sum of the increments from
all aircraft components. The component drag increment due to
surface roughness can be determined from the equation

$$\Delta C_D = (C_{f_R} - C_f)\frac{\Delta A_{wet}}{S_{ref}} \cdot FF \qquad (8-1)$$

where C_{f_R} is a composite skin-friction coefficient that includes
boundary-layer effects ahead of and behind the roughened region,
C_f is the skin friction coefficient of the undamaged component,
ΔA_{wet} is the wetted area affected by roughness and FF is a form
factor that relates friction drag of the three-dimensional component
to the 2-D flateplate friction drag. The flat-plate skin-friction
coefficient, C_f, is determined by the methods presented in Section
3.1.1.

143

The composite skin-friction coefficient, C_{f_R}, is defined by

$$C_{f_R} = \frac{2\,\theta_{TE}}{L} \qquad (8\text{-}2)$$

where the trailing-edge momentum thickness, θ_{TE}, must be solved for by an iterative process.
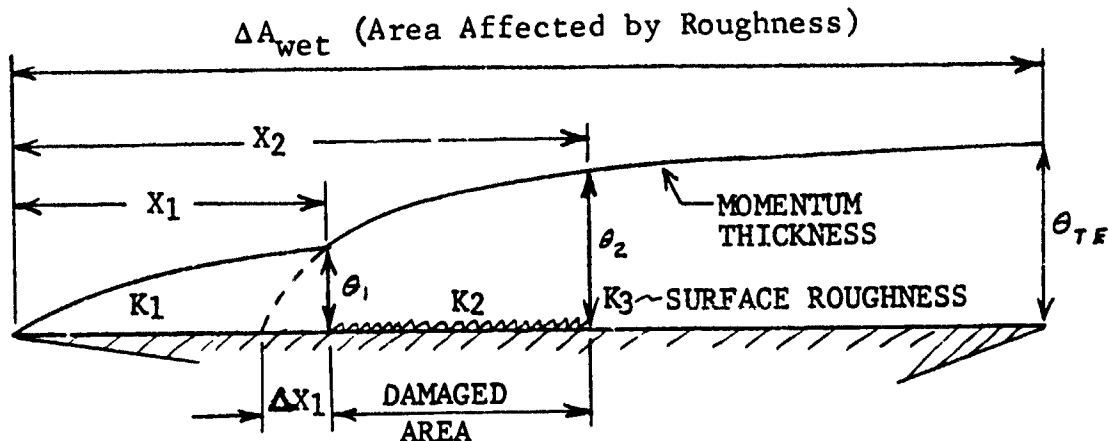
Figure 8-1 MOMENTUM THICKNESS PROFILE

The momentum thickness in the increased roughness area between X_1 and X_2 acts as if it starts at distance ΔX_1 ahead of the transition point X_1 as indicated in Figure 8-1. The momentum thickness at X_1, X_2 and the trailing edge are determined from the following equations:

$$2\,\theta_1 \equiv X_1 \quad C_f(k_1, X_1) = \Delta X_1 \cdot C_f(k_2, \Delta X_1) \qquad (8\text{-}3)$$

$$2\,\theta_2 \equiv (\Delta X_1 + X_2 - X_1) \cdot C_f \quad (k_2, \Delta X_1 + X_2 - X_1) \qquad (8\text{-}4)$$

$$= \Delta X_2 \cdot C_f(k_3, \Delta X_2)$$

$$2\,\theta_{TE} = (\Delta X_2 + L - X_2) \cdot C_f(k_3, \Delta X_2 + L - X_2) \qquad (8\text{-}5)$$

144

The value of ΔX_1 can be solved for by iterating on ΔX_1 until the right side of Equation 8-3 matches the left. The value of ΔX_2 is obtained in a similar iterative fashion from Equation 8-4. Finally, the value of θ_{TE} can be determined from Equation 8-5 and substituted into Equation 8-2 to define C_{f_R}.

8.1.2 Forward-Facing Steps

Reference 6 presents the following method that is used to evaluate the drag of forward-facing steps. The drag of N steps of average height, h, and width, w, uniformly distributed on a body between X_1 and X_2 is given by

$$C_{D_{\substack{\text{Fwd-Facing} \\ \text{Step}}}} = C_P \frac{w \cdot h}{S_{ref}} \sum_{i=1}^{N} \left(\frac{q_{eff}}{q_\infty} \right)_i \qquad (8-6)$$

and for a surface

$$C_{D_{\substack{\text{Fwd-Facing} \\ \text{Step}}}} = C_P \frac{w \cdot h}{S_{ref}} \sum_{i=1}^{N} m \cdot \cos^n \Lambda \cdot \left(\frac{q_{eff}}{q_\infty} \right)_i \qquad (8-7)$$

where

C_P = local pressure coefficient as shown in Figure 8-2.
Λ = sweep angle of the step
n = 3, for forward-facing steps
m = magnification factor. Effect caused by the pressure gradients on the boundary layer downstream of the step.
    m=1, for bodies or wing lower surface
    m=Factor for wing upper surface, see Figure 8-3

$\left(\dfrac{q_{eff}}{q_\infty} \right)_i$ = Effective local dynamic pressure ratio as determined from the 1/7th power law of velocity distribution and Prandtl's relationship for turbulent-flow boundary layer thickness :

$$\left(\frac{q_{eff}}{q_\infty} \right)_i = 7/9 \left(\frac{h}{\delta_i} \right)^{2/7} \quad \text{for } h \le \delta \qquad (8-8)$$

$$\left(\frac{q_{eff}}{q_\infty} \right)_i = 1 - 2/9 \left(\frac{\delta_i}{h} \right) \quad \text{for } h > \delta \qquad (8-9)$$

where

$$\delta_i = \frac{.37 \, X_i}{(R_{N X_i})^{1/5}} \qquad (8-10)$$
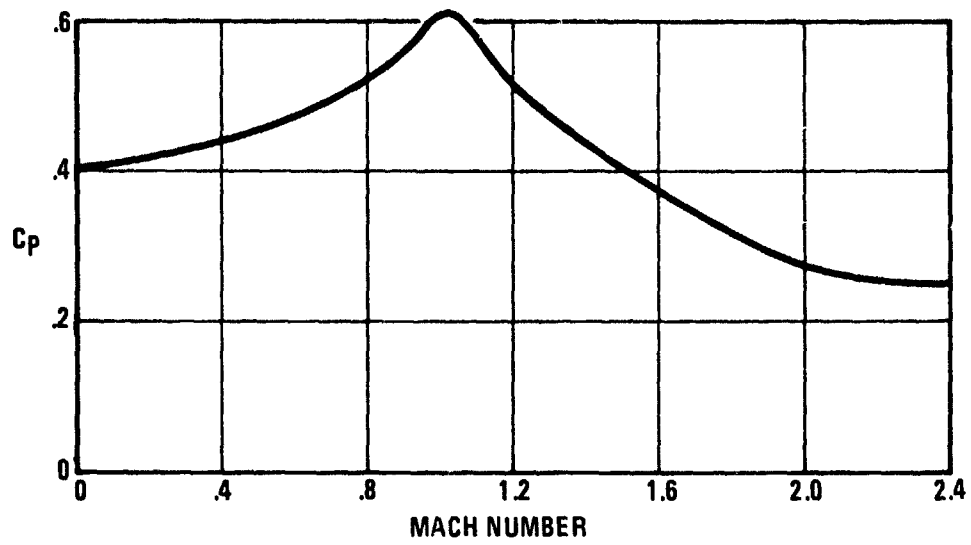
Figure 8-2   Pressure Coefficient on Fwd-Facing
            Steps
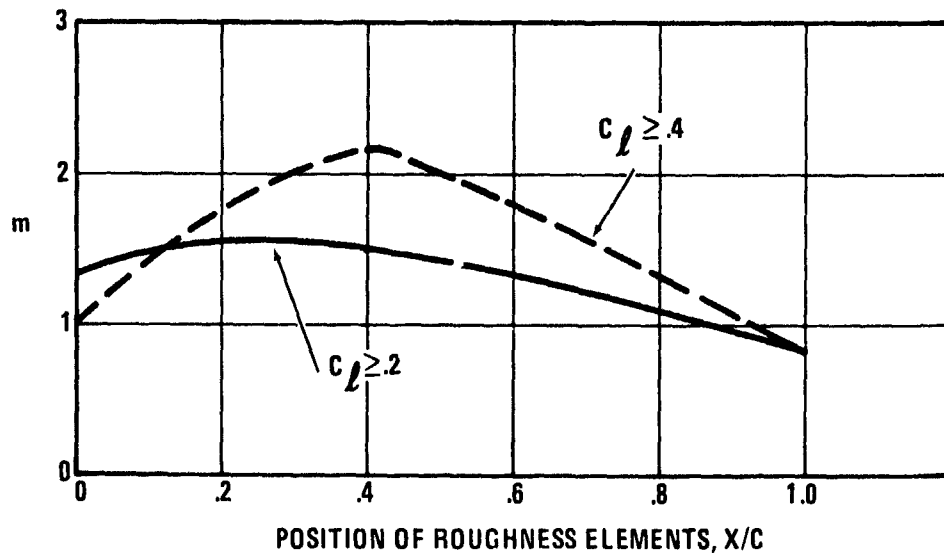
Figure 8-3   Roughness Drag Magnification Factor for
            Wing Upper Surface

8.1.3 Aft-Facing Steps

Methods used to estimate the drag of aft-facing steps are identical to those for the forward-facing steps with the following exceptions:

- The sign of the equations must be reversed.

- C_p, the local pressure coefficient is shown in Figure 8-4.

- n=2, for aft-facing steps.

8.1.4 Caved-in and Missing Panels

The drag due to N gaps or holes of average width, w, length 1, and depth, h, uniformly distributed between X_1 and X_2 is given by a method presented in Reference 6.

$$C_{D_{Holes}} = K_{COMP} \frac{w \cdot h}{S_{ref}} \sum_{i=1}^{N} (m \cdot C_{D_o}) \qquad (8-11)$$

where

K_{COMP} = compressibility factor, see Figure 8-5.

C_{D_o} is determined from Figure 8-6 for holes where panel is missing and from Figure 8-7 for holes where panel is caved in.

For bodies,

   m=1, unless in fuselage over wing

   m=2.31, for holes over wing/glove region.

For surfaces,

   m=1, for lower surfaces

   m=Factor for wing upper surface, see Figure 8-3.

Figure 8-4   Pressure Coefficient on
Aft-Facing Steps

Figure 8-5   Compressibility Factor

148

Figure 8-6 Drag Coefficient of Holes in Panels

Figure 8-7 Drag Coefficient of Caved-In Panels

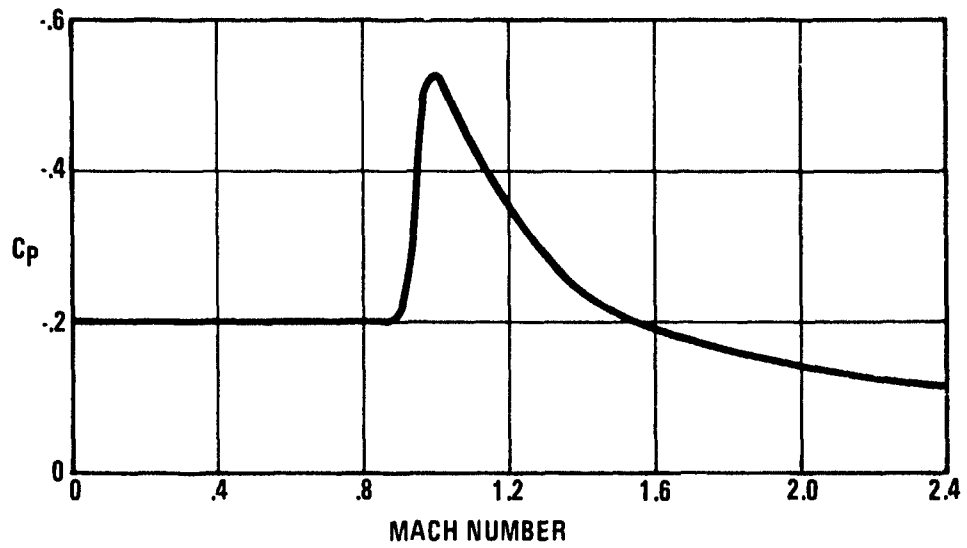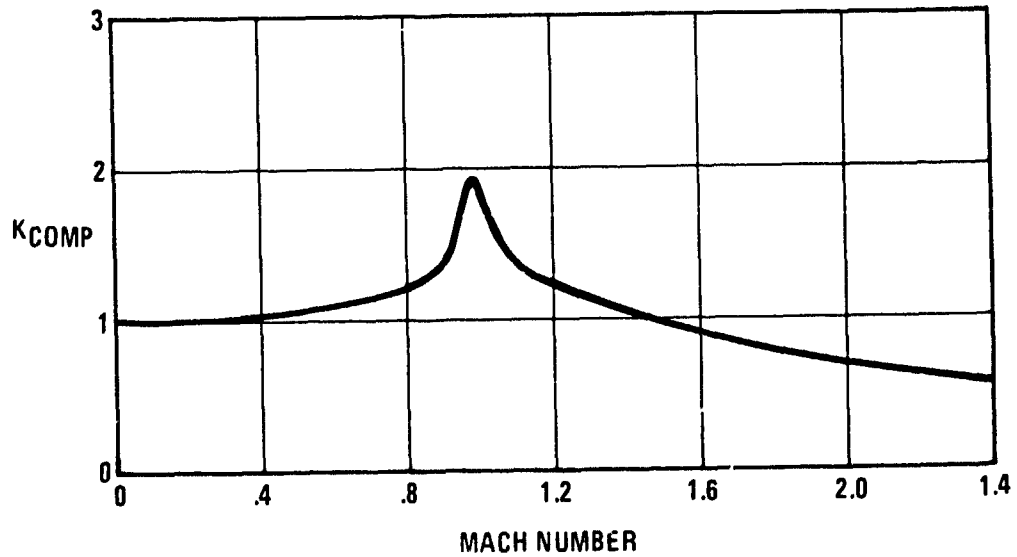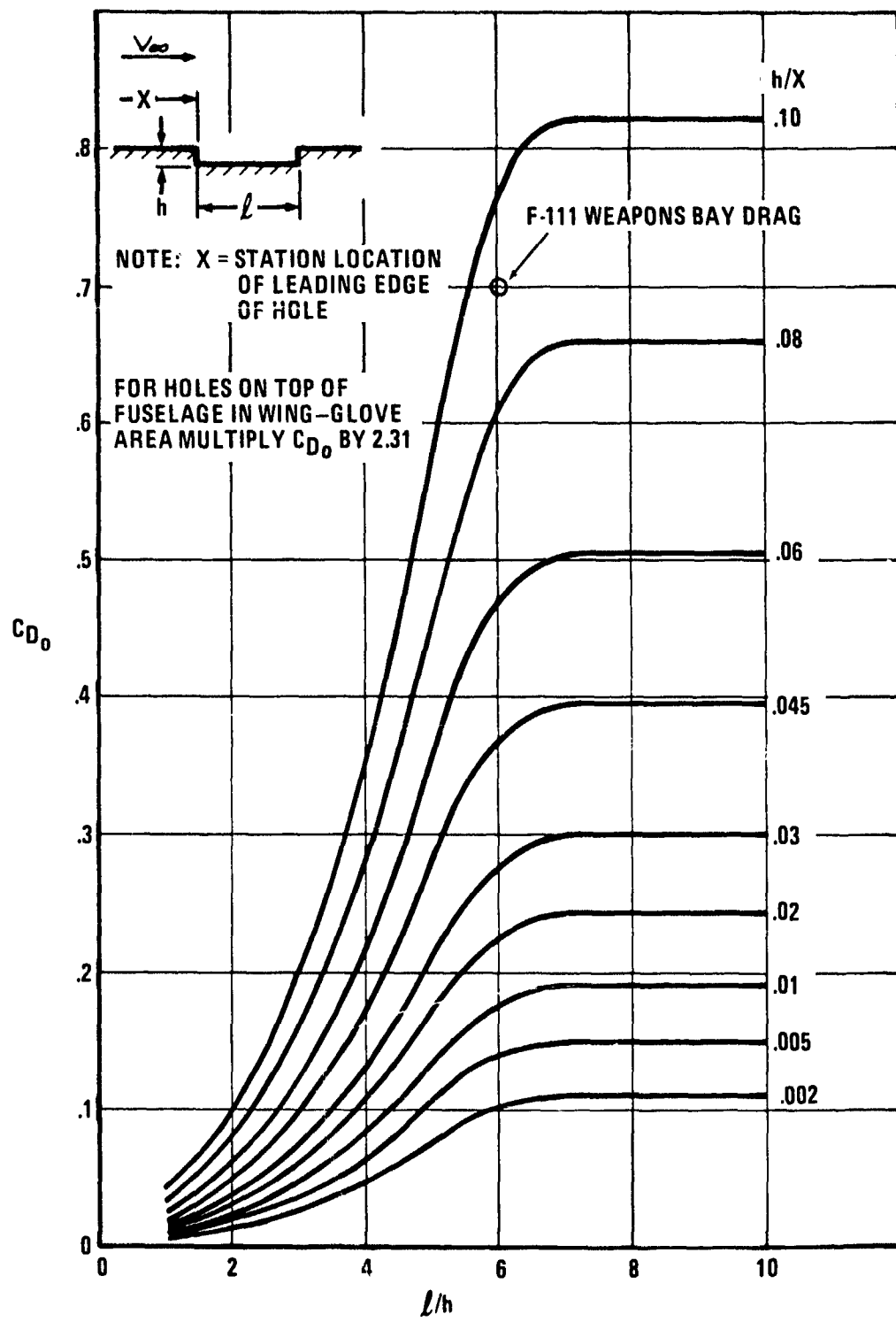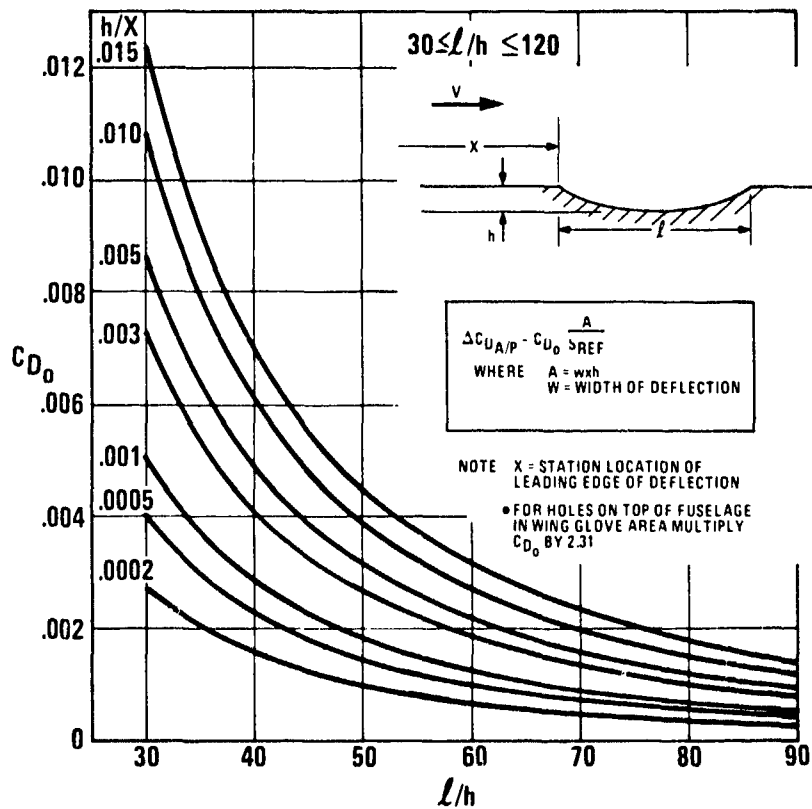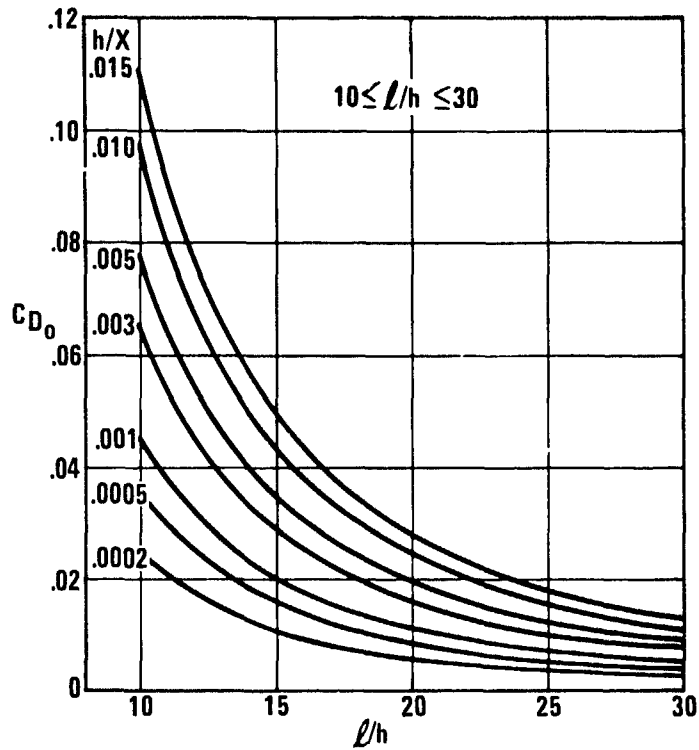The C_{D_O} for holes was developed by extending generalized data curves presented by Hoerner (Reference 7) for small gaps and holes. Wind tunnel data on the F-111 weapons bay and other data presented in Reference 42 were used in the extension of Hoerner's data.

8.1.5 Waviness

Panels that have been protruded or indented in a smooth manner by overpressure are treated as waves. Hoerner (Reference 7) shows the drag due to N waves of height, h, span, w, and length, 1, uniformly distributed from X_1 and X_2 for subsonic flow as

$$C_{D_{Waviness}} = 15 \cdot (h/1)^2 \frac{h \cdot w}{S_{ref}} \sum_{i=1}^{N} (m \cdot \frac{q_{eff}}{q_\infty})_i \qquad (8\text{-}12)$$

and for supersonic flow as:

$$C_{D_{Waviness}} = \frac{9.87}{\sqrt{M^2-1}} (h/1) \frac{h \cdot w}{S_{ref}} \sum_{i=1}^{N} (m)_i \qquad (8\text{-}13)$$

where (q_{eff}/q_∞) is described in Section 8.1.2 and m is discussed in Section 8.1.4.

8.1.6 Protuberances

Arbitrary objects which are not represented by the previous roughness methods can be handled as protuberances. The drag is estimated by:

$$C_{D_{Prot}} = \left(\frac{q_{eff}}{q_\infty}\right) \frac{\Delta f}{S_{ref}} \qquad (8\text{-}14)$$

where $\left(\frac{q_{eff}}{q_\infty}\right)$ is calculated as described in Section 8.1.2 and Δf

is the equivalent parasite drag area of the element in freestream.

8.1.7 Bluntness

Loss of the nose radome causes additional bluntness drag on the fuselage, which is also evaluated by the AAT procedure. The original objective was to account for drag due to a missing radome, but program logic is included to calculate bluntness on any component represented as a body.

Bluntness drag is estimated in two steps. First, data from Reference 43 were used to derive the drag due to shortening the nose length of a body while maintaining a spherical nose shape, the radius of which equals the radius of the original body at the point where the nose is severed. This drag increment is shown

151

in Figure 8-8. The slopes of the body are unchanged aft of the severed nose radome. This simulates a fuselage with radome replaced with a spherical shape. The second step is to estimate the increase in drag caused by decreasing the length of the nose shape at the point of sever. Data in Reference 44 were used to derive the effect of reducing the nose fineness ratio from that of a spherical shape to a completely flat nose. This drag increment is shown in Figure 8-9.

The drag of a blunted body is estimated in the AAT computer code as

$$C_{D_{Bluntness}} = \left(C_{D_o}\right)_1 \frac{A_{max}}{S_{ref}} + \left(C_{D_o}\right)_2 \frac{A_F}{S_{ref}} \tag{8-15}$$

where

$\left(C_{D_o}\right)_1$ is determined from Figure 8.8.

$\left(C_{D_o}\right)_2$ is determined from Figure 8-9.

A_{max} = Body maximum frontal area.

A_F = Body frontal area at point of severed nose fairing.

8.1.8 Missing Parts of Surfaces

Loss of a segment of a surface may cause serious aerodynamic problems. If it is a lifting surface the minimum drag, lift, drag due to lift, pitching moments, and rolling moments may all be affected. Effects on the minimum drag only are discussed in this section, and other effects are discussed in later sections.

Loss of a section of a surface decreases the wetted area which results in a decrease in minimum drag. The estimate for the drag decrease is made by reducing the component friction drag by the same percentage as the reduction in wetted area. This estimate is made to account for loss of a wing tip, wing trailing edge, or a portion of any other surface.

Loss of a segment of the wing leading edge or trailing edge also causes a bluntness drag or base drag that is more predominant than the friction drag. Minimum drag due to the loss of surface trailing edge is estimated by a method presented by Hoerner

152
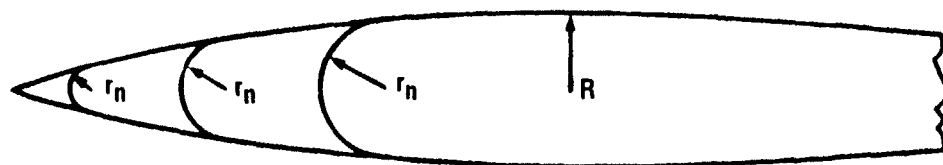
REF: NACA RM L53D14a

Figure 8-8   Effect of Nose Fineness Ratio on Drag

Figure 8-9   Effect of Nose Flatness on Drag

154

(Reference 7, page 3-22) for base drag less a term for the loss in wetted area friction drag.

$$\Delta C_{D_{TE}} = \frac{0.34}{(C_f)^{1/3}} \cdot \left(\frac{\Delta c}{c}\right)^{4/3} \cdot \left(\frac{t}{c}\right)^{4/3} \cdot \frac{\Delta b \cdot c}{S_{ref}} + C_f \frac{\Delta \eta (c - c')}{S_{ref}} \quad (8-16)$$

where Δb and Δc are the spanwise and chordwise dimensions of the missing trailing-edge panel, c is the average chor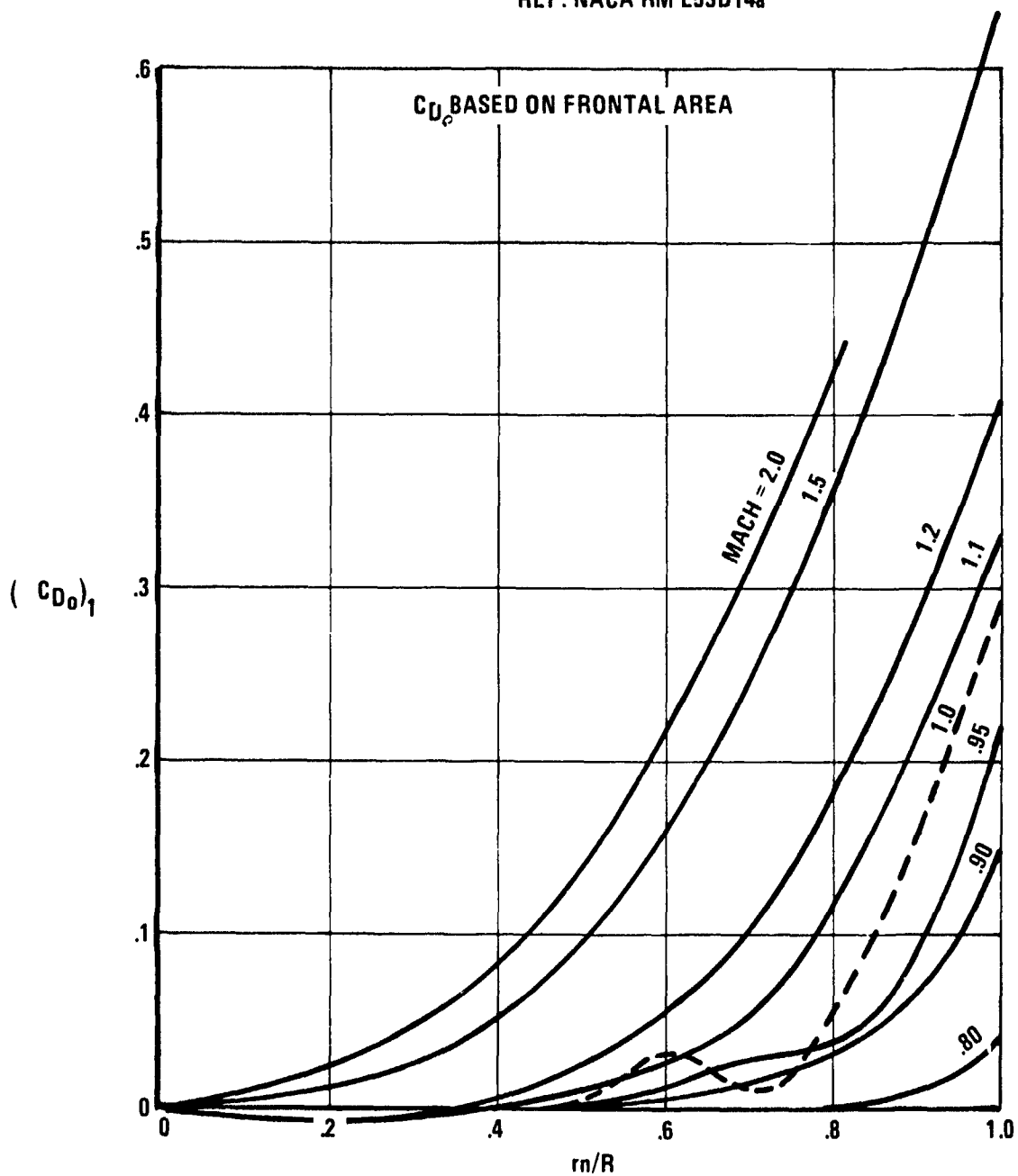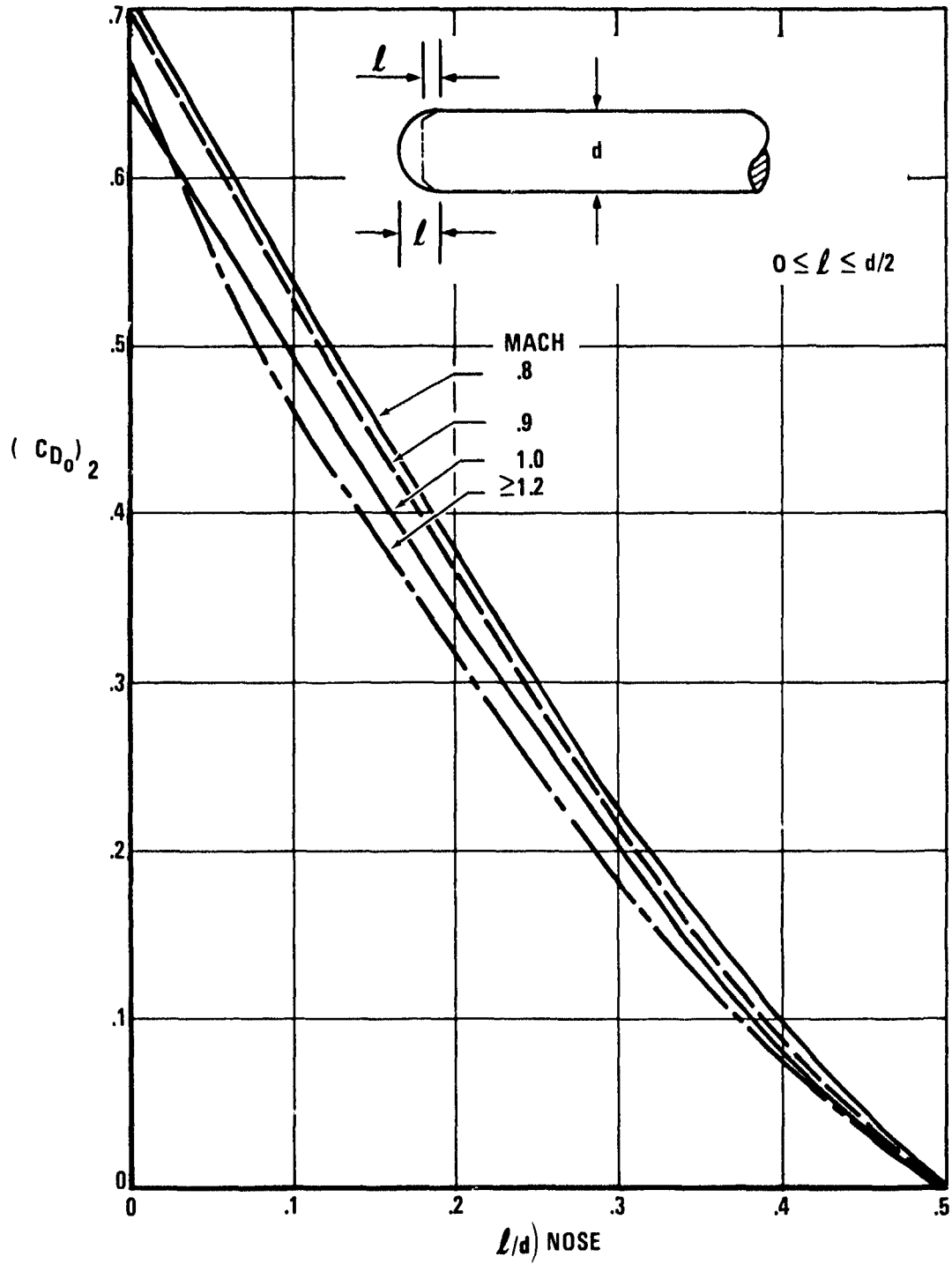d of the wing in the damaged area, and C_f is the coefficient of skin friction of the local airfoil ahead of the damage.

The drag due to missing or blunted leading edges can be estimated from the method presented in Reference 40 as

$$\Delta C_{D_{LE}} = F \frac{z/c}{t/c} \frac{\Delta b \cdot c}{S_{ref}} \quad (8-17)$$

where

$F = .010$ if damaged LE has round corners.

$= .015$ if damaged LE has sharp corners.

The ratio z/c to t/c is the thickness at the leading edge to the maximum wing thickness in the damaged region.

8.2   LIFT-CURVE SLOPE

Each type of damage that is accounted for in the AAT computer code affects the minimum drag level of the aircraft. Some types also reduce the lifting capability and necessitate an increase in the angle of attack required to sustain a given flight condition. These lift effects are accounted for in the program with an estimate of the incremental lift-curve slope caused by each of the lift-reducing types of damage. Final results are printed out as increments in angle of attack at constant lift.

8.2.1 Wing Leading-Edge and Trailing-Edge Cutouts

Wing cutouts, which result from the loss of a leading-edge or trailing-edge control device, disturb the air flow and change the lift-curve slope, pitching moment, and drag. AAT estimates for the effects on lift-curve slope are based on theoretical trends that were developed with the aid of Carmichael procedure, which is discussed in Reference 45. The Carmichael procedure is a subsonic/supersonic finite-element lifting-surface method developed for the NASA/Ames Research Center.

A matrix of wings was devised to cover variations of aspect ratio, sweep, cutout size, and cutout location. Twenty-four wings were selected from this matrix and evaluated with the Carmichael procedure to establish empirical charts for the effect of cutouts, for any arbitrary wing, on the lift-curve slope and aerodynamic center. Aspect ratio was varied from 0 to 40.0 degrees, taper ratio was held constant at 0.25, and the planform area was also held constant. Sixteen spanwise panels and eleven chordwise panels were used in the representation of each of the wings. Figures 8-10, 8-11, and 8-12 show the paneling scheme applied to three baseline wings with different sweep and aspect ratio.

Cutouts, with a 20 percent chord, were made in the leading edge and trailing edge of each of the basic wings. The spans and locations of these cutouts were systematically varied to produce data from which trends could be established. Figure 8-13 shows a sketch of cutout locations, and Table 8-2 shows the theoretical lift-curve slope for each wing evaluated.

The theoretical trends in incremental lift-curve slope due to a leading-edge cutout were empirically matched by the following equation:

$$\Delta C_{L_{\alpha\ LE}} = (\Delta C_{L\alpha_1} + \Delta C_{L\alpha_2} + \Delta C_{L\alpha_3}) \frac{\Delta C_{L_\alpha}}{\Delta C_{L_\alpha\ .2\ \bar{c}}} \qquad (8\text{-}18)$$

Equation 8-18 is for symmetric damage for both left and right wings. If only one side is damaged, this increment should be reduced by 50 percent.

TABLE 8-2   CALCULATED POTENTIAL LIFT-CURVE SLOPES

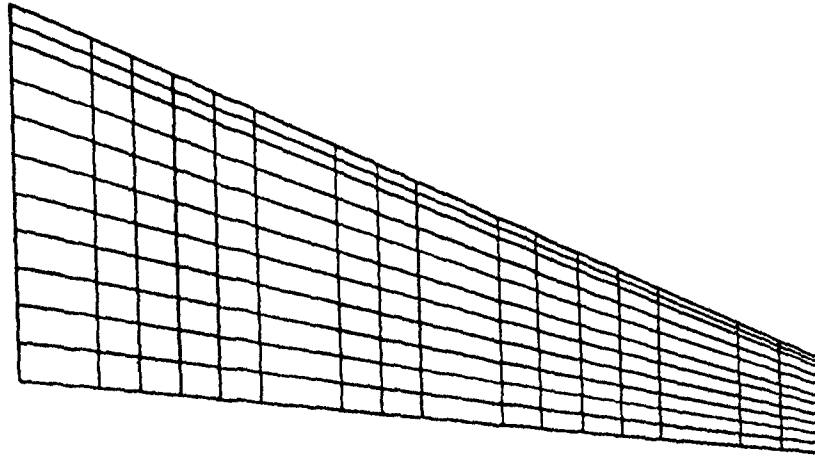| AR	$\Lambda c/4$	BASELINE WING	CUTOUT A	CUTOUT B	CUTOUT C	CUTOUT A+B+C	CUTOUT X	CUTOUT Y	CUTOUT Z	CUTOUT X+Y+Z
3	20	.0607		.0582				.0583		
3	40	.0570		.0544				.0544		
5	20	.0775		.0736				.0738		
7	0	.0889		.0841				.0844		
7	20	.0867	.0825	.0820	.0836	.0752	.0813	.0823	.0840	.0758
7	40	.0730		.0689				.0694		

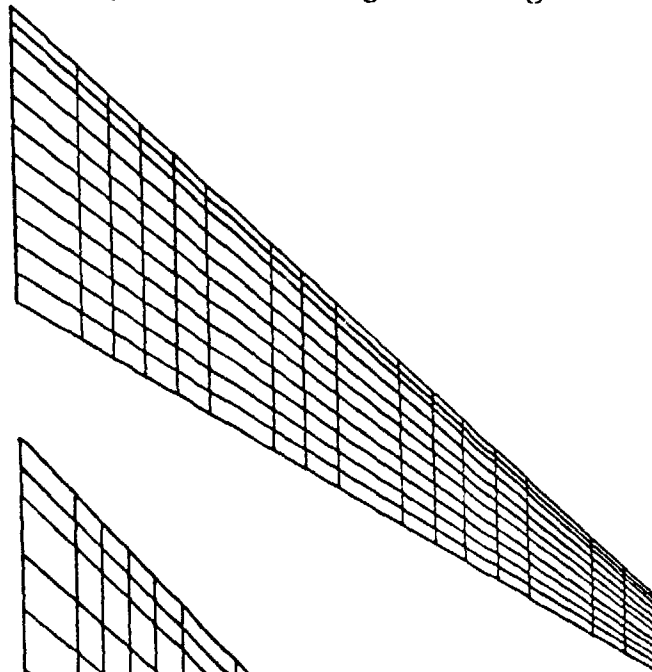Figure 8-10   Wing Paneling Scheme, $AR = 7$, $\Lambda_{C/4} = 20^{\circ}$

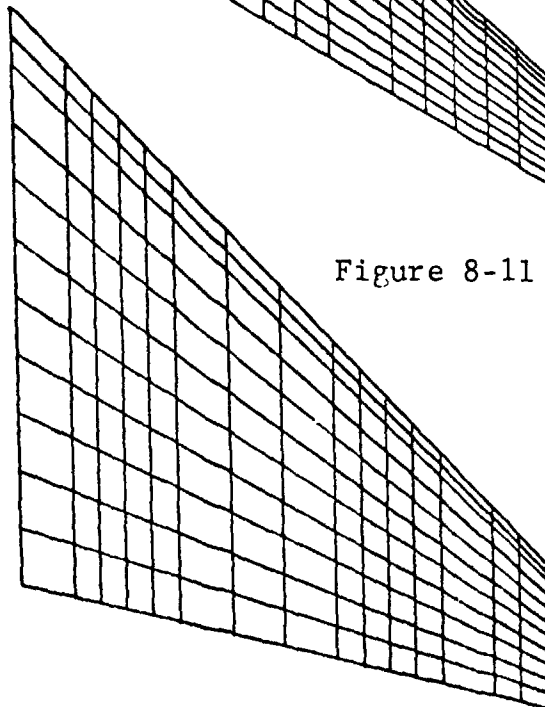Figure 8-11   Wing Paneling Scheme, $AR = 7$, $\Lambda_{C/4} = 40^{\circ}$

Figure 8-12   Wing Paneling Scheme, $AR = 3$, $\Lambda_{C/4} = 40^{\circ}$
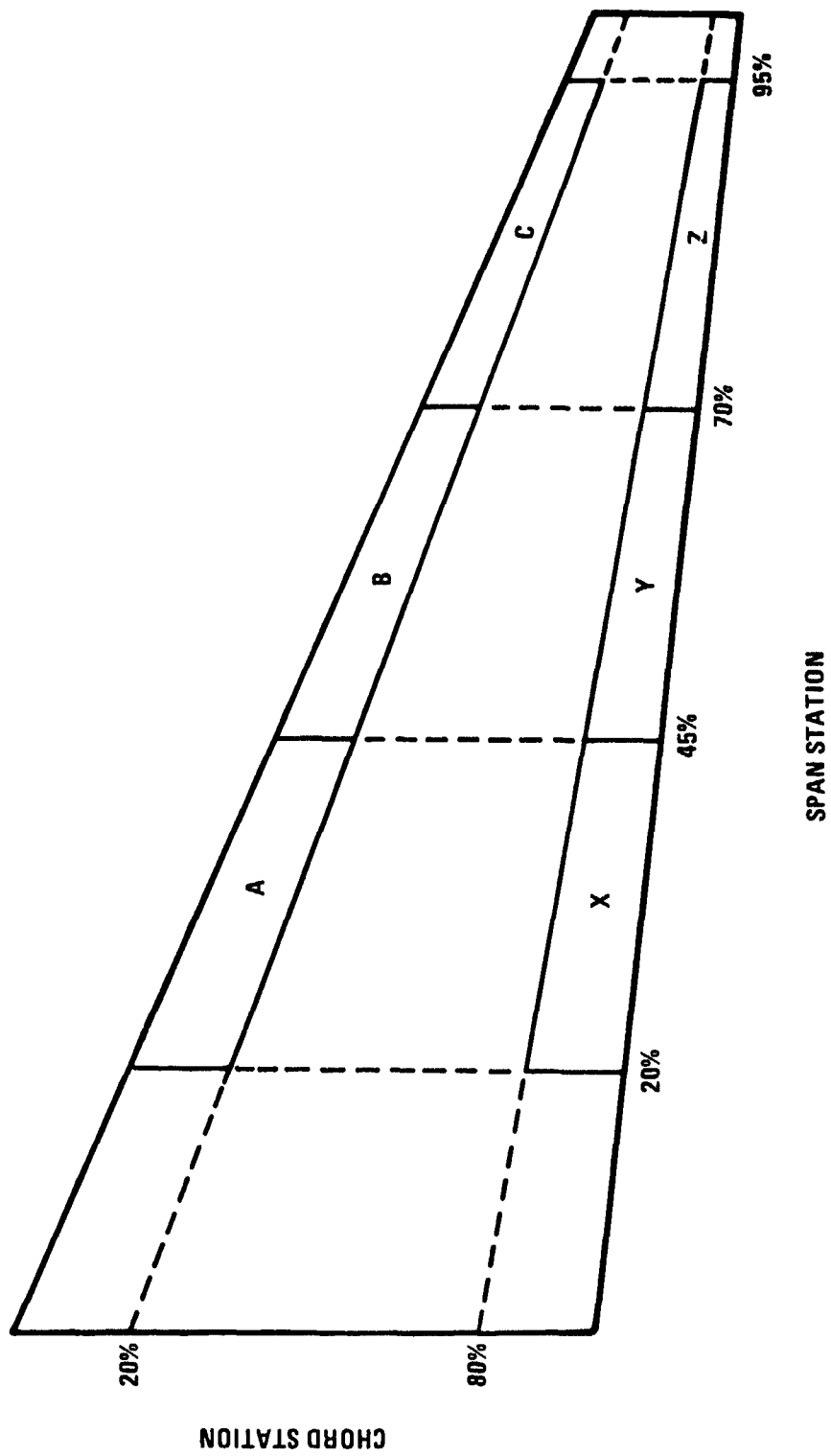
157

Figure 8-13 Cutout Locations

158

The incremental lift-curve slopes for leading-edge cutouts, shown in Figure 8-14, were developed from cross-plotting the theoretical data. Figure 8-14a shows the increment $\Delta C_{L_{\alpha_1}}$ for the cutout of 20 percent chord length, beginning at the 45 percent span station on a wing with a 20-degree quarter-chord sweep. This configuration was selected as the baseline cutout. Deviations from this configuration are accounted for with additional increments. The increment for the effect of wing quarter-chord sweep, $\Delta C_{L_{\alpha_2}}$, and cutout spanwise location, $\Delta C_{L_{\alpha_3}}$, are shown in Figures 8-14b and 8-14c. The effect of changing the outboard chord length is estimated with a multiplication factor shown in Figure 8-14d that was derived from data presented in Reference 46. These data determined the reduction in lift-curve slope caused by a rectangular, central cutout on a wing as a function of cutout chord length.

Data from the Carmichael runs also established the increments for trailing-edge cutouts shown in Figure 8-15. Data from Reference 46 are also used to account for the effect of trailing-edge-cutout chord length. The incremental lift-curve slope due to trailing-edge cutout is

$$\Delta C_{L_{\alpha\ TE}} = \left(\Delta C_{L_{\alpha\ 4}} + \Delta C_{L_{\alpha\ 5}} + \Delta C_{L_{\alpha\ 6}} \right) \frac{\Delta C_{L_\alpha}}{\Delta C_{L_{\alpha.2}}\ \bar{c}} \qquad (8-19)$$

Equation 8-19, like Equation 8-18, is also for symmetric wing damage. If only one wing is damaged, $\Delta C_{L_{\alpha\ TE}}$ should be reduced by 50 percent.

8.2.2 Missing Wing Tips

A missing wing tip, in the connotation used in the AAT description and utilization, means that an outboard section of the wing is missing. A missing wing tip is described by the fraction of wing semi-span that is lost ($\Delta \eta$), and may be as large as the exposed wing semi-span. The AAT procedure makes separate calculations for each wing; therefore, flexibility is provided for non-symmetrical damage to the wing tips. There are two aspects to the lift increment due to missing wing tips: potential lift and vortex lift.

Potential lift is computed by the method described in Section 6, and the incremental potential lift is determined as follows. Planform area, aspect ratio, taper ratio, and the ratio of fuselage diameter to wing span are computed for the damaged configuration and include the effects of the shortened wing span. Potential lift is calculated for the left and right wings independently since an arbitrary amount of missing span may be specified for each wing. The increment in potential lift-curve slope for each wing is
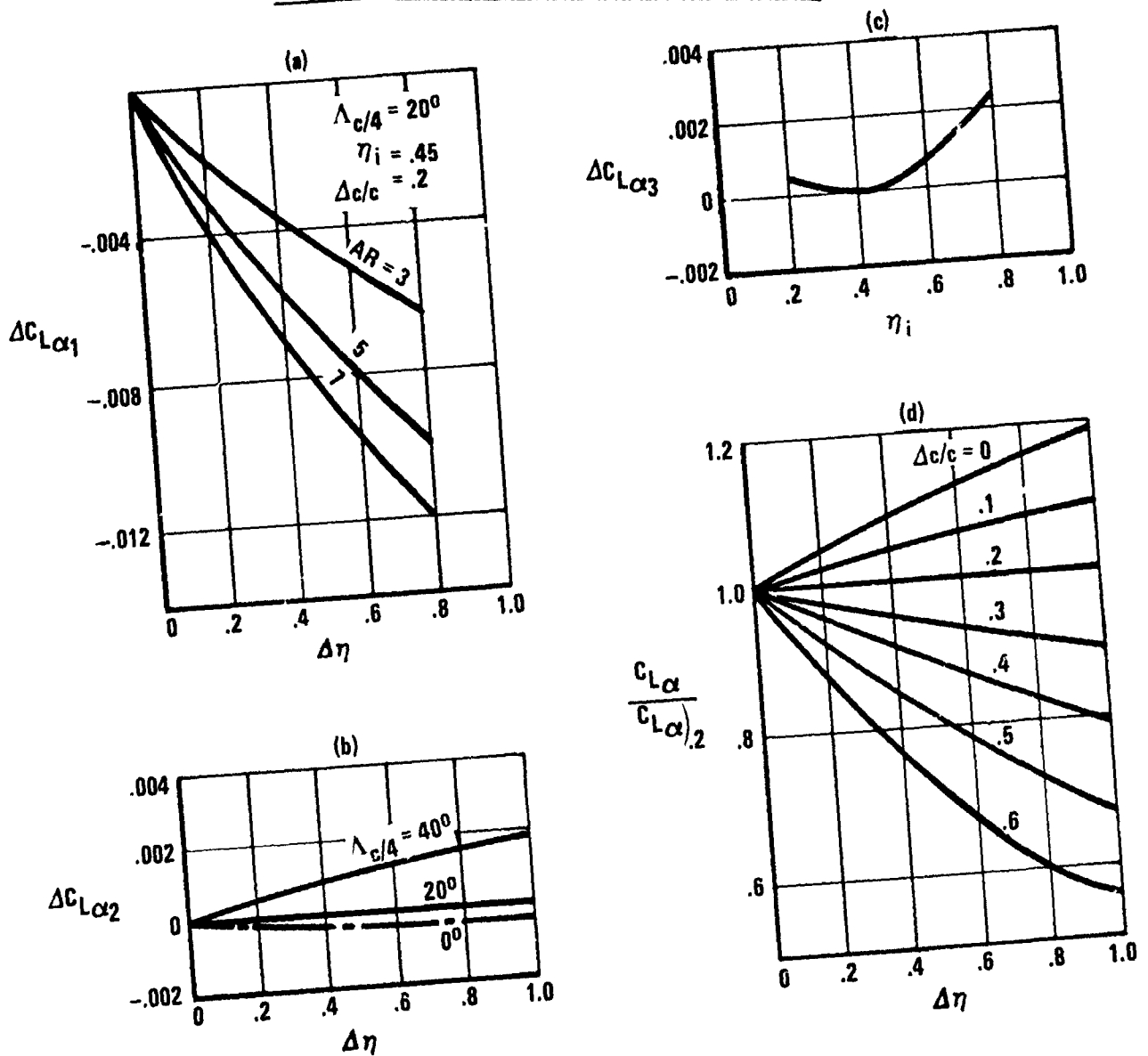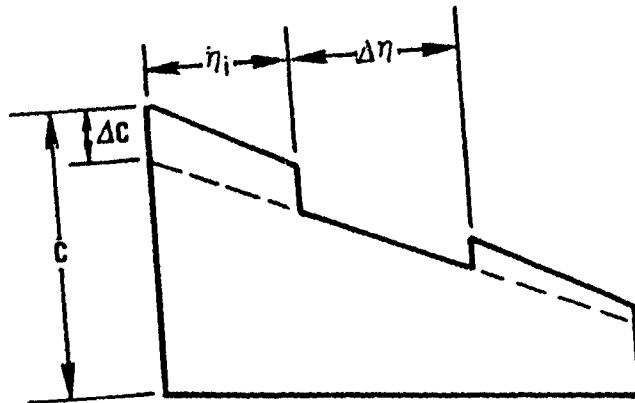
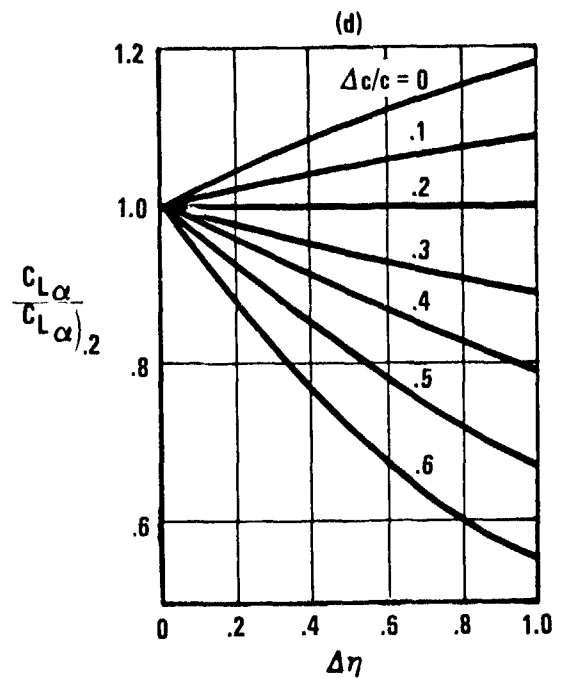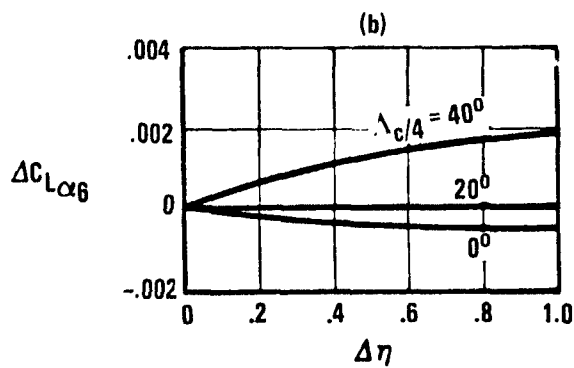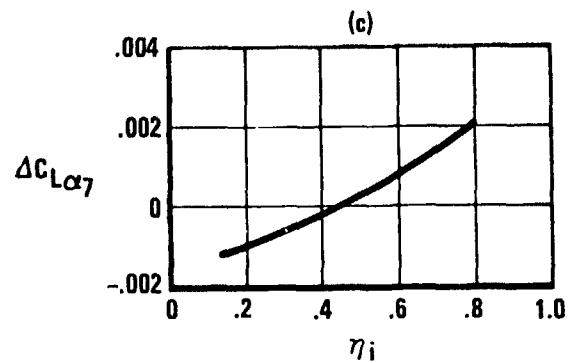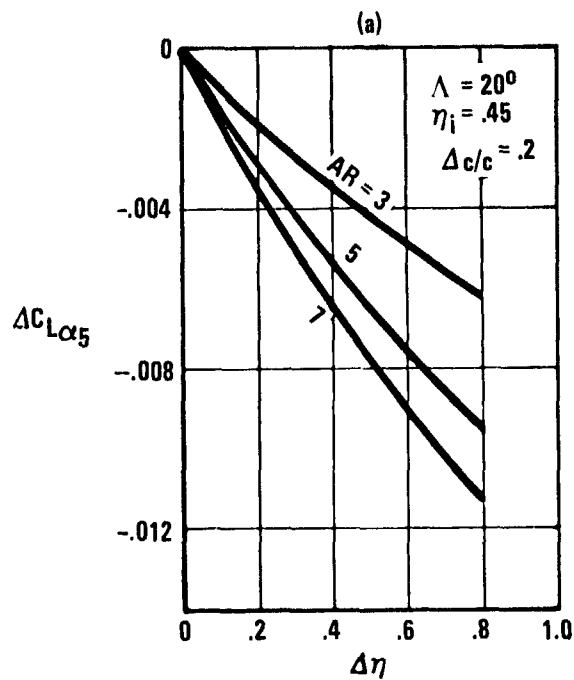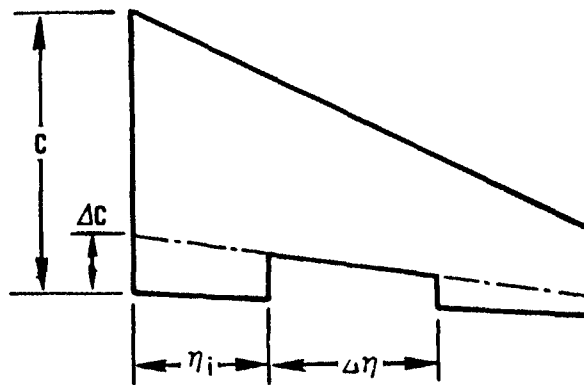Figure 8-14 Lift Increments Due to Leading-Edge Cutouts

Figure 8-15 Lift Increments Due to Trailing-Edge Cutouts

defined as the difference between the computed values for the damaged and undamaged wings. The total increment is defined as

$$\Delta C_{L_{\alpha}\text{ Potential}} = \Delta C_{L_{\alpha}\text{ Potential}\atop\text{Left}} + \Delta C_{L_{\alpha}\text{ Potential}\atop\text{Right}} \qquad (8\text{-}20)$$

Correlations with data indicate that the effect of the tip vortices can be a significant part of the total lift of low-aspect-ratio wings. Vortex lift methods that are used to compute the nonlinear lift of the undamaged aircraft are described in Section 6.7; however, a fast, alternative, linearized approximation to the change in vortex lift was derived for damage calculation.

Vortex-lift estimates for damage evaluation are based on an empirical correlation with wind tunnel data on a series of clipped wings presented in Reference 38. Potential lift predictions are compared with these data in Figures 6-10 through 6-13. Vortex lift was assumed to be the difference between the predicted potential lift and the wind tunnel data. Figure 8-16 shows the correlation that was derived for the vortex lift curve slope. Aspect ratio effects are predominant, while sweep effects are less significant and are ignored. The aspect ratio of the undamaged wing (AR) and the aspect ratio of the wing with a missing tip (AR') are used to estimate from Figure 8-16 the vortex lift for each wing. The change in vortex lift ($\Delta C_{L\alpha_{\text{vortex}}}$) is attributed to the missing wing tip.

This vortex lift increment is derived from subsonic data and must be adjusted for Mach number. Polhamus, in Reference 47 shows theoretically that vortex lift is fairly constant for Mach numbers below 1.0 and decreases to zero when the leading edge becomes sonic. This trend for the vortex lift is approximated with two straight line segments in the AAT procedure in the following manner. The Mach number at which the wing leading edge becomes sonic is defined by:

$$M_{\text{Sonic}} = 1/\cos \Lambda_{LE} \qquad (8\text{-}21)$$

and the vortex lift increment is defined by one of the following equations:

$$\Delta C_{L_{\alpha_{\text{Vortex}}}} = \Delta C_{L_{\alpha}\text{ Vortex}\atop\text{Subsonic}} \quad ; \quad M \le 1 \qquad (8\text{-}22)$$
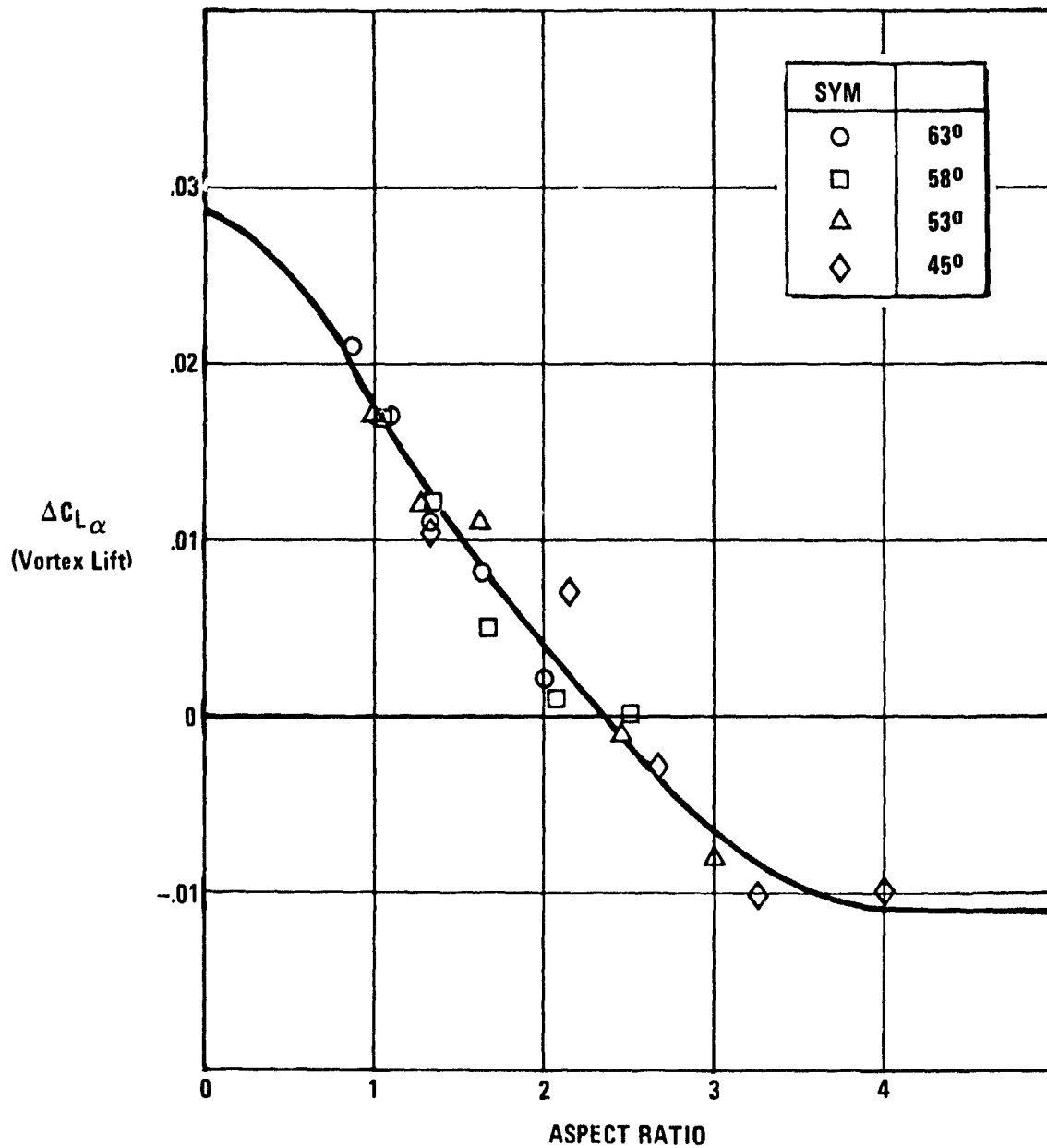
162

Figure 8-16 Vortex Lift Increment, M = .6

$$\Delta C_{L_{\alpha_{Vortex}}} = \Delta C_{L_{\alpha_{Vortex \atop Subsonic}}} \left(\frac{M'_{Sonic} - M}{M_{Sonic} - 1} \right) \quad ; \quad 1 < M < M_{Sonic} \qquad (8\text{-}23)$$

$$\Delta C_{L_{\alpha_{Vortex}}} = 0 \qquad\qquad\qquad\qquad ; \quad M \geq M_{Sonic} \qquad (8\text{-}24)$$

Vortex lift increments are computed independently for the effects of left and right wing tips missing, and the net effect is given by

$$\Delta C_{L_{\alpha_{Vortex}}} = \Delta C_{L_{\alpha_{Vortex \atop Left}}} + \Delta C_{L_{\alpha_{Vortex \atop Right}}} \qquad (8\text{-}25)$$

Vortex and potential lift increments are additive and the total increment in lift-curve slope due to missing wing tips is given by

$$\Delta C_{L_{\alpha_{Tips}}} = \Delta C_{L_{\alpha_{Potential}}} + \Delta C_{L_{\alpha_{Vortex}}} \qquad (8\text{-}26)$$

8.2.3 Wing Holes with Flow-Through Air

Reference 48 presents data from a wind tunnel test in which a full-scale A-4B was tested in the Ames Research Center's 40 x 80-foot wind tunnel to determine the effects of simulated and actual gun fire damage on the wing. Several damage configurations were tested that had holes in various locations of the upper and lower wing surfaces. Holes that allowed air to flow through the wing from the lower to the upper surface were found to cause a degradation in the lift-curve slope. Empirical factors have been derived from these data which relate the lift curve slope to the effective hole area, which is the minimum area of the air passage between surfaces. The lift-curve slope of a configuration with holes that allow air to flow through the wing is given by

$$C_{L_{\alpha}}' = C_{L_{\alpha}} \left(\frac{C_{L_{\alpha}}'}{C_{L_{\alpha}}} \right) \qquad (8\text{-}27)$$

where $C_{L_{\alpha}}'/C_{L_{\alpha}}$ is the ratio of lift-curve slopes between the damaged and undamaged configurations. Figure 8-17 shows this ratio as a function of effective hole area.

The incremental effect of holes with flow-through air on the lift-curve slope is given by

$$\Delta C_{L_{\alpha_{holes}}} = C_{L_{\alpha}}' - C_{L_{\alpha}} \qquad (8\text{-}28)$$

164

$$\frac{C_{L'_\alpha}}{C_{L_\alpha}}$$

EFFECTIVE HOLE AREA/WING PLANFORM AREA
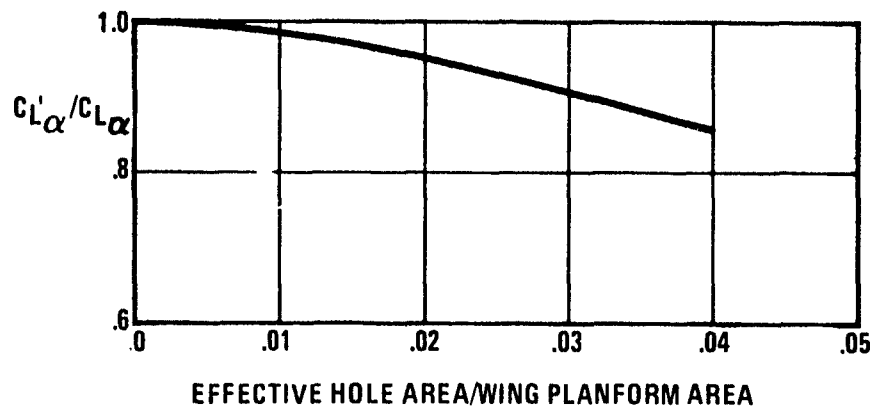
Figure 8-17 Effect of Flow-Through Air
on Lift Curve Slope

8.2.4 Horizontal Tail Damage

Loss of a section of the horizontal tail is specified in the AAT procedure by two input parameters: fraction of the left horizontal tail area missing and fraction of the right horizontal tail area missing. The lift-curve slope of the horizontal tail of zero deflection ($C_{L_{\alpha tail}}$) is calculated by the method presented in Section 6-2. Tail lift is estimated to be proportional to the tail planform area. Hence, the incremental lift curve slope is defined by

$$\Delta C_{L_{\alpha tail}} = -C_{L_\alpha \text{ tail}} \left(\frac{\text{Tail Area Lost}}{\text{Total Tail Area}} \right) \qquad (8-29)$$

8.2.5 Net Effect on Lift-Curve Slope

The net reduction in lift-curve slope is determined by summing the contributions from the components that are damaged.

$$\Delta C_{L_\alpha} = \Delta C_{L_{\alpha LE}} + \Delta C_{L_{\alpha TE}} + \Delta C_{L_{\alpha Tips}} + \Delta C_{L_{\alpha Holes}} + \Delta C_{L_\alpha \text{ Tail}} \qquad (8-30)$$

165

8.3   DRAG DUE TO LIFT

Aircraft damage that affects the lift-curve slope also affects the polar shape. These effects are accounted for by computing an increment in the polar shape factor for each of the types of damage.

8.3.1 Wing Leading-Edge and Trailing-Edge Cutouts

Cutouts on the leading edge or trailing edge of an aircraft wing produce an increment in the drag due to lift. These effects are accounted for by estimating the change in the parameters that are used to calculate the polar shape factor (K). Equation 4-2 defines the polar shape factor for the undamaged aircraft as

$$K = \frac{1-R}{C_{L_\alpha}} + \frac{R}{\pi eAR} \qquad (8-31)$$

The polar shape factor for the damaged aircraft is determined by estimating the effect of damage on the terms of Equation 8-31 and then recomputing the polar shape factor.

Parameters for the damaged aircraft are indicated with a prime ($'$) in the following discussion. The lift-curve slope for the aircraft with leading-edge and/or trailing-edge cutouts is defined as

$$C_{L_\alpha}' = C_{L_\alpha} + \Delta C_{L_{\alpha_{LE}}} + \Delta C_{L_{\alpha_{TE}}} \qquad (8-32)$$

where C_{L_α} is the lift curve slope of the undamaged aircraft and $\Delta C_{L_{\alpha_{LE}}}$ and $\Delta C_{L_{\alpha_{TE}}}$ are calculated by the methods described in Section 8.2.1.

The leading-edge suction parameter, R, is not affected by a trailing-edge cutout. A leading-edge cutout, however, reduces the suction over the span of the wing where the leading edge is missing. An estimate of this effect is made by reducing the leading-edge suction to 30 percent of its original value over the span where there are leading-edge cutouts.

$$R' = R (1-\Delta \eta) + 0.3 R (\Delta \eta) \qquad (8-33)$$

where $\Delta \eta$ is the fraction of wing span with the leading edge missing.

166

The Carmichael method was used to estimate the span efficiency of the zero-suction polars for each of the 24 wings described in Section 8.2.1. Full-suction polars from these wings' span load distributions were estimated by the Sivells-Neely method presented by Abbott and Von Doenhoff in Reference 49. From these zero- and full-suction polars, the span efficiencies were calculated. Attempts were made to develop trends in the span efficiency factors as a function of aspect ratio, sweep, cutout location, and cutout span. But the data were very erratic and trends were not sufficient to program into the AAT procedure. The data did, however, indicate a definite reduction in the span efficiency. Therefore, a nominal reduction of $\Delta e = -.05$ is assumed for all cases that have a leading-edge or trailing-edge cutout. The damaged-aircraft span efficiency is defined as

$$e' = e + \Delta e \qquad (8\text{-}34)$$

The adjusted values of lift-curve slope, leading-edge suction, and span efficiency are used to calculate the polar shape factor for an aircraft with cutouts.

$$K' = \frac{1-R'}{C_{L_\alpha}'} + \frac{R'}{\pi e' AR} \qquad (8\text{-}35)$$

The increment in polar shape factor due to leading-edge and trailing edge cutouts is defined by

$$\Delta K_{LE,TE} = K' - K \qquad (8\text{-}36)$$

8.3.2 Missing Wing Tips

Removal of the tip from a wing creates a shorter span, lower aspect ratio, and hence, an increase in the polar shape factor. A simple aspect ratio correction makes a good estimate of this damage effect. Aspect ratio is defined as

$$AR = \frac{b^2}{S_{plan}} = \frac{b^2}{\left(\frac{C_R + C_T}{2}\right)b} = \frac{2b}{C_R + C_T} \qquad (8\text{-}37)$$

and the incremental polar shape factor is defined as

$$\Delta K_{Tips} = K' - K = \frac{1}{\pi e\ AR'} - \frac{1}{\pi e\ AR} \qquad (8\text{-}38)$$

167

It is assumed that span efficiency is not affected by loss of a tip. Substitution of Equation 8-37 into Equation 8-38 gives

$$\Delta K_{Tips} = \frac{1}{\pi e \left(\frac{2b'}{C_R + C_T'}\right)} - \frac{1}{\pi e \left(\frac{2b}{C_R + C_T}\right)} \qquad (8-39)$$

$$\Delta K_{Tips} = \frac{1}{2 \pi e} \left(\frac{C_R + C_T'}{b'} - \frac{C_R + C_T}{b}\right) \qquad (8-40)$$

Equation 8-40 gives the change in polar shape factor in terms of the tip chords and spans of the undamaged and damaged wings.

8.3.3 Wing Holes with Flow-Through Air

The full-scale wind-tunnel data on an A-4B that are discussed in Section 8.2.3 were also used to derive an empirical relationship between the size of a passage that allows flow-through air and the span efficiency. This relationship, which is shown in Figure 8-18, is incorporated into the AAT procedure. The span efficiency of the damaged wing is defined as

$$e' = e\left(\frac{e'}{e}\right) \qquad (8-41)$$

and the incremental polar shape factor due to holes is defined by

$$\Delta K_{Holes} = K' - K = \frac{1}{\pi e' \ AR} - \frac{1}{\pi e \ AR} \qquad (8-42)$$

8.3.4 Horizontal Tail Damage

The lift increment due to horizontal tail damage is added to the lift of the undamaged aircraft along lines of constant angle of attack. No corresponding reduction in drag due to lift is assessed. The result is that horizontal tail damage is accounted for in the polar shape without having to compute an increment in the polar shape factor.
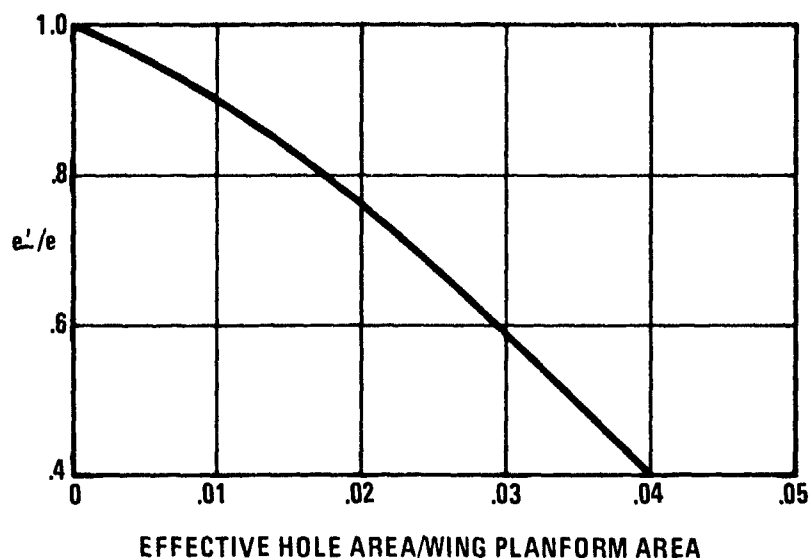
Figure 8-18   Effect of Flow-Through Air
on Wing Span Efficiency

8.3.5 Net Effect on Drag Due to Lift

The incremental polar shape factors computed in this section
are summed to determine a single increment that accounts for all
of the types of damage that affects drag due to lift. The total
incremental polar shape due to damage is

$$\Delta C_{D_L} = \Delta K \; C_L^2$$

where

$$\Delta K = \Delta K_{LE,TE} + \Delta K_{Tips} + \Delta K_{Holes}$$

(8-43)

169

8.4 PITCHING MOMENT

Aircraft pitching moments are affected by leading-edge and trailing-edge cutouts, missing wing tips, and horizontal tail damage. Wing damage is accounted for by calculating the change in pitching moment that results from an estimated movement of the wing-body aerodynamic center. Tail damage is accounted for by calculating the change in pitching moment that results from the reduction in tail lift.

8.4.1 Wing Leading-Edge and Trailing-Edge Cutouts

The effects of cutouts on the lift-curve slope were determined with a technique that used the Carmichael procedure to evaluate a matrix of flat-plate wings. Details of this technique are discussed in Section 8.2.1. The Carmichael runs that were made also gave an estimate of the wing aerodynamic center. Figure 8-19 shows empirical charts that were established to show the effect of cutout location, cutout size, wing sweep, and aspect ratio on the wing-body aerodynamic center. Figure 8-19a shows the estimate for aerodynamic center shift as a function of cutout span and wing aspect ratio. Wing quarter-chord sweep, cutout location, and cutout chord are held constant. Figure 8-19b shows the variation of aerodynamic center shift with wing sweep. Figure 8-19c shows the variation with spanwise location, and Figure 8-19d shows the variation with cutout chord. The net aerodynamic center shift is determined by

$$\left(\frac{\Delta X_{a.c.}}{\bar{c}}\right)_{LE} = \left(\frac{\Delta X_{a.c.}}{\bar{c}}\right)_1 + \left(\frac{\Delta X_{a.c.}}{\bar{c}}\right)_2 + \left(\frac{\Delta X_{a.c.}}{\bar{c}}\right)_3 + \left(\frac{\Delta X_{a.c.}}{\bar{c}}\right)_4 \tag{8-44}$$

Data in Figure 8-21 are used to make similar estimates for trailing-edge cutouts.

$$\left(\frac{\Delta X_{a.c.}}{\bar{c}}\right)_{TE} = \left(\frac{\Delta X_{a.c.}}{\bar{c}}\right)_5 + \left(\frac{\Delta X_{a.c.}}{\bar{c}}\right)_6 + \left(\frac{\Delta X_{a.c.}}{\bar{c}}\right)_7 + \left(\frac{\Delta X_{a.c.}}{\bar{c}}\right)_8 \tag{8-45}$$

8.4.2 Missing Wing Tips

Loss of a wing tip will, in general, shift the wing center of pressure inboard, and for swept-wing configurations the center of pressure will move forward. Equations presented in Reference 6 are used to calculate wing planform area, exposed wing characteristic length, aspect ratio, taper ratio, and the ratio of fuselage diameter to wing span for the aircraft wing with a missing wing tip. These parameters are used to establish the fuselage station of the leading edge of the exposed wing mean aerodynamic chord (X_{LE}). This point is calculated for both the damaged and undamaged wing. The subsonic aerodynamic center is assumed to be at the 25 percent mean aerodynamic
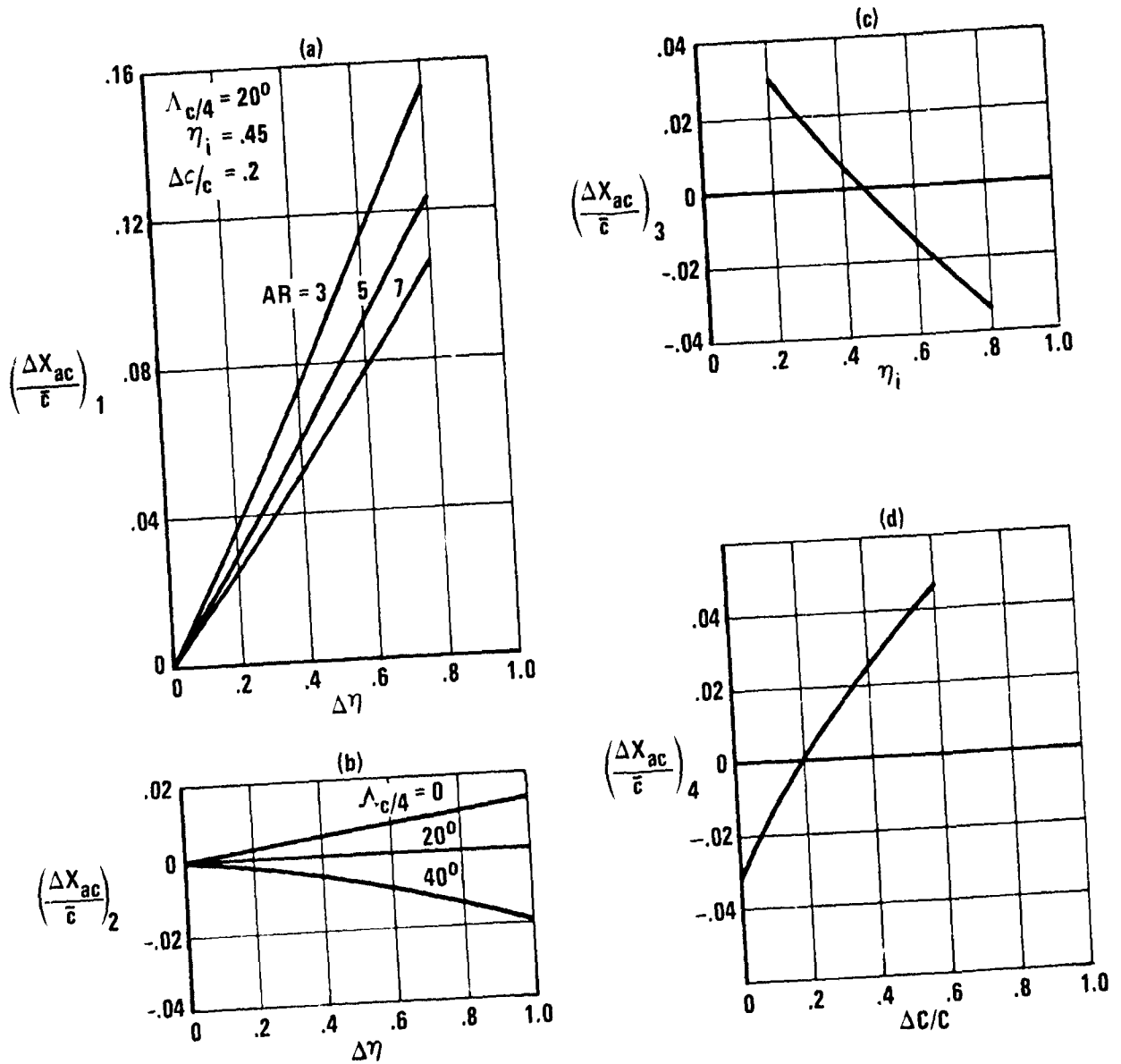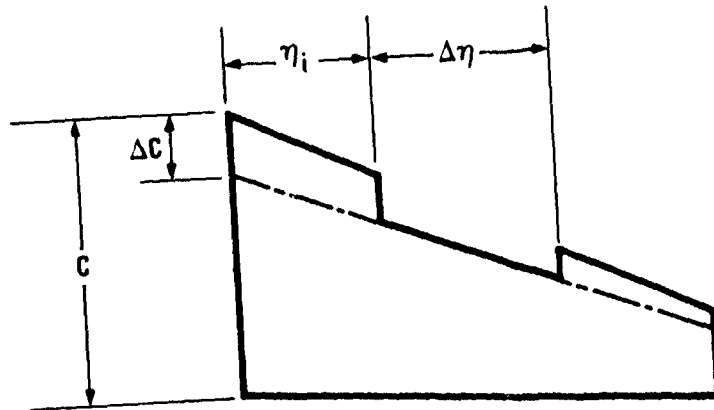
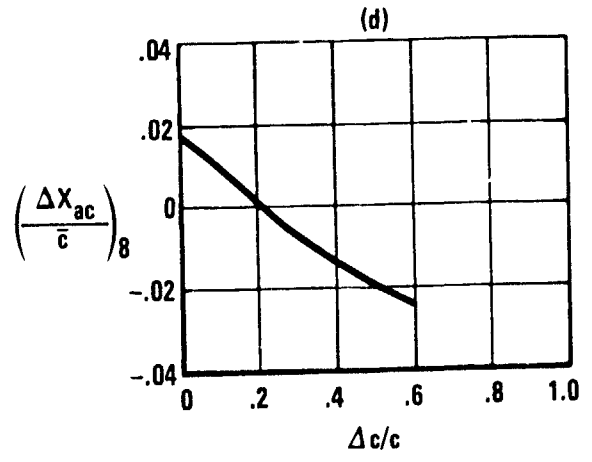Figure 8-19   Aerodynamic Center Shift Due to Leading-
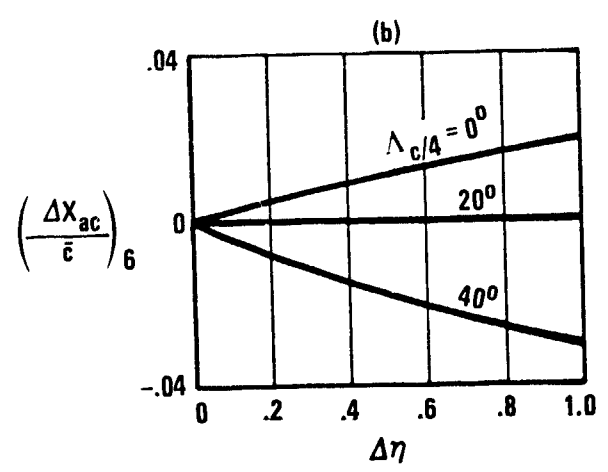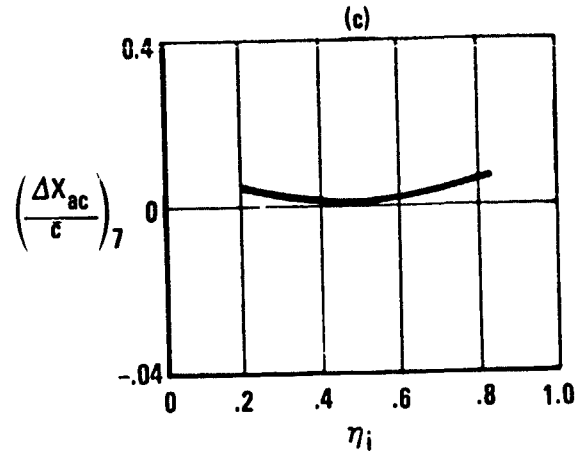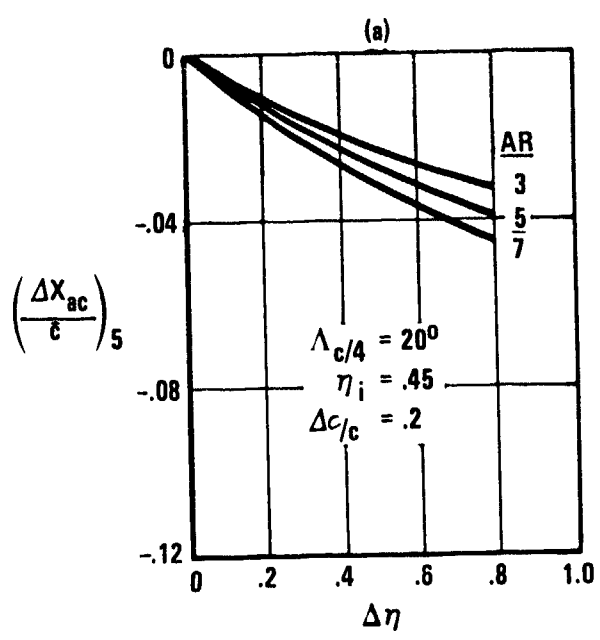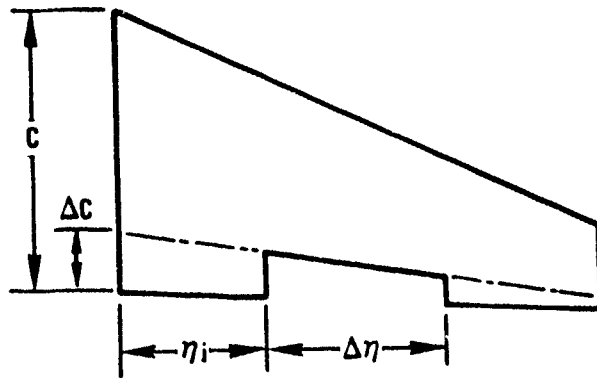Edge Cutouts

Figure 8-20 Aerodynamic Center Shift Due to Trailing-
Edge Cutouts

chord and the supersonic position at the 50 percent chord. The aerodynamic center shift can be calculated at subsonic speeds by

$$\Delta X = (X'_{LE} + 0.25\,\bar{c}) - (X_{LE} + 0.25\bar{c}) \tag{8-46}$$

and at supersonic speeds by

$$\Delta X = (X'_{LE} + 0.5\,\bar{c}) - (X_{LE} + 0.5\,\bar{c}) \tag{8-47}$$

An arbitrary amount of missing wing tip can be specified for each side of the wing in the AAT computer procedure. Therefore, the calculations for moment shift due to missing wing tips are made independently and averaged to get the net effect.

$$\left(\frac{\Delta X_{a.c.}}{\bar{c}}\right)_{Tips} = \frac{\Delta X_{left} + \Delta X_{right}}{\bar{c}} \tag{8-48}$$

8.4.3 Horizontal Tail Damage

Damage to the horizontal tail reduces its lift-curve slope, as discussed in Section 8.2.4. This change in tail lift can greatly impact the pitching moments because of the moment arm of the tail. The incremental pitching moment due to horizontal tail damage is defined at zero tail deflection by

$$\Delta C_{M_{Tail}} = -\Delta C_{L_{\alpha_{Tail}}} \cdot (\alpha - \alpha_{o_H}) \cdot \left(\frac{\ell_t}{\bar{c}}\right) \tag{8-49}$$

where ℓ_t is the distance from the wing quarter-chord to the tail quarter-chord, and α_{o_H} is the angle of attack at which the tail lift is zero.

8.4.4 Net Effect on Pitching Moment

Aerodynamic center shifts due to leading-edge cutouts, trailing-edge cutouts and missing wing tips are considered to be additive. The total shift of the damaged wing aerodynamic center is defined by

$$\frac{\Delta X_{a.c.}}{\bar{c}} = \left(\frac{\Delta X_{a.c.}}{\bar{c}}\right)_{LE} + \left(\frac{\Delta X_{a.c.}}{\bar{c}}\right)_{TE} + \left(\frac{\Delta X_{a.c.}}{\bar{c}}\right)_{Tip} \tag{8-50}$$

173

Lift on the damaged wing is defined by

$$C'_{L_{wing}} = (C_{L_{\alpha_{wing}}} + \Delta C_{L_{\alpha_{LE}}} + \Delta C_{L_{\alpha_{TE}}} + \Delta C_{L_{\alpha_{Tip}}} \quad (8\text{-}51)$$
$$+ \Delta C_{L_{\alpha_{Holes}}}) \cdot (\alpha - \alpha_0)$$

Pitching moments caused by wing damage are defined by the product of the wing lift and the distance that the wing aerodynamic center is moved. The incremental pitching moment coefficient is defined by

$$\Delta C_{M_{Wing}} = -C'_{L_{Wing}} \frac{\Delta X_{a.c.}}{\bar{c}} \quad (8\text{-}52)$$

The net pitching moment increment is determined by summing the contributions of the wing and horizontal tail.

$$\Delta C_M = \Delta C_{M_{Wing}} + \Delta C_{M_{Tail}} \quad (8\text{-}53)$$

8.5 ROLLING MOMENT

Rolling moment on the damaged aircraft is based on the differential lift that is developed on the wing surfaces and horizontal tail surfaces. The types of damage that reduce the lift-curve slope also cause rolling moment unless identical damage is incurred on both sides. Incremental lift is computed independently for left and right surfaces, and the contribution of each surface to the rolling moment is calculated.

8.5.1 Wing Leading-Edge and Trailing-Edge Cutouts

Cutout lift effects are evaluated for the left and right wing surfaces independently by the methods discussed in Section 8.2.1. The leading-edge lift increment is assumed to act at the 40 percent span station of the cutout; accordingly, the moment arm is defined by

$$Y_{LE} = (\eta_i + .4\Delta\eta)_{LE} (b/2) \quad (8\text{-}54)$$

where η_i is the spanwise location of the inboard edge of the cutout expressed as a fraction of semi-span, and $\Delta\eta$ is the cutout span similarly expressed.

The incremental lift-curve slope due to leading-edge cutouts is defined in Section 8.2.1 as $\Delta C_{L_{\alpha_{LE}}}$. If only one wing is damaged,

$$C_{L_{\alpha_{LE/Wing}}} = \Delta C_{L_{\alpha_{LE}}} \tag{8-55}$$

If both wings have leading-edge cutouts, then the incremental lift-curve slope for only one wing is

$$C_{L_{\alpha_{LE/Wing}}} = 0.5 \; \Delta C_{L_{\alpha_{LE}}} \tag{8-56}$$

The rolling moment produced by the leading-edge cutout lift force acting at the calculated moment arm (Y_{LE}) is computed as

$$\left(C_{\ell_{LE}}\right)_{Left} = C_{L_{\alpha_{LE/Wing}}} (\alpha - \alpha_0) \left(\frac{Y_{LE}}{b}\right) \tag{8-57}$$

$$\left(C_{\ell_{LE}}\right)_{Right} = -\; C_{L_{\alpha_{LE/Wing}}} (\alpha - \alpha_0) \left(\frac{Y_{LE}}{b}\right) \tag{8-58}$$

Total rolling moments due to leading-edge cutouts are obtained by summing left- and right-wing moments.

$$\Delta C_{\ell_{LE}} = \left(\Delta C_{\ell_{LE}}\right)_{Left} + \left(\Delta C_{\ell_{LE}}\right)_{Right} \tag{8-59}$$

Leading-edge cutouts on both wings produce rolling moments that cancel each other.

The procedure described above is also used to calculate rolling moments caused by cutouts on the wing trailing edge. Equations presented in this section are directly applicable to trailing-edge cutouts if the subscript 'LE' is replaced with 'TE'.

8.5.2 Missing Wing Tips

Loss of an outboard section of the wing shifts the aerodynamic center of the exposed wing inboard and can result in large rolling moments. To calculate the rolling moments, it is necessary to determine aerodynamic centers and lift coefficients for the wings with and without the tip removed.

The aerodynamic centers are assumed to be at the mean aerodynamic chord of the exposed wing. Hence, the moment arm of the lifting force is defined for the undamaged wing as

$$y = 1/3 \left(\frac{1 + 2\lambda}{1 + \lambda}\right)\left(\frac{b}{2}\right) + \frac{d}{2} \tag{8-60}$$

where d is the body diameter, b is the wing span, and λ is the exposed wing taper ratio. For the left wing with tip removed, the moment arm is

$$y'_{Left} = 1/3 \left(\frac{1 + 2\lambda'}{1 + \lambda'}\right)\left(\frac{b'}{2}\right) + \frac{d}{2} \tag{8-61}$$

A similar expression defines y'_{RIGHT}.

Methods of Section 8.2.2 are used to calculate the lift-curve slopes independently for the left and right wings with the specified amounts of wing tip removed. Rolling moments for each wing are computed by the following equations:

$$\Delta C_{l\,\substack{Tip \\ Left}} = \left(C'_{L_{\alpha\,\substack{Left \\ Wing}}} \frac{y'_{Left}}{b} - C_{L_{\alpha\,\substack{Left \\ Wing}}} \frac{y}{b}\right)(\alpha - \alpha_0) \tag{8-62}$$

$$\Delta C_{l\,\substack{Tip \\ Right}} = \left(C'_{L_{\alpha\,\substack{Right \\ Wing}}} \frac{y'_{Right}}{b} - C_{L_{\alpha\,\substack{Right \\ Wing}}} \frac{y}{b}\right)(\alpha - \alpha_0) \tag{8-63}$$

and the net rolling moment due to missing wing tips is obtained by summing the contributions of both wings.

$$\Delta C_{l\,Tip} = \Delta C_{l\,\substack{Tip \\ Left}} + \Delta C_{l\,\substack{Tip \\ Right}} \tag{8-64}$$

8.5.3 Horizontal Tail Damage

Damage to each horizontal tail surface is defined by the percentage of area lost, and the corresponding lift loss ($\Delta C_{L_{\alpha_{Tail}}}$) is defined in Section 8.2.4 for each tail surface.

The moment arm is assumed to be the distance from the centerline to the 33 percent exposed semi-span.

$$y_{Tail} = y_{Root} + 1/3 \, (y_{Tip} - y_{Root}) \tag{8-69}$$

Rolling moments due to each horizontal tail are defined as

$$\Delta C_{\ell_{Tail \atop Left}} = \Delta C_{L_{\alpha_{Tail \atop Left}}} (\alpha - \alpha_{o_H}) \left(\frac{y_{Tail}}{b} \right) \tag{8-66}$$

$$\Delta C_{\ell_{Tail \atop Right}} = -\Delta C_{L_{\alpha_{Tail \atop Right}}} (\alpha - \alpha_{o_H}) \left(\frac{y_{Tail}}{b} \right) \tag{8-67}$$

Where α_{o_H} is the angle of attack at which tail lift is zero.

Left and right horizontal tail contributions to the rolling moment are summed to obtain the net effect of tail damage.

$$\Delta C_{\ell_{Tail}} = \Delta C_{\ell_{Tail \atop Left}} + \Delta C_{\ell_{Tail \atop Right}} \tag{8-68}$$

8.5.4 Net Effect on Rolling Moment

The net effect of surface damage to the rolling moment is the sum of the contribution from each individual surface. Wing surface holes that have flow-through air cause a decrease in lift-curve slope and a corresponding rolling moment, unless the damage is symmetric. This contribution to the rolling moment is small compared to that produced by missing panels. Because of its relative magnitude and the requirement for additional AAT input data, the contribution of holes to the rolling moment is ignored. The net effect on rolling moment is defined by

$$\Delta C_{\ell} = \Delta C_{\ell_{LE}} + \Delta C_{\ell_{TE}} + \Delta C_{\ell_{Tips}} + \Delta C_{\ell_{Tail}} \tag{8-69}$$

8.6 UNTRIMMED DATA FOR DAMAGED AIRCRAFT

Sections 8.1 through 8.4 show the methods that are used to compute the incremental, longitudinal effects of damage. The integration of these increments into the untrimmed aerodynamic data is discussed in this section. These computations are made along lines of constant angles of attack.

Lateral-directional characteristics are affected if asymmetric damage is incurred to the wing or horizontal tail. The predominant effect of asymmetric damage is to the rolling moment. Side force and yawing moment changes are relatively small and have been determined to be of secondary importance. Incremental rolling moments are discussed in Section 8.5.

8.6.1 Lift Curve

The untrimmed lift curve for the damaged aircraft is determined by applying lift increments from Section 8.2 to the lift curve of the undamaged aircraft. The prime (') is used to denote the coefficients for the damaged aircraft.

$$C_L' = C_L + \Delta C_{L_\alpha}(\alpha - \alpha_o) \tag{8-70}$$

where C_L is the predicted lift coefficient for the undamaged aircraft.

8.6.2 Drag Polar

The drag polar of the damaged aircraft includes estimates for the increases in minimum drag and drag due to lift. Minimum drag increments are calculated by the methods of Section 8.1, and the wing damage effects on the polar shape are summarized with the term ΔK in Section 8.3.5. Therefore, the increment in wing drag due to lift is

$$\Delta C_{D_{L_{Wing}}} = \Delta K (C_L')^2 \tag{8-71}$$

Tail drag due to damage is estimated by retaining the drag due to lift of the undamaged tail while applying the lift reduction. This is estimated by

$$\Delta C_{D_{L_{Tail}}} = K \left[C_{L_\alpha}^2 - (C_{L_\alpha} + \Delta C_{L_{\alpha\ Tail}})^2 \right] (\alpha - \alpha_{o_H})^2 \tag{8-72}$$

The net drag of the damaged aircraft at a specified angle of attack is

$$C_D{}' = C_{D_X} + \Delta C_{D_{Min}} + \Delta C_{D_{L_{Wing}}} + \Delta C_{D_{L_{Tail}}} \qquad (8\text{-}73)$$

where C_{D_X} is the drag of the undamaged aircraft at the lift coefficient of the damaged configuration ($C_L{}'$).

8.6.3 Pitching Moment

The untrimmed pitching moment of the damaged aircraft at zero trim surface setting is determined by applying damage increments to the pitching moment curve of the undamaged configuration. The wing and tail are the only components that change the pitching moment when damaged. Equations 8-49 and 8-52 define the increments $\Delta C_{M_{Tail}}$ and $\Delta C_{M_{Wing}}$. The pitching moment of the damaged aircraft is defined by

$$C_M{}' = C_{M_X} + \Delta C_{M_{Wing}} + \Delta C_{M_{Tail}} \qquad (8\text{-}74)$$

where C_{M_X} is the pitching moment coefficient of the undamaged configuration at the lift coefficient of the damaged configuration ($C_L{}'$).

8.7 TRIM

8.7.1 Pitching Moment Trim

Lift and drag increments that result from trimming the pitching moments of the undamaged aircraft are determined by the methods described in Section 7. The results depend primarily upon four items: the pitching moment, the wing-body aerodynamic center, tail lift-curve slope, and tail effectiveness. Trim lift and drag for the damaged aircraft are also computed by the methods of Section 7; however, the four items mentioned above must be adjusted to reflect the damage that has been inflicted upon the aircraft.

The pitching moment of the damaged, untrimmed aircraft is given by Equation 8-74. Movement of the aerodynamic center ($\frac{\Delta X_{ac}}{c}$) was determined in the calculation of the untrimmed pitching moment and is given by Equation 8-50. The wing-body aerodynamic

179

center of the damaged aircraft can be calculated by

$$\left(\frac{X_{ac}}{\bar{c}}\right)'_{wing\text{-}body} = \left(\frac{X_{ac}}{\bar{c}}\right)_{wing\text{-}body} + \frac{\Delta X_{ac}}{\bar{c}} \tag{8-75}$$

Tail planform area that is lost causes a reduction in the tail lift-curve slope and also in the tail effectiveness. These parameters are assumed to be proportional to the tail area and are defined for the damaged configuration by

$$C_{L_{\alpha\,Tail}}' = C_{L_{\alpha\,Tail}} \left(1 - \frac{S_T'}{S_T}\right) \tag{8-76}$$

$$C_{L_{\delta_H}}' = C_{L_{\delta_H}} \left(1 - \frac{S_T'}{S_T}\right) \tag{8-77}$$

where S_T and S_T' are the exposed areas of the horizontal tail before and after damage occurs.

These modified terms are used in the methods of Section 7 to calculate the total trim lift ($\Delta C_{L_{Trim}}'$) and trim drag ($\Delta C_{D_{Trim}}'$) for the damaged configuration. The increment in trim lift due to damage is the difference between total trim lift of the undamaged aircraft and the total trim lift of the damaged aircraft.

$$\delta \Delta C_{L_{Trim}} = \Delta C_{L_{Trim}}' - \Delta C_{L_{Trim}} \tag{8-78}$$

and similarily for drag,

$$\delta \Delta C_{D_{Trim}} = \Delta C_{D_{Trim}}' - \Delta C_{D_{Trim}} \tag{8-79}$$

8.7.2 Rolling Moment Trim

Rolling moments induced by asymmetric damage to the wing or horizontal tail surfaces can be trimmed with a control surface deflection or sideslip. A horizontal tail, rudder, elevon, or spoiler can be used as a trim device. Since there are many alternatives for trimming the rolling moment, the AAT Program relies upon the user to specify the moment arm of the trimming device. The drag due to control surface deflection is defined as the drag component of the normal force required to counteract the rolling moment.

$$\Delta C_{D_{Roll}}' = \left| \Delta C_{\ell} \right| \frac{b}{\overline{Y}} \tan \alpha \tag{8-80}$$

where $\overline{Y}$ is the moment arm of the trimming device.

Side force and yawing moment effects due to asymmetric damage are small compared to the change in rolling moment. Small increments in side force and yawing moment can be offset with sideslip with negligible effect on lift and drag. Large amounts of yawing moment can be trimmed with asymmetric thrust.

8.7.3 Trimmed Lift and Drag

Trimmed lift and drag for the damaged aircraft are calculated by adding the trim increments to the untrimmed data.

$$C_{L_{Trim}}' = C_L' + \Delta C_{L_{Trim}}' \tag{8-81}$$

$$C_{D_{Trim}}' = C_D' + \Delta C_{D_{Trim}}' + \Delta C_{D_{Roll}}' \tag{8-82}$$

C_L' and C_D' are calculated by the Equations 8-70 and 8-73.

9. DATA COMPARISONS

9.1 UNDAMAGED CONFIGURATIONS

The accuracy of the aerodynamic methods for undamaged configurations has been demonstrated with comparisons of predictions with data. AAT problems were run to estimate the aerodynamic characteristics of several configurations at the exact conditions at which the data were recorded.

Reference 1 shows a comparison of predicted lift curves and drag polars with wind tunnel data for a series of 11 wing-body models in which there were systematic variations of sweep, thickness to chord ratio, position of maximum thickness, camber, and aspect ratio. The study was conducted over a Mach range from 0.23 to 0.94. The Large Aircraft Program, which is discussed in Reference 1, was used to make these predictions. Aerodynamic prediction methods used in this program are identical to those in the AAT procedure code. Therefore, the correlations presented in Reference 1 also demonstrate the capabilities of the AAT.

A study to demonstrate the capability of the Large Aircraft Program to make predictions for cranked-wing configurations is also presented in Reference 1 and is referenced as a source for verification of the AAT methods. Comparisons were made between data and predictions for the following items: lift-curve slope, drag-due-to-lift factor, minimum drag, and pitching moment slope. Each wing was planer and was mounted on a cylindrical body of revolution with a Sears-Haack nose. Model 1 had a 59 degree leading-edge triangular planform and Models 2 and 3 had two straight-line leading-edge segments of different sweep angles (referred to as "cranked" planforms). The three models were designed to have the same exposed span and exposed area.

9.1.1 F-16 Wind-Tunnel Model

A 1/15-scale model of the F-16 was tested in the Calspan 8-foot transonic wind tunnel (Test T03-483) and in the Langley Research Center's 4-foot supersonic wind tunnel (Test LRC-4-1156). The F-16 model, which is normally tested with missiles installed, had all items associated with the tip-mounted AIM-9 missiles removed. Since the AAT procedure does not estimate the effects of the missiles, these data were an obvious choice for comparison with predictions.

The configuration was represented in the program with the following components: fuselage, canopy, nacelle, single-panel wing, horizontal tail, vertical tail, and two ventral fins. Comparisons made for the lift, drag, and moment coefficients are shown in Figures 9-1, 9-2, and 9-3. It should be noted that the model data are adjusted to a capture area ratio of 1.0 since the AAT procedure does not estimate spillage drag. The subsonic estimate (Figure 9-1) closely approximates the data except for the lift coefficient at high angles of attack. The wing was simulated with only one panel; therefore, the lifting-surface of the strake was ignored except for its wetted area contribution to the friction drag. This slight over-simplification of the configuration and the fact that the effects of strong vortices (such as produced by the F-16 strake) are difficult to estimate are responsible for the discrepancy between subsonic data and predictions at high angles of attack.

9.1.2 Full-Scale FB-111

Substantiation of the aerodynamic, stability, and control characteristics of the FB-111 was accomplished with the aid of flight-test data and documented in References 50 and 51. AAT predictions were made for this configuration at the exact flight conditions as specified for the data. Comparisons of predictions and data are shown in Figures 9-4 through 9-10. Predictions for this configuration used the variable-geometry section of the program as the wing sweep was varied from the initial angle of 16 degrees to the aft-sweep angle of 72.5 degrees. Figures 9-4 through 9-8 show the effects of sweep variation at 0.8 Mach number. The flight-test data vary substantially as the wing is swept, and the predictions, although they do not match the data exactly, correctly indicate the trends. Predictions for the aft-sweep angle (72.5 degrees) are also compared with data at the supersonic Mach numbers of 1.2 and 2.0.

9.2 EFFECTS OF DAMAGE

Aerodynamics for the undamaged configuration are computed first, and then the damage effects are determined on an incremental basis and incorporated into the predictions. In keeping with this method of analysis, the comparisons for the effects of damage are also presented on an incremental basis. Only a few reports have been found that contain aerodynamic test data on the effects of aircraft damage. Predictions have been made and compared with data for the cases that are available.
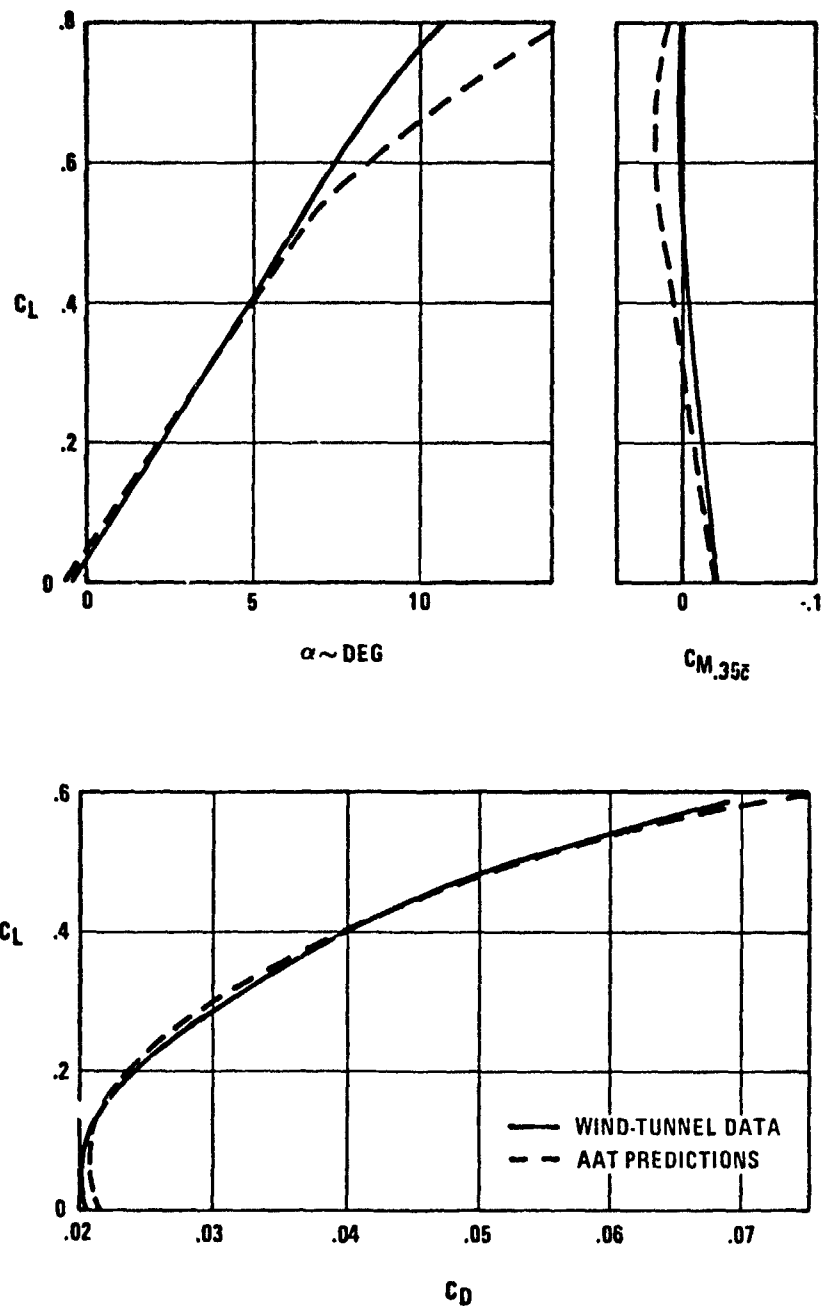
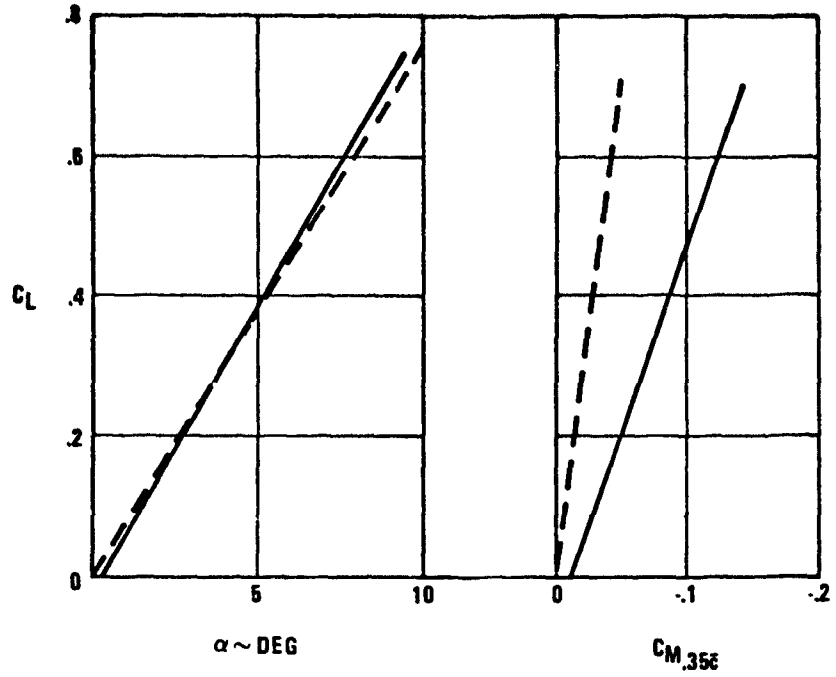Figure 9-1 F-16A Predictions Compared With Wind Tunnel
Data, M = 0.85
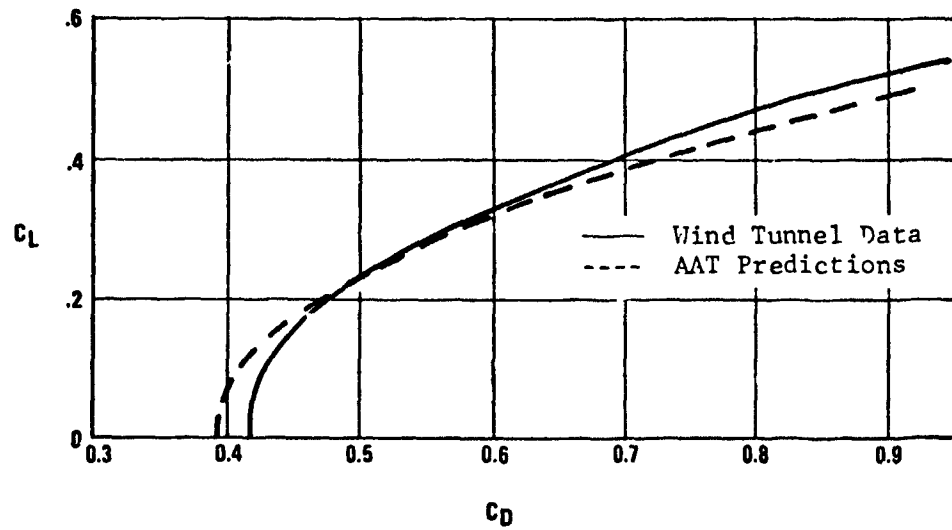
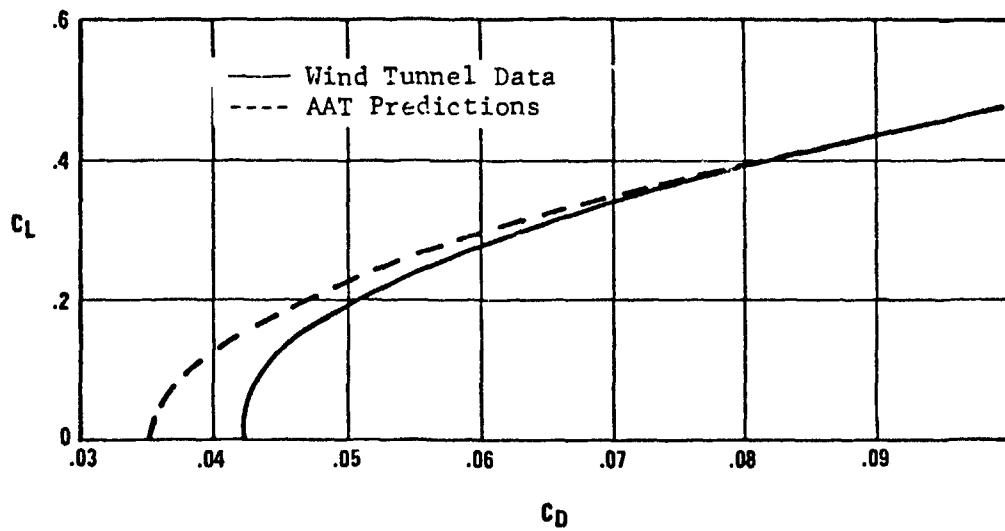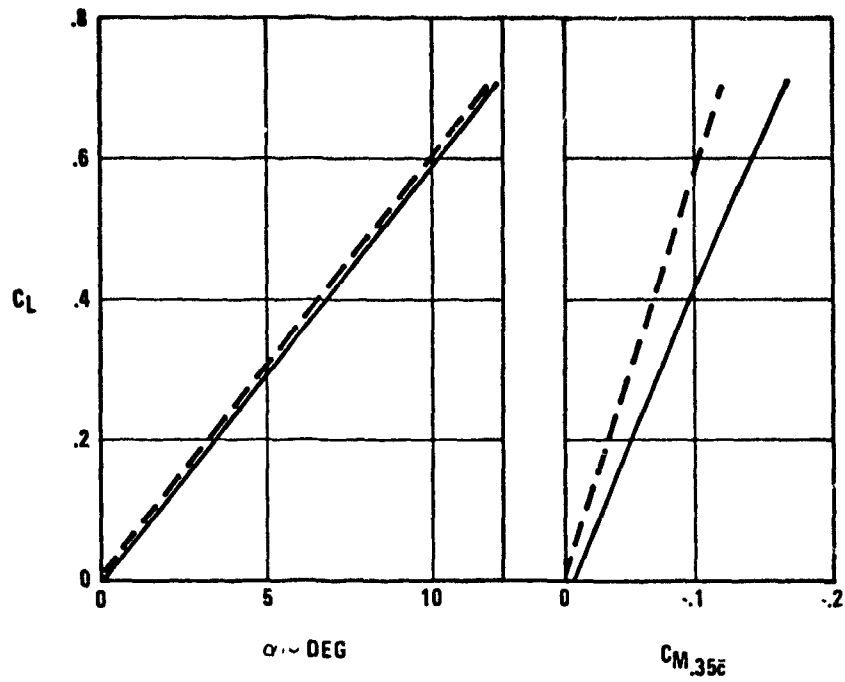Figure 9-2   F-16A Predictions Compared With Wind Tunnel Data, M = 1.2

Figure 9-3 F-16A Predictions Compared With Wind Tunnel
Data, M = 1.6

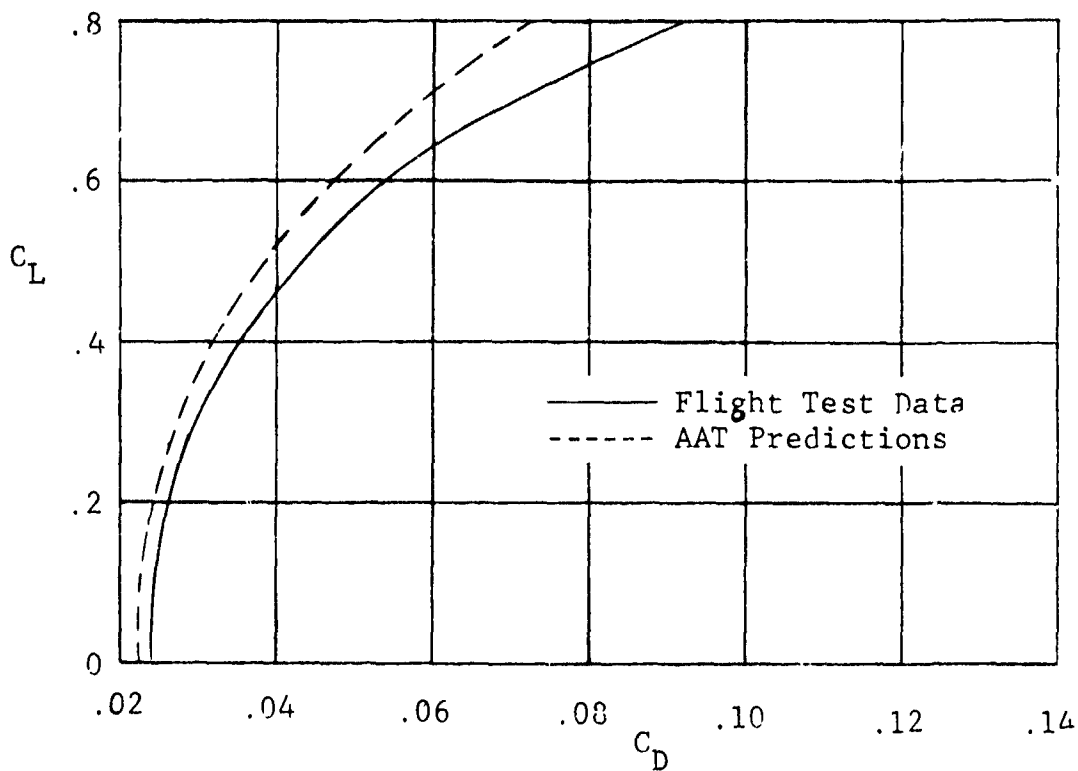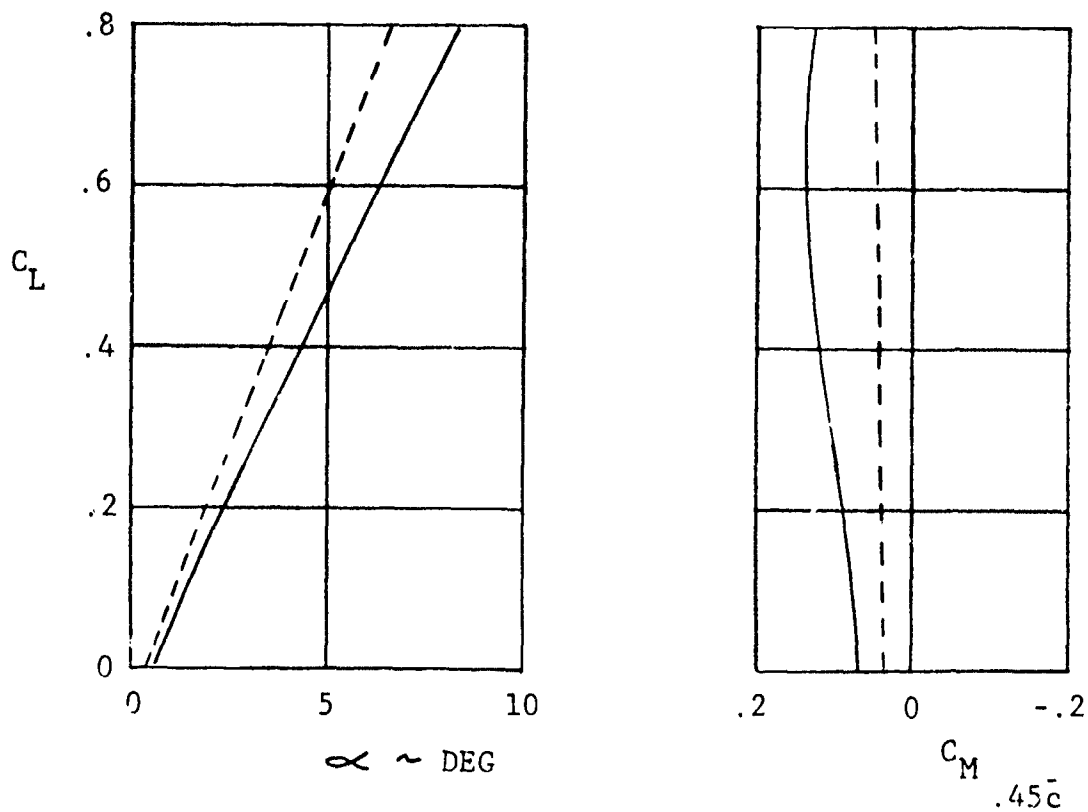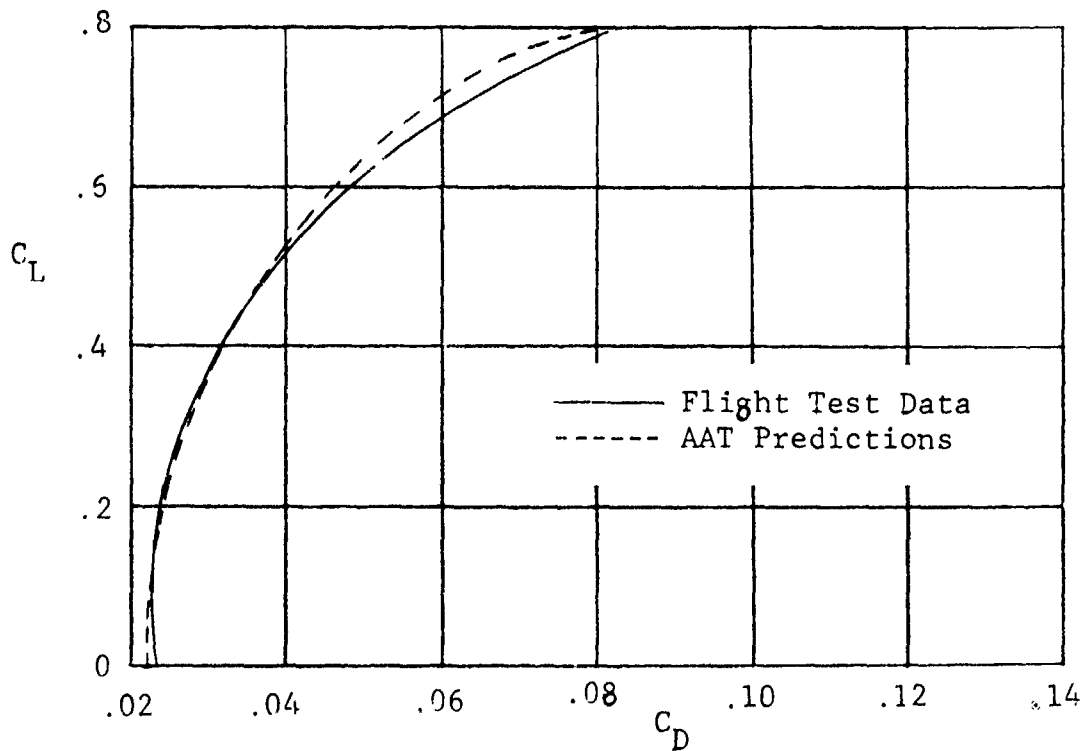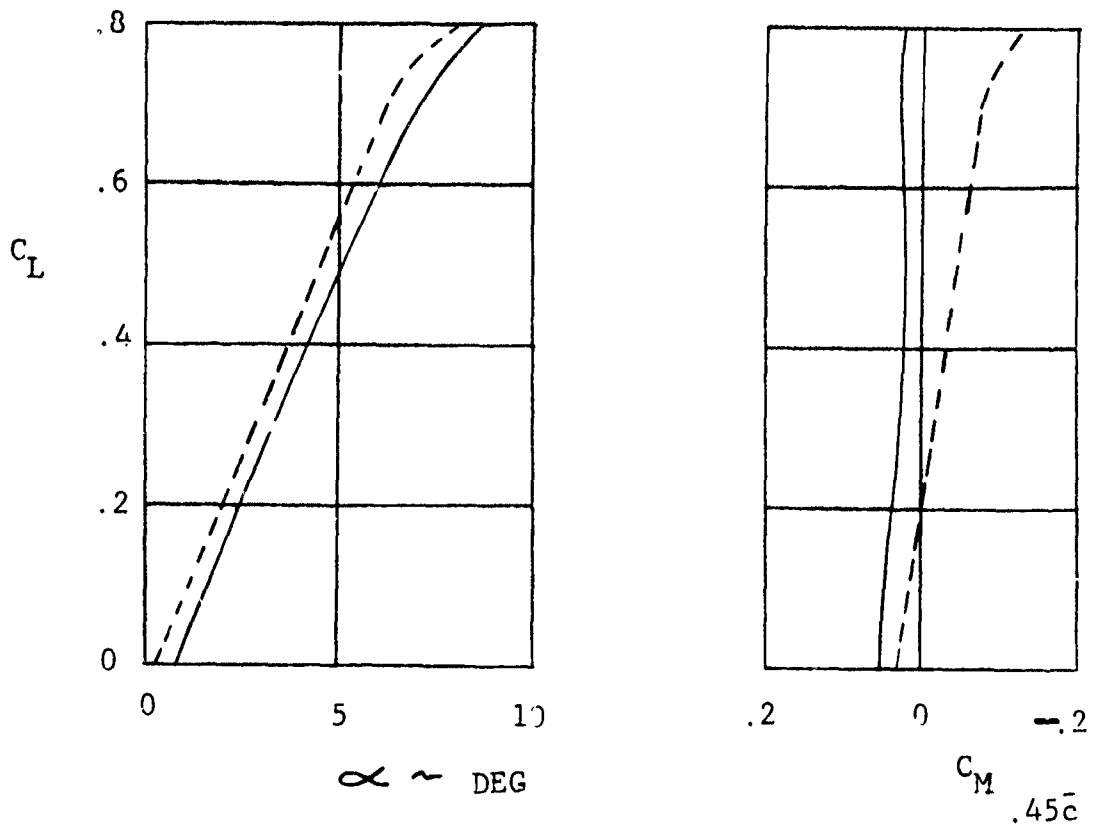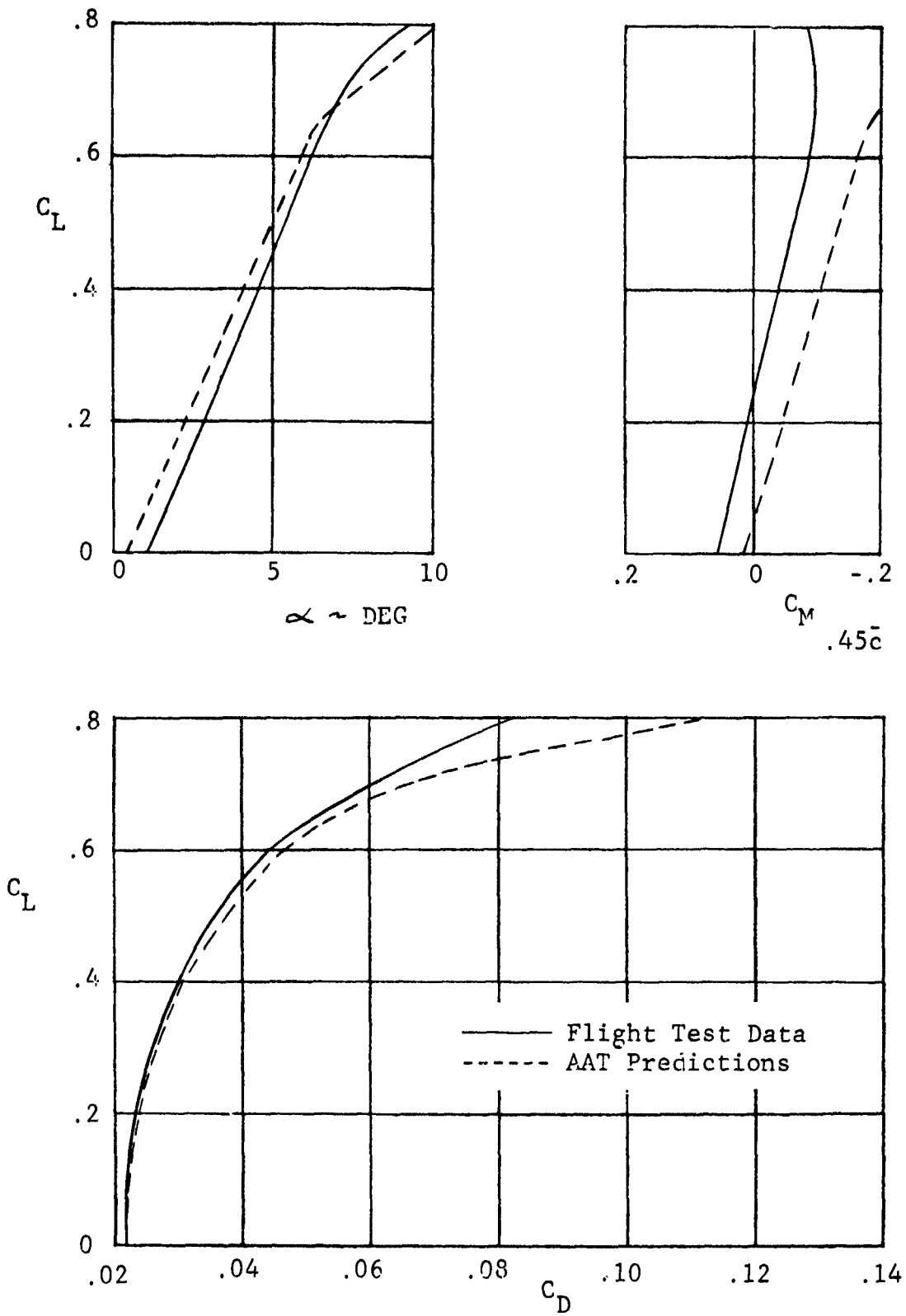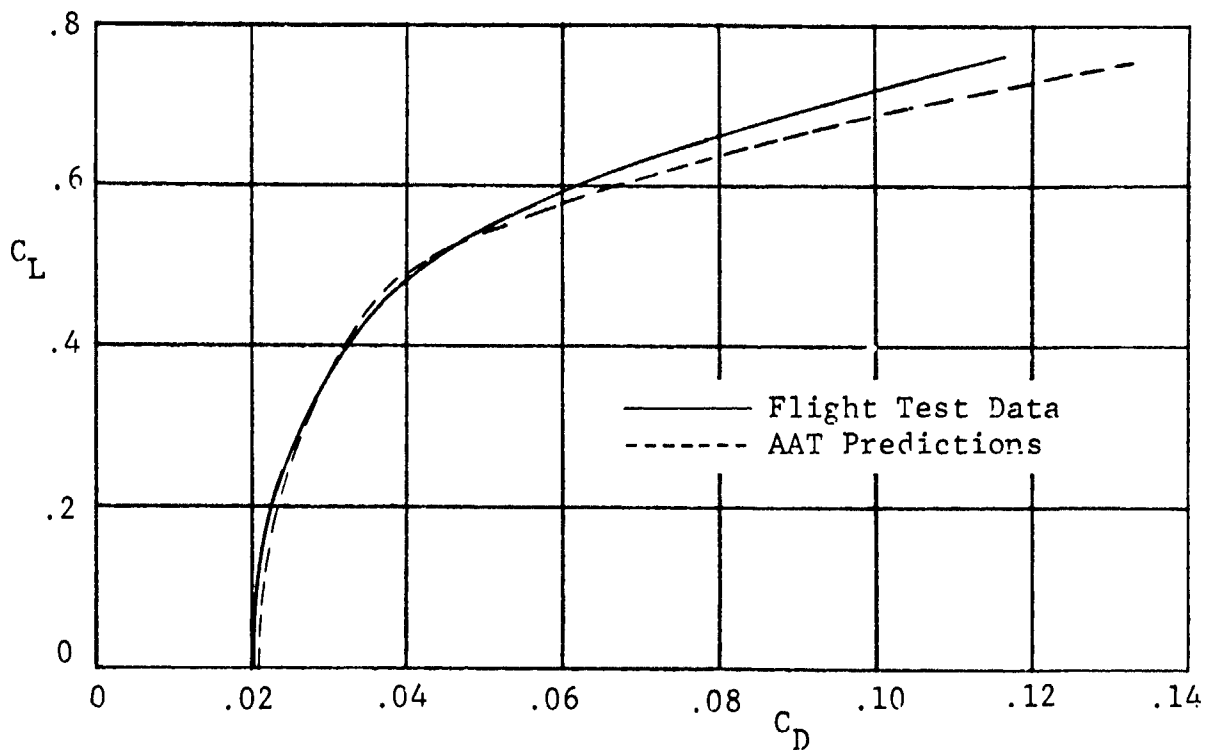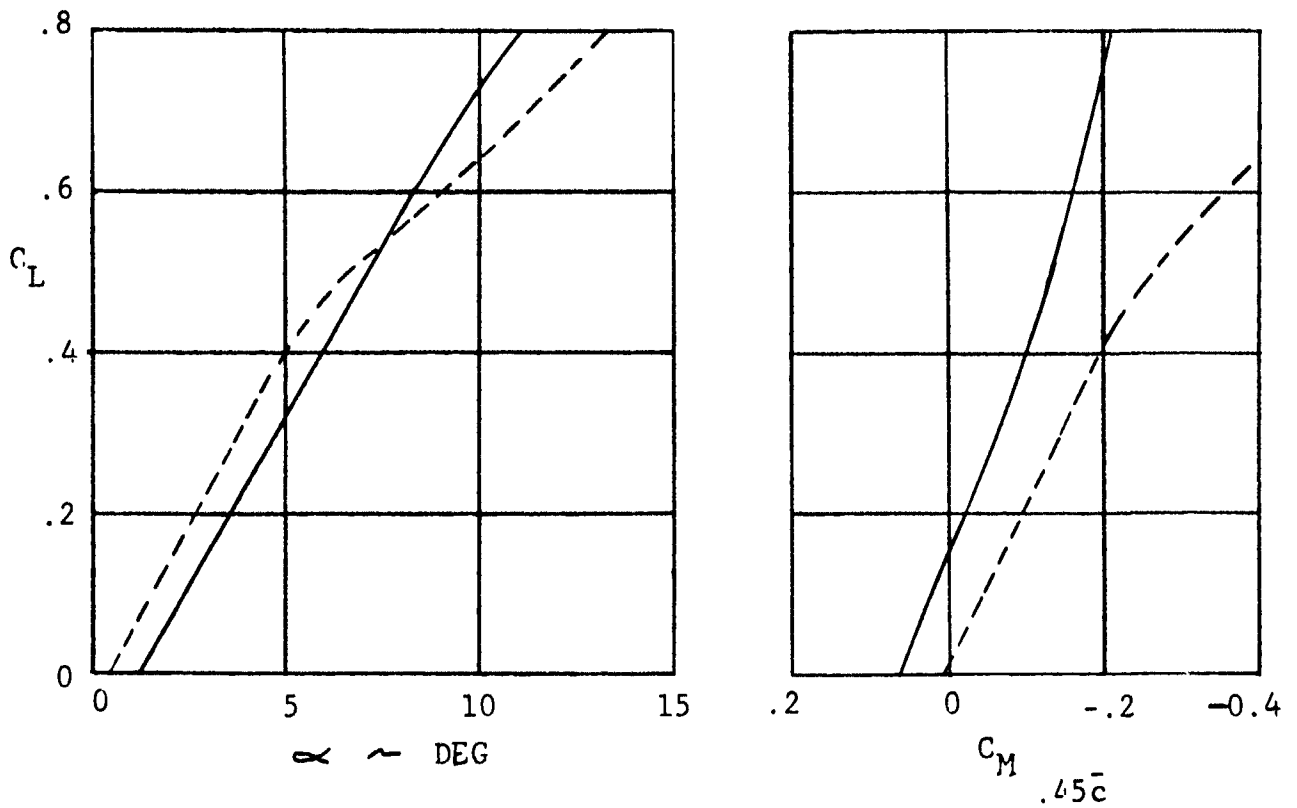Figure 9-4 FB-111 Predictions Compared With Flight Test
Data, M = .8, Λ = 16°

187

Figure 9-5   FB-111 Predictions Compared With Flight Test
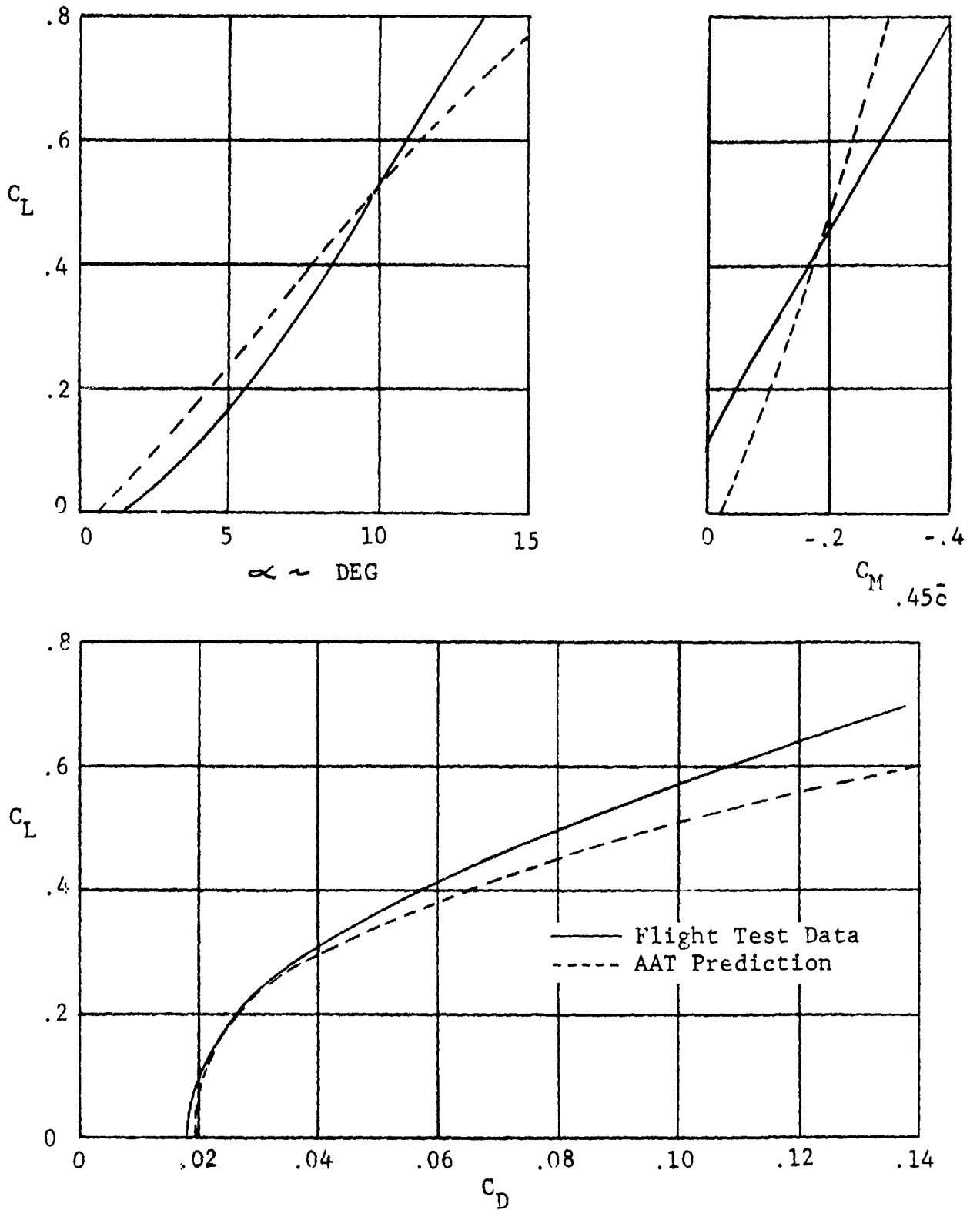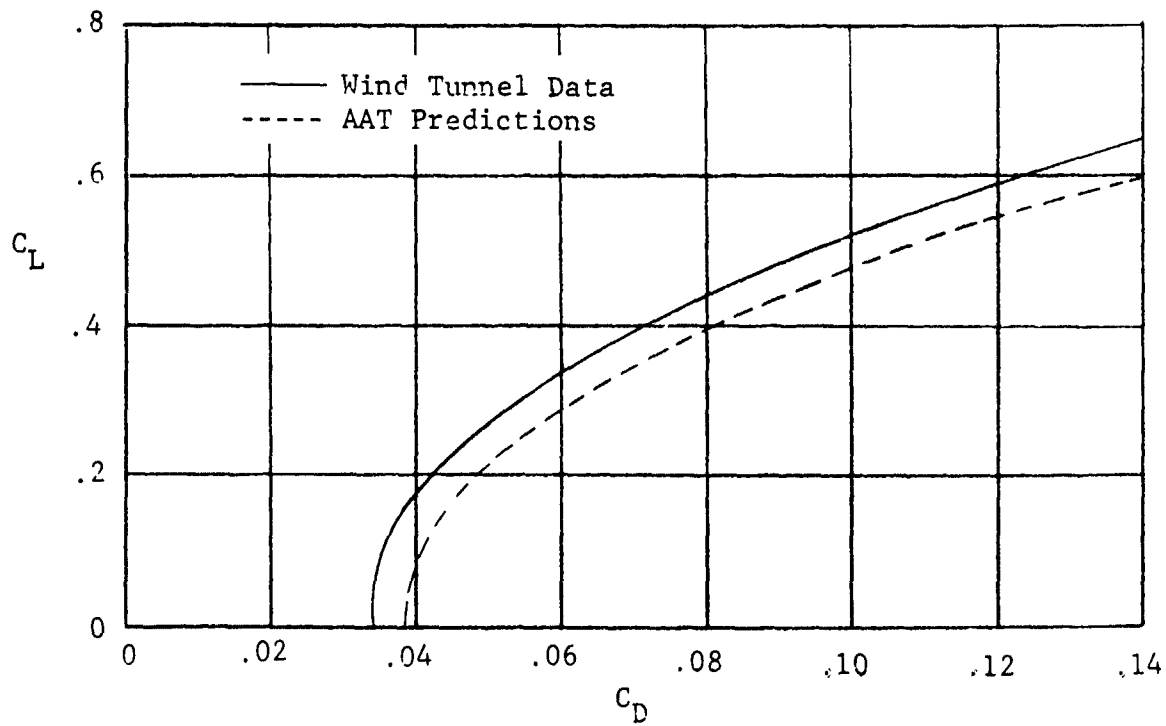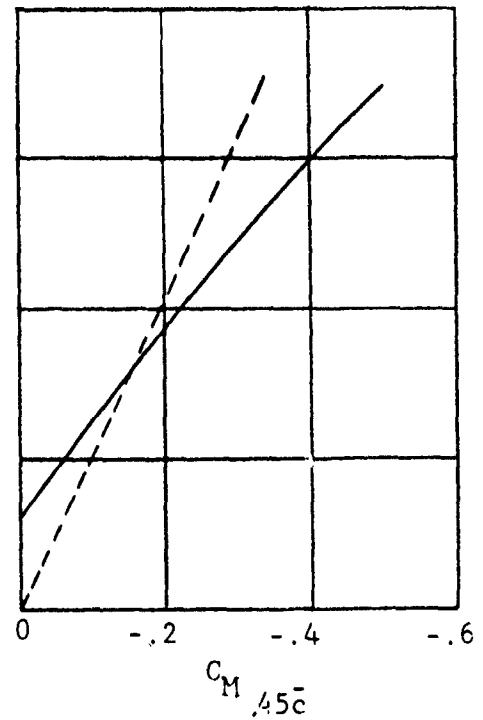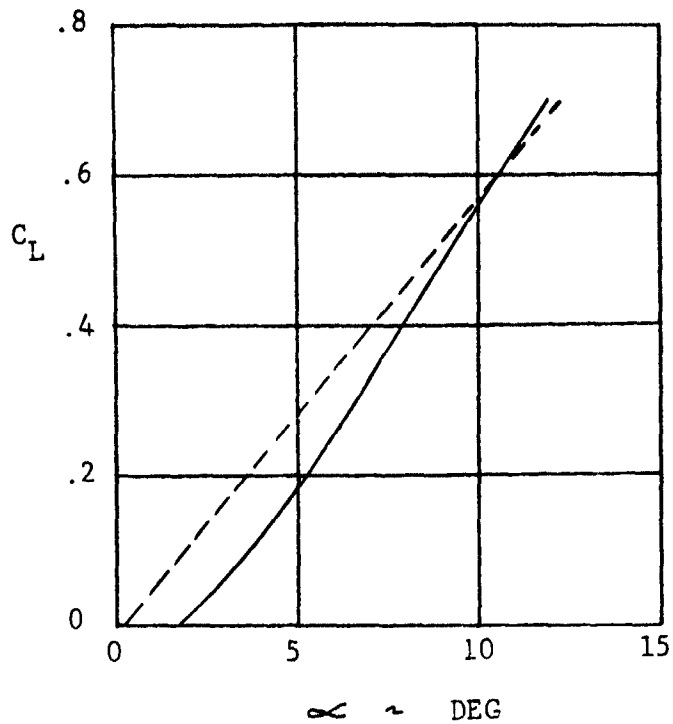Data, M = .8, Λ = 26°

188

Figure 9-6   FB-111 Predictions Compared With Flight Test
Data, M = .8, Λ = 35°

Figure 9-7   FB-111 Predictions Compared With Flight Test
Data, M = .8, Λ = 50°

190

Figure 9-8 FB-111 Predictions Compared With Flight Test
Data, M = .8, Λ = 72.5°
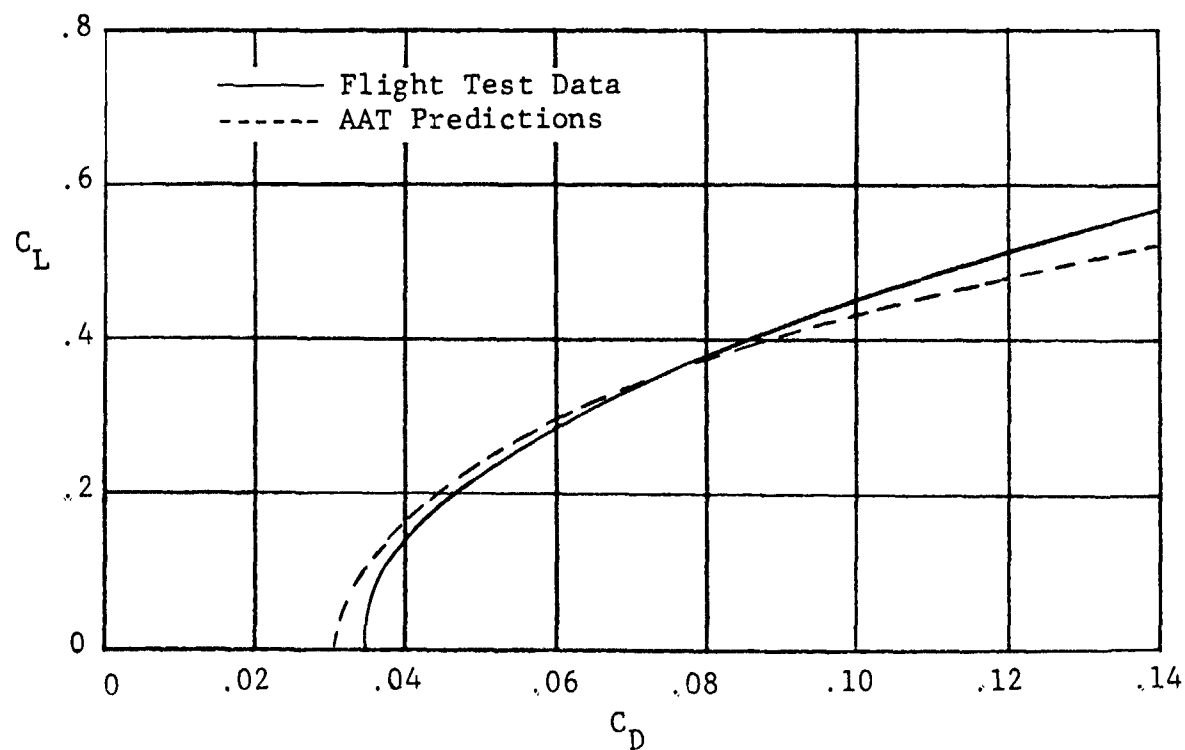
Figure 9-9 FB-111 Predictions Compared With Flight Test
Data, M = 1.2, Λ = 72.5°

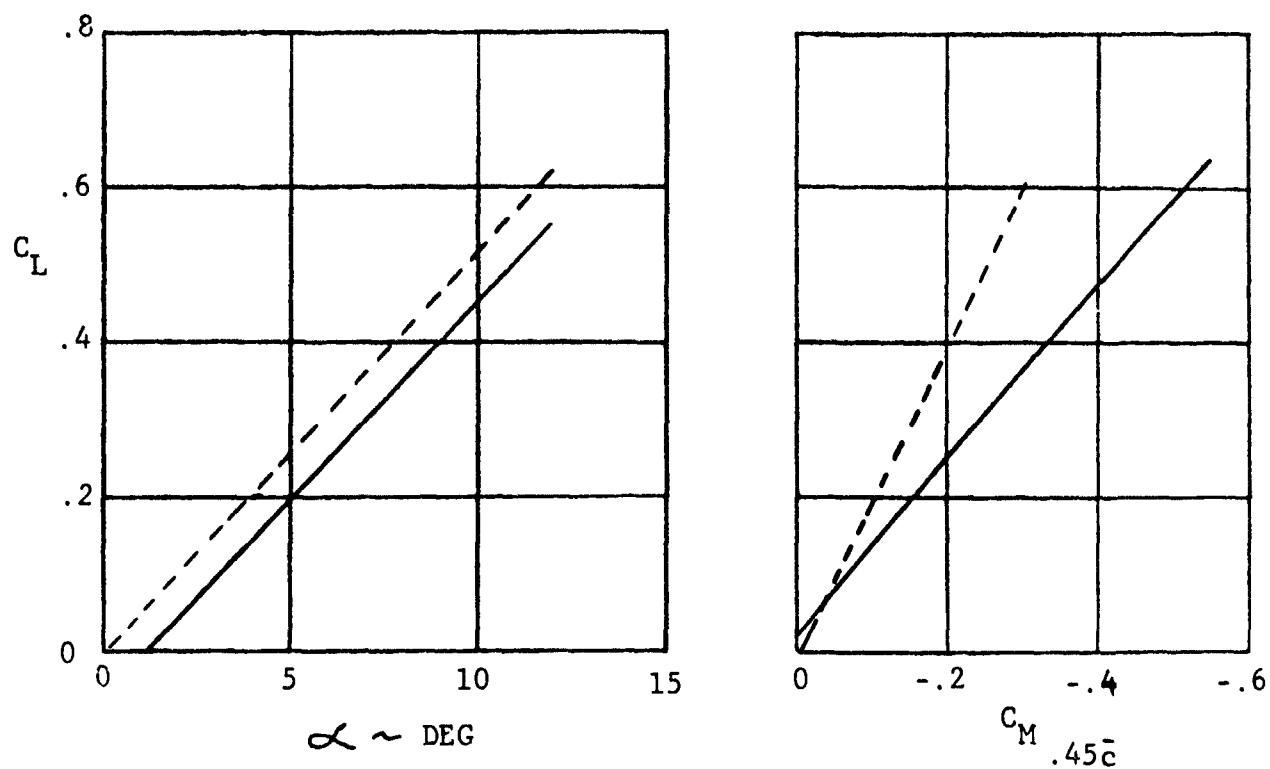Figure 9-10   FB-111 Predictions Compared With Flight Test
Data, M = 2.0, Λ = 72.5°

193

9.2.1 Two Dimensional Wing

Reference 52 presents wind tunnel data on a wing that was mounted between end plates to obtain section characteristics and the effects of surface waviness. Several cases that were tested are listed in Table 9-1, which shows the variations in wave length, wave amplitude, and number of waves.

Data from Reference 52 were obtained on a smooth model that had no provisions to cause the flow to transition from laminar to turbulent. The report states that natural transition on the model occurred at approximately 21 percent chord. When a wave was placed forward of this position on the wing upper surface, it caused the flow to transition at the point of the wave. Therefore, waves on the leading edge of the upper surface caused an increase in the friction drag because of the increase in turbulent flow. Transition as far aft as 21 percent is characteristic of smooth wind tunnel models. On the other hand, actual aircraft under normal flight conditions have transition very near the leading edge, and since the AAT procedure is designed to estimate the drag of actual aircraft, it assumes fully-turbulent flow. The result of this situation is that the wind-tunnel data include a friction increment that is not applicable to an actual aircraft and must be removed for a valid comparison with AAT predictions. The drag increments that must be removed to account for movements of the transition point are shown in Table 9-1.

Figure 9-11 shows comparisons of AAT predictions with adjusted wind tunnel data for the 12 cases that are described by Table 9-1. Predictions do not match data exactly in every case but they do make a reasonably good accounting for the effects of these arbitrary amounts of surface waviness.

9.2.2 F-105

References 53 and 54 present the results of a model test of the F-105 to determine the effects of simulated damage. Supersonic data were obtained for two cases of wing damage and two cases of horizontal tail damage. AAT estimates were made for lift, drag, pitching moments, and rolling moments for each case and compared with the data. Figure 9-12 shows the effects of losing 33 percent of the exposed area of the right wing. The wind tunnel minimum drag increment appears high for this particular case since a significant amount of wing wetted area was removed and still the drag level increased. If it had decreased, as logic suggests, the data and predictions would have

194

TABLE 9-1   WING WAVE CONFIGURATIONS

Case No.	No. on Upper Surface	No. On Lower Surface	Length (inches)	Amplitude (inches)	x/c First Wave	C_D Friction (Counts)
1	18	18	3.0	.120	.08	2.9
2	18	18	3.0	.048	.08	2.9
3	46	46	1.2	.048	.08	2.9
4	7	7	7.5	.120	.08	2.9
5	7	7	7.5	.300	.08	2.9
6	13	13	3.0	.120	.33	0
7	13	13	3.0	.048	.33	0
8	33	33	1.2	.048	.33	0
9	5	5	7.5	.120	.33	0
10	5	5	7.5	.300	.33	0
11	1	0	3.0	.120	.105	2.4
12	0	1	3.0	.120	.105	0
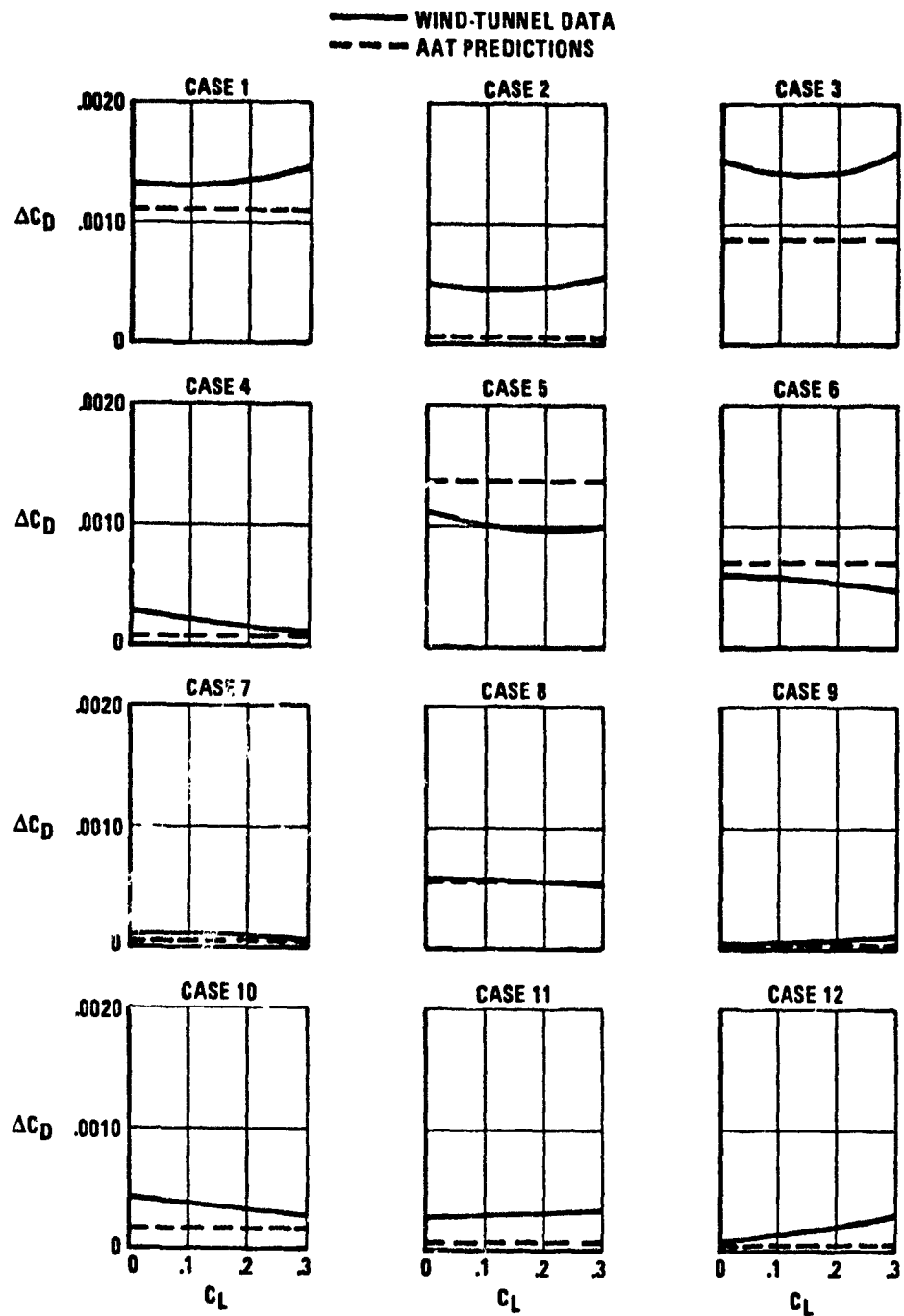
Figure 9-11 Drag Due to Waves on Wing Surface
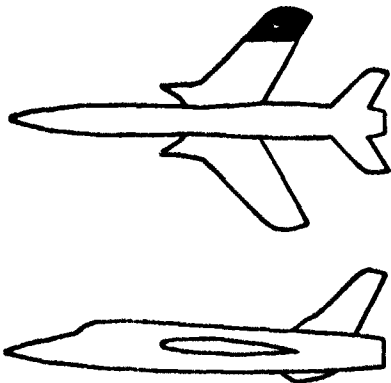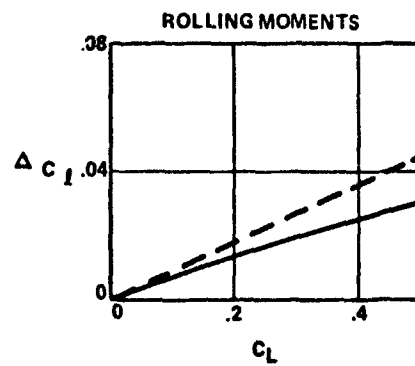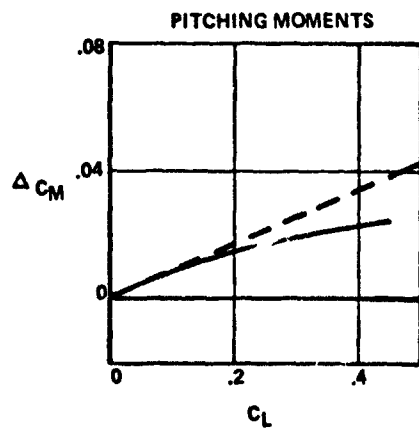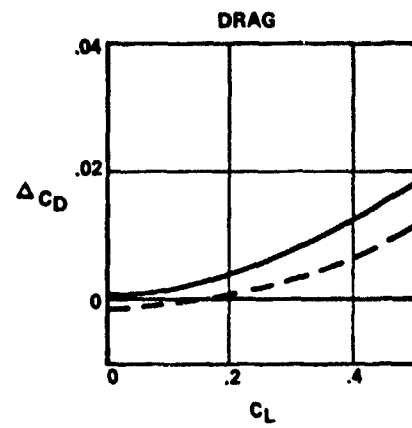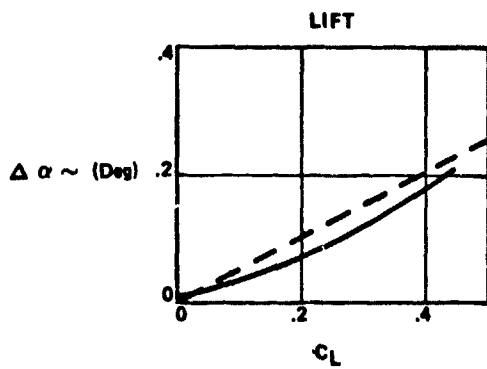
Figure 9-12   Effects of Removing 33% of Exposed Right
Wing From an F-105, M = 2.0

been much closer. Sixty-two percent of the exposed wing area
is missing for the case shown in Figure 9-13, and the expected
drag reduction is indicated by the data. The two cases of
horizontal tail damage are shown in Figures 9-14 and 9-15.

9.2.3 NASA Research Model No. 1

Reference 55 presents wind tunnel data on a delta-wing
research model that was tested to determine the effects of
wing damage. Figure 9-16 shows the lift, drag, pitching moments,
and rolling moments that result from removal of the wing aileron.
This case is simulated in the AAT procedure as a trailing-edge
cutout. Figure 9-17 shows the effects of removing 32 percent
of the exposed wing area, and Figure 9-18 shows the effects of
removing the entire vertical tail.

Wind tunnel data presented in Figure 9-18 show that removal
of the vertical tail caused no effects except on the drag.
Because the fuselage shields the vertical tail, the wind tunnel
drag decreased to zero as the angle of attack was increased.
AAT predictions make no accounting for shielding effects on the
surfaces. Therefore, the estimate for vertical tail removal
is only a minimum drag increment.

9.2.4 NASA Research Model No. 2

Reference 56 presents data on another model that was
tested by NASA to determine the effects of removal of certain
parts of the wing. Data were obtained at only two Mach numbers,
1.70 and 2.36. Comparisons are similar at both Mach numbers,
but those at 2.36 Mach were selected to be presented here.
Figure 9-19 shows the effects of losing the entire leading edge
of the right wing. The lift, drag, and rolling moment predictions
are very close to the data. Pitching moment effects, however,
are overpredicted. The prediction method was developed primarily
for cutouts over a smaller span, such as would result from losing
a leading-edge device. Use of this method to estimate the
effects of removing the entire leading edge is an extension of
its original intent. Still, predictions are good except for
the pitching moments.

Comparisons of data and predictions for the trailing edge
missing and for the entire right wing missing are shown in
Figures 9-20 and 9-21.
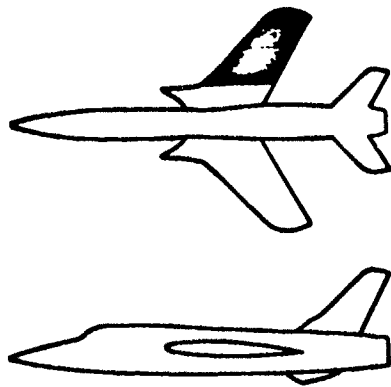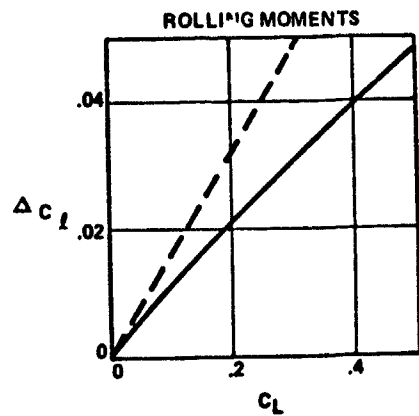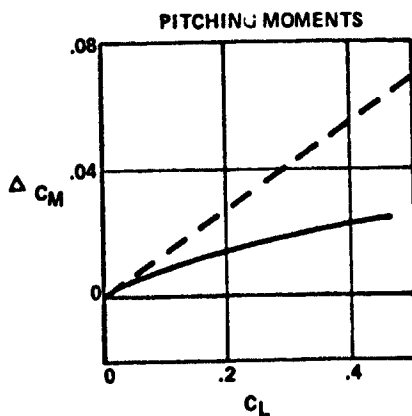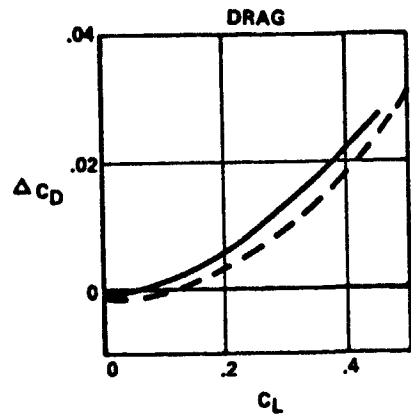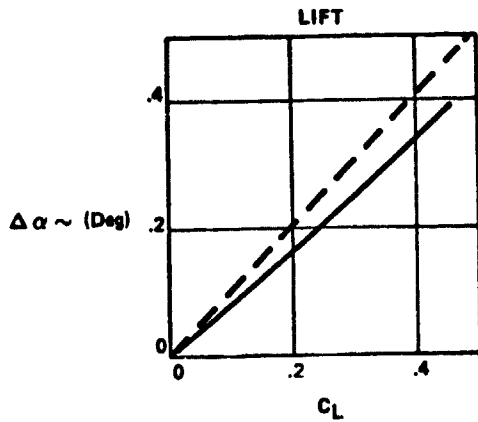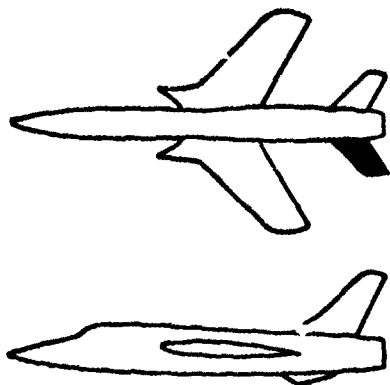
Figure 9-13   Effects of Removing 62% of Exposed Right
Wing From an F-105, M = 2.0

199

DAMAGE INPUT TO AAT

DWING (14) = 1.0, FRACTION OF LEFT H.T. MISSING
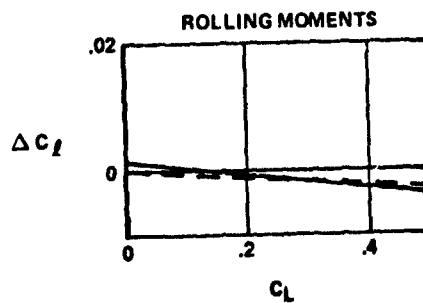
——— WIND-TUNNEL DATA
— — AAT PREDICTION
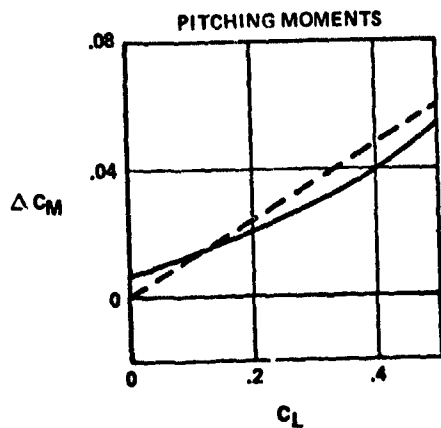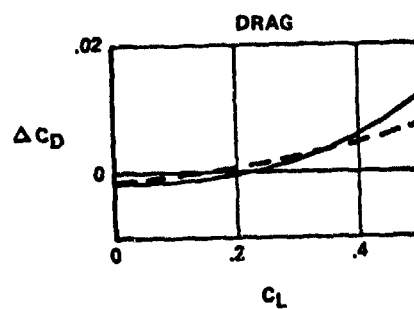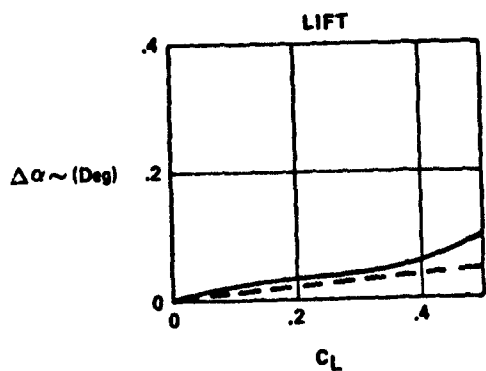
Figure 5-14   Effects of Removing Left Horizontal Tail
From an F-105, M = 2.0

DWING(14) = 1.0, Fraction of left H.T. missing
DWING(15) = 0.5, Fraction of right H.T. missing

—— WIND-TUNNEL DATA
– – AAT PREDICTION

LIFT

$\Delta \alpha \sim$ (Deg)

C_L

DRAG

ΔC_D

C_L

PITCHING MOMENTS

ΔC_M

C_L

ROLLING MOMENTS

WIND-TUNNEL
ROLLING MOMENTS
ARE NOT
AVAILABLE

ΔC_ℓ

C_L
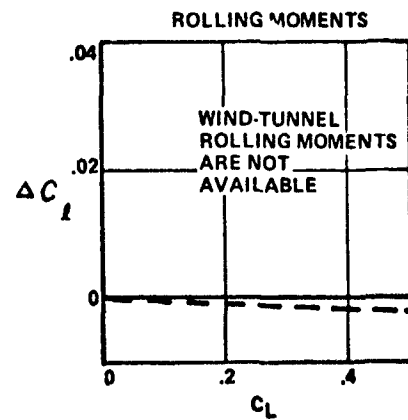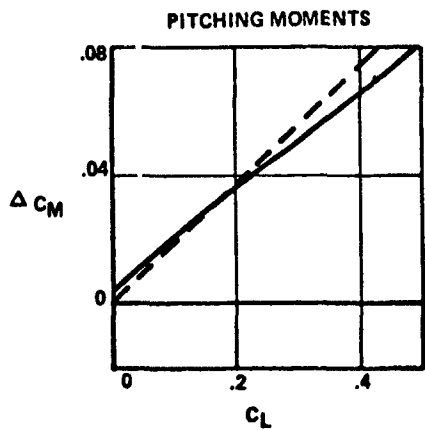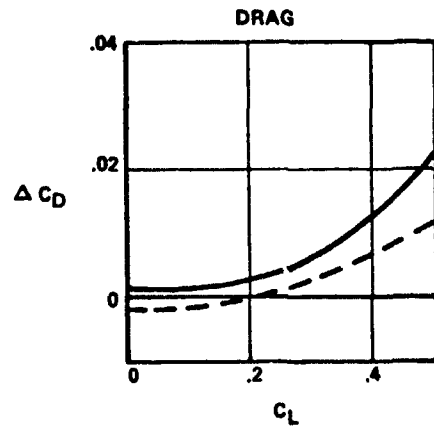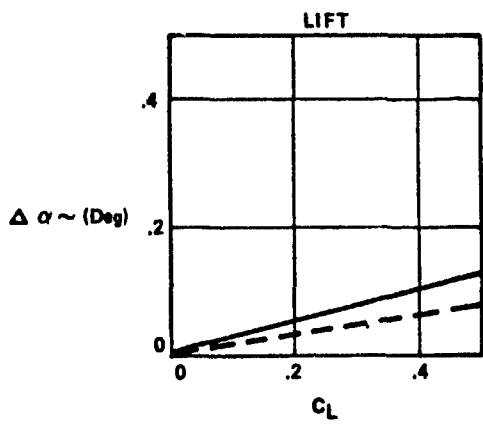
Figure 9-15   Effects of Removing Left Horiz. Tail and 50% of
Right Horiz. Tail from an F-105, M = 2.0
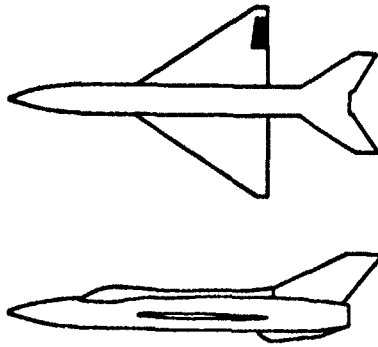
DAMAGE INPUT TO AAT

DWING (7) = 0.26   ΔC/C OF CUTOUT
DWING (8) = 0.57   η i, INBD EDGE OF CUTOUT
DWING (9) = 0.34   Δη, SPAN OF CUTOUT
DWING (10) = 2.0   INDICATOR FOR RIGHT SIDE ONLY

——————— WIND-TUNNEL DATA
— — — — AAT PREDICTIONS
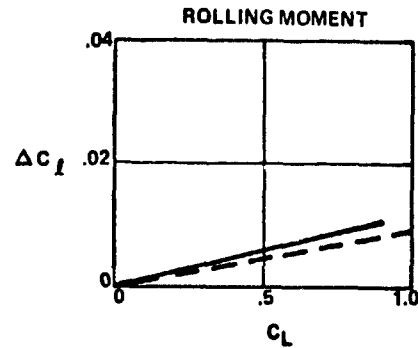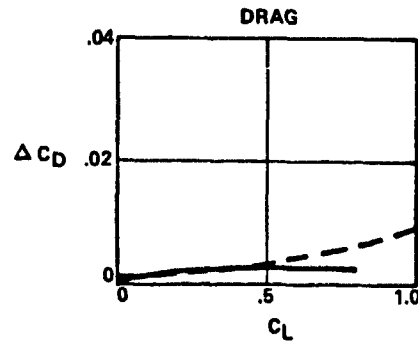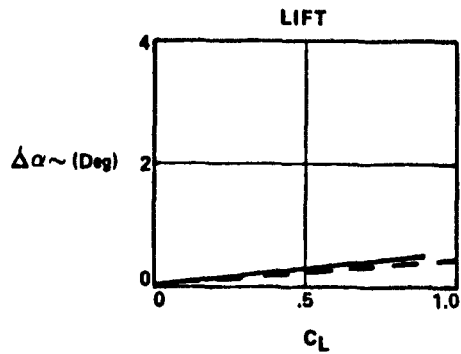
Figure 9-16   Effects of Removing Right Aileron From NASA Research
Model No. 1, M = 1.41

202

Figure 9-17 Effects of Removing 32% of Right Wing Exposed
Area from NASA Research Model No. 1, M = 1.41

DAMAGE INPUT TO AAT

DWING (16) = 1.0 FRACTION OF VERTICAL TAIL MISSING

——— WIND-TUNNEL DATA
— — AAT PREDICTIONS

LIFT

$\Delta \alpha \sim$ (Deg)

NO EFFECT

C_L

DRAG

ΔC_D

C_L

PITCHING MOMENT

ΔC_M

NO EFFECT

C_L

ROLLING MOMENT

ΔC_ℓ

NO EFFECT

C_L
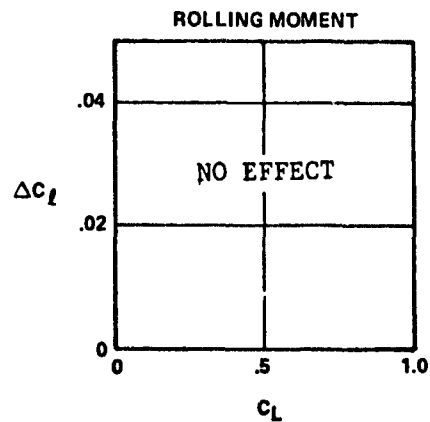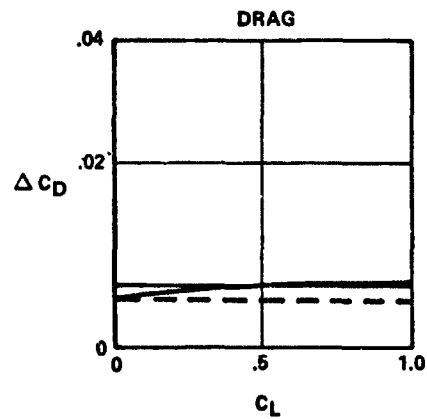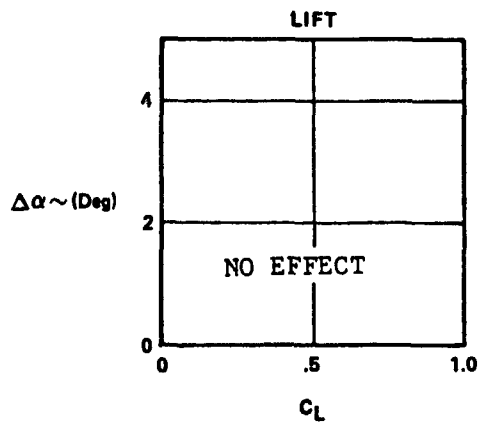
Figure 9-18   Effects of Removing Vertical Tail From NASA
Research Model No. 1, M = 1.41
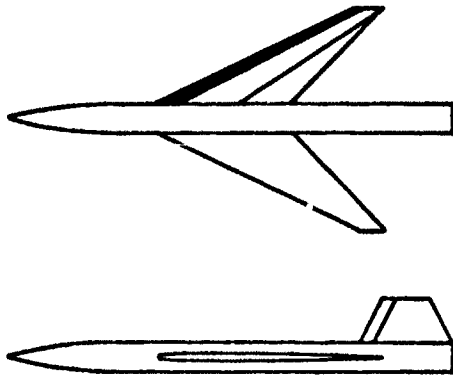
DAMAGE INPUT TO AAT

DWING (1) = 0.2 $\Delta C/C$ OF CUTOUT
DWING (2) = 0.15 z_i, INBD EDGE OF CUTOUT
DWING (3) = 0.85 Δz, SPAN OF CUTOUT
DWING (4) = 0.885   L.E. TO MAX THICKNESS
DWING (5) = 1.0   INDICATOR FOR ROUNDED CORNERS
DWING (6) = 2.0   INDICATOR FOR RIGHT WING ONLY

——— WIND-TUNNEL DATA
— — AAT PREDICTION
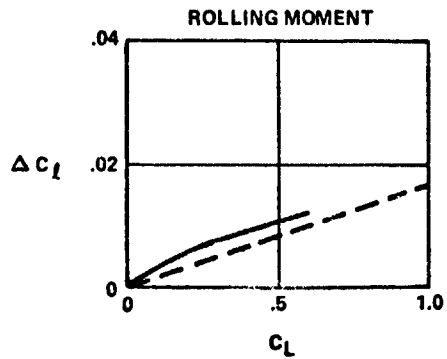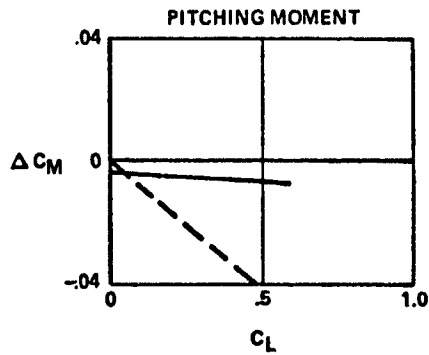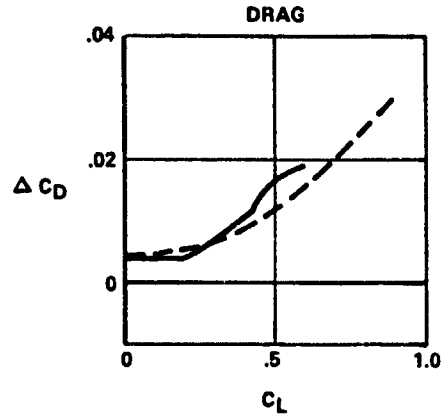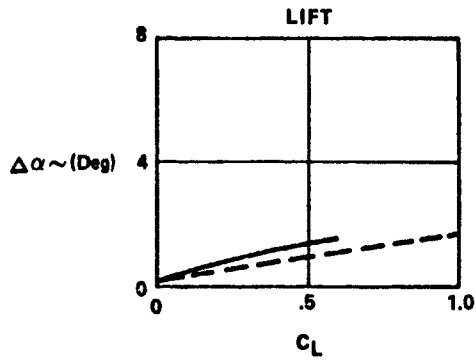
Figure 9-19   Effects of Removing Right-Wing Leading Edge
From NASA Research Model No. 2, M = 2.36

205
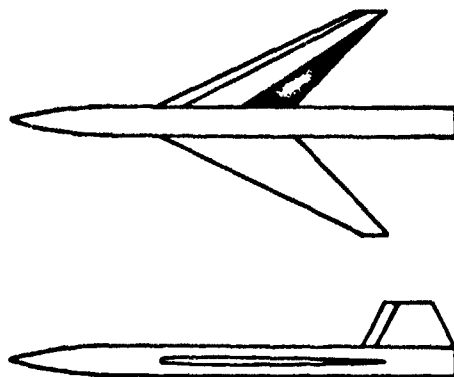
DAMAGE INPUT TO AAT

DWING (7)	= 0.368	△ C/C OF CUTOUT
DWING (8)	= 0.15	η i, INBD EDGE OF CUTOUT
DWING (9)	= 0.85	△ η, SPAN OF CUTOUT
DWING (10)	= 2.0	INDICATOR FOR RIGHT WING ONLY

———————— WIND-TUNNEL DATA
– – – – – AAT PREDICTION
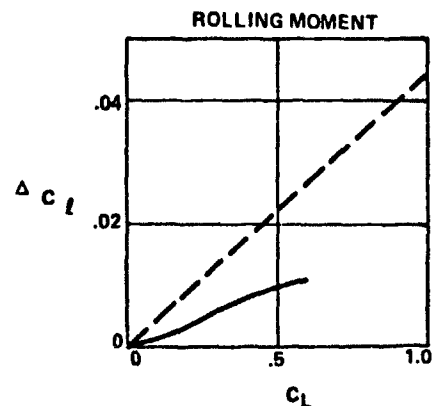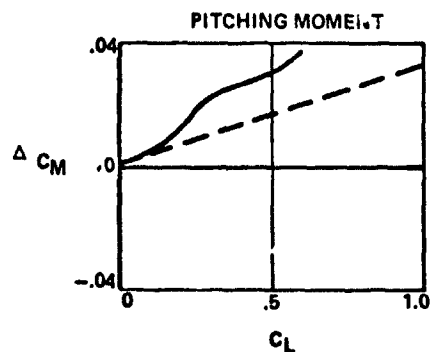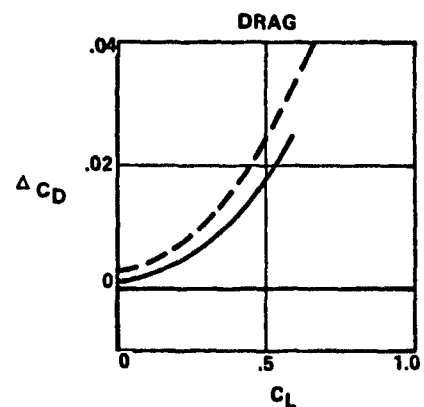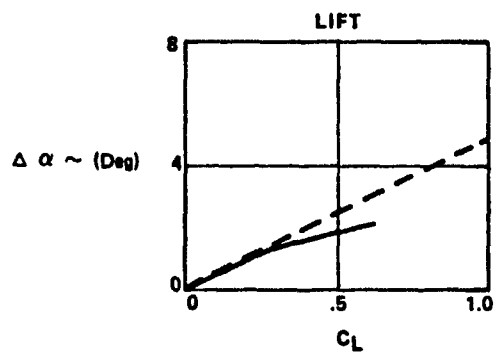
Figure 9-20   Effects of Removing Right-Wing Trailing Edge
from NASA Research Model No. 2, M = 2.36
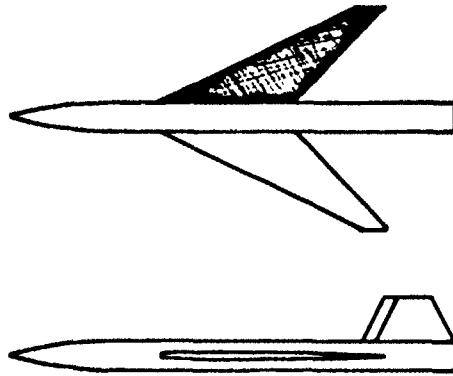
DAMAGE INPUT TO AAT.

DWING (12) = 0.85 $\Delta \eta$ MISSING FROM RIGHT
WING TIP.

—————— WIND-TUNNEL DATA
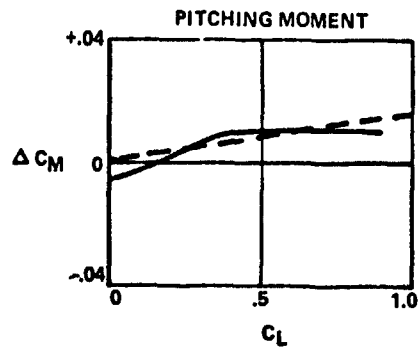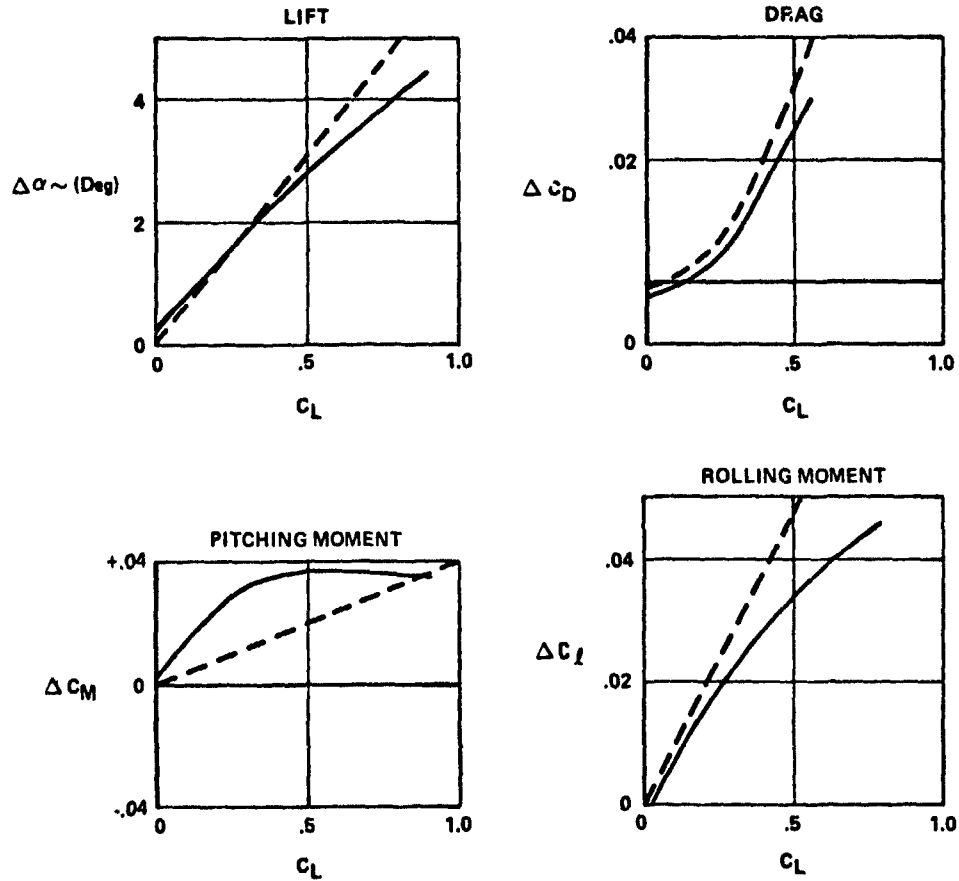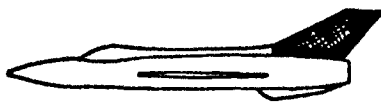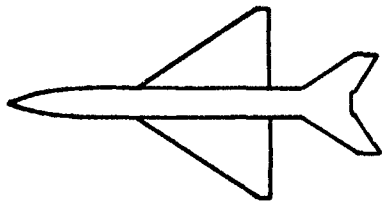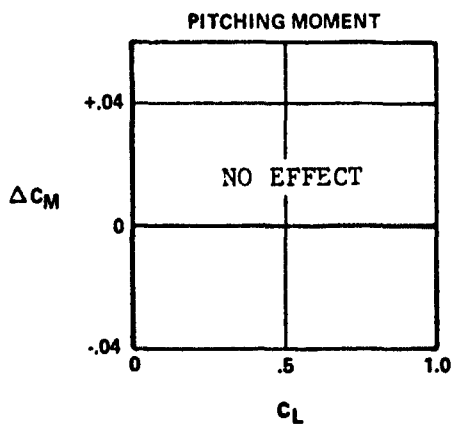— — — AAT PREDICTION

LIFT

DRAG

PITCHING MOMENT

ROLLING MOMENT
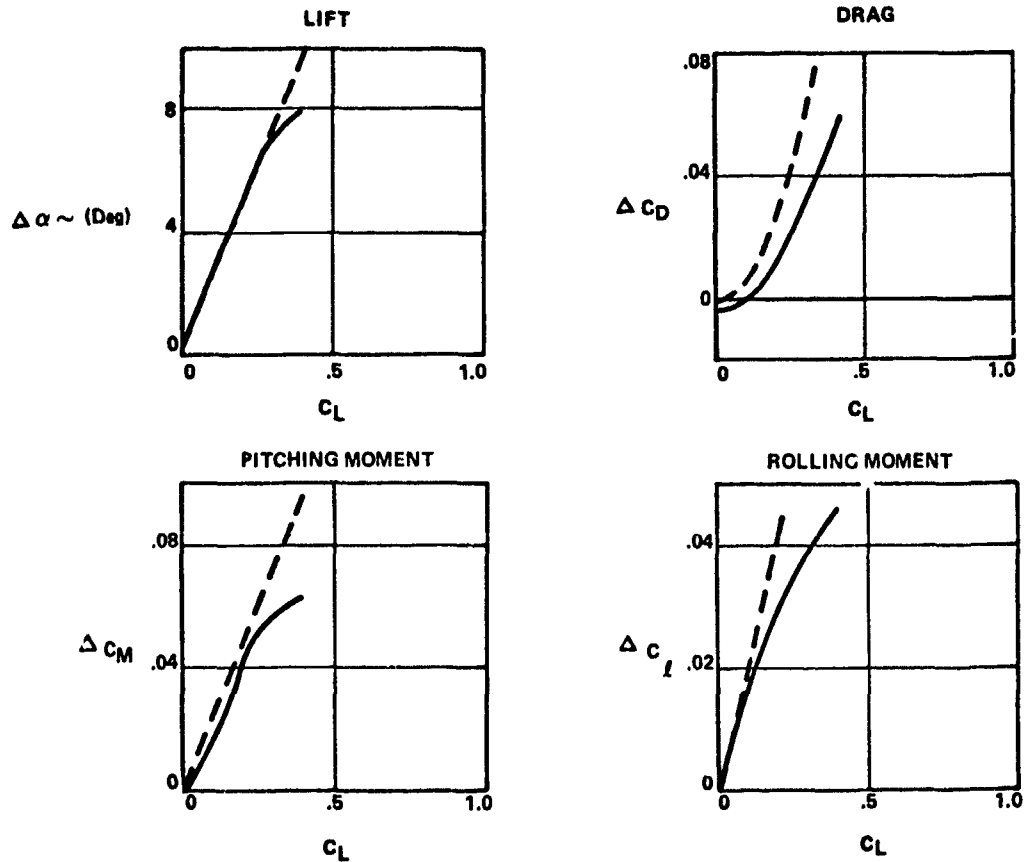
Figure 9-21   Effects of Removing Right-Wing From NASA
Research Model No. 2, M = 2.36

9.2.5 Full-Scale A-4B

Reference 48 presents data from a full-scale wind tunnel test of an A-4B aircraft to determine the aerodynamics with simulated and actual gunfire damage to one wing. These data are excellent for comparing with the AAT predictions for holes in the wing surface. Figures 9-22 through 9-25 show data and predictions for four of the configurations that were tested. Sketches on each figure show the wing panels that were removed from the upper and lower surfaces. AAT damage input parameters that are required to describe the holes are also listed on each figure. When multiple-hold cases are represented, an average length, width, and depth are used in the input.

9.2.6 Flat Plate Roughness

The Boeing Aerospace Company recently conducted a study (Reference 41) to determine the effects of nuclear thermal damage to the skin-friction drag of a series of flat-plate specimens. The force data measured for each test specimen, were used to determine an incompressible, skin-friction coefficient and an equivalent surface roughness value (k). Figure 9-26 shows a plot of skin-friction coefficient versus roughness that includes a data point for each specimen that produced consistent results over several runs.

An AAT problem was run to calculate the skin-friction drag on a flat plate under the same conditions as the test specimen. The methods in Section 8.1.1 were used to evaluate the skin-friction drag on a flat plate with two areas of different roughness. Calculations were first made for a smooth flat plate ($k=0$) to simulate the 17.5-inch section of tunnel floor that preceeded the specimen. The second AAT run was for a 22-inch flat plate on which the forward 17.5 inches again simulated the tunnel floor with a smooth section and aft 4.5 inches simulated the test specimen. Several runs were made with varying amounts of roughness on the aft 4.5 inches of the plate. Estimated drag on the simulated test specimen (aft 4.5 inches of the plate) was determined by subtracting the drag of the 17.5-inch smooth flat plate from the drag of the 22-inch plate with roughness. The prediction for the flat-plate specimen, which is shown as the solid line in Figure 9-26, is in very close agreement with the test data.
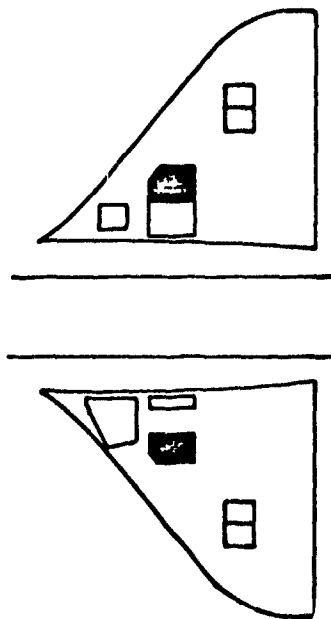
DAMAGE INPUT TO AAT

DSUR (1,31) =	1.0	NO. OF HOLES ON LOWER SURFACE
DSUR (1,32) =	1.0	NO. OF HOLES ON UPPER SURFACE
DSUR (1,33) =	2.80	AVG LENGTH OF HOLES
DSUR (1,34) =	1.70	AVG WIDTH OF HOLES
DSUR (1,35) =	0.36	AVG DEPTH OF HOLES
DSUR (1,36) =	0.25	X/C WHERE FIRST HOLE STARTS
DSUR (1,37) =	0.25	X/C WHERE LAST HOLE STARTS
DSUR (1,38) =	1.0	TYPE OF HOLE (Panel Missing = 1)
DSUR (1,39) =	0.438	POROSITY FACTOR

WIND-TUNNEL DATA
AAT PREDICTION

ΔC_D

C_L

ΔC_L

ANGLE-OF-ATTACK, α (Deg)
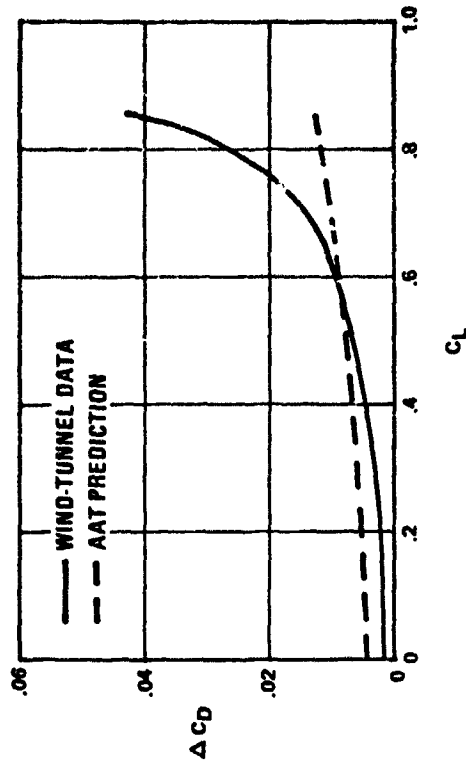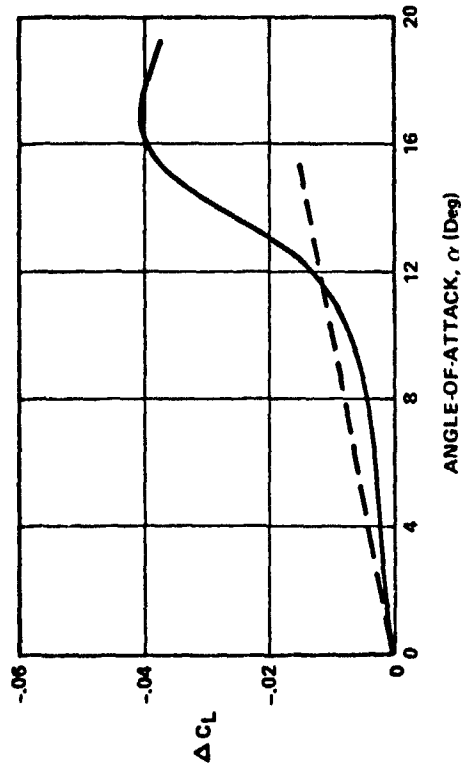
Figure 9-22   Effects of Holes in A-4B Wing, Test Configuration No. 4

DSUR (1, 31) = 1.0   NO. OF HOLES ON LOWER SURFACE
DSUR (1, 32) = 1.0   NO. OF HOLES ON UPPER SURFACE
DSUR (1, 33) = 3.40 AVG LENGTH OF HOLES
DSUR (1, 34) = 1.29 AVG WIDTH OF HOLES
DSUR (1, 35) = 0.25 AVG DEPTH OF HOLES
DSUR (1, 36) = 0.23 X/C WHERE FIRST HOLE STARTS
DSUR (1, 37) = 0.23 X/C WHERE LAST HOLE STARTS
DSUR (1, 38) = 1.0   TYPE OF HOLE (Panel Missing = 1)
DSUR (1, 39) = 0.344 POROSITY FACTOR

WIND-TUNNEL DATA
AAT PREDICTION

ΔC_D

C_L

ΔC_L

ANGLE-OF-ATTACK, α (Deg)
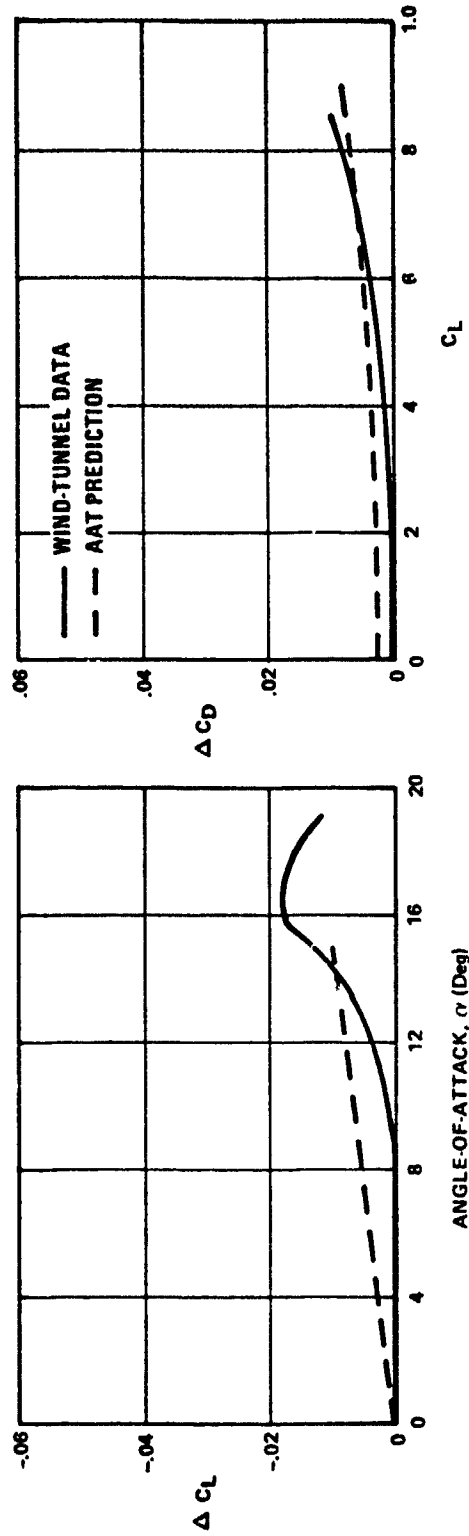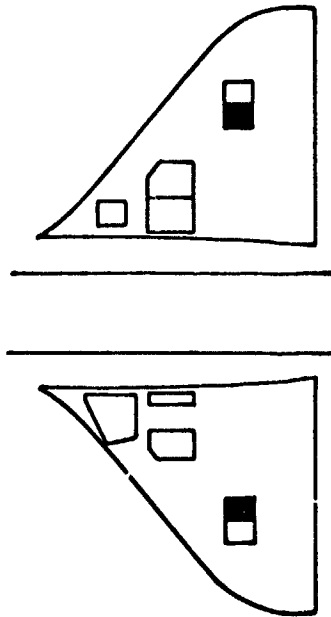
Figure 9-23 Effects of Holes in A-4B Wing, Test Configuration No. 7

210

DAMAGE INPUT TO AAT

DSUR (1, 31) = 1.0   NO. OF HOLES ON LOWER SURFACE
DSUR (1, 32) = 1.0   NO. OF HOLES ON UPPER SURFACE
DSUR (1, 33) = 3.40   AVG LENGTH OF HOLES
DSUR (1, 34) = 2.58   AVG WIDTH OF HOLES
DSUR (1, 35) = 0.25   AVG DEPTH OF HOLES
DSUR (1, 36) = 0.23   X/C WHERE FIRST HOLE STARTS
DSUR (1, 37) = 0.23   X/C WHERE LAST HOLE STARTS
DSUR (1, 38) = 1.0   TYPE OF HOLE (Panel Missing = 1)
DSUR (1, 39) = 0.345 POROSITY FACTOR

WIND-TUNNEL DATA
AAT PREDICTION
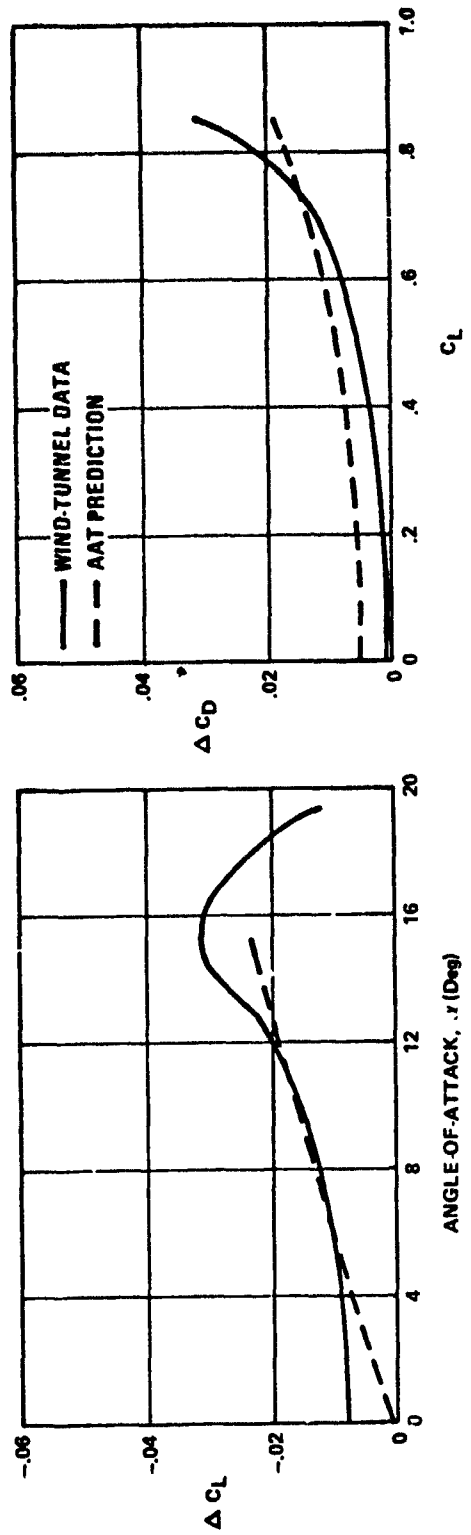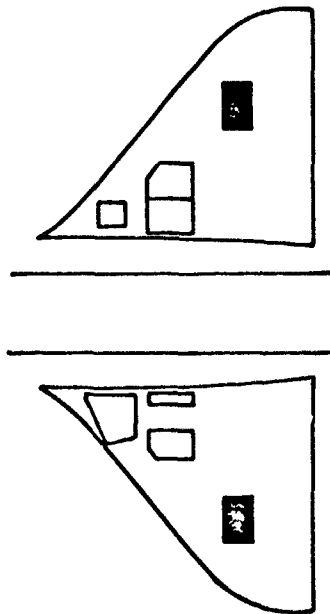
Figure 9-24   Effects of Holes in A-4B Wing, Test Configuration No. 8

211
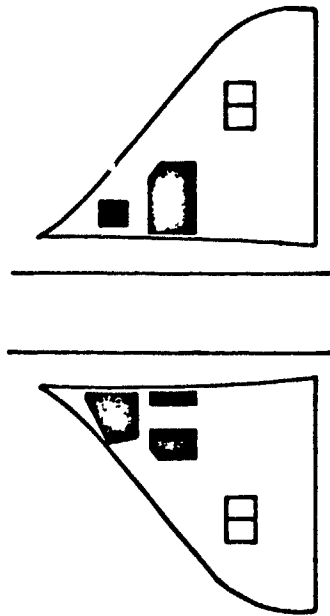
DAMAGE INPUT TO AAT

DSUR (1, 31)	= 1.0	NO. OF HOLES ON LOWER SURFACE
DSUR (1, 32)	= 2.0	NO. OF HOLES ON UPPER SURFACE
DSUR (1, 33)	= 3.26	AVG LENGTH OF HOLES
DSUR (1, 34)	= 2.61	AVG WIDTH OF HOLES
DSUR (1, 35)	= 0.36	AVG DEPTH OF HOLES
DSUR (1, 36)	= 0.13	X/C WHERE FIRST HOLE STARTS
DSUR (1, 37)	= 0.25	X/C WHERE LAST HOLE STARTS
DSUR (1, 38)	= 1.0	TYPE OF HOLE (Panel Missing = 1)
DSUR (1, 39)	= 0.824	POROSITY FACTOR

WIND-TUNNEL DATA
AAT PREDICTION

C_L

ΔC_D

ANGLE· ATTACK, α (Deg)

ΔC_L
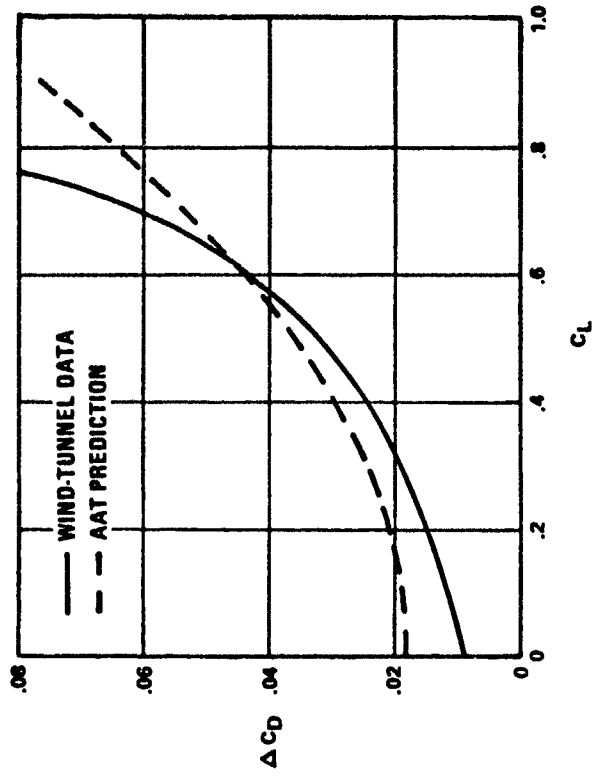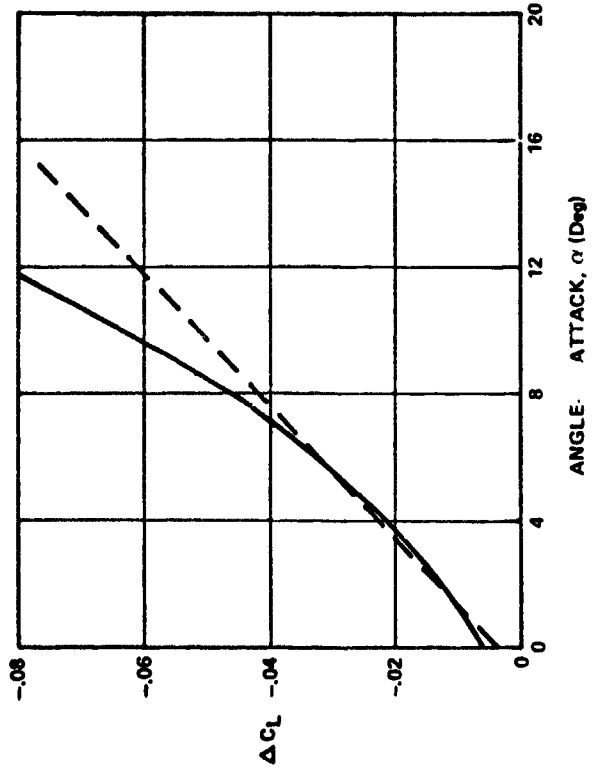
Figure 9-25 Effects of Holes in A-4B Wing, Test Configuration No. 13

212

SKIN FRICTION COEFFICIENT, C_{f_i}

.0055

.0050

.0045

.0040

.0035

.0030

.0025

AAT Prediction

Wind Tunnel Data

Specimen	C_{f_i}) avg	K x 10^{-3} (inches)
1-2	3.284	.559
1-3	3.437	.875
3-1	3.665	.999
3-2	4.29	1.92
4-2	3.76	2.083
4-3	3.665	.999
5-2	3.815	1.148
5-3	3.927	1.243
5-4	3.792	1.133
10-2	3.94	1.33
10-3	3.78	1.24
10-4	3.74	1.06
11-3	3.77	1.07
11-4	4.38	2 02
12-2	3.20	.50
12-3	4.96	3.42
12-4	4.53	2.35
12-7	4.293	1.867
13-1	4 17	1 92
13-3	4.89	3.05
13-7	4.23	1.78
14-1	4.71ᵧ	2.76
14-2	4.40	2.20
15-1	4.993	3.47
15-2	4.746	2.83
16-1	4.604	2.50
16-5	4.39	1.85
16-6	5.58	5.31
17-2	3.92	1.09
20-1	4.15	7.63
20-3	4.∪∪	1.61
20-5	5.01	3.48
21-2	4.19	1.73
22-3	4.79	3.04
23-2	4.40	2.07
23-3	4.41	2.12
24-5	4.68	2.68
24-9	5.00	3.43
25-3	3.81	1.11
26-1	3.26	0.58
26-3	3.72	0.98
27-6	4.65	2.63
29-2	5.38	4.60

0   .001   .002   .003   .004   .005

Roughness, K ~ Inches

Figure 9-26   Comparison of Predictions and Data for Flat-Plate Roughness Drag

10. CONCLUSIONS AND RECOMMENDATIONS

The Aerodynamic Accounting Technique Computer Code provides
the capabilities of evaluating basic aircraft aerodynamics and
estimating the aerodynamics effects of roughness and aircraft
damage. The first, and most fundamental, part of the program
estimates the lift, drag, and pitching-moment coefficients of
an arbitrary aircraft. The second part of the program evaluates
the effects of aircraft damage as described by one of the 14
modes of damage simulation that are provided. The 14 damage modes allow
the user to represent almost any type of actual aircraft damage that
may be encountered.

Successful operation of the program is verified by AAT pre-
dictions favorably comparing with F-16A wind-tunnel data and FB-111
flight-test data. Damage evaluation methods are verified by com-
parisons with data from tests on an F-105, an A-4B, and several
research models.

This computerized approach to aircraft analyses offers a
significant improveme ` over hand calculations based on handbook
methods. Some of the more important advantages are:

1. The program can handle complex relationships between
   geometric and aerodynamic parameters. Many of the
   details of these calculations would not be feasible
   in hand calculations.

2. Calculations done by hand require a great deal of time
   and are prone to error.

3. Hand calculations generally depend, to some extent,
   on the individual's judgment and may lead to results
   that are inconsistent. The program, on the other
   hand, is always consistent in its calculations.

This program can be used by simply following the instructions
provided in the Program User Guide. However, it is recommended
that the serious user familiarize himself with the methods that
are used in the program. It is also recommended that the user
make a run on a configuration for which test data are available
that is similar to the one being evaluated and correlate the
predictions with the test data to establish limits for credible
lift, drag, and moment predictions for the type of configuration
being evaluated.

The AAT program is constructed in a modular form that allows subroutines to be easily added or replaced in order to incorporate new or improved aerodynamic methods into the program. The damage evaluation section of the program is set up to allow the addition of 6 additional modes of damage evaluation without major revisions to the existing programming statements.

Methods used in the evaluation of the undamaged aircraft are highly refined and were developed over many years by engineers throughout the aerospace industry. Damage evaluation, on the other hand, has not been a priority topic until recently and consequently, the methods are not as highly refined. Checkout problems (Section 9) show that the methods are quite accurate for the cases that were analyzed and compared with data. Additional wind tunnel testing for damage effects could, however, be used to verify and enhance the methods that are now being used in the program.

References

1. Schemensky, R.T., _Development of an Empirically Based Computer Program to Predict the Aerodynamic Characteristics of Aircraft_, Air Force Flight Dynamics Laboratory AFFDL-TR-73-144, November 1973.

2. _USAF Stability and Control DATCOM_, Air Force Flight Dynamics Laboratory, October 1960 (Revised August 1968).

3. White, F.M., and Christoph, G.H., _A Simple New Analysis of Compressible Turbulent Two-Dimensional Skin Friction Under Aribtrary Conditions_, AFFDL TR 70 133, February 1971.

4. Schlichting, H., _Boundary-Layer Theory_, McGraw-Hill, 1955.

5. Goddard, F.E., Jr., "Effect of Uniformly Distributed Roughness on Turbulent Skin-Friction Drag at Supersonic Speeds". Journal of the Aero/Space Sciences, Vol. 26, No. 1, January 1959.

6. _Aerospace Handbook_, Second Edition (C.W. Smith, Ed.), General Dynamics' Convair Aerospace Division Report FZA-381-II, October 1972.

7. Hoerner, S.F., _Fluid-Dynamic Drag_ (Published by the author, Midland Park, New Jersey, 1965).

8. Linnell, R.D., _Similarity Rule Estimation Methods III, Flow Around Cones and Parabolic Noses_, General Dynamic' Convair Aerospace Division Report MR-A-1059, 10 August 1955.

9. Peake, D.J., "Three-Dimensional Flow Separations on Upswept Rear Fuselages," _Canadian Aeronautics and Space Journal_, Vol. 15 (December 1969), p. 399.

10. Frost, R.C., and Rutherford, R.G., "Subsonic Wind Span Efficiency," _AIAA Journal_, Vol. 1, No. 4 (April 1963).

11. Benepe, D.B., et al., _Aerodynamic Characteristics of Non-Straight-Taper Wings_, AFFDL-TR-66-73, October 1966.

12. Henderson, W.P., _Studies of Various Factors Affecting Drag Due to Lift at Subsonic Speeds_, NASA TN D-3584, October 1966.

References, (Continued)

13. John, H., <u>On Induced-Drag Calculation of Uncambered and Untwisted Wings as a Function of the Reynolds Number</u>, Boeing Comparny Report B-819.41, March 1969 (Originally published by VFX, for GDLR Aerodunamics Colliquium, Berlin, October 1968).

14. Simon, W.E., et al., <u>Prediction of Aircraft Drag Due to Lift</u>, AFFDL TR-71-84, July 1971.

15. Ray, E.J., and Taylor, R.T., "Buffet and Static Aerodynamic Characteristics of a Systematic Series of Wings Determined From a Subsonic Wind-Tunnel Study, NASA TN D-5805, June 1970.

16. <u>A Method of Estimating Drag-Rise Mach Number for Two-Dimensional Aerofoil Sections,</u> Royal Aero. Soc. Transonic Data Memorandum 6407, July 1964.

17. Sinnott, C.S., "Theoretical Prediction of the Transonic Characteristics of Airfoils," <u>Journal of the Aerospace Sciences,</u> Vol. 29, No. 3 (March 1962).

18. <u>Method for Predicting the Pressure Distribution on Swept Wings with Subsonic Attached Flow</u>, Royal Aero. Soc. Transonic Data Memorandum 6312, December 1963.

19. Miller, B.D., <u>Notes on Wing Design Methods for Supercritical Airfoils,</u> General Dynamics' Convair Aerospace Division Report ARM-061, October 1971.

20. <u>Drag-Rise Mach Number of Aerofoils Having a Specified Form of Upper-Surface Pressure Distribution: Charts and Comments on Design</u>, Royal Aero. Soc. Transonic Data Memorandum 67009, January 1967.

21. Lowry, J.G., and Polhamus, E.C., <u>A Method for Predicting Lift Increments Due to Flap Deflection at Low Angles of Attack in Incompressible Flow</u>, NACA TN 3911, 1957.

22. Spencer, B., Jr., <u>A Simplified Method for Estimating Subsonic Lift-Curve Slope at Low Angles of Attack for Irregular Planform Wings,</u> NASA TM X-525, May 1961.

23. Polhamus, E.C., Summary of Results Obtained by Transonic-Bump Method on Effects of Planform and Thickness on Lift and Drag Characteristics of Wings at Transonic Speeds, NACA RM L51H30, 30 November 1951.

24. Nelson, W.H., and McDevitt, J.B., The Transonic Characteristics of 17 Rectangular, Symmetrical Wing Models of Varying Aspect Ratio and Thickness, NACA RM A51A12, 10 May 1951.

25. Tinling, B.E., and Kolk, W.R., The Effects of Mach Number on the Aerodynamic Characteristis cf Several 12-Percent-Thick Wings Having 35 Degrees of Sweepback and Various Amounts of Camber, NACA RM A50K27, 23 February 1951.

26. Donlan, C.J., and Weil, J., Characteristics of Swept Wings at High Speeds, NACA RM L52A15, January 1952.

27. Hoerner, S.F., The Lift of a Body-Wing Combination, Wright-Patterson Air Force Base Air Documents Diviion Report F-TR-1187-ND, September 1948.

28. Schemensky, R.T., Braymen, W.W., and Crosthwait, E.L., Aerodynamic Configuration Analysis Procedure, AeroModule, Version IA, General Dynamics' Fort Worth Division Report ERR-FW-931, 31 December 1969.

29. Pitts, W., Nielsen, J., and Kaattari, G., Lift and Center of Pressure Wing-Body-Tail Combinations at Subsonic, Transonic, and Supersonic Speeds, NACA TR 1307, 1957.

30. Sills, J.A., and Hadley, S.K., Conceptual Wind-Tunnel Tests of Tandem-Wing Combinations, General Dynamics Fort Worth Division, ARM No. 136, 29 March 1974.

31. Sherrer, H.J., Jr., and Crosthwait, E.L., The Prediction of Lift Considering Body Cross Section and Complete Configuration Planform, General Dynamics' Fort Worth Division Report AIM-261, 17 September 1969.

32. Gilman, B.G., and Burdges, K.P., "Rapid Estimation of Wing Aerodynamic Characteristics for Minimum Induced Drag," Journal of Aircraft, Vol. 4, No. 6 (November - December 1967.

References,(Continued)

33. Polhamus, E.C., "Prediction of Vortex-Lift on Leading-Edge Suction Analogy," AIAA Paper No. 69-1133, October 1969.

34. Schemensky, R.T., Prediction of the Lift Characteristics of Low Aspect Ratio Wings, General Dynamics' Convair Aerospace Division Report ARM-098, 14 November 1972.

35. Polhamus, E.C., Charts for Predicting the Subsonic Vortex-Lift Characteristics of Arrow, Delta, and Diamond Wings, NASA TN D-6243, April 1971.

36. Benepe, D.B., Analysis of Nonlinear Lift of Sharp- and Round-Leading-Edge Delta Wings, General Dynamics' Fort Worth Division Report ERR-FW-799, December 1968.

37. Küchemann, D., A Simple Method for Calculating the Span and Chordwise Loading on Straight and Swept Wings of any Given Aspect Ratio at Subsonic Speeds, A.R.C. Technical Report R&M No. 2935, August 1952.

38. Emerson, H.F., Wind-Tunnel Investigation of the Effect of Clipping the Tips of Triangular Wings of Different Thickness, Camber, and Aspect Ratio - Transonic Bump Method, NASA TN-3671, June 1956.

39. Young, A. D., The Drag Effects of Roughness at High Subcritical Speeds, Jour. Roy. Aero. Soc. 18, dated 1950.

40. Snodgrass, Robert R., A Method for Determining Aerodynamic Characteristics for Mission Completion Studies in a Nuclear Environment, AST-TR-75-3, July 1975.

41. Skin Friction Drag Increase Due to Nuclear Thermal Damage, The Boeing Aerospace Company, Final Report on Contract No. DNA 001-77-C-0090, dated 30 September 1977.

42. Rossiter, J. E., and Kurn, A. G., Wind Tunnel Measurements of the Unsteady Pressures in and Behind a Bomb Bay, A.R.C., C.P. 728, 1965.

43. Wallskog, Harvey A., and Hart, Roger G., Investigation of the Drag of Blunt-Nosed Bodies of Revolution in Free Flight at Mach Numbers From 0.6 to 2.3, NACA RM L53D14a, June 1953.

44. Stoney, William E., Collection of Zero-Lift Drag Data on Bodies of Revolution from Free-Flight Investigation, NACA TN 4201, January 1958.

References, (Continued)

45. Carmichael, R. L., Castellano, C. R., and Chen, F. C., "The Use of Finite Element Methods for Predicting the Aerodynamics of Wing-Body Combinations," Analytical Methods in Aircraft Aerodynamics, a symposium held at Ames Research Center, NASA SP-228, 28-30 October 1969.

46. Engineering Sciences Data Unit, Aerodynamics Sub-Series, Volume 2a, Wings 01.01.04, Royal Aeronautical Society, May 1974.

47. Polhamus, Edward C., Predictions of Vortex-Lift Characteristics Based on a Leading-Edge Suction Analogy, AIAA Paper No. 69-1133, October 1969.

48. Betzina, Mark D., and Brown, David H., Aerodynamic Characteristics of an A-4B Aircraft with Simulated and Actual Gunfire Damage to One Wing, NASA TM X-73-119, July 1976.

49. Abbott, Ira H., and Von Doenhoff, Albert E., Theory of Wing Sections, Dover Publications, Inc., 1959.

50. Aerodynamic Data Substantiation for Standard Aircraft Characteristics Charts and Regular Flight Manual FB-111 Aircraft, General Dynamics' Report FZA-12-6007, 1 April, 1970.

51. Final Preliminary Stability and Control Aerodynamic Data for the F-111B Airplane, General Dynamics' Report FZM-12-4207, November 23, 1966.

52. Hood, Manley J., The Effects of Surface Waviness and of Rib Stitching on Wing Drag, NACA TN-724, August 1939.

53. Blair, A.B., Jr., Effects of Simulated Damage on Stability and Control Characteristics of a Swept-Wing Fighter Airplane at Mach 1.57 and 2.00, (Unpublished).

54. Tufts, O.B., Evaluation of F-105F Wind Tunnel Aerodynamic Damage Tests, Cornell Aeronautical Laboratory Report, (Unpublished).

55. Fuller, Dennis E., and Watson, Carolyn B., Effects of Simulated Damage on the Stability and Control Characteristics of a Delta-Wing Fighter Airplane Model at Mach Numbers of 1.41 and 2.01, NASA TM X-1750, March 1969.

References,(Concluded)

56. Hayes, Clyde, _Effects of Simulated Wing Damage on the Aerodynamic Characteristics of a Swept-Wing Airplane Model_, NASA TM X-1550, April 1968.

LIST OF SYMBOLS

A	Area
AR	Aspect Ratio
b	Wing span
C_D	Drag coefficient
C_{D_L}	Drag due to lift
C_{DR}	Drag rise
C_f	Skin friction coefficient
c_f/c	Flap chord to wing chord ratio
C_L	Lift coefficient
C_{L_D}	Wing design lift coefficient
C_{ℓ_d}	Section camber lift coefficient
$C_{L_{DB}}$	Value of C_L for flow separation
C_P	Pressure coefficient
$C_{L_{PB}}$	Value of C_L where drag polar ceases to be parabolic
C_M	Pitching moment coefficient
C_R	Root chord
$\bar{c}$	Mean geometrical chord
C_{L_α}	Lift-curve slope
d	Body diameter
e	Net polar span efficiency
e_o	Wing-body polar span efficiency
e_w	Theoretical wing-alone polar span efficiency
Δf	Equivalent parasite area
i	Incidence angle

222

LIST OF SYMBOLS, continued

K̈	Polar shape factor
k	Surface roughness height
K_{comp}	Compressibility factor
l	Length
m	Drag magnification factor
M	Mach number
MAC	Mean geometrical chord
M_{CR}	Critical Mach number
q	Dynamic pressure
R	Leading-edge suction factor
R_N	Reynolds number
S	Surface area
t/c	Wing thickness-to-chord ratio
X	Longitudinal location
Y	Lateral location
Z	Vertical location
α	Angle of attack
β	$\sqrt{M^2-1}$ or $\sqrt{1-M^2}$
ΔC_L	Polar displacement at minimum drag
ΔC_{L_o}	Lift displacement at $\alpha = 0$
Δy	Airfoil leading-edge sharpness parameter
Λ	Sweep angle
λ	Taper ratio
$\emptyset_{TE}$	Airfoil section trailing-edge angle

223

δ	Deflection or boundary layer thickness
η	Fraction of semi-span

Subscripts

ac	Aerodynamic center
BT	Boattail
c/4	Quarter-chord
c/2	Mid-chord
CG	Center of gravity
e	Effective value or exposed
exp	Exposed
HT	Horizontal tail
i	Inboard
LE	Leading edge
LER	Airfoil Leading-edge radius
max	Maximum value
min	Minimum value
N	Nose or number of wing panels
o	Zero lift or outboard
PB	Value at $C_{L_{PB}}$
plan	Planform
ref	Reference
sex	Exposed airfoil surface
t	Tail surface
TE	Trailing edge
WB	Wing-Body
wet	Wetted area

DISTRIBUTION LIST

DEPARTMENT OF DEFENSE

Assistant to the Secretary of Defense
Atomic Energy
    ATTN: Executive Assistant

Defense Documentation Center
12 cy ATTN: DD

Defense Nuclear Agency
    ATTN: DDST
    ATTN: SPAS
    ATTN: STSP
4 cy ATTN: TITL

Field Command
Defense Nuclear Agency
    ATTN: FCPR

Livermore Division, Field Command, DNA
Lawrence Livermore Laboratory
    ATTN: FCPRL

Commandant
NATO School (SHAPE)
    ATTN: U.S. Documents Officer

Under Secretary of Defense for Rsch. & Engrg.
    ATTN: Strategic & Space Systems (OS)

DEPARTMENT OF THE ARMY

Harry Diamond Laboratories
    ATTN: DELHD-N-NP
    ATTN: DELHD-N-P, J. Gwaltney

U.S. Army Ballistic Research Labs.
    ATTN: DRXBR-BLE, W. Taylor
    ATTN: DRDAR-BLV, J. Meszaros

U.S. Army Materiel Dev. & Readiness Cmd.
    ATTN: DRCDE-D, L. Flynn

U.S. Army Nuclear & Chemical Agency
    ATTN: Library

DEPARTMENT OF THE NAVY

Naval Material Command
    ATTN: MAT 08T-22

Naval Research Laboratory
    ATTN: Code 2627

Naval Surface Weapons Center
    ATTN: K. Caudle

Naval Weapons Evaluation Facility
2 cy ATTN: L. Oliver

Office of Naval Research
    ATTN: Code 464

Strategic Systems Project Office
    ATTN: NSP-272

DEPARTMENT OF THE AIR FORCE

Aeronautical Systems Division, AFSC
    ATTN: ENFT, R. Bachman
4 cy ATTN: ENFTV, D. Ward
10 cy ATTN: ENFTA, R. Sarver

Air Force Materials Laboratory
    ATTN: MBE, G. Schmitt

Air Force Weapons Laboratory
    ATTN: SUL
    ATTN: DYV, G. Campbell
4 cy ATTN: DYV, A. Sharp

Foreign Technology Division, AFSC
    ATTN: PDBF, Mr. Spring

Strategic Air Command/XPFS
    ATTN: XPFS, B. Stephan

DEPARTMENT OF DEFENSE CONTRACTORS

Aerospace Corporation
    ATTN: W. Barry

Avco Research & Systems Group
    ATTN: J. Patrick
    ATTN: P. Grady

Boeing Company
    ATTN: S. Strack
    ATTN: R. Dyrdahl
    ATTN: E. York

Boeing Wichita Company
    ATTN: R. Syring

Calspan Corporation
    ATTN: M. Dunn

Effects Technology, Inc.
    ATTN: R. Parisse
    ATTN: E. Bick
    ATTN: R. Wengler

General Dynamics Corporation
Pomona Division
    ATTN: R. Schemensky

General Dynamics Corporation
Forth Worth Division
    ATTN: G. Howell

General Electric Co.-TEMPO
Center for Advanced Studies
    ATTN: DASIAC

General Research Corp.
Santa Barbara Division
    ATTN: T. Stathacopoulos

Kaman AviDyne
Division of Kaman Sciences Corp.
    ATTN: E. Criscione
    ATTN: N. Hobbs
    ATTN: R. Ruetenik

DEPARTMENT OF DEFENSE CONTRACTORS (Continued)

Kaman Sciences Corporation
    ATTN: D. Sachs

Los Alamos Technical Associates
    ATTN: P. Hughes

McDonnell Douglas Corporation
    ATTN: J. McGrew

Prototype Development Associates, Inc.
    ATTN: C. Thacker
    ATTN: J. McDonald

R&D Associates
    ATTN: C. MacDonald
    ATTN: F. Field
    ATTN: J. Carpenter

Rockwell International Corp.
    ATTN: K. Sparling

Sandia Laboratories
    ATTN: Doc. Con. for A. Lieber

Science Applications, Inc
    ATTN: D. Hove

SRI International
    ATTN: G. Abrahamson